

VAGNER CANDIDO DE SOUSA

***Efeitos de molas com memória de forma
superelásticas no comportamento aeroelástico de
uma seção típica: aplicações em atenuação passiva
de vibrações e coleta de energia***

São Carlos

2016

VAGNER CANDIDO DE SOUSA

***Efeitos de molas com memória de forma
superelásticas no comportamento aeroelástico de
uma seção típica: aplicações em atenuação passiva
de vibrações e coleta de energia***

Tese apresentada à Escola de Engenharia de
São Carlos da Universidade de São Paulo,
como parte dos requisitos para obtenção do
título de Doutor em Ciências.

Área de Concentração: Aeronaves

Orientador: Prof. Dr. Carlos De Marqui Junior

ESTE EXEMPLAR TRATA-SE DA VER-
SÃO CORRIGIDA. A VERSÃO ORIGINAL
ENCONTRA-SE DISPONÍVEL JUNTO AO
DEPARTAMENTO DE ENGENHARIA ME-
CÂNICA DA EESC-USP.

São Carlos

2016

AUTORIZO A REPRODUÇÃO TOTAL OU PARCIAL DESTE TRABALHO,
POR QUALQUER MEIO CONVENCIONAL OU ELETRÔNICO, PARA FINS
DE ESTUDO E PESQUISA, DESDE QUE CITADA A FONTE.

Candido de Sousa, Vagner
C126e Efeitos de molas com memória de forma
superelásticas no comportamento aeroelástico de uma
seção típica: aplicações em atenuação passiva de
vibrações e coleta de energia / Vagner Candido de
Sousa; orientador Carlos De Marqui Junior. São Carlos,
2016.

Tese (Doutorado) - Programa de Pós-Graduação em
Engenharia Mecânica e Área de Concentração em Aeronaves
-- Escola de Engenharia de São Carlos da Universidade
de São Paulo, 2016.

1. Vibrações mecânicas. 2. Aeroelasticidade. 3.
Ligas com memória de forma. 4. Geração de energia. I.
Título.

FOLHA DE JULGAMENTO

Candidato: Engenheiro **VAGNER CANDIDO DE SOUSA**.

Título da tese: "Efeito de molas com memória de forma superelásticas no comportamento aeroelástico de uma seção típica: aplicações em atenuação passiva de vibrações e coleta de energia".

Data da defesa: 27/06/2016.

Comissão Julgadora:

Resultado:

Prof. Dr. **Carlos De Marqui Junior (Orientador)**
(Escola de Engenharia de São Carlos/EESC)

Aprovado

Prof. Associado **Marcelo Areias Trindade**
(Escola de Engenharia de São Carlos/EESC)

Aprovado

Prof. Dr. **Marcelo Amorim Savi**
(Universidade Federal do Rio de Janeiro/UFRJ)

Aprovado

Prof. Dr. **Domingos Alves Rade**
(Instituto Tecnológico de Aeronáutica/ITA)

Aprovado

Prof. Dr. **Carlos José de Araújo**
(Universidade Federal de Campina Grande/UFCG)

Aprovado

Coordenador do Programa de Pós-Graduação em Engenharia Mecânica:
Prof. Associado **Gherhardt Ribatski**

Presidente da Comissão de Pós-Graduação:
Prof. Associado **Luis Fernando Costa Alberto**

To my family.

ACKNOWLEDGMENTS

I would like to thank to Dr. Carlos De Marqui Junior for his guidance and patience while supervising my graduate studies since 2009. His help is greatly appreciated.

I would like to thank to the Department of Aeronautical Engineering at the São Carlos School of Engineering of the University of São Paulo. Thanks to all of the professors (in particular to Volnei Tita, Ricardo Angélico and Marcelo Leite) and employees (Gisele, João, Cláudio, Gallo, Mário, Rosana and many others). Also, thanks to Prof. Reginaldo (NUMA/EESC-USP) and Pereira (IFSC-USP). Many thanks to my “lab-mate” friends (José Augusto, Tarcísio, Douglas, Wander, Marcel, Pagani) and “department-mate” friends (a lot of them).

I would like to thank to CAPES – Brazilian Federal Agency for Support and Evaluation of Graduate Education within the Ministry of Education of Brazil – for its financial support through processes DS-00011/07-0 and PDSE-99999.002891/2015-08.

I would like to thank to Dr. Mohammad Elahinia, director of the SMART Lab at the MIME Department of The University of Toledo (Toledo, OH - USA), for receiving me in his lab during six wonderful months. I also would like to thank to all of his students that I had the opportunity of meeting there (Ahmadreza, Amir, Arman, Bahram, Feng, Hamdy, Mehram, Mohsen, Narges, Sajedeh, Wonsang) for being great lab-mates and friends during (and after) my staying at their lab. I had such a great time there.

I would like to thank to Marcia Salazar-Valentine (Executive Director of International Programs and Partnerships at Bowling Green State University), the “mother” of the brazillian students in Ohio. Her help and friendship are greatly appreciated. She helped us a lot with finding a place to live, taking us to many places in town, receiving us at her own home for great weekends and introducing us to great people. Also, many thanks to her friend Judy for picking us up at Detroit Int’l Airport.

I would like to thank to all friends from *English Corner* and *Water for Ishmael*, such as Betsy and Prof. Don White, Wes Blood, Vicki, Don Spiegel, Robert “Bob” Fair (a WWII Veteran) and his daughter Roberta, Jennifer and Mark, Marla and Rachel, to name a few, and to many other great people we met in the US such as Javir and Ejaza, although being impossible to name all of them.

I also would like to thank to Luciana Rolsen from Fort Wayne Metals for a great guided tour to FWM headquarters in Fort Wayne (Indiana) and for very nice NiTi SMA samples.

Last but not least, I would like to thank to my wife Fernanda for her patience, support and for giving up on her own plans to join me for six months in the US.

Many thanks!

Even if the open windows of science at first make us shiver after the cosy indoor warmth of traditional humanizing myths, in the end the fresh air brings vigour, and the great spaces have a splendour of their own.

Bertrand Russell

Resumo

SOUSA, V. C. **Efeitos de molas com memória de forma superelásticas no comportamento aeroelástico de uma seção típica: aplicações em atenuação passiva de vibrações e coleta de energia.** 2016. 190f. Doutorado – Escola de Engenharia de São Carlos, Universidade de São Paulo, São Carlos, 2016.

A modelagem, análise e verificação experimental de uma seção típica aeroelástica com dois graus de liberdade e molas com memória de forma superelásticas são apresentadas. O foco é investigar os efeitos da histerese pseudoelástica das molas com memória de forma nos comportamentos de *flutter* e pós-*flutter* da seção típica. A cinética das transformações de fase nas molas com memória de forma é descrita por uma versão modificada de modelos fenomenológicos amplamente conhecidos. O modelo de molas helicoidais com memória de forma é baseado em teoria clássica de molas (com a hipótese de cisalhamento puro) e modificado para representar os efeitos não lineares de transformação de fase. A seção transversal do fio da mola com memória de forma é representada por uma distribuição radial e linear de deformações de cisalhamento e por distribuições radiais e não lineares de tensões cisalhantes e de frações martensíticas. As equações de movimento de uma seção típica linear são modificadas para incluir as molas com memória de forma. Um modelo aerodinâmico linear não estacionário é utilizado para se determinar as cargas aerodinâmicas. O modelo proposto é representado em espaço de estados e resolvido com um método Runge-Kutta. Mostra-se, numérica e experimentalmente, que a histerese pseudoelástica de molas com memória de forma pode ser efetivamente explorada para melhorar o comportamento aeroelástico de uma seção típica ao transformar oscilações instáveis de *flutter* em oscilações estáveis e de amplitudes aceitáveis em uma faixa de velocidades do escoamento, provendo um método útil de controle aeroelástico passivo. Como o comportamento aeroelástico modificado (pela histerese pseudoelástica) é atrativo para a coleta de energia do escoamento, um acoplamento eletromecânico é modelado no grau de liberdade de deslocamento linear, juntamente com uma carga resistiva no domínio elétrico do problema para se estimar a potência elétrica gerada. A exploração da histerese pseudoelástica das molas com memória de forma é mais atrativa para a performance da coleta aeroelástica de energia do que o uso de não linearidades concentradas típicas (como o enrijecimento não linear do aço) em termos de melhoria na potência elétrica gerada.

Palavras-chave: Vibrações mecânicas. Aeroelasticidade. Ligas com memória de forma. Geração de energia.

Abstract

SOUSA, V. C. **Effects of superelastic shape memory springs on the aeroelastic behavior of a typical airfoil section: passive vibration attenuation and energy harvesting applications.** 2016. 190f. Tese (Doutorado) – Escola de Engenharia de São Carlos, Universidade de São Paulo, São Carlos, 2016.

The modeling, analysis and experimental verification of a two-degree-of-freedom typical aeroelastic section with superelastic shape memory alloy springs are presented. The focus is to investigate the effects of the pseudoelastic hysteresis of the shape memory alloy springs on the flutter and post-flutter behaviors of the typical section. The shape memory alloy phase transformation kinetics is described by a modified version of well-known phenomenological models. The shape memory alloy spring model is based on classical spring design (with the pure shear assumption) and modified to account for the nonlinear effects of phase transformation. The cross-section of the shape memory alloy wire is represented by a linear radial distribution of shear strain and nonlinear radial distributions of shear stress and martensitic fraction. The equations of motion of a linear typical section are modified to include the shape memory alloy springs. A linear unsteady aerodynamic model is employed to determine the aerodynamic loads. The proposed model is cast into state-space representation and solved with a Runge-Kutta method. It is numerically and experimentally shown that the pseudoelastic hysteresis of shape memory alloy springs can be effectively exploited to enhance the aeroelastic behavior of a typical section by replacing unstable flutter oscillations by stable oscillations of acceptable amplitudes over a range of airflow speeds, providing a useful method of passive aeroelastic control. Since the modified aeroelastic behavior is attractive for wind energy harvesting purposes, electromechanical coupling is also modeled in the plunge degree-of-freedom along with a resistive load in the electrical domain for electrical power estimation. The exploitation of the shape memory alloy pseudoelastic hysteresis is more attractive for airfoil-based wind energy harvesting performance than the use of typical concentrated nonlinearities (*e.g.*, hardening steel) in terms of enhanced electrical power output.

Keywords: Mechanical vibrations. Aeroelasticity. Shape memory alloys. Energy harvesting.

List of Figures

Figure – 1	Two types of LCO response due to (a) supercritical and (b) subcritical bifurcations with changing airflow speed (U_c is the linear flutter speed).	30
Figure – 2	Behavior of an SMA element during stress-induced phase transformation followed by a shape recovery promoted by heating.	42
Figure – 3	SMA phase transformation diagram with tension-compression asymmetry.	49
Figure – 4	Cross-sectional representation of the coiled SMA wire – (a) martensitic fraction (detail) and (b) shear strain (left), shear stress (middle) and martensitic fraction (right).	56
Figure – 5	A 2-DOF typical aeroelastic section model (with piezoelectric coupling).	58
Figure – 6	Motion of a typical section.	59
Figure – 7	A schematic model of a typical aeroelastic section with SMA helical springs at the pitch DOF.	69
Figure – 8	Critical shear stresses for phase transformation: constant for $T \leq M_s$ and a linear function of temperature for $T > M_s$	76
Figure – 9	Shear stress-strain behavior for different temperature conditions. The shape memory effect is represented by curves such that $T < A_f$ (with residual strain) and the pseudoelastic effect is represented by curves such that $T \geq A_f$ (with no residual strain).	77
Figure – 10	Mechanical loading-unloading cycle and corresponding (a) martensite fraction and (b) shear modulus for $T = A_f$ (arbitrary loading rate).	77
Figure – 11	Real part of the plunge DOF eigenvalue for increasing airflow speed (a), (b) dimensionless plunge DOF time response, (c) dimensionless pitch DOF time response, (d) shear stress versus change in the length of SMA spring S_1	79
Figure – 12	The aeroelastic displacements decrease as the preload increases and contributes more significantly to the occurrence of phase transformation – (a) plunge DOF phase projections, (b) plunge amplitude (reduction of 54%), (c) pitch DOF phase projections, (d) pitch amplitude (reduction of 56%).	

	In (b) and (d) the amplitudes for a linear (elastic) steel spring with equivalent effective stiffness is shown for comparison.	80
Figure – 13	Steady-state shear stress split into two portions: one due to preload and another due to pitch displacement at its maximum at the linear flutter speed (phase transformation occurs for $f_0 \geq 2$ N). The resulting shear stress exhibits no expressive increase as the SMA springs operate in the transformation region.	81
Figure – 14	Aeroelastic response and material behavior for $f_0 = 3$ N and $U_\infty = U_{LF}$ – (a) plunge displacement, (b) pitch displacement, (c) change in the length of SMA spring S_1 , (d) shear stress, (e) martensite fraction, (f) stiffness and (g) shear stress versus change in the length of SMA spring S_1 . The case with no preload ($f_0 = 0$ N) is shown for comparison.	83
Figure – 15	Detail of the transient response for $f_0 = 3$ N and $U_\infty = U_{LF}$ – (a) shear stress, (b) martensite fraction. Both forward and reverse phase transformations are incomplete. A and B stand for austenite and martensite, respectively.	84
Figure – 16	Pitch response for $f_0 = 4.5$ N and different directions of the initial condition applied to the plunge DOF ($\bar{h}_0 = 0.08$ and $\bar{h}_0 = -0.08$)	84
Figure – 17	Airflow speeds at which persistent oscillations with maximum acceptable amplitudes occur for increasing preload (a); resulting shear stress (b) – the contribution due to preload is the same as in Fig. 13, whereas the pitch contribution is more expressive due to larger aeroelastic displacements at higher airflow speeds (on the left).	86
Figure – 18	Aeroelastic response for $f_0 = 3$ N and $U_\infty = 14 \text{ m}\cdot\text{s}^{-1}$ – (a) plunge displacement, (b) pitch displacement, (c) deformation of SMA spring S_1 , (d) shear stress, (e) martensitic fraction, (f) spring stiffness, (g) shear stress versus change in the length of spring S_1	87
Figure – 19	Shear stress for SMA spring S_1 for different preload levels and $U_\infty \geq U_{LF}$. Upper boundaries are related to the forward phase transformation (loading cycles) and lower boundaries are related to the reverse phase transformation (unloading cycles).	88
Figure – 20	Steady-state material properties of the two SMA springs – (a) martensitic fractions and (b) stiffness. The imbalance of the material properties between the two springs is evident for $U_\infty = U_{LF}$ when $f_0 > 3$ N and negligible for $U_\infty > U_{LF}$	89
Figure – 21	Aeroelastic behavior of the typical section for the same model parameters	

	and two different assumptions for the cross-sectional representation of the coiled SMA wire – (a) effects of preload and (b) effects of the number of annular regions.	92
Figure – 22	Cross-sectional distributions of shear strain, shear stress and martensitic fraction for 1, 3, 5, 10, 20 and 30 annular regions.	93
Figure – 23	Maximum airflow speeds with increasing number of annular regions at the post-flutter regime.	93
Figure – 24	Normalized simulation time for increasing number of annular regions (normalized by the elapsed time when considering one single annular section).	94
Figure – 25	Constitutive behavior for the sets of SMA parameters – (a) stress-strain behavior and (b) phase transformation slopes.	98
Figure – 26	Dimensionless pitch and plunge peak amplitudes and spring elongation for the SMA properties of Tab. 3 and increasing airflow speed. Non-preloaded SMA springs in (a) and preloaded springs in (b).	101
Figure – 27	Aeroelastic behavior of the typical section over time for different sets of SMA properties – (a) plunge and (b) pitch displacements for no preload and for applied preload (c, d). G99, A13 and S15 are represented by the same curve in (a, b), as well as G98, T99 and S15 in (c, d).	102
Figure – 28	Typical section motion during one transient cycle of oscillation at the flutter boundary for the SMA properties of Tokuda et al. (1999) without preload. The surfaces represent the cross-section of the coiled SMA wire.	104
Figure – 29	Phase transformation behavior from transient to steady-state response for the SMA properties of Tokuda et al. (1999). Normalized shear stress (τ/τ_s^{M+}) and martensitic fraction (ξ).	105
Figure – 30	Post-flutter behavior for the SMA properties of Tokuda et al. (1999), without and with applied preload – (a) time responses of the plunge and pitch DOFs and (b) SMA spring elongation versus the normalized maximum shear stress.	106
Figure – 31	Post-flutter behavior for the SMA properties of Tokuda et al. (1999). Steady-state cross-sectional distributions of shear stress and martensitic fraction for no preload (a, b) and applied preload (c, d). Dashed lines in the $r - \tau$ plane represent the effect of preload.	106
Figure – 32	Cross-sectional distributions of shear stress and martensitic fraction for the SMA properties of Sameallah et al. (2014) during a complete pitch cycle at the flutter boundary and with no preload. Transient (a, b) and steady-state	

	(c) cycles.	107
Figure – 33	Cross-sectional distributions of shear stress and martensitic fraction for the SMA properties of Sameallah et al. (2014) during a complete pitch cycle at the flutter boundary and with applied preload. Transient (a, b) and steady-state (c, d) cycles.	108
Figure – 34	Post-flutter behavior for the SMA properties of Sameallah et al. (2014). No preload and airflow speed of $13.1 \text{ m}\cdot\text{s}^{-1}$. With applied preload and airflow speed of $13.3 \text{ m}\cdot\text{s}^{-1}$. Plunge and pitch displacements (a). Normalized maximum shear stress versus spring elongation diagram (b).	109
Figure – 35	Cross-sectional distributions of shear stress and martensite fraction for the SMA properties of Sameallah et al. (2014) during a complete steady-state pitch cycle of the post-flutter case. No preload (a, b) and with applied preload (c, d).	109
Figure – 36	Time response of the plunge DOF for the SMA parameters of Sameallah et al. (2014) and different initial conditions. No preload (a, b) and with applied preload (c, d). Transient shear stress versus spring elongation for no preload and applied preload (e, f).	113
Figure – 37	SMA spring stiffness (k) and the corresponding distance w between the elastic axis and the SMA springs for increasing coil diameter (a) and wire diameter (b).	116
Figure – 38	Number of active coils (N) for varying coil (D) and wire (d) diameters. ...	117
Figure – 39	Steady-state aeroelastic behavior for different SMA spring diameters (with variable stiffness and constant number of coils).	118
Figure – 40	Steady-state aeroelastic behavior for different SMA spring diameters (with constant stiffness and variable number of coils).	119
Figure – 41	Time response of the plunge and pitch DOFs for the reference case (without preload, with larger amplitudes), the nominal geometry with applied preload (with intermediate amplitudes) and the case which yields the smallest amplitudes.	120
Figure – 42	Sketch of the typical section design employed for the experimental model.	122
Figure – 43	Blower wind tunnel (picture).	123
Figure – 44	Verification of the wind tunnel airflow speed capability.	123
Figure – 45	Photography of the typical section model. Views from the leading edge (a)	

	and trailing edge (b).	124
Figure – 46	Photography of the experimental apparatus for testing the SMA springs. . .	127
Figure – 47	Experimental force-displacement curves for the two tested SMA springs: the 45 °C spring in (a) and the 20 °C spring in (b).	128
Figure – 48	Infrared pictures of the 45 °C SMA spring during the test.	129
Figure – 49	Photography of the SMA springs used in the aeroelastic tests.	130
Figure – 50	Photography of the typical section in a pendulum configuration for the me- asurement of the moment of inertia.	132
Figure – 51	Free-vibration test for the plunge DOF.	133
Figure – 52	Static displacement test for the plunge DOF.	134
Figure – 53	Static displacement test followed by a free-vibration test.	134
Figure – 54	Pitch DOF with SMA springs (picture). Views from the leading edge (a) and trailing edge (b).	136
Figure – 55	Distance between the SMA springs and the elastic axis (picture).	136
Figure – 56	Free-vibration tests for the pitch DOF.	136
Figure – 57	Static displacement test for the pitch DOF. Experimental data (a) and pho- tography of the test (b).	137
Figure – 58	Experimental plunge displacement in time for different airflow speeds (sligh- tly below the linear flutter speed) and small preload applied to the SMA springs.	141
Figure – 59	Experimental plunge and pitch displacements in time at slightly above the linear flutter speed and for small preload applied to the SMA springs.	141
Figure – 60	Experimental plunge displacement in time for different airflow speeds (cons- tant preload level).	143
Figure – 61	Aeroelastic behavior of the typical section with preloaded SMA springs at the flutter boundary for different initial conditions.	143
Figure – 62	Experimental plunge displacement for 80% of the critical preload and in- creasing airflow speed.	144
Figure – 63	Experimental plunge displacement for 80% of the critical preload and in- creasing airflow speed (detail).	145
Figure – 64	Experimental plunge displacement for 90% of the critical preload and in-	

	creasing airflow speed.	145
Figure – 65	Experimental plunge displacement for 90% of the critical preload and increasing airflow speed (detail).	146
Figure – 66	Experimental plunge displacement for the critical preload and increasing airflow speed.	146
Figure – 67	Experimental plunge displacement for the critical preload and increasing airflow speed (detail).	147
Figure – 68	Experimental plunge displacement for slightly above the critical preload and increasing airflow speed.	147
Figure – 69	Experimental plunge displacement for slightly above the critical preload and increasing airflow speed (detail).	148
Figure – 70	RMS amplitudes of the plunge displacement for increasing airflow speeds and different preload levels.	149
Figure – 71	Detail of the RMS amplitudes of the experimental plunge displacement for increasing airflow speeds and different preload levels along with simulation results.	149
Figure – 72	Stress-temperature relationship of the SMA considered in the energy harvesting problem.	153
Figure – 73	Shear stress with the elongation of the SMA springs in the energy harvesting problem.	154
Figure – 74	Steady-state plunge displacement (left axis, continuous line) and pitch angle (right axis, dashed line) in the energy harvesting problem.	155
Figure – 75	Time responses for $U_\infty = 11.85 \text{ m}\cdot\text{s}^{-1}$, $R_l = 100 \text{ k}\Omega$ and preloads of 3.5 N and 4.0 N – (a) pitch angle, (b) plunge displacement and (c) electrical power output.	155
Figure – 76	Limiting airflow speeds for acceptable aeroelastic displacements with increasing preload (in the energy harvesting problem).	157
Figure – 77	Electroaeroelastic behavior for increasing airflow speed, different preload conditions and $R_l = 100 \text{ k}\Omega$ – (a) peak amplitude of the pitch angle, (b) peak amplitude of the plunge displacement, (c) SMA spring elongation, (d) peak amplitude of the voltage and (e) the corresponding electrical power output.	158
Figure – 78	Aeroelastic responses in time for $f_0 = 3.5 \text{ N}$, $R_l = 100 \text{ k}\Omega$ and different air-	

	flow speeds – (a) pitch angle, (b) plunge displacement, (c) electrical power output and (d) hysteretic behavior of the SMA springs.	159
Figure – 79	Effects of the electrical boundary condition on the aeroelastic behavior for $U_\infty = 13 \text{ m}\cdot\text{s}^{-1}$ and $f_0 = 3.5 \text{ N}$ – (a) plunge displacement (left axis, continuous line) and pitch angle (right axis, dashed line); (b) voltage (left axis, continuous line) and electrical power output (right axis, dashed line).	160
Figure – 80	(a) Plunge and (b) pitch peak amplitudes (continuous lines: isothermal; dashed lines: non-isothermal).	187
Figure – 81	Behavior of the SMA springs – (a) elongation and (b) shear stress in time (continuous lines: isothermal; dashed lines: non-isothermal).	187
Figure – 82	Behavior of the SMA springs – (a) shear stress-elongation diagrams (for $f_0 = 0 \text{ N}$ and $11.6 \text{ m}\cdot\text{s}^{-1}$, $f_0 = 3 \text{ N}$ and $11.6 \text{ m}\cdot\text{s}^{-1}$ and also $f_0 = 3 \text{ N}$ and $14 \text{ m}\cdot\text{s}^{-1}$), (b) detail of the diagram for $14 \text{ m}\cdot\text{s}^{-1}$, (c) martensitic fraction, (d) stiffness and (e) electrical resistance (continuous lines: isothermal; dashed lines: non-isothermal).	188
Figure – 83	Temperature variations (a) and the corresponding critical stress τ_s^M (b) (continuous lines: isothermal; dashed lines: non-isothermal).	189

List of Tables

Table – 1	SMA constitutive properties.	75
Table – 2	Aeroelastic parameters used in the simulations.	78
Table – 3	Sets of shape memory alloy properties.	96
Table – 4	Derived SMA critical stresses for phase transformations.	97
Table – 5	Derived SMA spring-related parameters.	99
Table – 6	Experimental aeroelastic parameters.	138
Table – 7	Experimental SMA constitutive properties.	139
Table – 8	SMA thermal and electrical properties.	186

Acronyms

SMA	Shape memory alloy, p. 27
A	Austenite, p. 40
M	Martensite, p. 40
M ^t	Twinned martensite, p. 40
M ^d	Detwinned martensite, p. 40
A → M	Austenite to martensite phase transformation, p. 40
A → M ^t	Austenite to twinned martensite phase transformation, p. 40
A → M ^d	Austenite to detwinned martensite phase transformation, p. 40
M → A	Martensite to austenite phase transformation, p. 40
M ^t → A	Twinned martensite to austenite phase transformation, p. 40
M ^d → A	Detwinned martensite to austenite phase transformation, p. 40
M ^t → M ^d	Twinned to detwinned martensite phase transformation, p. 41
DSC	Differential scanning calorimetry, p. 43
CG	Center of gravity, p. 59

List of Symbols

M_s	Martensite start temperature, p. 41
M_f	Martensite finish temperature, p. 41
A_s	Austenite start temperature, p. 41
A_f	Austenite finish temperature, p. 41
σ	Normal stress, p. 41
M_s^σ	Martensite start temperature (with applied stress), p. 42
M_f^σ	Martensite finish temperature (with applied stress), p. 42
A_s^σ	Austenite start temperature (with applied stress), p. 42
A_f^σ	Austenite finish temperature (with applied stress), p. 42
σ_s^{\min}	Minimum martensite start stress, p. 42
σ_f^{\min}	Minimum martensite finish stress, p. 42
σ_s^M	Temperature-dependent martensite start stress, p. 42
σ_f^M	Temperature-dependent martensite finish stress, p. 42
σ_s^A	Temperature-dependent austenite start stress, p. 42
σ_f^A	Temperature-dependent austenite finish stress, p. 42
σ	Normal stress, p. 46
D	Elastic modulus, p. 46
ε	Axial strain, p. 46
Ω	Transformation factor, p. 46
ξ	Martensite volume fraction, p. 46
Θ	Thermal expansion coefficient, p. 46
T	Temperature, p. 46
0	(subscript) Reference state, p. 46
ξ_T	Twinned martensite volume fraction, p. 47
ξ_S	Detwinned martensite volume fraction, p. 47
D_A	Austenitic elastic modulus, p. 47
D_M	Martensitic elastic modulus, p. 47

*	(superscript) SMA quantity affected by tension-compression asymmetry, p. 49
+	(superscript) SMA quantity for tension, p. 49
–	(superscript) SMA quantity for compression, p. 49
Y_{MD}^*	Hardening function of stress-induced phase transformation, p. 51
$c(T, M_s)$	Temperature-dependent auxiliary function, p. 51
Y_A^*	Hardening function of reverse phase transformation, p. 51
τ	Shear strain, p. 52
G	Shear modulus, p. 53
γ	Shear strain, p. 53
Ω_τ^*	Transformation factor in shear behavior, p. 53
μ_P	Poisson's ratio, p. 53
G_A	Austenitic shear modulus, p. 53
G_M^*	Martensitic shear modulus, p. 53
F	External force, p. 54
R	Spring mean coil radius, p. 54
r	Spring wire radius, p. 54
N	Number of active coils, p. 54
y	Spring deflection, p. 54
k	Spring stiffness, p. 54
r_{rc}	Radial coordinate, p. 56
r^{crit}	Critical radius for phase transformation, p. 57
A	Area of a cross-sectional region, p. 57
h	Plunge displacement, p. 58
α	Pitch angle, p. 58
U_∞	Airflow speed, p. 58
c	Distance from the midchord to the elastic axis, p. 59
b	Semichord length, p. 59
x_α	Dimensionless distance between the elastic axis and CG, p. 59
l	Span length of the typical aeroelastic section, p. 59
k_h	Stiffness (per unit of span length) of the plunge DOF, p. 59
k_α	Stiffness (per unit of span length) of the pitch DOF, p. 59

d_h	Damping coefficient of the plunge DOF, p. 59
d_α	Damping coefficient of the pitch DOF, p. 59
δ	Variation, p. 60
T_E	Total kinetic energy, p. 60
U_E	Total potential energy, p. 60
W_{ie}	Internal electrical energy, p. 60
W_{nce}	Electrical charge's virtual work, p. 60
W_{nca}	Aerodynamic loading's virtual work, p. 60
W_{sd}	Structural damping's virtual work, p. 60
m	Mass of the pitch DOF, p. 60
m_t	Total mass of the pitch and plunge DOFs, p. 60
I_α	Moment of inertia, p. 61
θ	Electromechanical coupling term, p. 61
v	Voltage, p. 61
C_p^{eq}	Equivalent capacitance of the piezoceramic layers, p. 61
Q	Electrical charge, p. 61
q_i	Generalized coordinate, p. 61
\mathcal{Q}_i	Non-conservative force, p. 61
R_l	Resistive load, p. 62
\tilde{v}	Reference voltage, p. 63
r_α	Radius of gyration, p. 63
\bar{h}	Dimensionless plunge displacement, p. 63
ω_α	Uncoupled natural frequency of the pitch DOF, p. 63
ω_h	Uncoupled natural frequency of the plunge DOF, p. 63
μ	Plunge-to-pitch mass ratio, p. 63
v	Dimensionless voltage, p. 63
t	Dimensional time, p. 63
\bar{t}	Dimensionless time, p. 63
\prime	Dimensionless time derivative, p. 63
ζ_α	Damping ratio of the pitch DOF, p. 64
ζ_h	Damping ratio of the plunge DOF, p. 64

η_α	Pitch-to-plunge frequency ratio ω_α/ω_h , p. 64
ψ	Dimensionless capacitance, p. 64
χ	Dimensionless electromechanical coupling term, p. 64
λ	Dimensionless resistive load, p. 64
\bar{p}	Dimensionless electrical power, p. 64
\bar{M}_α	Dimensionless pitching moment, p. 64
\bar{L}	Dimensionless lift, p. 64
I	Identity matrix, p. 64
T	(superscript) Transposed vector, p. 64
Θ_e	Electromechanical coupling, p. 64
\mathcal{F}	Vector of aerodynamic loads, p. 64
M	Matrix of dimensionless inertial parameters, p. 64
K	Matrix of dimensionless stiffness parameters, p. 64
B	Matrix of dimensionless damping parameters, p. 64
ρ	Air density, p. 66
$C(\kappa)$	Generalized Theodorsen function, p. 66
κ	Reduced frequency, p. 66
μ_a	Virtual mass, p. 67
x_{ai}	Augmented aerodynamic states, p. 67
\mathbf{x}_a	Vector of aerodynamic states, p. 67
\mathbf{S}_i	Vectors related to the circulatory aerodynamics, p. 67
D	Aerodynamic coupling in the structural equations, p. 67
R	Vectors related to the circulatory aerodynamics, p. 67
$\tilde{\mathbf{M}}$	Total inertial matrix, p. 68
$\tilde{\mathbf{K}}$	Total stiffness matrix, p. 68
$\tilde{\mathbf{B}}$	Total damping matrix, p. 68
\mathbf{M}_{nc}	Non-circulatory contribution to mass, p. 68
\mathbf{K}_{nc}	Non-circulatory contribution to stiffness, p. 68
\mathbf{B}_{nc}	Non-circulatory contribution to damping, p. 68
$\tilde{\mathbf{E}}_i$	Aerodynamic-to-structural coupling terms, p. 68
$\tilde{\mathbf{F}}_p$	Aerodynamic terms, p. 68

$\tilde{\mathbf{D}}$	Dimensionless \mathbf{D} matrix, p. 68
\mathbf{A}	Dimensionless piezoaeroelastic matrix, p. 68
\mathbf{x}	Dimensionless piezoaeroelastic state vector, p. 68
w	Distance between the elastic axis and the SMA springs, p. 69
ϑ	Dimensionless elastic moment due to the SMA springs, p. 69
y_0	Pre-deflection imposed to the SMA springs, p. 70
y_α	Spring deflection amplitude, p. 99
f_0^{crit}	Critical spring preload, p. 99
\bar{r}	Coordinate along the wire radius, p. 103
u_P	Displacement at the beginning of a cycle, p. 132
u_Q	Displacement at the end of a cycle, p. 132
c	Damping coefficient, p. 132
c_{crit}	Critical damping, p. 132
ω_n	Undamped natural frequency, p. 132
u_{st}	Arbitrary static displacement, p. 133

Content

1	Introduction	27
1.1	Content Overview	36
1.2	Overview of the Main Contributions	37
2	Shape Memory Materials, Metallic Alloys and Springs	39
2.1	General Aspects of SMAs	39
2.2	Phase Transformations in SMAs	40
2.2.1	Stress-Free Phase Transformation	41
2.2.2	Phase Transformation with Applied Stress	41
2.2.3	Brief Note on the Critical Temperatures for Phase Transformation	43
2.2.4	A Note on Thermal Effects in SMAs	44
2.3	SMA Model	45
2.3.1	Thermomechanical Constitutive Modeling of SMAs	45
2.3.2	A Brief Review of Brinson’s Model	46
2.3.3	Modification of Brinson’s Model for Tension-Compression Asymmetry	48
2.4	A Model for SMA Helical Springs	52
2.4.1	Mechanical Constitutive Relationship for Shear Behavior	52
2.4.2	Modeling of the SMA Springs	53
2.4.3	Cross-Sectional Representation of the Coiled SMA Wire	55
3	Model of a Piezoelectrically Coupled Typical Aeroelastic Section	58
3.1	Derivation of the Equations of Motion of the Typical Section	60
3.2	Dimensionless Representation of the Equations of Motion in State-Space Form	62
3.2.1	Nondimensionalization of the Equations of Motion	63

3.2.2	Representation of the Equations of Motion in State-Space Form	64
3.3	Unsteady Aerodynamic Model for Arbitrary Airfoil Motions	65
3.4	Typical Section Model with SMA Springs	69
3.5	Iterative Procedure for the Determination of the Mechanical Stress and Martensitic Fraction	71
4	Effects of the SMA Pseudoelastic Hysteresis on the Aeroelastic Behavior of the Typical Section	74
4.1	Simulation of the Constitutive Behavior of an SMA Element	75
4.2	Effect of Pseudoelastic Hysteresis on the Aeroelastic Behavior of a Typical Section	77
4.2.1	Effect of Pseudoelastic Hysteresis on the Aeroelastic Behavior of the Typical Section at the Linear Flutter Speed	78
4.2.2	Effect of Pseudoelastic Hysteresis on the Aeroelastic Behavior of the Typical Section at the Post-Flutter Regime	84
4.2.3	A Discussion on the SMA Spring Behavior for the Flutter Boundary and Post-Flutter Cases	89
4.3	Analysis of Different Assumptions for the Cross-Sectional Representation of the Coiled SMA Wire	91
5	Effects of Different SMA Constitutive Properties on the Aeroelastic Behavior of the Typical Section	95
5.1	Description of the Considered Sets of SMA Constitutive Properties	95
5.1.1	Constitutive Behavior of the Different Sets of SMA Properties	97
5.1.2	Description of Derived SMA Spring-Related Properties	98
5.2	Analysis of the Aeroelastic Behavior of the Typical Section for the Different Sets of SMA Properties	99
5.2.1	Aeroelastic Behavior Considering Different Sets of SMA Properties	100
5.2.2	A Discussion on the Attractive Cases	103
5.2.3	General Effects of SMA Parameters on the Aeroelastic Behavior	110
5.3	Additional Analyses	111
5.3.1	Effects of the Initial Conditions Applied to the Typical Section	111

5.3.2	A Note on Intermediate Preload Levels	114
6	Effects of the Geometric Properties of the SMA Springs on the Aeroelastic Behavior of the Typical Section	115
7	Experimental Verification of the Aeroelastic Behavior of the Typical Section with SMA Springs	121
7.1	General Description of the Experimental Apparatus	121
7.1.1	Instrumentation Used in the Experiments	125
7.2	Identification of the Experimental Parameters	126
7.2.1	SMA Properties	126
7.2.2	Typical Section Parameters	131
7.2.3	Summary of the Experimental Model Parameters	138
7.3	Effect of Pseudoelastic Hysteresis on the Aeroelastic Behavior of a Typical Section	139
7.3.1	General Aeroelastic Behavior at the Flutter Boundary	140
7.3.2	Post-Flutter Behavior of the Typical Section	144
7.3.3	Further Discussions on the Experimental Behavior of the Typical Section with SMA Springs	149
8	Airfoil-Based Piezoelectric Energy Harvesting by Exploiting the Pseudoelastic Hysteresis of Shape Memory Alloy Springs	152
8.1	Electroaeroelastic Behavior of the Typical Section with SMA Springs at the Flutter Boundary	153
8.2	Electroaeroelastic Behavior of the Typical Section in the Post-Flutter Regime	156
9	Summary and Conclusions	162
9.1	Conclusions	162
9.2	Suggestions for Future Work	167
	References	169
	APPENDIX A - Lagrange Equations for the Piezoaeroelastic System	179

APPENDIX B - Matrices of the Aerodynamic Model	181
APPENDIX C - Theodorsen Constants	183
APPENDIX D - Isothermal and Non-Isothermal Assumptions for the SMA Behavior	185
Publications	190

Introduction

The use of smart materials as sensors, actuators, and their combined application for several engineering problems has been widely reported in the literature. More recently, the energy harvesting potential from dynamical systems using a transduction mechanism of a smart material has also been investigated. Leo (2007) defines smart materials as those that exhibit coupling between different physical domains. Common examples are the piezoelectric materials, that present coupling between mechanical and electrical domains, and shape memory alloys (SMAs), that exhibit coupling between mechanical and thermal domains (or between mechanical and magnetic domains in some cases). There are several different smart materials (such as the magnetostrictive materials exhibiting coupling between magnetic field and mechanical motion, electrostrictive materials exhibiting coupling between electric field and mechanical motion, or even electrochromic materials, that present interesting use for systems that incorporate controlled color changes) that are not the main focus of this dissertation and will not be discussed in details this work.

Vibration control researches are among the most popular use of smart materials in engineering applications reported in the literature. In general, the main control techniques using the smart materials are the passive and active ones. Active control systems involve the use of smart materials as actuators along with sensors, control laws and external energy sources to produce an actuation signal to cancel vibrations. In passive control, dissipation of vibration energy without increasing the total energy of a primary system is observed. In the first case (active

systems) the amount of power required for actuation and the additional hardware are among the main issues of the control system, although large control authority is in general achieved. On the other hand, simple passive systems (in general they do not required complex hardware) present reduced control authority or limited frequency bandwidth.

Although different smart materials are available, SMAs have received growing attention in vibration control problems. For active control problems, the shape memory effect (the property by which very large mechanical strains can be recovered by heating the material above a critical temperature and leading to large contractions in the material) enables the use as thermomechanical actuators. SMA elements have also been investigated in passive control problems since their hysteretic behavior (related to the pseudoelastic effect) provides energy dissipating and damping capabilities. The stress-induced hysteretic behavior of SMAs is related to austenite-martensite phase transformations when the alloy is subjected to cyclic stress-strain loading at a relatively high temperature (LAGOUDAS, 2008).

The effectiveness of the pseudoelastic hysteresis of SMAs for passive structural damping has been investigated in the literature to enhance the vibration performance and safety of civil structures (JANKE, 2005; IBRAHIM, 2008; OZBULUT; HURLEBAUS; DESROCHES, 2011). In a recent work, Bhowmick and Mishra (2015) proposed an SMA-based damper for seismic vibration mitigation in which a ferrous SMA (namely, a Fe-Ni-Co-Al-Ta-B alloy) exhibits an impressive recoverable strain on the order of 12%, in contrast with the usual 6-7% of Ni-Ti alloys and 5% of Cu-Al-Be alloys. Gandhi and Chapuis (2002) presented the influence and effectiveness of an SMA damper on the dynamic behavior of a clamped-free beam with tip mass under varying excitation force amplitudes. Rezaei Da, Kadkhodaei and Nahvi (2012) investigated the nonlinear free vibration and damping of a clamped-clamped Euler-Bernoulli beam with embedded pre-strained SMA wires employed in the pseudoelastic state. SMA-based vibration isolation devices with adaptive capabilities have also been reported in the literature. These adaptive absorbers simultaneously use the variation of mechanical properties due to temperature-induced phase transformations and energy dissipation related to the hysteretic behavior related to stress-induced transformations (AGUIAR et al., 2013; MISHRA; GUR;

CHAKRABORTY, 2013; MANI; SENTHILKUMAR, 2015).

Several constitutive models have described the behavior of SMA elements such as wires and fibers (TANAKA; KOBAYASHI; SATO, 1986; LIANG; ROGERS, 1990; BRINSON, 1993). Researchers have also employed such models to represent the behavior of SMA helical springs. The models range from simple equivalent one-dimensional models (LIANG; ROGERS, 1997; AGUIAR; SAVI; PACHECO, 2010; AN et al., 2012) to accurate solutions considering the complex stress and strain distributions in the springs (MIRZAEIFAR; DESROCHES; YAVARI, 2011; BAGHANI; NAGHDABADI; ARGHAVANI, 2012; SALEEB et al., 2013; FROST et al., 2015). In general, the simple equivalent models have good correspondence to experimental results for springs with large spring index and small helix angle (AGUIAR; SAVI; PACHECO, 2010; AN et al., 2012). Enemark, Savi and Santos (2014) presented an experimentally verified modeling of an SMA spring using an updated Brinson's model (with a new smooth hardening function and a new sub-loop function) to describe the behavior of the SMA spring.

The literature also includes publications reporting use of SMA elements to modify the behavior of aeroelastic systems. Before discussing some topics related to SMA and aeroelasticity, a brief discussion related to linear and nonlinear aeroelastic system is included. Although different static and dynamic aeroelastic phenomena are reported (THEODORSEN, 1935; BISPLINGHOFF; ASHLEY; HALFMAN, 1955; HODGES; PIERCE, 2002; DOWELL, 2015), flutter is certainly the most investigated one due to its catastrophic nature. Flutter is a dynamic aeroelastic phenomenon related to interactions of inertial, elastic and aerodynamic forces. When a linear aeroelastic system is considered, the usual linear aeroelastic behavior is verified. The system is stable for airflow speeds smaller than the linear flutter speed (or critical speed). Theoretically, the linear system is critically damped at the linear flutter speed and strongly dependent on the initial conditions. Any further increase in the airflow speed (above the critical one) leads to instability: self-sustained aeroelastic oscillations with increasing amplitude. Often nonlinearities are present in aeroelastic systems in the forms of (1) free play, or bilinear stiffness due to loosely connected components, (2) material and geometric nonlinearity (typically yielding nonlinear stiffness effect) (3) dry friction and other forms of nonlinear damping, (4)

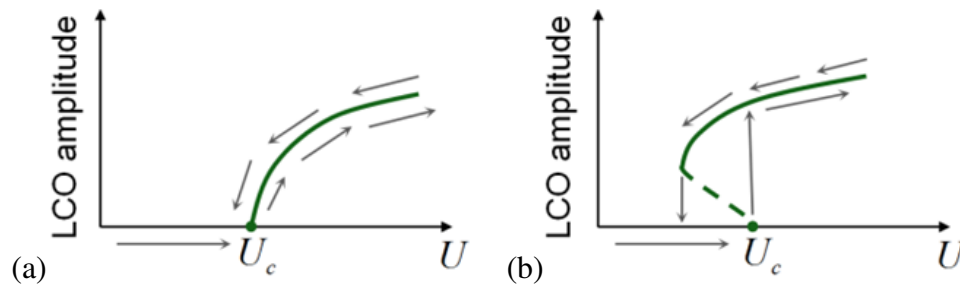


Figure 1 – Two types of LCO response due to (a) supercritical and (b) subcritical bifurcations with changing airflow speed (U_c is the linear flutter speed).

and aerodynamic nonlinearities. The presence of such nonlinearities may result in limit-cycle oscillations (LCO) at airflow speeds above (Figs. 1(a) and 1(b)) or below (Fig. 1(b)) the linear flutter speed. The LCO mechanism in Fig. 1(b) leads to both stable (solid line) and unstable (dashed line) LCO below the linear flutter speed and it is not preferred in a real aircraft. However, as reported by Dowell (2015), sometimes nonlinearities are welcome in aeroelastic systems since the catastrophic linear flutter behavior above the linear flutter speed can be replaced by LCOs of acceptable amplitudes. Such modified behavior has been also reported in the literature of wind energy harvesting as an important source of persistent electrical power and it deserves separate investigation.

Traditional anti-flutter techniques such as mass balance and structural reinforcement usually introduce significant weight penalties. In the first case, the goal is to reduce the offset between center of mass of a lifting surface and the elastic axis (or the offset between the center of mass and hinge line of a control surface). In the second case, additional stiffness is added to the structure through reinforcement elements that also lead to additional mass. In this regard, modern strategies considering smart materials (SMAs in the particular case of this work) for the enhancement of the aeroelastic behavior of structures have been pointed out in the literature as topics that deserve investigation. The literature also includes publications reporting the use of SMA elements to modify the behavior of aeroelastic systems.

Tawfik, Ro and Mei (2002) report a study on the thermal post-buckling and aeroelastic behavior of SMA-reinforced panels. A nonlinear finite element model of thermal post-buckling of SMA-reinforced plates is presented. The effects of the SMA fibers in enhancing the stiffness

and the critical buckling temperature as well as in suppressing thermal post-buckling deflection of the composite plates are reported. The model is also extended to include dynamic terms and the effects of SMA fibers on the aeroelastic behavior of the plate are discussed. Yun, Kim and Kim (2006) present a study on the stability augmentation of helicopter rotor blades using the (passive) hysteretic damping of SMA wires. Experimental tests on the effects of preload as well as of cyclic loading amplitude and frequency on the damping behavior of SMA wires are followed by an investigation on helicopter's aeroelastic and ground resonance stability. Bachmann et al. (2012) compare the use of SMA wires and the use of piezoelectric shunt circuits as strategies for passive damping augmentation in open rotor composite fan blade prototypes of complex geometry. The authors also report that pre-straining superelastic SMAs is necessary for fully exploiting the passive damping associated with the pseudoelastic behavior. Additionally, piezoelectric shunt damping (resonant circuit and nonlinear switching circuit) increases the damping of the blade further than the SMA, however, with the drawback of more additional weight for the structure.

Barzegari et al. (2012) present the modeling and analysis of a nonlinear cantilever wing with embedded SMA wires under unsteady aerodynamic loads. The stability margin is increased and amplitude of LCOs is reduced since the equivalent stiffness of the wing increases with increasing induced in-plane load of SMA wires at a temperature above austenite finish temperature. In another paper, Barzegari, Dardel and Fathi (2015) report the aeroelastic control of a cantilever wing with embedded SMA wires and piezoelectric actuators. The SMA wires are employed to generate in-plane loads and increase the total stiffness of the wing. Simultaneously, piezoelectric actuators are employed for active control using the state-dependent Riccati equation method. The required active control input is significantly reduced in the cases of flutter and LCO suppression (when compared to the case of aeroelastic control using only piezoelectric actuators) due to the increased stiffness related to the SMA wires.

The literature has also reported the use of SMAs in other aerospace problems. Hartl and Lagoudas (2007) review the aerospace applications of SMAs actuators in fixed-wing and rotorcraft cases. Bil, Massey and Abdullah (2013) and Barbarino et al. (2014) present reviews on SMA

actuators for morphing aircraft concepts. This work adds to the field of aeroelasticity by investigating the effects of the hysteretic response of SMAs on the dynamic aeroelastic behavior of a two-degree-of-freedom (2-DOF) typical airfoil section (the classical airfoil). The SMA springs are introduced in the pitch DOF of the typical section, while the plunge DOF is supported by linear elastic steel springs. The well-known lumped parameter aeroelastic equations governing a 2-DOF typical section (BISPLINGHOFF; ASHLEY; HALFMAN, 1955; HODGES; PIERCE, 2002; DOWELL, 2015) are modified to include the phase transformation effects of the SMAs. The SMA behavior is represented based on classical models, mainly on the works of Liang and Rogers (1990, 1992, 1997) and Brinson (1993). Additional features are included mainly based on the works of Bucchi et al. (2014) and Poorasadion et al. (2014) and described later in Chapter 2. The two-state approximation of Edwards, Ashley and Breakwell (1979) to the classical aerodynamics of Theodorsen (1935) is used to determine the unsteady aerodynamic loads (pitch moment and lift).

The numerical model of the 2-DOF typical section with SMA springs is employed for several analyses. An original typical section that has linear steel springs for the pitch and plunge DOFs is used as a reference case (the same geometric and dynamical properties are assumed for the original typical section and for the typical section with SMA springs). First, the effects of the hysteretic behavior of the SMA springs under different preload levels on the aeroelastic behavior of the typical section are investigated over a range of airflow speeds (from the linear flutter speed of the reference typical section to the largest airflow speed with LCOs of acceptable amplitude). The linear aeroelastic behavior of the original typical section (stable below the linear flutter speed and unstable above the flutter speed) using steel springs is modified to a nonlinear aeroelastic behavior due to the pseudoelastic hysteresis when the SMA springs are employed under certain levels of preloads. The catastrophic unstable post flutter regime of the linear case (typical section with linear steel springs in pitch) is replaced by stable LCOs of acceptable amplitudes (that are related to the preload applied to the SMA springs). Later, the effects of different assumptions for the cross-sectional representation of the coiled SMA wire on the aeroelastic behavior of the typical section are also discussed. It is important to note, however, that the aeroelastic behavior of the previous cases is only investigated for an SMA

spring with specific constitutive properties and geometry. Therefore, the third analysis extends the previous investigations and performs a parametric study in order to assess the effects of the constitutive properties of the SMAs (pseudoelastic hysteresis) on the aeroelastic behavior of a typical section. The effects of different characteristics of SMAs such as loop sizes, critical stress levels and tensile-compressive asymmetry are investigated by using six different sets of parameters previously presented in the literature. In practice, an optimum set of properties could be obtained by proper choice of materials, fabrication routes and heat treatment procedures (ELAHINIA et al., 2012).

Finally, the predicted aeroelastic behavior for a specific set of SMA parameters is experimentally verified in wind tunnel tests. In general, the simulations and experimental results show that the pseudoelastic hysteresis of SMA springs can enhance the aeroelastic behavior of the typical section by transforming unstable flutter oscillations into stable LCOs over a range of airflow speeds.

Another focus in this work is to explore the modified aeroelastic behavior of a typical section due to the pseudoelastic hysteresis of SMA springs for wind energy harvesting. The recent literature in the field of wind energy harvesting reports several research efforts in order to enable geometrically scalable and low-profile flow energy harvesters. The goal is to power small electronic components for applications ranging from health monitoring in aircraft and rotorcraft structures to wireless sensors located in high wind areas. Bluff body-based and airfoil-based configurations combined with an appropriate transduction mechanism are convenient ways to create persistent aeroelastic oscillations for wind energy harvesting (ELVIN; ERTURK, 2013).

The bluff body - PVDF (polyvinylidene fluoride) membrane configuration tested under water by Allen and Smits (2001) appears to be the earliest implementation of a piezoelectric based flow energy harvester. In the last five years, the problem of flow energy harvesting has received great attention. For the piezoaeroelastic problem of energy harvesting from airflow excitation of a cantilevered plate with embedded piezoceramics, De Marqui Jr, Erturk and Inman (2010) and De Marqui Jr et al. (2011) presented finite-element models based on the vortex-lattice method (De Marqui Jr; ERTURK; INMAN, 2010) and the doublet-lattice method (De Marqui Jr et al.,

2011) of aeroelasticity (BISPLINGHOFF; ASHLEY; HALFMAN, 1955; DOWELL, 2015). Time-domain simulations (De Marqui Jr; ERTURK; INMAN, 2010) were given for a cantilevered plate with embedded piezoceramics for various airflow speeds below the linear flutter speed and at the flutter boundary. Frequency-domain simulations (De Marqui Jr et al., 2011) considering resistive and resistive-reactive shunt circuits were also presented focusing on the linear response at the flutter boundary. Bryant and Garcia (2011) studied the aeroelastic energy harvesting problem for a 2-DOF typical section by using the finite state theory of Peters, Karunamoorthy and Cao (1995), while Erturk et al. (2010) presented an experimentally validated lumped-parameter model for a wing-section (airfoil) with piezoceramics attached onto plunge stiffness DOF using Theodorsen's unsteady aerodynamic model (THEODORSEN, 1935) for piezoelectric power generation at the flutter boundary. Sousa et al. (2011) investigated the nonlinear version of the same experimental setup of Erturk et al. (2010). In order to increase the operating envelope of the wind energy harvester, hardening cubic nonlinearity and free play were combined to keep the oscillation amplitudes at an acceptable level over a range of airflow speeds while reducing the cut-in speed.

The interest in nonlinear aeroelastic systems for wind energy harvesting has increased (BAE; INMAN, 2015; ABDELKEFI; NAYFEH; HAJJ, 2012a, 2012b; ABDELKEFI; HAJJ, 2013) in the last years. Bae and Inman (2015) investigated the piezoaeroelastic behavior of a 2-DOF typical section with free play and cubic nonlinearity separately in the pitch DOF. The effect of pitch-to-plunge frequency ratio on the nonlinear aeroelastic behavior is discussed as well as the use of stable LCOs for wind energy harvesting. In an experimental investigation, Abdelkefi, Nayfeh and Hajj (2012a) showed that the cut-in speed of subcritical instability decreases with increasing free play gap of an airfoil section. Abdelkefi, Nayfeh and Hajj (2012b) exploited the nonlinear piezoaeroelastic behavior of wind energy harvesting avoiding subcritical Hopf bifurcations and also presented (ABDELKEFI; HAJJ, 2013) a comprehensive nonlinear analysis of piezoaeroelastic wind energy harvesters.

As an alternative to airfoil-based and cantilevered wing-based configurations, St. Clair et al. (2010) presented a design that uses a piezoelectric beam embedded within a cavity under

airflow. More recently, Perez et al. (2015) proposed a new flow energy harvester by coupling the fluttering effect to an electret-based converter. The flow-induced movements of a membrane are converted into electricity due to an electret-based electrostatic converter. Vortex-induced oscillations of piezoelectric cantilevers located behind bluff bodies were investigated by Pobering, Ebermeyer and Schwesinger (2009) and Akaydin, Elvin and Andreopoulos (2010a, 2010b) through experiments and numerical simulations.

Tang et al. (2009) presented a rigorous analysis of the energy transfer from fluid to structure for self-excited vibrations under axial flow over a cantilever. Piezoelectric energy harvesting from LCOs under axial flow over a cantilever beam has also been discussed by Dunnmon et al. (2011). Kwon (2010) considered a T-shaped cantilever beam that causes vortex-induced vibration of a cantilever in response to axial flow. In a similar configuration, Zhao, Tang and Yang (2016) investigated the use of a beam stiffener in three different types of harvesters based on galloping, vortex induced vibration and flutter. The effect of the stiffener is to increase the electromechanical coupling, leading to an enhanced performance over the conventional designs without the beam stiffener. Recent efforts have also employed electromagnetic induction for converting aeroelastic vibrations into electricity through flutter (DIAS; De Marqui Jr; ERTURK, 2013; DIAS; De Marqui; ERTURK, 2015), wake galloping (JUNG; LEE, 2011) and bluff body-based oscillations (ZHU et al., 2010).

As previously discussed, the pseudoelastic hysteresis of SMA springs leads to stable LCOs over a range of airflow speeds creating a post-flutter regime. Stable flow induced oscillations over a range of airflow speeds are attractive for persistent power generation in wind energy harvesting cases (ERTURK et al., 2010). The literature of wind energy harvesting reports the use of concentrated structural nonlinearities (*e.g.*, freeplay and polynomial nonlinearities) to create stable LCOs over a range of airflow speeds as source of persistent electrical power (SOUSA et al., 2011; ABDELKEFI; NAYFEH; HAJJ, 2012a, 2012b; ABDELKEFI; HAJJ, 2013; BAE; INMAN, 2015). The nonlinear aeroelastic behavior due to the pseudoelastic hysteresis of SMA explored in this work is a different mechanism that enhances the electroaeroelastic performance of an airfoil based wind energy harvester. Therefore, as the last case study, the modified ae-

roelastic behavior of the typical section (due to the SMAs) is exploited as an innovative wind energy harvesting device. Piezoelectric coupling is added to the plunge DOF and a load resistance is considered in the electrical domain to estimate the electrical power output. The interaction between the aeroelastic behavior and electrical power generation is investigated for a range of preload values applied to the SMA springs and for a range of load resistances (from short circuit to open circuit conditions) in the electrical domain of the problem. Enhanced electroelastic performance is observed when compared with nonlinear wind energy harvesting considering typical sections with hardening springs as sources of nonlinearities.

1.1 Content Overview

In this chapter, the field of study was introduced along with a brief literature review. It was highlighted that, among several aeroelastic phenomena, flutter is particularly important due to its potentially destructive nature. Strategies to counter-act flutter which employ smart materials were also briefly described. The pseudoelastic hysteresis of SMAs was then introduced as another mechanism for the enhancement of the flutter response of a typical aeroelastic section.

Chapter 2 provides a basis for the SMA phase transformation behavior along with the SMA spring modeling. Chapter 3 provides the analytical description of the typical section model. A state-space model which includes the coupled equations of motion of the typical section (with SMA springs) and the unsteady aerodynamic model employed for the determination of the aerodynamic loads is presented.

Chapter 4 addresses the general aeroelastic behavior of the typical section with SMA springs at the flutter boundary and also at post-flutter regime. The effects of preloading the SMA springs are mainly of concern. Chapter 5 discusses the aeroelastic behavior of the typical section when different sets of SMA constitutive properties are considered. Attractive SMA characteristics (for the enhancement of the aeroelastic behavior of the typical section) are pointed out in that chapter. Chapter 6 discusses the effects of considering SMA springs of different geometries by changing the coil diameter, the wire diameter and the number of active coils.

Chapter 7 presents the experimental verification of the aeroelastic behavior of a typical section model. Parameter-identification tests are described for both the SMA springs and the typical section model. Aeroelastic tests are then presented for different levels of preload applied to the SMA springs and increasing airflow speeds. The effects of preload at the flutter boundary and at post-flutter regime are of concern.

Chapter 8 proposes a novel mechanism for airfoil-based wind energy harvesting over a range of airflow speeds by using superelastic SMAs (instead of the exploitation of structural nonlinearities such as polynomial stiffening, for example).

Chapter 9 summarizes concluding remarks for this work. A brief review of the proposed model along with the most pertinent findings is presented. Suggestions for future work are presented.

Appendices are included to provide additional information. Appendix A describes the Lagrange equations for the piezoaeroelastic system. Appendix B presents the matrices of the aerodynamic model while Appendix C presents the Theodorsen (1935) constants (required for the aerodynamic matrices of Appendix B).

1.2 Overview of the Main Contributions

This work adds to the field of aeroelasticity by presenting the modeling of a typical aeroelastic section with SMA springs along with numerical and experimental case studies. Recent works from the literature on aeroelasticity and smart materials have focused mainly on the use of piezoceramics. The literature on general vibration control and smart materials have focused on the use of piezoceramics and also SMA elements. A few number of works, however, has proposed the use of SMA elements in aeroelasticity. Therefore, this work presents basic studies concerning the general aeroelastic behavior of the typical section with SMA springs, the effects of preloading the springs, the effects of considering different SMA constitutive properties and the effects of different spring geometries. An experimental verification of the most general case is presented, confirming some of the numerical predictions. In short, this work shows that SMA

elements have potential for being employed in aeroelastic applications to enhance the flutter and post-flutter behaviors.

The association of a typical aeroelastic section with SMA elements enables the exploitation of many distinct mechanisms for the enhancement of the aeroelastic behavior of the typical section. One can, for example, exploit the superior loss factor of SMA elements (with respect to that of conventional materials such as steel) to increase the linear flutter speed of the typical section. One can also exploit the ability of controllable change of elastic properties of the SMAs to modify the flutter behavior of the typical section by adaptively adjusting its frequency characteristics. Dynamic structural reinforcement is also possible by exploiting the change of elastic properties (*e.g.*, by increasing structural stiffness through heating of SMA elements). This work, however, focuses on the use of the pseudoelastic hysteresis of SMA springs as a fully passive damping mechanism to modify the aeroelastic behavior of the typical section.

This work also proposes the use of the pseudoelastic hysteresis of superelastic SMA elements (springs) as a novel mechanism to enable aeroelastic energy harvesting over a range of airflow speeds, in contrast with many recent works from the literature that employ concentrated structural nonlinearities (such as polynomial stiffening) for the same purpose. The proposed configuration of typical section with SMA springs can generate much more electrical power than the same typical section with a hardening steel spring (and the same amount of piezoelectric material). No other work in the literature (from other authors) reports on a similar mechanism.

Shape Memory Materials, Metallic Alloys and Springs

This chapter introduces fundamental concepts of shape memory materials and models of SMAs. The macroscopic behavior of SMAs is of concern. In the end of the chapter, the modeling of SMA helical springs is discussed and the model assumed in this work is presented. This model will be later added to the governing equations of the 2-DOF typical section in order to investigate the effects of the pseudoelastic damping on the aeroelastic behavior of the system.

A “shape memory” material can change its shape through external stimuli such as temperature (BUEHLER; WANG, 1968), magnetic field (KIEFER; LAGOUDAS, 2005) and several other forms of excitation (MENG et al., 2013). Among different materials which exhibit shape memory behavior are the shape memory polymers (LIU et al., 2014; SCALET et al., 2015) and the SMAs (such as the CuAlBe, CuZnAl, CuAlNi, CuAlZnMn and NiTi alloys) (HUANG, 2002; POORASADION et al., 2014). The near-equiatomic NiTi alloys usually exhibit attractive properties (with reasonable cost) and are widely used in academy and industry.

2.1 General Aspects of SMAs

An SMA element usually exhibits two different nonlinear phenomena: the shape memory effect and pseudoelastic effect, which are exploited depending on the application. The shape

memory effect is observed when the SMA is substantially deformed at a relatively low temperature and is later heated to recover its initial (undeformed) shape. If a mechanical constraint (*e.g.*, clamped ends, springs or dead weights) impedes the SMA of freely recovering its initial shape upon heating, internal stresses are generated. Such stresses are the mechanisms behind SMA actuators. The other effect, the pseudoelastic effect (or pseudoelasticity), is observed when the SMA is deformed at a relatively high temperature and recovers its initial shape as the deforming force is removed. If such a high temperature is below the room temperature, that SMA can be named “superelastic” by some authors (as throughout this work), although pseudoelastic and superelastic are synonyms for other authors. A shape memory material exhibiting the pseudoelastic effect exhibits a very large hysteresis loop in the stress-strain curve.

The reversible behavior of SMAs is related to cooperative atom movements at its crystallographic microstructure during the deformation, characterizing a diffusionless process. This way, the atoms may return to their original position during the shape recovery (BUEHLER; WANG, 1968; LAGOUDAS, 2008).

2.2 Phase Transformations in SMAs

The SMA behavior may be represented by the transition between two different crystallographic phases: the austenitic (or parent) phase (A) and the martensitic (or product) phase (M). The phase transformation (from A to M) is due to a shear distortion of the crystallographic lattice, known as martensitic transformation. During the transformation, each single martensitic crystal may assume a particular orientation or variant: “twinned” (M^t) or “detwinned” (M^d). Thus, forward phase transformations (from A to M) are denoted by $A \rightarrow M$, $A \rightarrow M^t$ or $A \rightarrow M^d$ in this study. Similarly, reverse phase transformations (from M to A) are denoted by $M \rightarrow A$, $M^t \rightarrow A$ or $M^d \rightarrow A$.

The twinned (or self-accommodated) martensite may be induced by low temperature while the detwinned (or reoriented) martensite may be induced by mechanical stress. The SMA temperature, however, affects the level of mechanical stress required for a stress-induced phase transformation. As well, the level of stress also affects the temperatures at which phase trans-

formations take place. This relationship between temperature and mechanical stress is described next in Sections 2.2.1 and 2.2.2.

2.2.1 Stress-Free Phase Transformation

An SMA element initially at austenitic phase and in the absence of stress and deformation is of concern¹. Its crystallographic structure may change from austenite to martensite if the material is cooled down. This process may result in the formation of several variants (yielding twinned martensite), depending on the considered alloy. The arrangement of the variants takes place in such a way that the macroscopic shape change is negligible. If the same SMA element (currently in the martensitic phase) is heated, the austenitic phase is recovered. As well, there is no macroscopic shape change since the material had no initial deformation. The microstructure of the SMA element, however, has changed from austenite to twinned martensite and then to austenite again.

Four critical temperatures may be associated with the (stress-free) phase transformation process. In a forward phase transformation, the change from austenite to twinned martensite begins at the martensite start temperature (M_s) and finishes at the martensite finish temperature (M_f). In a reverse phase transformation, the change from twinned martensite to austenite begins at the austenite start temperature (A_s) and finishes at the austenite finish temperature (A_f).

2.2.2 Phase Transformation with Applied Stress

By considering that an SMA element is initially cooled down below M_f in the absence of stress and deformation, such an SMA is in a twinned martensite phase. If the SMA temperature is then increased such that $M_s < T < A_s$, no phase transformation is expected to occur (neither forward or reverse), and the SMA maintains its current state. By assuming that enough mechanical loading is applied, resulting in a mechanical stress of magnitude σ , a conversion of twinned to detwinned martensite ($M^t \rightarrow M^d$) takes place, yielding a macroscopic shape change. The deformed configuration is preserved after the removal of the mechanical loading, and the

¹This assumption is frequent throughout this thesis and is usually implicit.

M^d phase is preserved as well. By increasing the SMA temperature above A_f , the austenitic phase, and hence the SMA initial shape, are recovered. The SMA may be cooled down again, with no shape change. On the other hand, by considering the SMA heated above A_f in a stress-free condition (yielding an initial austenitic phase) and then subject to enough mechanical loading, cooling it down yields a phase transformation from austenite to detwinned martensite, with a corresponding shape change. Heating the SMA again yields a shape recovery while that same mechanical loading is still applied. This behavior (related to the shape memory effect) is widely exploited by SMA-based actuators. A stress-induced phase transformation followed by a shape recovery due to heating is illustrated in Fig. 2.

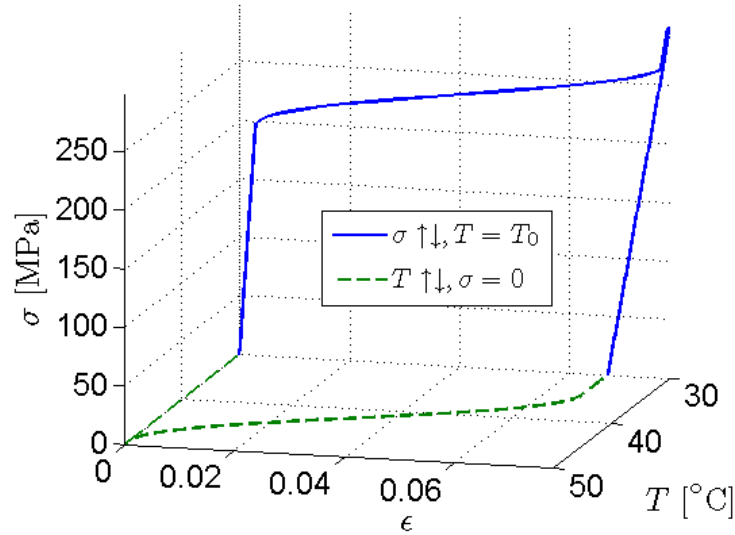


Figure 2 – Behavior of an SMA element during stress-induced phase transformation followed by a shape recovery promoted by heating.

The critical temperatures for phase transformation (described in Section 2.2.1) increase with applied stress. Such stress-dependent critical temperatures are denoted by M_s^σ , M_f^σ , A_s^σ and A_f^σ . In addition, there are minimum stress values for the onset and completion of a stress-induced phase transformation, denoted by σ_s^{\min} and σ_f^{\min} , respectively. Depending on the SMA temperature, the actual stress levels for the onset and completion of a stress-induced phase transformation may be higher than these minimum values. Such stress values are denoted by σ_s^M and σ_f^M . The austenitic phase may be recovered in the presence of stress when the mechanical loading decreases from σ_s^A to σ_f^A . If $T \geq A_f^\sigma$, the shape recovery is complete (characterizing the

pseudoelastic effect). If $A_s^\sigma < T < A_f^\sigma$, the shape recovery is only partial (characterizing a form of the shape memory effect).

Some aspects that determine the critical temperatures for phase transformation are briefly discussed in Section 2.2.3.

2.2.3 Brief Note on the Critical Temperatures for Phase Transformation

SMA's may be produced to exhibit specific critical temperatures. The alloy composition along with proper heat and mechanical treatments are determining factors (MELTON, 1990; LIU et al., 2008; ELAHINIA et al., 2012; ANDANI et al., 2014; HABERLAND et al., 2014). Sczerzenie and Gupta (2004) report that the critical temperatures of a quenched NiTi SMA increase almost linearly from $-150\text{ }^\circ\text{C}$ to $100\text{ }^\circ\text{C}$ (approximately) as its Ti-content increases from 48.5% to 50.5% (also approximately). The referred study also report that the critical temperatures of an aged SMA (of similar composition) exhibit a moderate increase between $10\text{ }^\circ\text{C}$ and $40\text{ }^\circ\text{C}$ for an increase of Ti-content between 48.5% and 49.5%. Between 49.5% and 50.5% of Ti-content, both processes (quenching and ageing) result in very similar critical temperatures. The refered study also point out the A_s temperature as the most reliable critical temperature for the characterization of an SMA because only a small standard deviation was found upon hundreds of differential scanning calorimetry (DSC) tests.

A rigorous experimental analysis by Frenzel et al. (2010) resulted in conclusive findings regarding the effects of the Ni/Ti ratio on the thermal characteristics of NiTi SMA's. The authors report that Ni-rich alloys exhibit lower critical temperatures, in agreement with the findings of Sczerzenie and Gupta (2004)). A linear relationship with slope of $-83\text{ K}\cdot(\text{at.}\%\text{Ni})^{-1}$ was reported for quenched samples with 49.8% to 50.8% Ni. Frenzel et al. (2010) also provided expressions for the critical temperatures in terms of the Ni-concentration. Therefore, considering the findings reported by the authors (Frenzel et al. (2010) as well as Sczerzenie and Gupta (2004)), it is possible to determine a NiTi ratio in order to obtain suitable critical temperatures for specific SMA-based applications. For example, the NiTi ratio can be calculated in order to have SMA springs exhibiting pseudoelasticity at room temperature and avoid the use of external

heat sources, as in some of the applications to be discussed along the next chapters of this work.

2.2.4 A Note on Thermal Effects in SMAs

Forward phase transformations in SMAs are exothermic due to the release of latent heat while reverse phase transformations are endothermic due to the absorption of latent heat (LAGOUDAS, 2008). When the loading rate is sufficiently small, the heat exchange with the environment during the forward phase transformation allows one to assume isothermal conditions. As the loading rate increases, the isothermal assumption fails due to the temperature variation related to convective heat. In such a case, the SMA temperature (1) increases above its initial value during the forward phase transformation (according to the loading rate); (2) decreases due to convection when that phase transformation ceases; (3) further decreases (in a more suddenly way, according to the rate of unloading) when the reverse phase transformation takes place (possibly leading the SMA temperature to below its initial value); (4) increases to the initial value (*e.g.*, the ambient temperature) when the reverse phase transformation ceases.

In brief, temperature changes affect the critical stresses for phase transformations in SMAs, as will be described in Section 2.3.3. With temperature-dependent critical stresses, the SMA behavior becomes more difficult to be predicted. Some works focus specifically on that aspect of SMAs (ELAHINIA; AHMADIAN, 2005a, 2005b). Other works assume isothermal conditions for simplicity, despite the thermal effects mentioned above, as in the case of this work. In the case studies that will be later presented, the predicted phase transformations are small (incomplete) in all cases. Since the thermal effects are mostly verified during phase transformations and the phase transformations are small in all cases of this work, isothermal conditions are assumed (as negligible temperature variations would be observed for such conditions). In order to justify the decision for the isothermal assumption of this work, Appendix D is included with a brief comparison between isothermal and non-isothermal conditions concerning the aeroelastic behavior of the typical section.

2.3 SMA Model

This section presents the SMA model employed in this work. The general behavior of the SMA material is described based mainly on the well-known works of Liang and Rogers (1990, 1992, 1997), Brinson (1993) and also on more recent contributions by Bucchi et al. (2014) and Poorasadion et al. (2014). The SMA constitutive behavior and the phase transformation kinetics for an SMA element subjected to uniaxial loading are based on Liang and Rogers (1990) and Brinson (1993). The modification of the case for uniaxial loading to a case of shear stress-strain behavior (in order to model SMA helical springs) is based on Liang and Rogers (1992, 1997). The SMA model (based on the classical works referred above) is modified to account for asymmetry behavior between tensile-compressive loadings based on the work of Poorasadion et al. (2014) (by separating the stress variable into positive and negative components). The model is further modified based on the work of Bucchi et al. (2014) to represent cross-sectional distributions of shear strain, shear stress and martensitic fraction along the radius of the coiled SMA wire (to produce a helical spring).

2.3.1 Thermomechanical Constitutive Modeling of SMAs

A variety of different constitutive models has been proposed aiming the prediction of the complex thermomechanical behavior of SMAs. Regardless the variety of available models, constitutive models with external (observable) and internal (non-observable) state variables are widely employed. A combination of external and internal variables can be considered to describe the thermodynamic state of an SMA material undergoing phase transformation. Although different thermodynamical internal variables can be chosen, an additional internal variable can be introduced to represent the martensitic volume fraction in the SMA material (LAGOUDAS, 2008). This is the case for the well-known constitutive models of Tanaka, Kobayashi and Sato (1986), Liang and Rogers (1990) and Brinson (1993) (employed in this work).

Tanaka-based SMA models (TANAKA; KOBAYASHI; SATO, 1986; LIANG; ROGERS, 1990; BRINSON, 1993) have been widely employed to represent the behavior of SMAs with reasonable correspondence with experimental verifications. In short, Tanaka, Kobayashi and

Sato (1986) proposed a thermomechanical constitutive equation to represent the macroscopic material behavior along with exponential functions to represent the phase transformation kinetics. Liang and Rogers (1990) modified the exponential functions of Tanaka, Kobayashi and Sato (1986) to cosine functions. The latter, however, considered only two distinct SMA material phases, namely austenite and stress-induced martensite. In addition, it was assumed that the material properties, such as the elastic modulus, are constant (independent of the current material phase). Brinson (1993) modified the model of Liang and Rogers (1990) by proposing a distinction between stress-induced (reoriented) and low-temperature-induced (self-accommodated) martensitic phases, allowing the representation of shape memory behaviors at low temperatures (in particular, the shape memory effect). In addition, non-constant material properties were considered in Brinson (1993). Since the required parameters for such models can be obtained by uniaxial stress-strain tests conducted at a few different temperatures, they are widely employed for the modeling of engineering applications since difficult-to-measure parameters (*e.g.*, free energy) can be avoided (ELAHINIA; AHMADIAN, 2005a).

Many further improvements reported in the literature of SMAs (LIANG; ROGERS, 1997; ELAHINIA; AHMADIAN, 2005a, 2005b; ENEMARK; SAVI; SANTOS, 2014; MEHRABI et al., 2014; POORASADION et al., 2014) contribute to the use of such models also in up-to-date state-of-the-art research.

2.3.2 A Brief Review of Brinson's Model

Liang and Rogers (1990) presented the following constitutive relationship for a uniaxially loaded SMA element,

$$\sigma - \sigma_0 = D(\varepsilon - \varepsilon_0) + \Omega(\xi - \xi_0) + \Theta(T - T_0), \quad (2.1)$$

where σ is the mechanical stress, D is the elastic modulus, ε is the axial strain, Ω is the phase transformation factor, ξ is the martensitic fraction, Θ is the thermal expansion coefficient, T is the material (SMA) temperature and subscript "0" denotes a reference state.

Brinson (1993) improved the model of Liang and Rogers (1990) by separating the marten-

sitic fraction into two distinct components,

$$\xi = \xi_T + \xi_S, \quad (2.2)$$

where ξ_T and ξ_S are the amounts of twinned and detwinned martensite, respectively. Secondly, Brinson (1993) considered non-constant material functions. The elastic modulus was expressed as a linear function of the martensitic fraction,

$$D(\xi) = D_A + \xi(D_M - D_A), \quad (2.3)$$

where D_A is the elastic modulus at fully austenitic phase and D_M is the elastic modulus at fully martensitic phase. This martensite-dependent modulus, $D(\xi)$, however, had previously appeared in Tanaka, Kobayashi and Sato (1986) and was also discussed (but not added to their modeling approach) in Liang and Rogers (1990). The transformation factor was also expressed in terms of the martensitic fraction, *i.e.*, $\Omega(\xi)$. The thermal expansion coefficient, Θ , was kept independent of ξ due to its lower order of magnitude with respect to the elastic modulus (about five orders lesser).

A differential form of the constitutive equation (Eq. (2.1)) for non-constant material functions is,

$$d\sigma = D(\xi)d\varepsilon + \Omega(\xi)d\xi_S + \Theta dT, \quad (2.4)$$

which yields,

$$\sigma - \sigma_0 = D(\xi)\varepsilon - D(\xi_0)\varepsilon_0 + \Omega(\xi)\xi_S - \Omega(\xi_0)\xi_{S0} + \Theta(T - T_0) \quad (2.5)$$

after integrating for a reference state. In this study, however, no (low) temperature-induced phase transformation is considered (only pseudoelasticity is of concern), so that $\xi_T = 0$ and thus $\xi = \xi_S$.

Brinson (1993) proposed the following kinetics functions to represent the martensitic fraction during a forward phase transformation,

$$\xi = \frac{1 - \xi_0}{2} \cos \left\{ \frac{\pi}{\sigma_s^{\min} - \sigma_f^{\min}} [\sigma - \sigma_f^M] \right\} + \frac{1 + \xi_0}{2}, \quad (2.6)$$

and the following kinetic function during a reverse phase transformation,

$$\xi = \frac{\xi_0}{2} \left\{ \cos \left[\frac{\pi}{A_f - A_s} \left(T - A_s - \frac{\sigma}{C_A} \right) \right] + 1 \right\}, \quad (2.7)$$

where the hardening function is described by a cosine function, as in Liang and Rogers (1990). Brinson's model, however, accounts for the existence of a minimum value of stress below which no stress-induced phase transformation is expected to occur (in agreement with a commonly observed experimental behavior).

2.3.3 Modification of Brinson's Model for Tension-Compression Asymmetry

The literature (*e.g.*, Achenbach, Atanackovic and Müller (1986), Gall et al. (1999), Tokuda et al. (1999), Mehrabi, Kadkhodaei and Elahinia (2014), Poorasadion et al. (2014)) usually reports an asymmetry behavior between tensile and compressive loadings when testing an SMA specimen. Gall et al. (1999) relate such a phenomenon to the heat treatment and crystallographic orientation of the alloy. Experimental tests reported in the referred paper show that the maximum recoverable strain and the critical transformation stress are strongly affected SMA properties. Paiva et al. (2005) proposed an SMA constitutive model that accounts for tensile-compressive asymmetry (and also plasticity, not considered in this work). The model presented in the referred paper was verified by using experimental data from Gall et al. (1999). In another investigation, Savi et al. (2008) considered the effects of asymmetry on the dynamical behavior of an SMA oscillator.

In this work, asymmetry behavior is included so that its effects on the aeroelastic behavior of the typical section can also be investigated. Although many different papers address asymmetry behavior in SMAs, the modifications (concerning asymmetry) in the classical SMA model employed in this work are based on Poorasadion et al. (2014).

PHASE TRANSFORMATION DIAGRAM

Fig. 3 displays a phase transformation diagram accounting for tensile-compressive asymmetry behavior. Arbitrary SMA properties are used for illustration purposes. The SMA tem-

perature (T) axis starts at M_s because no self-accommodated (twinned) martensite formation due to low temperature (*i.e.*, below the martensite start temperature M_s) is considered in this work². Tensile behavior is represented above the zero-stress axis, and compressive behavior is represented below that axis. The highlighted areas represent phase transformation regions. The boundaries of the transformation regions at different slopes (comparing tensile behavior with compressive behavior) are related to asymmetry effects. The SMA parameters which depend on the loading direction are denoted with a superscript “*”, which assumes “+” for tension and “-” for compression. The stress-induced transformation regions (in blue, between solid lines) are indicated by $A \rightarrow M_D^*$. The austenitic transformation regions (in yellow, between dashed lines) are indicated by $M_D^* \rightarrow A$.

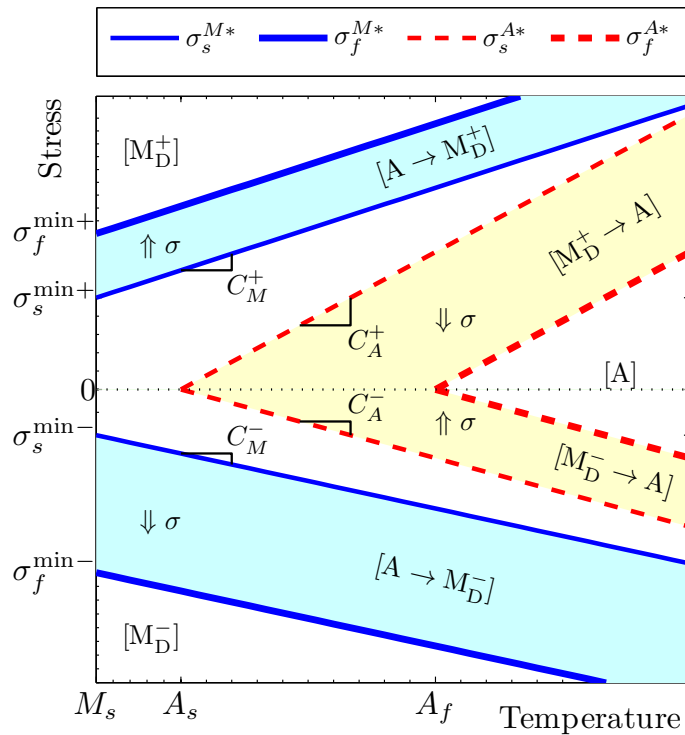


Figure 3 – SMA phase transformation diagram with tension-compression asymmetry.

By assuming a fully austenitic initial phase, $T > M_s$ and increasing stress (σ) in either tension or compression, the stress-strain behavior is linear elastic while $|\sigma| < |\sigma_s^{M^*}|$, where $\sigma_s^{M^*} = \sigma_s^{\min^*} + C_M^*(T - M_s)$. If $|\sigma| \geq |\sigma_s^{M^*}|$, stress-induced phase transformation takes place

²Please refer to Poorasadion et al. (2014) for a complete phase diagram.

across a vertical path (assuming no temperature variation) until $\sigma = \sigma_f^{M*}$, where $\sigma_f^{M*} = \sigma_f^{\min*} + C_M^*(T - M_s)$, at which the detwinning process finishes and the SMA is fully martensitic. Further increase in stress (exceeding σ_f^{M*}) yields linear elastic behavior with martensitic properties. From that state and by decreasing the stress, linear unloading occurs while $|\sigma| > |\sigma_s^{A*}|$, where $\sigma_s^{A*} = C_A^*(T - A_s)$. Further unloading will result in either (1) partial strain recovery if $A_s \leq T < A_f$ and σ reaches zero (related to the shape memory effect) or (2) complete recovery if $T \geq A_f$ and $|\sigma| \leq |\sigma_f^{A*}|$ (related to pseudoelasticity). No phase transformation is considered outside those regions and the martensitic fraction remains unchanged.

A method for the computation of the martensitic fraction which accounts for asymmetry in tension and compression is described next.

STRESS-INDUCED (FORWARD) PHASE TRANSFORMATION

Poorasadion et al. (2014) decompose the stress-induced martensitic fraction into tensile and compressive components: $\xi = \xi^+ + \xi^-$. Such components are denoted here by ξ^* . In the referred paper, a distinct set of functions for the determination of the martensitic fraction that corresponds to each possible kind of phase transformation is presented. However, those functions are similar to each other (with changes mostly in parameters) and can be represented in a compact form. Here, an “independent” term and a “dependent” term are assumed. The “independent” term is directly related to the ongoing phase transformation, and is the first term to be computed. The “dependent” term is then updated to conform to the constraint of total martensitic fraction between zero and unity.

The “independent” term is given by,

$$\xi^{\text{indep}} = \frac{1 - Y_{\text{MD}}^*}{2} + \xi_0^{\text{indep}} \frac{1 + Y_{\text{MD}}^*}{2}, \quad (2.8)$$

and the “dependent” term is,

$$\xi^{\text{dep}} = \xi_0^{\text{dep}} \frac{1 - \xi^{\text{indep}}}{1 - \xi_0^{\text{indep}}}, \quad (2.9)$$

where $\xi^{\text{indep}} = \xi^+$ and $\xi^{\text{dep}} = \xi^-$ for tensile loading or $\xi^{\text{indep}} = \xi^-$ and $\xi^{\text{dep}} = \xi^+$ for compressive loading. The hardening functions of stress-induced martensitic fraction (in tension and

compression), Y_{MD}^* , are represented by,

$$Y_{MD}^* = \cos \left(\pi \frac{\sigma - \sigma_s^{M^*}}{\sigma_f^{\min^*} - \sigma_s^{\min^*}} \right), \quad (2.10)$$

where $\sigma_s^{M^*} = \sigma_s^{\min^*} + c(T, M_s)$, and $c(T, M_s) = C_M^*(T - M_s)$ for $T > M_s$ or $c(T, M_s) = 0$ otherwise.

REVERSE PHASE TRANSFORMATION

The austenitic phase is recovered during unloading as the stress decreases from $\sigma_s^{A^*}$ to $\sigma_f^{A^*}$. In such a case, the martensitic fraction can be given by,

$$\xi = \frac{\xi_0}{2} (Y_A^* + 1), \quad (2.11)$$

where the corresponding hardening function, Y_A^* , is,

$$Y_A^* = \cos \left(\pi \frac{T - A_s^{\sigma^*}}{A_f - A_s} \right), \quad (2.12)$$

and $A_s^{\sigma^*} = A_s + \sigma/C_A^*$ is the austenite critical start temperature for non-zero stress. The martensitic components (in tension and compression) can be updated by $\xi^* = \xi_0^* (\xi/\xi_0)$.

This compact representation of the phase transformation model is convenient for numerical implementation. The equations can be wrapped in very few functions with a reduced number of formal parameters, while only the input parameters have to be modified depending on the kind of the ongoing phase transformation.

MECHANICAL CONSTITUTIVE RELATIONSHIP

The elastic modulus may assume different values for each possible phase, including the stress-induced martensitic phase in compression (*i.e.*, $D_A \neq D_M^+ \neq D_M^-$). The modulus for an arbitrary state of phase transformation is, therefore,

$$D(\xi) = D_A + \xi^+ (D_M^+ - D_A) + \xi^- (D_M^- - D_A), \quad (2.13)$$

with all variables previously defined.

Since the maximum recoverable strain may change between tension and compression (GALL

et al., 1999), the transformation factor becomes,

$$\Omega^*(\xi) = -\varepsilon_L^* D(\xi), \quad (2.14)$$

where the variables were also previously defined.

The constitutive equation of Brinson for non-constant material parameters and in differential form, Eq. (2.4), is rewritten as,

$$d\sigma = D(\xi) d\varepsilon + \Omega^+(\xi) d\xi^+ + \Omega^-(\xi) d\xi^- \quad (2.15)$$

and by substituting Eq. (2.14) into Eq. (2.15), and integrating the resulting equation, a constitutive relationship for SMAs accounting for asymmetry behavior may be obtained as,

$$\sigma - \sigma_0 = D(\xi) \varepsilon - D(\xi_0) \varepsilon_0 + \Omega^+(\xi) \xi^+ - \Omega^+(\xi_0) \xi_0^+ + \Omega^-(\xi) \xi^- - \Omega^-(\xi_0) \xi_0^- \quad (2.16)$$

for a given reference state (denoted by subscript “0”).

2.4 A Model for SMA Helical Springs

In this section, a model for SMA helical springs is presented. A pure shear assumption is considered for relating the normal stress-strain behavior to shear stress-strain behavior. The phase transformation model described in the previous section is used to introduce the nonlinear SMA behavior into the spring model. A further improvement is included to represent cross-sectional distributions of shear strain, shear stress and martensitic fraction along the radius of the coiled SMA wire. Later, such a model will be used to add SMA springs to the (piezo)aeroelastic model of the 2-DOF typical section considered in this work.

2.4.1 Mechanical Constitutive Relationship for Shear Behavior

Liang and Rogers (1997) adopted a pure shear approach for the modeling of SMA helical springs. The normal and shear stresses (σ and τ , respectively) were related to each other as $\sigma = \sqrt{3}\tau$. Then a constitutive relation was obtained in terms of shear quantities. With a similar

procedure, Eq. (2.16) is rewritten as,

$$\tau - \tau_0 = G(\xi) \gamma - G(\xi_0) \gamma_0 + \Omega_{\tau}^+(\xi) \xi^+ - \Omega_{\tau}^+(\xi_0) \xi_0^+ + \Omega_{\tau}^-(\xi) \xi^- - \Omega_{\tau}^-(\xi_0) \xi_0^-, \quad (2.17)$$

where G is the shear modulus, γ is the shear strain and $\Omega_{\tau}^* = -\gamma_L^* G(\xi)$, in which γ_L^* is the maximum recoverable shear strain of the SMA. The elastic modulus and shear modulus are related to each other by,

$$G(\xi) = \frac{D(\xi)}{2(1 + \mu_P)}, \quad (2.18)$$

where μ_P is Poisson's ratio. Thus, Eq. (2.13) is rewritten as,

$$G(\xi) = G_A + \xi^+ (G_M^+ - G_A) + \xi^- (G_M^- - G_A), \quad (2.19)$$

where G_A is the fully austenitic shear modulus and G_M^* represents the shear moduli of the fully detwinned martensitic phases.

One should note the constitutive mechanical relationship for asymmetry behavior presented in Section 2.3.3 is expressed in general terms (for an arbitrary SMA element subjected to uniaxial tensile or compressive loading). Due to the particular case of SMA helical springs considered in the aeroelastic problem of this work, the modification of Eq. (2.16) to shear behavior was presented in Eq. (2.17). Therefore, it is assumed onward in this work that “tensile loading” represents positive (shear) stress values related to the elongation of the SMA springs. Similarly, “compressive loading” represents negative (shear) stress values related to the compression of the SMA springs.

2.4.2 Modeling of the SMA Springs

Based on classical spring design (BUDYNAS; NISBETT, 2014), Liang and Rogers (1997) presented a model for SMA helical springs. One of their assumptions is that the shear stress, shear strain and martensitic fraction are constant along the radius of the coiled SMA and their respective values are the ones observed at the surface of the wire. Thus, the shear stress is given by,

$$\tau = \frac{2FR}{\pi r^3}, \quad (2.20)$$

where F is an applied (external) force, R is the mean coil radius of the spring and r is the radius of the wire used to fabricate the spring.

The shear strain

$$\gamma = \frac{\tau}{G} = \frac{2FR}{\pi r^3 G} \quad (2.21)$$

is obtained from the torsion version of the Hooke's law.

The angle between two element sections is,

$$d\varphi = \frac{\gamma dx}{r}, \quad (2.22)$$

and the angular deflection of an end of the wire with respect to the other end is,

$$\varphi = \int_0^{2\pi RN} \frac{\gamma}{r} dx = \frac{4FR^2 N}{r^4 G}, \quad (2.23)$$

where N is the number of active coils of the spring. The total spring deflection is,

$$y = \varphi R = \frac{4FR^3 N}{r^4 G}, \quad (2.24)$$

and the spring stiffness is, therefore,

$$k = \frac{F}{y} = \frac{r^4 G}{4R^3 N}, \quad (2.25)$$

that is modified to

$$k(\xi) = \frac{r^4}{4R^3 N} G(\xi) \quad (2.26)$$

when an SMA spring is modeled.

The constitutive relation of Eq. (2.17) is rewritten as,

$$\tau = G(\xi) \gamma + \Omega_{\tau}^{+}(\xi) \xi^{+} + \Omega_{\tau}^{-}(\xi) \xi^{-} \quad (2.27)$$

when no initial stress or strain are assumed.

Solving Eq. (2.27) for γ ,

$$\gamma = \frac{1}{G(\xi)} (\tau - \Omega_{\tau}^{+}(\xi) \xi^{+} - \Omega_{\tau}^{-}(\xi) \xi^{-}) \quad (2.28)$$

and combining with $y = R \int_0^{2\pi RN} \frac{\gamma}{r} dx$ (obtained from Eqs. (2.23) and (2.24)), leads to

$$y = \frac{2\pi R^2 N}{rG(\xi)} (\tau - \Omega_{\tau}^{+}(\xi) \xi^{+} - \Omega_{\tau}^{-}(\xi) \xi^{-}), \quad (2.29)$$

that is the SMA spring deflection.

The SMA spring deflection in terms of the applied force is given by

$$y = \frac{4R^3 N}{r^4 G(\xi)} F - \frac{2\pi R^2 N}{rG(\xi)} (\Omega_{\tau}^{+}(\xi) \xi^{+} + \Omega_{\tau}^{-}(\xi) \xi^{-}) \quad (2.30)$$

when Eq. (2.20) is used in Eq. (2.29).

The SMA spring model is modified in the next section to represent distributions of shear strain, shear stress and martensitic fraction along the radius of the coiled SMA wire.

2.4.3 Cross-Sectional Representation of the Coiled SMA Wire

The cross-section of the coiled SMA wire is represented by several annular regions (Fig. 4). This approach has been used in the literature (BUCCHI et al., 2014; RAO; SRINIVASA, 2015) to improve the representation of SMA spring behavior represented by models such as the one described in the previous section.

For large enough mechanical loading, the annular regions may have distinct phase transformation states. Fig. 4(a) displays the cross-sectional distribution of martensitic fraction for an arbitrarily loaded SMA spring (initially at austenitic phase). Three regions are represented: (1) an austenitic core, (2) a mixed austenitic-martensitic region and (3) a fully martensitic (outer) region. Fig. 4(b) displays the distributions for 5 and 15 annular regions (top and bottom rows, respectively). The shear strain is displayed on the left, the shear stress on the middle and the martensitic fraction on the right. The blue dashed lines (from the center to the wire surface) represent the distribution profile of the corresponding quantity along the radius.

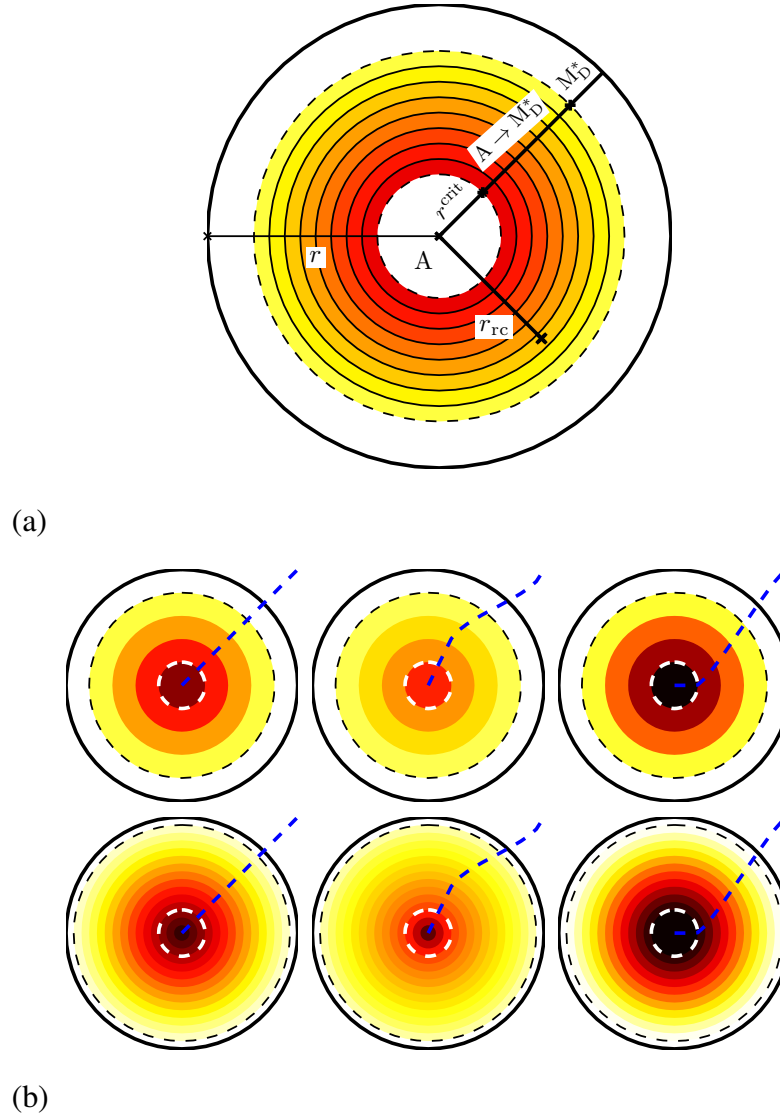


Figure 4 – Cross-sectional representation of the coiled SMA wire – (a) martensitic fraction (detail) and (b) shear strain (left), shear stress (middle) and martensitic fraction (right).

The distribution of shear strain is assumed linear along the wire radius and given by,

$$\gamma(r_{rc}) = \left(\frac{r_{rc}}{r}\right) \gamma^{\max}, \quad (2.31)$$

where r_{rc} is a radial coordinate and,

$$\gamma^{\max} = \frac{ry}{2\pi NR^2}, \quad (2.32)$$

is the shear strain at the outer annular region of the SMA spring (from Eqs. (2.21) and (2.24)).

Usually, the shear stress is unable to induce phase transformation at the inner most regions, so that an austenitic core may be present in the coiled SMA wire. At that core, linear behavior is verified for austenitic properties. As the radial coordinate reaches a critical value, given by (AGUIAR; SAVI; PACHECO, 2010),

$$r^{\text{crit}} = \frac{\pi NR^2 \tau_s^{M^*}}{r\gamma G(\xi)}, \quad (2.33)$$

stress-induced phase transformation takes place and the distribution of shear stress becomes nonlinear. In such a case, mixed austenite and martensite are present in the SMA and the martensite-dependent properties assume intermediate values (between their fully austenitic and fully martensitic values) in the phase transformation region. If the stress-induced phase transformation is completed, as in the outer regions of Fig. 4, linear elastic behavior is verified for martensitic properties.

The total martensitic fraction is estimated by a weighted average in which the contribution of each annular region is proportional to its area,

$$\xi = \sum_{j=1}^n \frac{A_j}{r^2} \xi_j, \quad (2.34)$$

where

$$A = \left\{ r_{\text{rc}1}^2 \quad \{ r_{\text{rc}j}^2 - r_{\text{rc}j-1}^2 \} \Big|_{j=2..n} \right\} \quad (2.35)$$

is related to the area of each annular region. It is clear that such an assumption yields to a lower martensitic fraction than that obtained when a constant value (equal to the maximum) is assumed.

Model of a Piezoelectrically Coupled Typical Aeroelastic Section

Aeroelastic phenomena such as flutter and LCOs can be studied by considering a typical section model as that displayed in Fig. 5 (BISPLINGHOFF; ASHLEY; HALFMAN, 1955; HODGES; PIERCE, 2002; DOWELL, 2015). The typical section can undergo plunge and pitch displacements (as illustrated in Fig. 6), denoted by h and α , respectively, when subjected to an airflow speed (U_∞). The plunge displacement is measured at the elastic axis (positive downward). The pitch angle is measured about the elastic axis (positive clockwise).

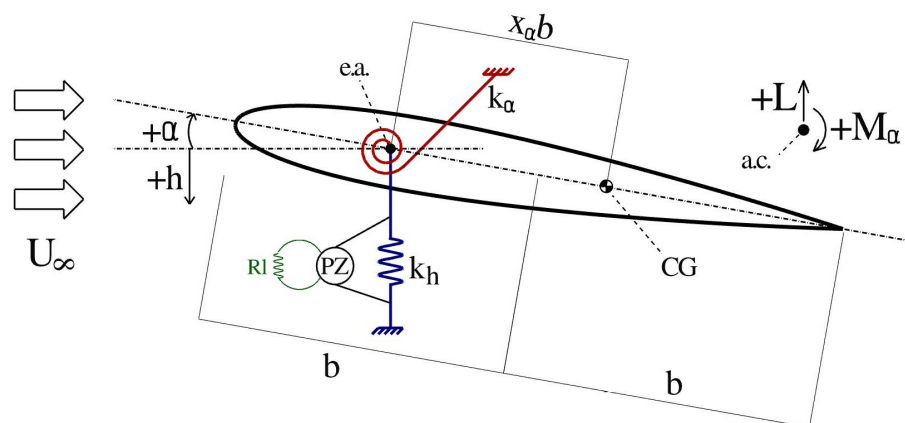


Figure 5 – A 2-DOF typical aeroelastic section model (with piezoelectric coupling).

The elastic axis is defined from the midchord position of the typical section chord line (a dashed line from the leading edge to the trailing edge in Fig. 5) and is positive in the aft

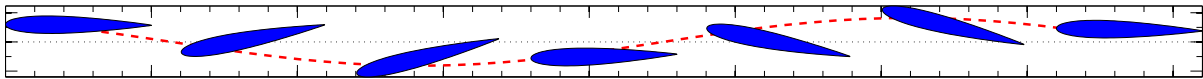


Figure 6 – Motion of a typical section.

direction. Such a distance (in semichords) is denoted by c (omitted in Fig. 5). The semichord length is b and the dimensionless distance (in semichords) between the elastic axis and the center of gravity (CG) is x_α . It is usual in aeroelasticity to normalize the aeroelastic parameters by the span length l . Thus, the stiffness per unit of span length of the plunge and pitch DOFs are k_h and k_α , respectively (subscript h denotes the plunge DOF while subscript α denotes the pitch DOF). Viscous damping is assumed and, similarly, represented by d_h and d_α (also defined per unit of span length and omitted in Fig. 5 for clarity). The unsteady aerodynamic lift per unit of span length, L , acts at the aerodynamic center of the typical section. For subsonic regime, such a location is at the quarter-chord length of the typical section. The unsteady pitching moment per unit of span length, M_α , acts at the elastic axis of the typical section. In the particular case of this study, the elastic axis is also at the quarter-chord of the typical section.

In our Laboratory of Aeroelasticity, typical section models have been considered for the investigation of aeroelastic phenomena such as flutter and LCOs. The general goals are to mitigate those oscillations or to exploit them for airfoil-based wind energy harvesting. In both instances, smart materials (mainly piezoceramics) are used (ERTURK et al., 2010; SOUSA et al., 2011; DIAS; De Marqui Jr; ERTURK, 2013; D’ASSUNÇÃO; De Marqui Jr, 2015). In this work, the goal is the investigation of the effects of pseudoelastic hysteresis of SMA springs on the aeroelastic behavior of a 2-DOF typical section. Based on the general aeroelastic behavior of the typical section with SMA springs that will be presented later in the next chapters, two distinct applications are proposed: 1) passive control of aeroelastic oscillations and 2) envelope enhancement of an airfoil-based wind energy harvester.

As previously discussed in the Introduction, the effects of different preload levels applied to the SMA springs as well as the effects of geometric nonlinearities and SMA constitutive properties are first investigated. Later, piezoelectric coupling is added to the typical section with

SMA elements for wind energy harvesting and the performance is compared to previously published airfoil-based wind energy harvester with concentrated nonlinearities. Therefore, the derivation presented in this chapter considers a 2-DOF typical section with SMA springs and also electromechanical coupling in the plunge DOF. This derivation leads to the most general case investigated in this work (wind energy harvesting) and the electromechanical coupling is not considered in the other case studies. For this reason, piezoelectric coupling (indicated by “PZ” in Fig. 5) is included in the derivation of the typical section model presented in the next section, yielding a piezoaeroelastic typical section model. A resistive load is considered in the electric domain to estimate the electrical power output, also indicated in Fig. 5.

3.1 Derivation of the Equations of Motion of the Typical Section

The coupled equations of motion of the piezoaeroelastic typical section with electromechanical coupling considered in the plunge DOF are derived by using Lagrange’s Method. Hamilton’s Principle applied to an electroaeroelastic system yields (ERTURK; INMAN, 2011),

$$\int_{t_1}^{t_2} (\delta T_E - \delta U_E + \delta W_{ie} + \delta W_{nce} + \delta W_{nca} + \delta W_{sd}) dt = 0, \quad (3.1)$$

where δ denotes the first variation of a functional. Thus, δT_E , δU_E and δW_{ie} denote, respectively, the variations of the total kinetic, potential and (internal) electrical energies, all of them expressed as per unit of span length. δW_{nce} , δW_{nca} and δW_{sd} are the non-conservative components of the virtual work due to the electrical charge, aerodynamic loads and structural damping, respectively (also per unit of span length).

The kinetic energy component is¹,

$$T_E = \frac{1}{2} m_t \dot{h}^2 + \frac{1}{2} I_\alpha \dot{\alpha}^2 + m x_\alpha b \dot{h} \dot{\alpha}, \quad (3.2)$$

where m is the pitch DOF mass per unit of span length and m_t is the total mass (pitch and plunge) per unit of span length. In the case of a non-ideal typical section model, the masses of

¹Detailed derivation can be found in Trickey (2000).

the plunge and pitch DOFs may differ from each other as will be shown later in Chapter 7 for the experimental model (due to the mass of the springs and components attaching the typical section to a stationary frame). Moreover, I_α is moment of inertia of the typical section (per unit of span length) with respect to the elastic axis. Overdot denotes time derivative.

The potential energy component due to the elastic springs and to an equivalent stiffness related to the piezoelectric material is,

$$U_E = \frac{1}{2}k_h h^2 + \frac{1}{2}k_\alpha \alpha^2 - \frac{1}{2} \frac{\theta}{l} h v, \quad (3.3)$$

where θ is the electromechanical coupling term and v is the voltage across the resistive load considered in the electrical domain.

The internal electrical energy component is,

$$W_{ie} = \frac{1}{2} \frac{C_p^{eq}}{l} v^2, \quad (3.4)$$

where C_p^{eq} is the equivalent capacitance of the piezoceramic layers².

The non-conservative components of the virtual work are,

$$\delta W_{nce} = \frac{Q}{l} \delta v \quad (3.5)$$

$$\delta W_{nca} = -L \delta h + M_\alpha \delta \alpha \quad (3.6)$$

$$\delta W_{sd} = -d_h \dot{h} \delta h - d_\alpha \dot{\alpha} \delta \alpha, \quad (3.7)$$

where Q is the electrical charge. These quantities are expressed as per unit of span length.

The Lagrange equations for the piezoaeroelastic typical section are represented by,

$$\frac{d}{dt} \left(\frac{\partial T}{\partial \dot{q}_i} \right) - \frac{\partial T}{\partial q_i} + \frac{\partial U}{\partial q_i} - \frac{\partial W_{ie}}{\partial q_i} = \mathcal{Q}_i \quad (i = 1, \dots, n), \quad (3.8)$$

where q_i is a generalized coordinate and \mathcal{Q}_i is a non-conservative force (details in Appendix

²According to the experimental configuration employed in Sousa et al. (2011) and assumed to be the same in this work.

A). By applying Eq. (3.8) to the typical section, yields,

$$\frac{d}{dt} \left(\frac{\partial T_E}{\partial \dot{\alpha}} \right) - \frac{\partial T_E}{\partial \alpha} + \frac{\partial U_E}{\partial \alpha} - \frac{\partial W_{ie}}{\partial \alpha} = M_\alpha - d_\alpha \dot{\alpha} \quad (3.9)$$

$$\frac{d}{dt} \left(\frac{\partial T_E}{\partial \dot{h}} \right) - \frac{\partial T_E}{\partial h} + \frac{\partial U_E}{\partial h} - \frac{\partial W_{ie}}{\partial h} = -L - d_h \dot{h} \quad (3.10)$$

$$\frac{d}{dt} \left(\frac{\partial T_E}{\partial \dot{v}} \right) - \frac{\partial T_E}{\partial v} + \frac{\partial U_E}{\partial v} - \frac{\partial W_{ie}}{\partial v} = \frac{Q}{l}. \quad (3.11)$$

By replacing T_E , U_E , W_{ie} , δW_{nce} , δW_{nca} and δW_{sd} (defined by Eqs. (3.2) to (3.7)) into Eqs. (3.9) to (3.11), and by taking the time derivative of Eq. (3.11) and also employing Ohms's law, $\dot{Q} = v/R_l$, where R_l is the resistive load, yields,

$$I_\alpha \ddot{\alpha} + m x_\alpha b \ddot{h} + d_\alpha \dot{\alpha} + k_\alpha \alpha = M_\alpha \quad (3.12)$$

$$m x_\alpha b \ddot{\alpha} + (m + m_f) \ddot{h} + d_h \dot{h} + k_h h - \frac{\theta}{l} v = -L \quad (3.13)$$

$$C_p^{eq} \dot{v} + \frac{v}{R_l} + \theta \dot{h} = 0, \quad (3.14)$$

which are the electromechanically coupled equations of motion of the piezoaeroelastic typical section.

In the next section, Eqs. (3.12) to (3.14) are represented in dimensionless state-space form.

3.2 Dimensionless Representation of the Equations of Motion in State-Space Form

By rewriting Eqs. (3.12) to (3.14) in dimensionless terms, one may establish similarities between models in different scales (BISPLINGHOFF; ASHLEY; HALFMAN, 1955). Another advantage is that a class of models may be analyzed instead of a particular model (HEMATI, 1995). The representation of the equations of motion in state-space form, in turn, is convenient for their solution by using numerical methods such as the Runge-Kutta scheme (used in the simulations presented throughout this work).

3.2.1 Nondimensionalization of the Equations of Motion

The parameters assumed for the nondimensionalization of Eqs. (3.12) to (3.14) are the typical section mass (per unit of span length) and the semichord length (m and b , respectively). To introduce the dimensionless terms of Theodorsen (1935), Eq. (3.12) is multiplied by $(mb^2)^{-1}$ and Eq. (3.13) is multiplied by $(mb)^{-1}$. Since electromechanical coupling is considered here, Eq. (3.14) is multiplied by $\tilde{v}(mb^2l)^{-1}$, where \tilde{v} is assumed as 1 Volt. Thus,

$$r_\alpha^2 \ddot{\alpha} + x_\alpha \ddot{h} + \frac{d_\alpha}{mb^2} \dot{\alpha} + r_\alpha^2 \omega_\alpha^2 \alpha = \frac{M_\alpha}{mb^2} \quad (3.15)$$

$$x_\alpha \ddot{\alpha} + \mu \ddot{h} + \frac{d_h}{m} \dot{h} + \omega_h^2 \bar{h} - \frac{\theta \tilde{v}}{mbl} v = -\frac{L}{mb} \quad (3.16)$$

$$\frac{C_p^{eq} \tilde{v}^3}{mb^2 l} \dot{v} + \frac{\tilde{v}^2}{mb^2 l R_l} v + \frac{\theta \tilde{v}}{mbl} \dot{h} = 0, \quad (3.17)$$

where r_α is the radius of gyration divided by the semichord, $\bar{h} = hb^{-1}$ is the dimensionless plunge displacement (in semichords), ω_α and ω_h are the uncoupled natural frequencies of the pitch and plunge DOFs, respectively, $\mu = m_t/m$ is the ratio of the translating mass to the rotating mass and $v = \tilde{v}^{-1}$ is the dimensionless voltage.

A dimensionless time is also considered and defined as,

$$\bar{t} = \omega_h t,$$

where t is the dimensional time.

The time derivatives are related to each other as,

$$\frac{dx}{dt} = \omega_h \frac{dx}{d\bar{t}},$$

or, equivalently,

$$\dot{x} = \omega_h x',$$

where x is an arbitrary time-dependent variable (α , h or v in this study) and the prime ($'$) denotes differentiation with respect to the dimensionless time. The second derivative is,

$$\ddot{x} = \omega_h^2 x''.$$

Thus, Eqs. (3.12) to (3.13) are also multiplied by ω_h^{-2} and Eq. (3.14) is multiplied by ω_h^{-3} .

The dimensionless equations of motion are, therefore,

$$r_\alpha^2 \alpha'' + x_\alpha \bar{h}'' + \zeta_\alpha \alpha' + \eta_\alpha^2 r_\alpha^2 \alpha = \bar{M}_\alpha \quad (3.18)$$

$$x_\alpha \alpha'' + \mu \bar{h}'' + \zeta_h \bar{h}' + \bar{h} - \chi v = -\bar{L} \quad (3.19)$$

$$\psi v' + \lambda^{-1} v + \chi \bar{h}' = 0, \quad (3.20)$$

where $\zeta_\alpha = d_\alpha (mb^2 \omega_h)^{-1}$ and $\zeta_h = d_h (m \omega_h)^{-1}$ are the damping ratios of the pitch and plunge DOFs (per unit of span length), respectively, and η_α is the pitch-to-plunge frequency ratio ($\eta_\alpha = \omega_\alpha \omega_h^{-1}$).

The dimensionless capacitance is $\psi = C_p^{eq} \bar{v}^3 (mb^2 l \omega_h^2)^{-1}$, the dimensionless electromechanical coupling term is $\chi = \theta \bar{v} (mbl \omega_h^2)^{-1}$ and the dimensionless resistive load is $\lambda = mb^2 l \omega_h^3 R_l \bar{v}^{-2}$. A dimensionless electrical power is defined as $\bar{p} = v^2 \lambda^{-1}$.

The dimensionless aerodynamic loads are expressed as $\bar{M}_\alpha = M_\alpha (mb^2 \omega_h^2)^{-1}$ and $\bar{L} = L (mb \omega_h^2)^{-1}$.

3.2.2 Representation of the Equations of Motion in State-Space Form

Eqs. (3.18) to (3.20) may be represented in state-space form as,

$$\begin{bmatrix} \mathbf{I} & \mathbf{0} & \mathbf{0} \\ \mathbf{0} & \mathbf{M} & \mathbf{0} \\ \mathbf{0} & \mathbf{0} & \psi \end{bmatrix} \begin{Bmatrix} \mathbf{x}'_s \\ \mathbf{x}''_s \\ v' \end{Bmatrix} + \begin{bmatrix} \mathbf{0} & -\mathbf{I} & \mathbf{0} \\ \mathbf{K} & \mathbf{B} & -\Theta_e^T \\ \mathbf{0} & \Theta_e & \lambda^{-1} \end{bmatrix} \begin{Bmatrix} \mathbf{x}_s \\ \mathbf{x}'_s \\ v \end{Bmatrix} = \begin{Bmatrix} \mathbf{0} \\ \mathcal{F} \\ 0 \end{Bmatrix}, \quad (3.21)$$

where \mathbf{I} is a 2x2 identity matrix. Vector $\mathbf{x}_s = \{ \alpha \ \bar{h} \}^T$ represents the structural states (superscript T denotes a transposed vector). Vector $\Theta_e = \{ 0 \ \chi \}$ contains the electromechanical coupling term. Vector $\mathcal{F} = \{ \bar{M}_\alpha \ \bar{L} \}^T$ represents the aerodynamic loads. Matrices \mathbf{M} , \mathbf{K} and \mathbf{B} contain the dimensionless inertial, stiffness and damping parameters. These matrices are

given,

$$\mathbf{M} = \begin{bmatrix} r_\alpha^2 & x_\alpha \\ x_\alpha & \mu \end{bmatrix} \quad (3.22)$$

$$\mathbf{K} = \begin{bmatrix} r_\alpha^2 \eta_\alpha^2 & 0 \\ 0 & 1 \end{bmatrix} \quad (3.23)$$

$$\mathbf{B} = \begin{bmatrix} \zeta_\alpha & 0 \\ 0 & \zeta_h \end{bmatrix}. \quad (3.24)$$

The unsteady aerodynamic model used in this study is described (and included in Eq. (3.21)) in the next section.

3.3 Unsteady Aerodynamic Model for Arbitrary Airfoil Motions

The unsteady aerodynamic model employed for the determination of the pitching moment and lift is based on the work of Edwards (1977). In short, the referred study presents a state-space model (which is convenient for numerical solution) valid for arbitrary airfoil motions. This is in contrast with the classical Theodorsen (1935) model, from which Edwards' model was derived, that is valid only for harmonic motion. Edwards' model was previously used (and experimentally verified) in Sousa et al. (2011), where structural nonlinearities, and hence nonlinear aeroelastic behavior, were of concern. As well, nonlinear behavior is expected in this work (including post-flutter LCOs) and the same aerodynamic model is employed.

Incompressible subsonic flow without flow separation effects (hence, small pitch angles) is assumed. In Theodorsen (1935)³, the velocity potential due to the flow around the typical section is split into non-circulatory and circulatory portions. The non-circulatory portion satisfies a time-dependent boundary condition which accounts for the presence of the typical section in the flow field. This portion is obtained by a distribution of *doublers* (sources and sinks) in both the upper and lower surfaces of the typical section. The circulatory portion satisfies the ‘‘Kutta

³Theodorsen (1935) originally derived expressions for a 3-DOF typical section (including a control surface).

condition”, in which pressure and velocity should be finite and continuous at the trailing edge of the typical section. This portion is obtained by a vortex pattern placed on both the typical section and its wake. Bernoulli theorem for unsteady flow is then employed to determine the local pressures acting on the typical section. By integrating such pressures, the pitching moment and lift are obtained as,

$$M_\alpha = -\rho b^2 \left[\begin{array}{l} \pi \left(\frac{1}{2} - a\right) U b \dot{\alpha} + \pi b^2 \left(\frac{1}{8} + a^2\right) \ddot{\alpha} - \\ \dot{\alpha} \pi b \ddot{h} \end{array} \right] + 2\rho U b^2 \pi \left(a + \frac{1}{2}\right) C(\kappa) f(t), \quad (3.25)$$

$$L = -\rho b^2 (U \pi \dot{\alpha} + \pi \dot{h} - \pi b a \ddot{\alpha}) - 2\pi \rho U b C(\kappa) f(t), \quad (3.26)$$

where U is the airflow speed (the subscript ∞ is dropped for convenience in this section), ρ is the air density, $C(\kappa)$ is known as the Generalized Theodorsen function and $f(t)$ is given,

$$f(t) = U \alpha + \dot{h} + b \left(\frac{1}{2} - a\right) \dot{\alpha}. \quad (3.27)$$

Theodorsen’s function, $C(\kappa)$, represents the effects of vortex shedding at the trailing edge of the typical section (PENG; ZHU, 2009) and depends on the “reduced” frequency $\kappa = \omega b/U$. The reduced frequency is an indication of the relative “unsteadiness” of the flow (EDWARDS, 1977), and also introduces the limitation of harmonic motion (ALIGHANBARI, 1995; CONNER, 1996). A workaround for such a limitation was proposed in Wagner (1925). Instead of assuming that the typical section motion starts at $t = -\infty$ (as in the original Theodorsen’s model), it was assumed that the motion starts at $t = 0$, so that the aerodynamic formulation may be represented in the Laplace domain. Step inputs in the pitch angle were also assumed for the derivation of the circulatory loads. Finally, by a sum of elementary solutions, the unsteady aerodynamic loads associated with arbitrary motions could be determined. Alighanbari (1995) provides a comprehensive description of Wagner’s procedure. Another workaround is required, however, since the final expression of Wagner’s function is not convenient for numerical solution.

The exponential approximation of Jones (1938) to Wagner’s function,

$$\phi(s) \approx C_0 + C_1 e^{C_3 s} + C_2 e^{C_4 s}, \quad (3.28)$$

is commonly used in the literature (BISPLINGHOFF; ASHLEY; HALFMAN, 1955), and was also used in Edwards (1977). Although having no physical meaning, such equation reproduces the Wagner's function almost exactly, being widely accepted for engineering purposes (JONES, 1939; EDWARDS; ASHLEY; BREAKWELL, 1979)⁴. The coefficients are $C_0 = 2\mu_a$, $C_1 = -0.33\mu_a$, $C_2 = -0.67\mu_a$, $C_3 = -0.0455$ and $C_4 = -0.3$, where $s = Ut/b$ (THEODORSEN, 1935; JONES, 1938) and μ_a represents the additional (virtual) mass. For a typical section, $\mu_a = \pi$, and by normalizing by 2π , yields,

$$\phi(s) \approx 1 - 0.165e^{-0.0455s} - 0.335e^{-0.3s}. \quad (3.29)$$

By employing Eq. (3.29) along with additional treatments involving Duhamel's integral and Padé approximants (EDWARDS, 1977; ALIGHANBARI, 1995; TRICKEY, 2000), the $C(\kappa)f(t)$ term of Eqs. (3.25) and (3.26) may be replaced by,

$$C(\kappa)f(t) \approx (C_0 + C_1 + C_2)f(t) + C_3C_4(C_1 + C_2)x_{a_1} + (C_1C_3 + C_2C_4)\dot{x}_{a_2}, \quad (3.30)$$

where two aerodynamic states, x_{a_1} and x_{a_2} , are included in the model. Such states are given by,

$$\dot{\mathbf{x}}_a = \left(\frac{U}{b}\right) \mathbf{S}_1 \mathbf{x}_s + \mathbf{S}_2 \dot{\mathbf{x}}_s + \begin{bmatrix} -C_3C_4 \left(\frac{U^2}{b}\right) & (C_3 + C_4) \left(\frac{U}{b}\right) \end{bmatrix} \mathbf{x}_a, \quad (3.31)$$

where $\mathbf{x}_a = \{ x_{a_1} \ x_{a_2} \}^T$. Vectors \mathbf{S}_1 and \mathbf{S}_2 are related to the circulatory aerodynamics and are given in Appendix B.

Two terms are added to Eqs. (3.12) and (3.13), relating the structural domain to the aerodynamic domain. In matrix form, such terms are,

$$\mathbf{D} = \mathbf{R}\mathbf{S}_3, \quad (3.32)$$

where \mathbf{R} and \mathbf{S}_3 are also related to the circulatory aerodynamics (given in Appendix B).

Eqs. (3.31) and (3.32) are differentiated with respect to the dimensionless time defined in Section 3.2.1 and included in Eq. (3.21). The resulting (dimensionless) piezoaeroelastic model

⁴Jones (1939) depicts such a correspondence for several aspect ratios, including infinite ratio as in the case of a typical section. Edwards, Ashley and Breakwell (1979) provide a comparison with the exact solution.

is presented,

$$\begin{bmatrix} \mathbf{I} & \mathbf{0} & \mathbf{0} & \mathbf{0} \\ \mathbf{0} & \tilde{\mathbf{M}} & \mathbf{0} & \mathbf{0} \\ \mathbf{0} & \mathbf{0} & \tilde{\mathbf{I}} & \mathbf{0} \\ \mathbf{0} & \mathbf{0} & \mathbf{0} & \psi \end{bmatrix} \begin{Bmatrix} \mathbf{x}'_s \\ \mathbf{x}''_s \\ \mathbf{x}'_a \\ v' \end{Bmatrix} = \begin{bmatrix} \mathbf{0} & \mathbf{I} & \mathbf{0} & \mathbf{0} \\ -\tilde{\mathbf{K}} & -\tilde{\mathbf{B}} & \tilde{\mathbf{D}} & \Theta_e^T \\ \tilde{\mathbf{E}}_1 & \tilde{\mathbf{E}}_2 & \tilde{\mathbf{F}}_p & \mathbf{0} \\ \mathbf{0} & -\Theta_e & \mathbf{0} & -\lambda^{-1} \end{bmatrix} \begin{Bmatrix} \mathbf{x}_s \\ \mathbf{x}'_s \\ \mathbf{x}_a \\ v \end{Bmatrix} \quad (3.33)$$

where $\tilde{\mathbf{M}}$ is the inertial matrix, $\tilde{\mathbf{K}}$ is the stiffness matrix and $\tilde{\mathbf{B}}$ is the damping matrix. Such matrices have both structural and aerodynamic contributions, and are given,

$$\tilde{\mathbf{M}} = \mathbf{M} - \frac{\rho b^2}{m} \mathbf{M}_{nc}, \quad (3.34)$$

$$\tilde{\mathbf{K}} = \mathbf{K} - \frac{\rho b^2}{m} \left(\frac{U}{\omega_h b} \right)^2 \left(\mathbf{K}_{nc} + \frac{1}{2} \mathbf{R} \mathbf{S}_1 \right), \quad (3.35)$$

$$\tilde{\mathbf{B}} = \mathbf{B} - \frac{\rho b^2}{m} \left(\frac{U}{\omega_h b} \right) \left(\mathbf{B}_{nc} + \frac{1}{2} \mathbf{R} \mathbf{S}_2 \right), \quad (3.36)$$

where the non-circulatory contributions to mass, stiffness and damping, are \mathbf{M}_{nc} , \mathbf{K}_{nc} and \mathbf{B}_{nc} , respectively. The circulatory contributions are related to vectors \mathbf{R} , \mathbf{S}_1 and \mathbf{S}_2 . Matrices $\tilde{\mathbf{E}}_1$, $\tilde{\mathbf{E}}_2$ and $\tilde{\mathbf{F}}_p$ (in Eq. (3.33)) correspond to the two first-order equations of the aerodynamic model, and $\tilde{\mathbf{D}}$ is the dimensionless version of \mathbf{D} (in dimensionless time). All of the aerodynamic matrices (and vectors) are given in Appendix B. Such matrices are defined in terms of the Theodorsen constants, given in Appendix C.

Eq. (3.33) may be expressed as,

$$\mathbf{x}' = \mathbf{A} \mathbf{x}, \quad (3.37)$$

in which,

$$\mathbf{A} = \begin{bmatrix} \mathbf{0} & \mathbf{I} & \mathbf{0} & \mathbf{0} \\ -\tilde{\mathbf{M}}^{-1} \tilde{\mathbf{K}} & -\tilde{\mathbf{M}}^{-1} \tilde{\mathbf{B}} & \tilde{\mathbf{M}}^{-1} \tilde{\mathbf{D}} & \tilde{\mathbf{M}}^{-1} \Theta_e^T \\ \tilde{\mathbf{I}}^{-1} \tilde{\mathbf{E}}_1 & \tilde{\mathbf{I}}^{-1} \tilde{\mathbf{E}}_2 & \tilde{\mathbf{I}}^{-1} \tilde{\mathbf{F}}_p & \mathbf{0} \\ \mathbf{0} & -\psi^{-1} \Theta_e & \mathbf{0} & -(\psi \lambda)^{-1} \end{bmatrix}, \quad (3.38)$$

and $\mathbf{x} = \{ \mathbf{x}_s \quad \mathbf{x}'_s \quad \mathbf{x}_a \quad v \}^T$.

In the next section, Eq. (3.37) is modified to replace the linear torsional spring of the pitch

DOF by SMA helical springs.

3.4 Typical Section Model with SMA Springs

Fig. 7 displays a schematic model of a typical aeroelastic section with SMA helical springs at the pitch DOF. A rigid rod (assumed without mass) is attached to the elastic axis. The SMA springs are perpendicularly attached to the ends of that rod. The other ends of the SMAs are assumed fixed with respect to pitch motions (yielding spring deflections) but move along with plunge motions. The SMAs are attached at a distance w from the elastic axis.

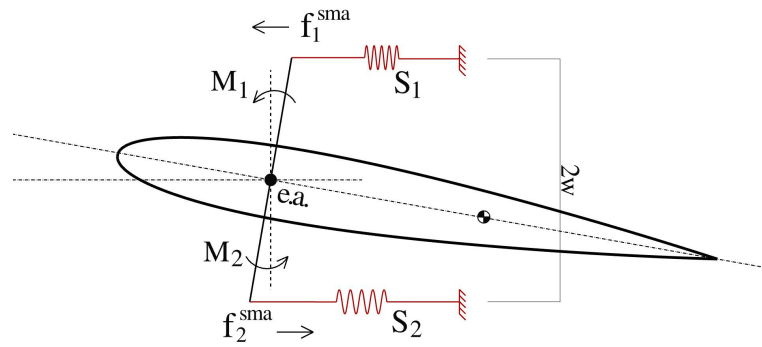


Figure 7 – A schematic model of a typical aeroelastic section with SMA helical springs at the pitch DOF.

The equations of motion are rewritten according to the configuration of Fig. 7 as,

$$r_{\alpha}^2 \alpha'' + x_{\alpha} \bar{h}'' + \zeta_{\alpha} \alpha' + \vartheta(\alpha, \xi_1, \xi_2) = \bar{M}_{\alpha} \quad (3.39)$$

$$x_{\alpha} \alpha'' + \mu \bar{h}'' + \zeta_h \bar{h}' + \bar{h} - \chi v = -\bar{L} \quad (3.40)$$

$$\psi v' + \lambda^{-1} v + \chi \bar{h}' = 0, \quad (3.41)$$

where the (dimensionless) elastic restoring moment term of Eq. (3.18), $\eta_{\alpha}^2 r_{\alpha}^2 \alpha$, is replaced by $\vartheta(\alpha, \xi_1, \xi_2)$. The latter is the (dimensionless) resulting moment due to the SMA springs, and is given by,

$$\vartheta(\alpha, \xi_1, \xi_2) = \frac{w}{mlb^2 \omega_h^2} [-f_1^{\text{sma}}(\alpha, \xi_1) + f_2^{\text{sma}}(\alpha, \xi_2)], \quad (3.42)$$

where subscript 1 and 2 denote the SMA springs S_1 and S_2 , respectively. Thus, ξ_i represents the martensitic fraction of each SMA spring (i assumes 1 or 2). This notation is also used for any other SMA property which depends on the martensitic fraction. It is also worth mentioning that the distance w may change to adjust the resulting moment. This will be useful later in Chapters 5 and 6 to obtain a moment which is equivalent to that due to the (ideal and linear) torsional spring defined in Fig. 5 (of stiffness k_α) when different SMA springs are considered. In such a case, the distance w may be estimated by,

$$w = \sqrt{\frac{k_\alpha l}{2k(\xi)}}. \quad (3.43)$$

Based on the SMA spring model described in Section 2.4.2, the spring forces are estimated by,

$$f_i^{\text{sma}}(\alpha, \xi_i) = k(\xi_i)y_i(\alpha) + Y(\xi_i), \quad i = 1 \text{ or } 2, \quad (3.44)$$

where the equivalent stiffness $k(\xi)$ of an SMA spring was previously defined in Eq. (2.26). Moreover, $y_i(\alpha)$ denotes the axial deflection of the SMA springs. For small pitch angles, the spring deflections may be approximated by,

$$y_1(\alpha) \cong y_0 - w\alpha \quad (3.45)$$

$$y_2(\alpha) \cong y_0 + w\alpha, \quad (3.46)$$

where y_0 is an initial deflection due to the presence of mechanical preload.

In Eq. (3.44), $Y(\xi)$ accounts for the effects of phase transformation on the spring force. Based on the equations of Section 2.4.2 (mostly on Eq. (2.30)), this term is given by,

$$Y(\xi) = -\frac{\pi r^3}{2R} G(\xi) \xi \varepsilon_{\text{res}}. \quad (3.47)$$

The SMA model is complete at this point and may be included into the (linear) state-space model of Eq. (3.37). The resulting (and nonlinear) state-space equation is,

$$\mathbf{x}' = \mathbf{A}\mathbf{x} + \mathbf{a}\mathbf{x}_c, \quad (3.48)$$

where,

$$\mathbf{a} = \begin{bmatrix} \mathbf{0} & \mathbf{0} & \mathbf{0} & \mathbf{0} \\ -\mathbf{M}^{-1}\mathbf{K}_1 & \mathbf{M}^{-1}\mathbf{K}_2 & \mathbf{0} & \mathbf{0} \\ \mathbf{0} & \mathbf{0} & \mathbf{0} & \mathbf{0} \\ \mathbf{0} & \mathbf{0} & \mathbf{0} & \mathbf{0} \end{bmatrix}, \quad (3.49)$$

and

$$\mathbf{x}_c = \left\{ y_1(\alpha) \quad 1 \quad y_2(\alpha) \quad 1 \quad 0 \quad 0 \quad 0 \right\}^T. \quad (3.50)$$

Matrices \mathbf{K}_i are given by,

$$\mathbf{K}_i = \frac{w}{mlb^2\omega_h^2} \begin{bmatrix} k(\xi_i) & Y(\xi_i) \\ 0 & 0 \end{bmatrix}, \quad i = 1 \text{ or } 2. \quad (3.51)$$

Since the torsional stiffness terms related to the SMAs are included in matrix \mathbf{a} , the term related to the ideal torsional spring is excluded from Eq. (3.23) for consistency, yielding,

$$\mathbf{K}_s = \begin{bmatrix} 0 & 0 \\ 0 & 1 \end{bmatrix}. \quad (3.52)$$

3.5 Iterative Procedure for the Determination of the Mechanical Stress and Martensitic Fraction

In the previous section, the aeroelastic model was modified to include the SMA springs to the pitch DOF of the system. The pseudoelastic hysteresis of the SMAs is related to phase transformations which affect the martensitic fraction. The change from austenite to martensite is induced by stress due to mechanical loading, increasing the martensitic fraction. During mechanical unloading, internal stresses are generated by an attempt of shape recovery related to the austenitic transformation (assuming $T \geq A_f$), thus decreasing the martensitic fraction. An attempt of solving the constitutive equation (Eq. (2.16)) for the shear stress in terms of the shear strain, however, results in a mutual dependence between stress and martensitic fraction, $\sigma(\xi) = f(\xi(\sigma))$.

This section describes the method employed in this work to determine the (shear) stress and the martensitic fraction of the SMAs. Since the same method is applied for both SMA springs of Fig. 7, the distinction between the springs (S_i , where $i = 1$ or 2) is omitted. The method assumes that the stress and the martensitic fraction are initially unknown. On the other hand, the pitch angle of the typical section is known at each time step of the solution. By using Eqs. (3.45) and (3.46), the spring deflections are calculated in terms of the pitch angle. By also assuming a fully austenitic initial phase (thus, $\xi = 0$) and rewriting Eq. (2.29) as,

$$\gamma(y_i, \alpha) = \frac{r}{2\pi R^2 N} y_i(\alpha), \quad (3.53)$$

the shear strain at the perimeter of the coiled SMA wire may be estimated in terms of the spring deflection. By assuming, *a priori*, the linear relation of Eq. (2.21) (Hooke's law for torsion, $\tau = G\gamma$), the corresponding shear stress may be estimated. The computed value, however, is used only for verification purposes (not for determining the stress state of the SMA). It is used to check if the SMA is in a phase transformation condition (nonlinear regime). A stress-induced phase transformation is detected if,

$$\tau_s^M \leq \tau \leq \tau_f^M \quad \text{and} \quad \dot{\xi} > 0, \quad (3.54)$$

while an austenitic phase transformation is detected if,

$$\tau_s^A \geq \tau \geq \tau_f^A \quad \text{and} \quad \dot{\xi} < 0, \quad (3.55)$$

at each time step of the aeroelastic solution.

By considering that one of the above conditions is true, the next step is the computation of possible values for the martensitic fraction (by using an iterative procedure). If Eq. (3.54) is true, then Eq. (2.8) is used to compute the martensitic fraction which corresponds to different values of shear stress in the range,

$$\tau_{\text{teste}} = [\tau_s^M, \tau_f^M] \quad (3.56)$$

and if Eq. (3.55) is true, then Eq. (2.11) is used for the range,

$$\tau_{\text{teste}} = \left[\tau_s^A, \tau_f^A \right] \quad (3.57)$$

while pairs of shear stress and martensitic fraction, along with the shear strain obtained by Eq. (3.53) and also the current state of the SMA, are verified in the constitutive equation (Eq. (2.17)). The pair which satisfies that equation represents the current shear stress and martensitic fraction of the SMA. The martensite-dependent properties of the SMA may then be updated.

If no phase transformation is taking place (*i.e.*, both conditional Eqs. (3.54) and (3.55) are false), the SMA spring behavior is assumed linear elastic as that of a conventional spring (made of an inactive material such as steel). In such a case, no special treatment (the iterative procedure described above) is necessary because there is no change in the martensitic fraction.

*Effects of the SMA Pseudoelastic
Hysteresis on the Aeroelastic Behavior of
the Typical Section*

This chapter reports three case studies using the previously described models. In the first case study, the constitutive behavior of an SMA is discussed. In the second case, the effect of preloaded SMA springs on the aeroelastic behavior of the typical section at the linear flutter speed is investigated. In the third case study, the effect of preloaded SMA springs on the aeroelastic behavior of the typical section in the post-flutter regime is investigated. The SMA parameters shown in Table 1 are used in the simulations of all cases. The parameters are based on Aguiar et al. (2013) and are estimated for a commercially available SMA spring that is suitable for the physical dimensions of an existing experimental typical section described in Sousa et al. (2011). Most of this chapter (excepting the last section) describes the model behavior assuming that the shear strain, shear stress and martensitic fraction are homogeneous across the cross-section of the coiled SMA wire. The last section discusses the effects of different cross-sectional assumptions.

Table 1 – SMA constitutive properties.

Property	Value	Unit
M_f	302	K
M_s	315	K
A_s	316	K
A_f	331	K
C_M	4	MPa·K ⁻¹
C_A	6	MPa·K ⁻¹
σ_s^{\min}	100	MPa
σ_f^{\min}	170	MPa
ε_{res}	6.7	%
G_M	11.5	GPa
G_A	14.5	GPa
μ_P	0.3	–

4.1 Simulation of the Constitutive Behavior of an SMA Element

In this case study, the SMA behavior is described for different conditions of the material temperature and shear stress. The effect of temperature on the transformation stresses was described in Section 2.2.2 and is displayed in Fig. 8 for the SMA properties of Table 1. The stress-induced phase transformation starts when $\tau \geq \tau_s^{\min}$ (where $\tau_s^{\min} = \sigma_s^{\min} / \sqrt{3}$) and completes only for $\tau \geq \tau_f^{\min}$ (where $\tau_f^{\min} = \sigma_f^{\min} / \sqrt{3}$). The critical stresses are constant when $T \leq M_s$. For $T > M_s$, the critical stresses increase with increasing temperature and a linear relation is assumed.

Fig. 9 shows the shear stress-strain behavior for different temperatures. In all cases, 100% initial austenitic phase is assumed. The curves for $T < A_f$ exhibit a residual strain after a complete unloading, which is related to the shape memory effect. The hysteretic behavior for $T \geq A_f$ is related to pseudoelasticity. As expected, the hysteresis loop moves upward in the stress-strain plane as the temperature increases. Additionally, the area inside the hysteresis loop decreases with increasing temperature due to higher values of C_A with respect to C_M (see Table 1).

The particular case of $T = A_f$ (in Fig. 9) is detailed in Fig. 10. The stress represents a

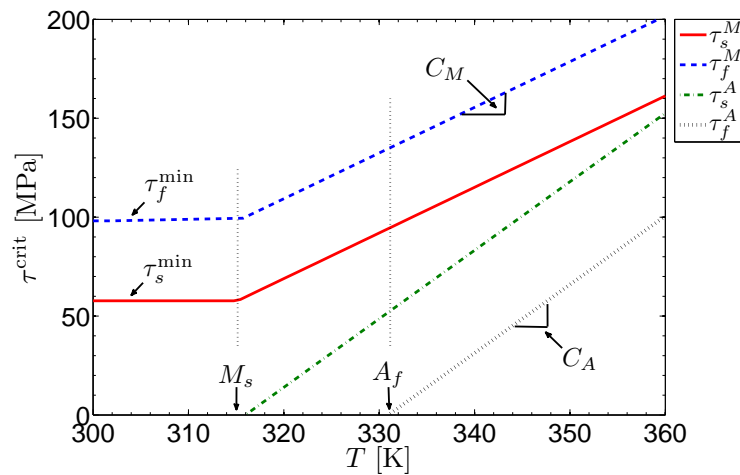


Figure 8 – Critical shear stresses for phase transformation: constant for $T \leq M_s$ and a linear function of temperature for $T > M_s$.

mechanical loading-unloading cycle. As the stress increases from τ_s^M up to τ_f^M , the martensite fraction grows from 0% to 100% (Fig. 10(a)). After the complete phase transformation, the SMA mechanical properties remain unchanged. During mechanical unloading, the austenitic phase is recovered when the stress decreases from τ_s^A to τ_f^A . The SMA is fully austenite and exhibits no residual deformation when completely unloaded. The corresponding change in shear modulus is shown in Fig. 10(b). The change in the material properties and increase of the inelastic strain are related to the hysteretic behavior shown in Fig. 9, which is related to the energy dissipation.

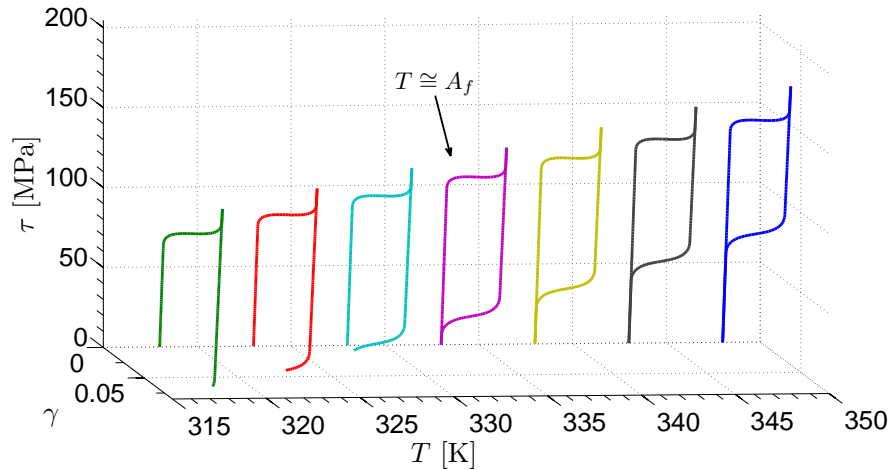


Figure 9 – Shear stress-strain behavior for different temperature conditions. The shape memory effect is represented by curves such that $T < A_f$ (with residual strain) and the pseudoelastic effect is represented by curves such that $T \geq A_f$ (with no residual strain).

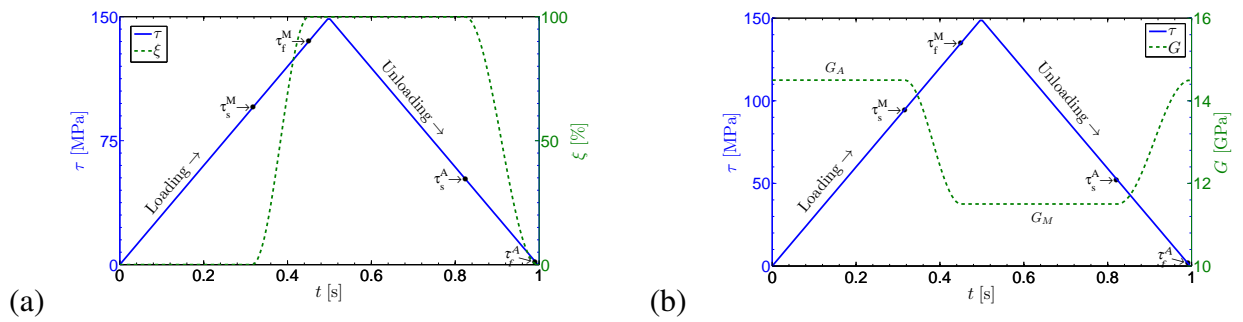


Figure 10 – Mechanical loading-unloading cycle and corresponding (a) martensite fraction and (b) shear modulus for $T = A_f$ (arbitrary loading rate).

4.2 Effect of Pseudoelastic Hysteresis on the Aeroelastic Behavior of a Typical Section

The effect of the pseudoelastic hysteresis of SMA springs on the aeroelastic behavior of a typical section is investigated and discussed. The material properties provided in Table 1 and the properties of the typical section given in Table 2 are used. The dimensionless parameters of Table 2 are based on dimensional (physical) parameters from Sousa et al. (2011), who considered an airfoil whose semichord length is 0.125 m. The SMA coil springs considered have 0.95 mm wire diameter, 8 mm coil diameter and 16.5 active coils. The SMA springs are 36.7 mm long with the minimum allowed length of 20 mm. The SMA temperature is assumed constant at 331 K in all simulations. At such a temperature, the SMA is fully austenite for a stress-free state.

The corresponding stiffness of each coil spring is $k = 175 \text{ N}\cdot\text{m}^{-1}$ (using $w = 85 \text{ mm}$, please check Fig. 7). The critical stresses for the phase transformation are $\tau_s^M = 95 \text{ MPa}$, $\tau_f^M = 135 \text{ MPa}$, $\tau_s^A = 52 \text{ MPa}$ and $\tau_f^A = 0 \text{ MPa}$ (see Fig. 8). In all simulations the initial condition is assumed a plunge displacement ($h_0 = 10 \text{ mm}$ or $\bar{h}_0 = 0.08$).

Table 2 – Aeroelastic parameters used in the simulations.

Parameter	Value	Unit
l	0.5	m
b	0.125	m
c	-0.5	–
x_α	0.256	–
m	1.542	$\text{kg}\cdot\text{m}^{-1}$
m_f	2.548	$\text{kg}\cdot\text{m}^{-1}$
I_α	0.0072	$\text{kg}\cdot\text{m}$
k_α	5.08	$\text{N}\cdot\text{rad}^{-1}$
k_h	4200	$\text{N}\cdot\text{m}^{-2}$
ζ_α	0.088	–
ζ_h	0.0035	–

4.2.1 Effect of Pseudoelastic Hysteresis on the Aeroelastic Behavior of the Typical Section at the Linear Flutter Speed

In this case study, the effect of pseudoelastic hysteresis on the aeroelastic behavior of the typical section at the linear flutter speed is investigated. It is important to remember that the linear steel spring usually employed in the pitch DOF of a typical section was replaced by a pair of SMA springs. When linear steel springs are considered in the typical section the usual linear aeroelastic behavior is verified: the typical section is stable for airflow speeds smaller than the linear flutter speed and unstable for airflow speeds larger than the linear flutter speed. The same linear aeroelastic behavior is verified when no stress-induced phase transformations are achieved in the SMA springs replacing a linear steel spring. This way, the term “linear flutter speed” refers to the flutter boundary of a typical section with steel springs or the flutter boundary of the modified typical section (with SMA springs) when no stress-induced phase transformations are achieved.

Fig. 11 displays the flutter boundary, pitch and plunge displacements as well as shear stress

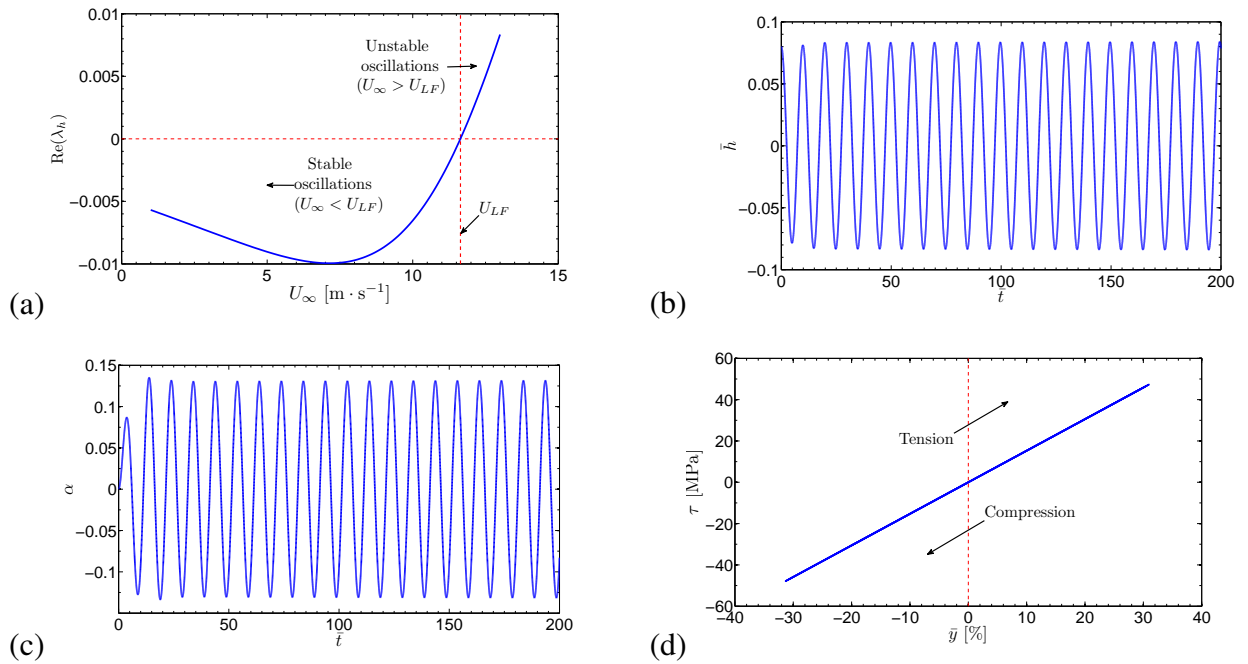


Figure 11 – Real part of the plunge DOF eigenvalue for increasing airflow speed (a), (b) dimensionless plunge DOF time response, (c) dimensionless pitch DOF time response, (d) shear stress versus change in the length of SMA spring S_1 .

of each SMA spring introduced in the pitch DOF. Fig. 11(a) shows the real part of the eigenvalue for the plunge DOF (λ_h) for increasing airflow speed (U_∞). The linear flutter speed (U_{LF}) is predicted as $11.6 \text{ m} \cdot \text{s}^{-1}$, in agreement with Sousa et al. (2011). The dimensionless plunge and pitch time histories at the linear flutter speed are shown in Figs. 11(b) and (c). The pitch SMA springs are subjected to deformations due to the pitch displacement, reaching the maximum length of 47.7 mm and minimum length of 25.7 mm (larger than the minimum allowed length of 20 mm). The maximum achieved shear stress of each coil spring in the pitch DOF is (Fig. 11(d)), which is lower than the critical stress for the onset of the phase transformation (95 MPa). Therefore, the typical section with SMA springs behaves exactly as a linear aeroelastic system (since stress-induced phase transformations are not achieved). The amplitudes of oscillation (the pitch displacement in particular) would be excessively large in order to reach the critical stress value. Therefore, a set of preload values is considered ($f_0 = 1.5, 2.0, 2.5, 3.0, 3.5, 4.0$ and 4.5 N symmetrically for both springs) in this work to fully use the damping capability of SMAs and investigate its effect on the aeroelastic behavior of the typical section.

The aeroelastic behavior of the typical section at the linear flutter speed with increasing

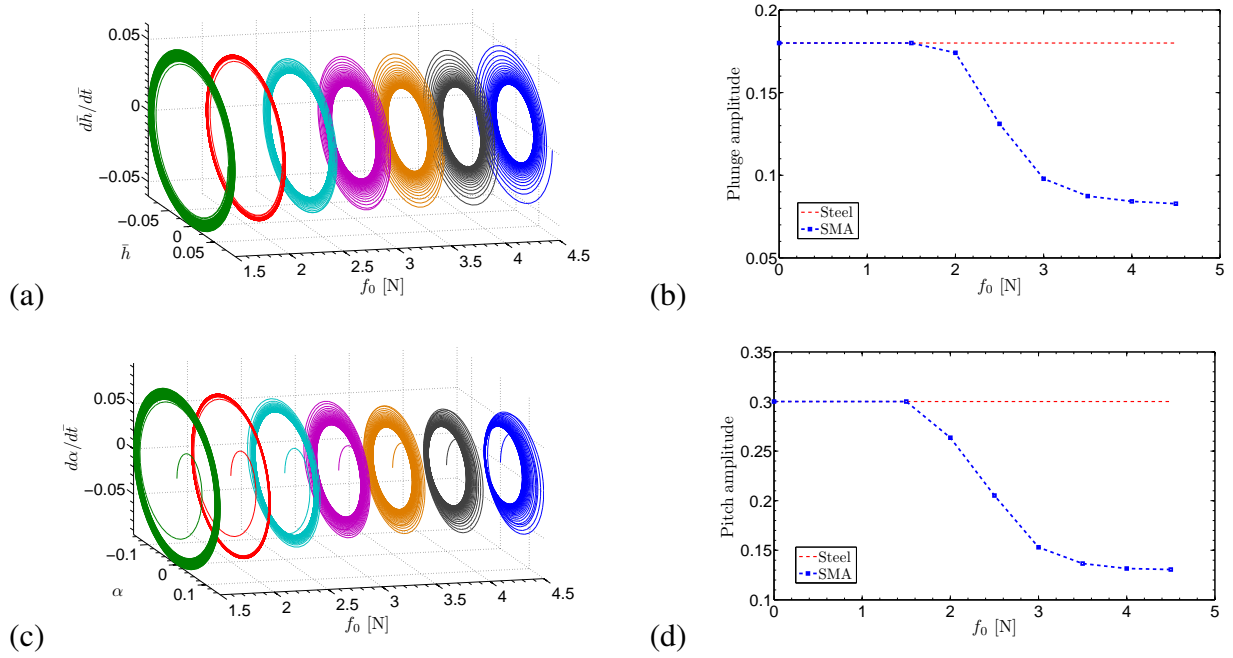


Figure 12 – The aeroelastic displacements decrease as the preload increases and contributes more significantly to the occurrence of phase transformation – (a) plunge DOF phase projections, (b) plunge amplitude (reduction of 54%), (c) pitch DOF phase projections, (d) pitch amplitude (reduction of 56%). In (b) and (d) the amplitudes for a linear (elastic) steel spring with equivalent effective stiffness is shown for comparison.

preload is shown in Fig. 12. Fig. 12(a) to (d) shows that both plunge and pitch displacements decrease with increasing preload on the SMA springs (for preload values larger than 1.7 N). For the preload value of 4.5 N, the plunge amplitude is 54% smaller than the plunge amplitude of the typical section with no preload on the SMA springs (Fig. 12(b)) and the pitch amplitude is 56% smaller than the pitch amplitude of Fig. 12(d). However, the pitch and plunge DOFs become less sensitive to the variations in the preload values for $f_0 > 4$ N.

For comparison purposes, the plunge and pitch amplitudes of a typical section with a pair of steel springs in pitch DOF (that gives the same pitch elastic moment of the SMA springs with no preload) is also presented in Figs. 12(b) and (d). Pitch and plunge amplitudes are insensitive to applied preload on the steel springs. Moreover, the same mechanical outputs are obtained for preload values smaller than 1.5 N of both cases. Effects due to preload other than stress increase (which would be expected also for steel springs, *e.g.*, friction) are neglected because of the low forces involved.

The variation of the resulting shear stress (due to preload and pitch displacement contributions) with increasing preload level is shown in Fig. 13. The pitch angle required for stress-induced phase transformation (leading to pseudoelastic effect) decreases with increasing preload value. For preload values larger than 2 N, the resulting shear stress is enough to induce the onset of forward phase transformations ($\tau > \tau_s^M$). The transformations lead to a hysteretic behavior of the SMA springs and, consequently, to the aeroelastic behavior presented in Fig. 12. Very large pitch angles would be required for stress-induced phase transformation in the range $0 \leq f_0 \leq 1.5$ N. Consequently, the typical section with SMA springs behaves as a linear aeroelastic system (as well as the one with steel springs) for this preload range. For $f_0 \geq 2$ N, the resulting shear stress is almost constant (and slightly larger than τ_s^M , the dotted line in Fig. 13) since the shear stress is quite constant when the martensitic plateau (transformation region) is reached. In addition, one should note that the amount of shear stress due to pitch displacement is the same for $0 \leq f_0 \leq 2$ N and decreases with increasing preload value since the aeroelastic displacements decrease for preload values larger than 2 N (Fig. 12). For $f_0 \geq 4$ N, the resulting shear stress is almost fully due to preload on the SMA spring.

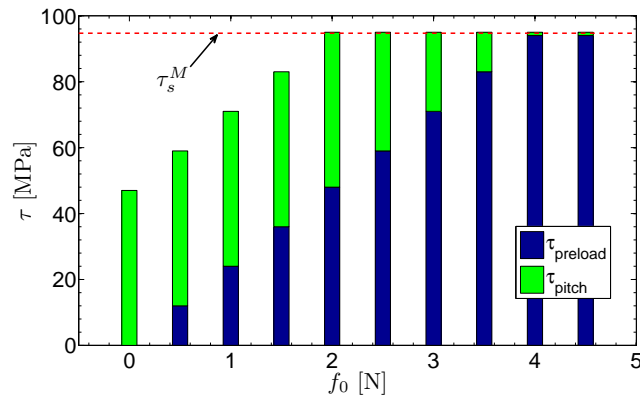


Figure 13 – Steady-state shear stress split into two portions: one due to preload and another due to pitch displacement at its maximum at the linear flutter speed (phase transformation occurs for $f_0 \geq 2$ N). The resulting shear stress exhibits no expressive increase as the SMA springs operate in the transformation region.

The particular case of $f_0 = 3$ N is shown in Fig. 14 (the case with no preload, $f_0 = 0$ N, is also shown for reference). Figs. 14(a) and (b) show the dimensionless plunge and pitch time histories obtained slightly above the linear flutter speed of Fig. 11(a). The unstable behavior

for $f_0 = 0$ N (growing oscillations) is converted to LCOs when the preload value is increased to 3 N. Fig. 14(c) to (f) shows the corresponding change in the length of SMA spring S_1 , the shear stress, the martensite fraction and the stiffness (due to the change in the shear modulus), respectively. Fig. 14(g) shows the shear stress against the length of the SMA spring.

Figs. 15(a) and (b) show a detail of the shear stress and a detail of the corresponding martensite fraction, respectively, for the case of Fig. 14 ($f_0 = 3$ N). Critical stresses are displayed and an incomplete phase transformation can be observed.

Fig. 12(c) shows that the equilibrium position of the steady-state pitch response changes with increasing preload. By increasing the preload value, the critical stress for a complete reverse phase transformation (τ_f^A) (unloading) is never reached. After the first forward phase transformation the martensitic fraction is always larger than zero. Additionally, the SMA springs undergo different stress states due to the initial condition ($\bar{h}_0 = 0.08$ or $h_0 = 10$ mm). Although symmetric springs with respect to the chord line are assumed, an imbalance in the martensite fraction occurs. Since the elastic modulus of SMAs depends on the martensite fraction, the springs exhibit a small difference in stiffness, which leads to different equilibrium positions. However, it is important to remember that the previously discussed aeroelastic behavior (Figs. 12 and 13) is only related to the damping capabilities of the preloaded SMA springs (not due to the small stiffness variation). Fig. 16 confirms such a behavior by showing the pitch response for $f_0 = 4.5$ N and two different initial conditions, namely $\bar{h}_0 = 0.08$ and $\bar{h}_0 = -0.08$.

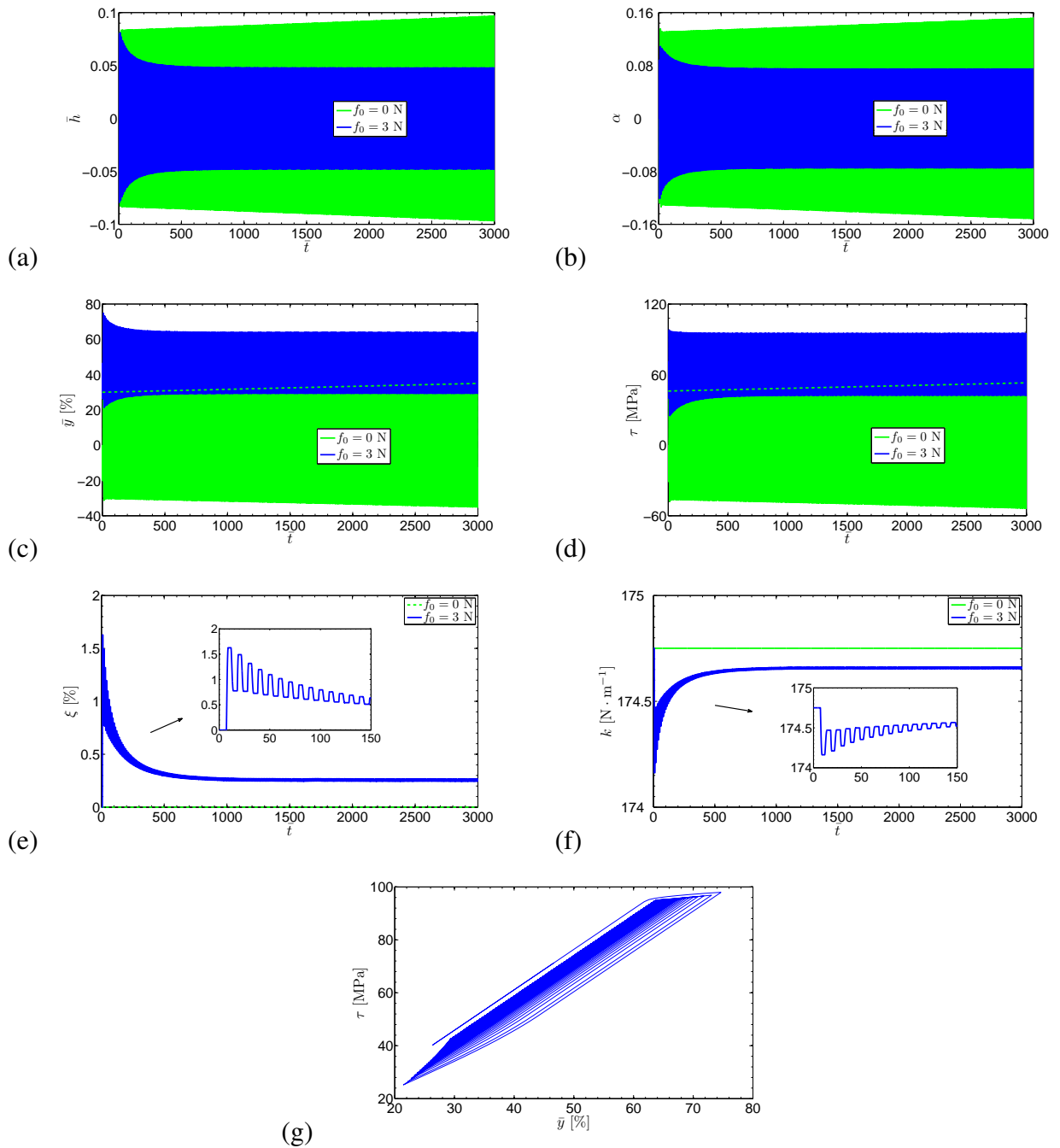


Figure 14 – Aeroelastic response and material behavior for $f_0 = 3 \text{ N}$ and $U_\infty = U_{LF}$ – (a) plunge displacement, (b) pitch displacement, (c) change in the length of SMA spring S_1 , (d) shear stress, (e) martensite fraction, (f) stiffness and (g) shear stress versus change in the length of SMA spring S_1 . The case with no preload ($f_0 = 0 \text{ N}$) is shown for comparison.

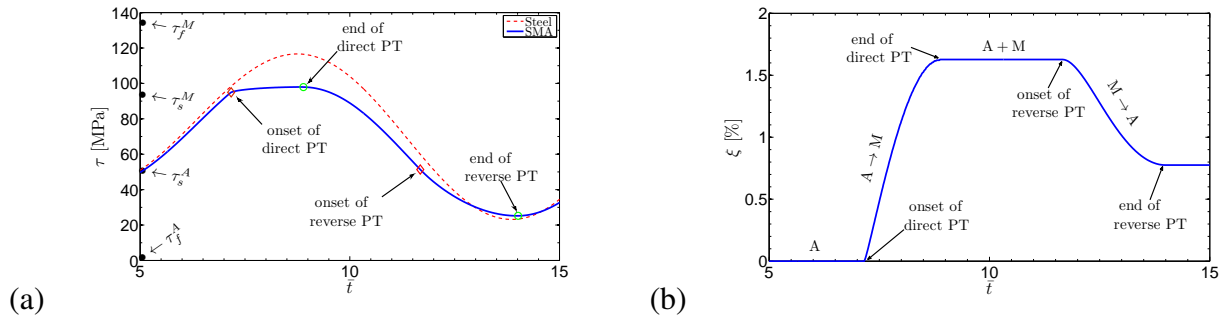


Figure 15 – Detail of the transient response for $f_0 = 3$ N and $U_\infty = U_{LF}$ – (a) shear stress, (b) martensite fraction. Both forward and reverse phase transformations are incomplete. A and B stand for austenite and martensite, respectively.

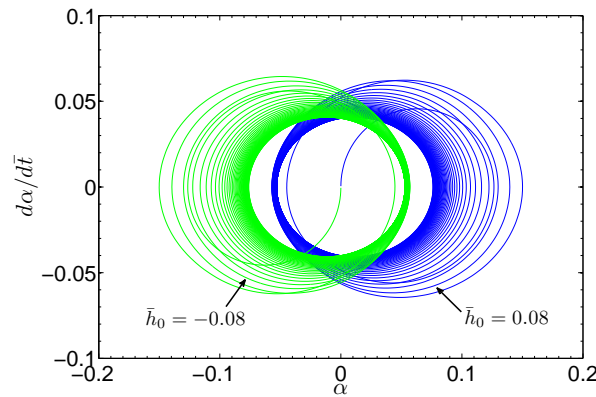


Figure 16 – Pitch response for $f_0 = 4.5$ N and different directions of the initial condition applied to the plunge DOF ($\bar{h}_0 = 0.08$ and $\bar{h}_0 = -0.08$)

4.2.2 Effect of Pseudoelastic Hysteresis on the Aeroelastic Behavior of the Typical Section at the Post-Flutter Regime

The effect of pseudoelastic hysteresis of SMA springs on the aeroelastic behavior of the typical section at the linear flutter boundary was discussed in the previous case study. Pitch and plunge amplitudes decrease with increasing preload on the SMA springs. Also, unstable aeroelastic motions at an airflow speed slightly above the linear flutter speed were converted to LCO due to the nonlinear (hysteretic) response of the preloaded SMA springs (above certain preload value). The presence of nonlinearities in aeroelastic systems often results in bifurcations with LCOs above or below the linear flutter speed (DOWELL, 2015). Sometimes, nonlinearities are welcome in aeroelastic system since the catastrophic linear flutter behavior above the linear flutter speed can be replaced by LCOs of acceptable amplitudes. Therefore, this case study

investigates the effect of pseudoelastic hysteresis of preloaded SMA springs on the aeroelastic behavior of the typical section at the post-flutter regime. The same set of preload values of Section 4.2.1 is considered. Due to the limitations of the aerodynamic model employed to calculate the aerodynamic loads (linear aerodynamics that is valid for small mechanical motions), the aeroelastic behavior is investigated in this case study for airflow speeds ranging from the linear flutter speed up to $15 \text{ m}\cdot\text{s}^{-1}$ (about 30% above the linear flutter speed). In this range, the maximum plunge displacement is always smaller than twice the initial condition in the plunge ($\bar{h} < 2\bar{h}_0$; $\bar{h} = 0.08$), and the pitch displacement is smaller than 0.2 radians (for specific preload value).

Fig. 17(a) shows the variation of the maximum airflow speed that satisfies the limiting solution (in terms of pitch and plunge amplitudes) with increasing preload on the SMA springs. Fig. 17(b) shows the resulting shear stress (due to preload induced stress and pitch-induced stress) for each maximum airflow speed that satisfies the limiting solution of Fig. 17(a). Linear aeroelastic behavior is verified for preload values smaller than 1.5 N since stress-induced transformations are not verified for this range of preloads and pitch displacement. Therefore, the typical section is unstable for any airflow speed higher than $11.6 \text{ m}\cdot\text{s}^{-1}$ (the linear flutter speed) and stable for airflow speeds below the linear flutter speed. Persistent and bounded oscillations of acceptable amplitude (LCOs) are obtained for the gray area of Fig. 17(a). For airflow speeds larger than the limiting solution, the response amplitude becomes very large (LCOs of large amplitudes) and the aerodynamic model is not valid. Since the aeroelastic displacements at the post-flutter regime are larger than the displacements at the flutter boundary (since the aerodynamic loads increase with airflow speed), the shear stress contribution due to pitch displacement is slightly larger in Fig. 17(b) than in Fig. 13 (τ exceeds the τ_s^M line) for preload values larger than 1.5 N (nonlinear aeroelastic behavior). The resultant shear stress is also constant for larger preload values due to the same reasons discussed in the previous case study.

Fig. 18(a) to (f) shows the time histories of dimensionless plunge displacement, dimensionless pitch displacement, elongation of SMA spring (S_1), shear stress, martensitic fraction, and stiffness of pitch DOF for $f_0 = 3 \text{ N}$ and $U_\infty = 14 \text{ m}\cdot\text{s}^{-1}$. The elongation of the spring (Fig.

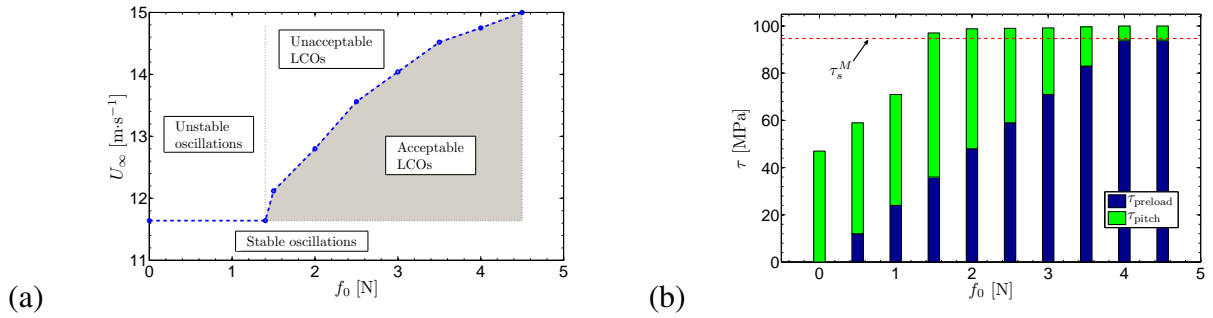


Figure 17 – Airflow speeds at which persistent oscillations with maximum acceptable amplitudes occur for increasing preload (a); resulting shear stress (b) – the contribution due to preload is the same as in Fig. 13, whereas the pitch contribution is more expressive due to larger aeroelastic displacements at higher airflow speeds (on the left).

18(c)) and the corresponding shear stress (Fig. 18(d)) show that stress-induced phase transformation is achieved due to the preload condition at the airflow speed of $14 \text{ m}\cdot\text{s}^{-1}$. Although the martensitic fraction (Fig. 18(e)) is approximately 3%, LCOs of acceptable amplitude are verified in the post-flutter regime due to the nonlinear pseudoelastic behavior of the SMA springs (Fig. 18(g)).

Fig. 19 shows the variation of the shear stress of one of the SMA pitch springs for increasing preload levels at the linear flutter speed and also at the highest airflow speed for LCOs of acceptable amplitude (limiting solution of Fig. 17(a)) under a post-flutter condition. The springs (S_1 and S_2 in Fig. 7(b)) are under loading-unloading conditions due to the harmonic motion of the typical section at the flutter speed or harmonic motion of LCOs in post-flutter condition. The upper boundaries in Fig. 19 (preload-induced stress plus pitch displacement-induced stress) are related to forward phase transformations (loading stages). In such case, the elongation of spring S_1 is due to pitch displacements in the opposite direction to the preload. The lower boundaries are related to reverse phase transformations (unloading stages) and the resultant stress is the preload induced stress minus the stress from the negative extreme of the pitch displacement (maximum spring shortening). During unloading stages, the pitch motion has the same direction of the preload. Depending on the preload level, the spring can be under tension for the entire pitch range. Therefore, positive stress values may also be observed in the lower boundaries of Fig. 19 as the preload increases. The full recovery of the austenitic phase is not observed in the

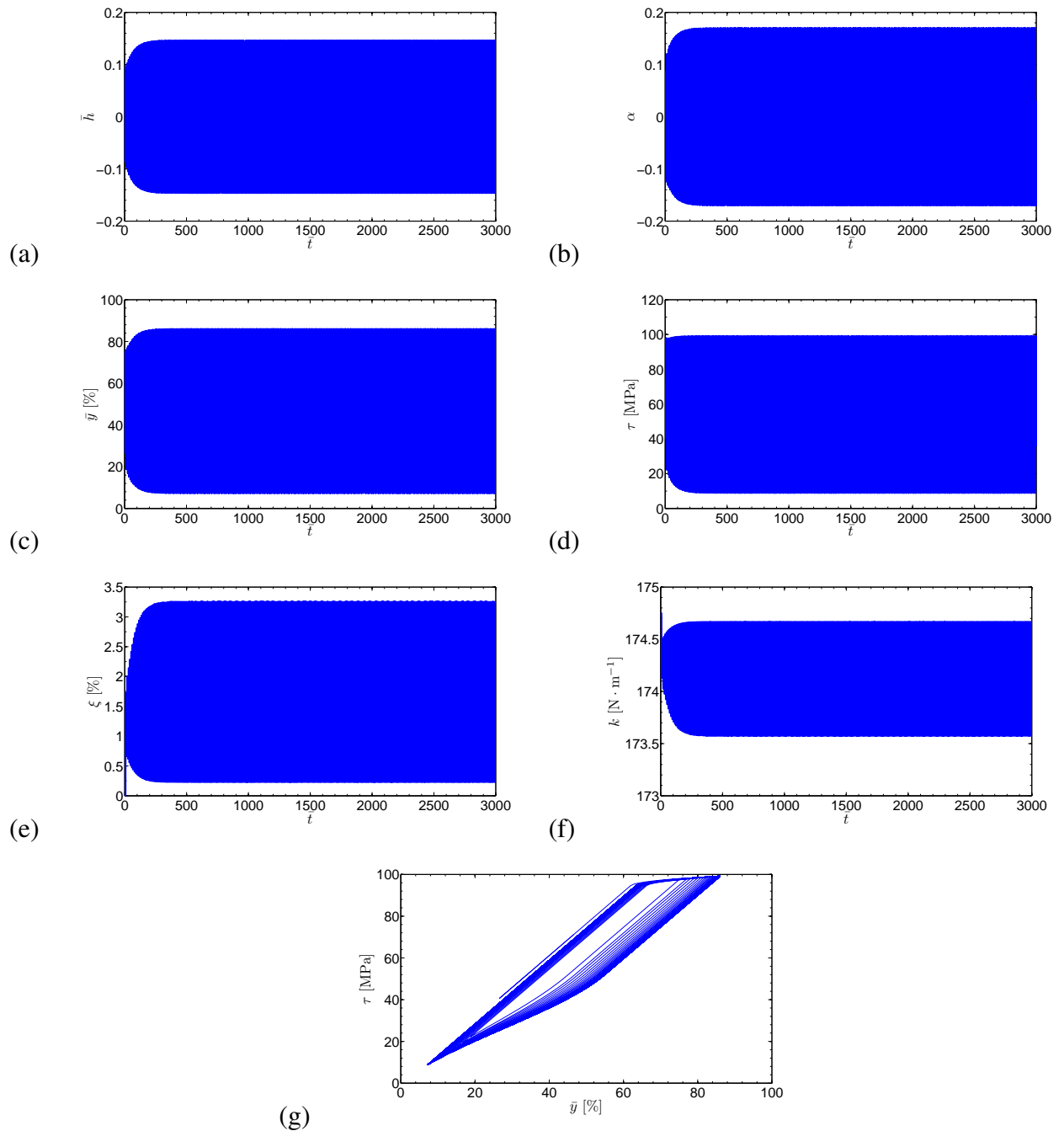


Figure 18 – Aeroelastic response for $f_0 = 3 \text{ N}$ and $U_\infty = 14 \text{ m} \cdot \text{s}^{-1}$ – (a) plunge displacement, (b) pitch displacement, (c) deformation of SMA spring S_1 , (d) shear stress, (e) martensitic fraction, (f) spring stiffness, (g) shear stress versus change in the length of spring S_1 .

unloading stages of Fig. 19 due to the positive stresses related to larger preload values.

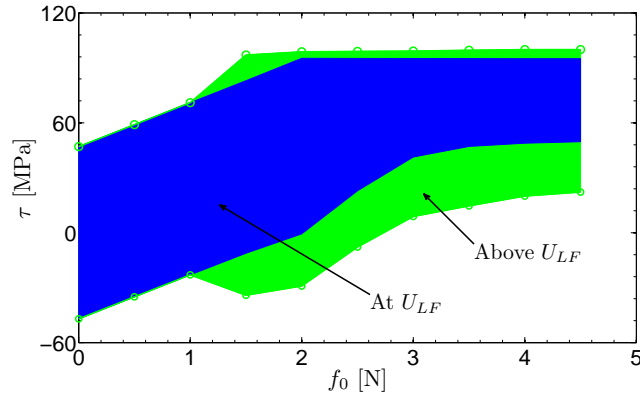


Figure 19 – Shear stress for SMA spring S_1 for different preload levels and $U_\infty \geq U_{LF}$. Upper boundaries are related to the forward phase transformation (loading cycles) and lower boundaries are related to the reverse phase transformation (unloading cycles).

Fig. 20(a) shows the martensitic fractions of springs S_1 and S_2 and Fig. 20(b) shows the stiffness of each spring obtained at both linear flutter speed and limiting solution of each preload in the post-flutter regime. The stiffness of the each spring is identical in the post-flutter regime for the range of preloads considered. At the linear flutter speed, the martensitic fraction and the stiffness of S_1 and S_2 springs are different for higher preload values. Since the pitch and plunge displacements increase with increasing airflow speed, the austenitic phase recovery is more evident for $U_\infty > U_{LF}$ (the lower boundary in Fig. 19). Therefore, the effect of preload and initial condition on the equilibrium position of the pitch steady-state response at the linear flutter speed (Figs. 12(c) and 16) is not observed in the post-flutter condition (Figs. 18(b) and 20(a) and (b)). The aeroelastic behavior of the typical section at the flutter boundary or at post-flutter condition is insensitive to a variation of stiffness shown in Fig. 20(b) (assuming that no hysteretic behavior is present). Therefore, the hysteretic response of the SMA springs (and consequently the damping capabilities of the SMA springs) is the specific factor modifying the aeroelastic behavior of the typical section.

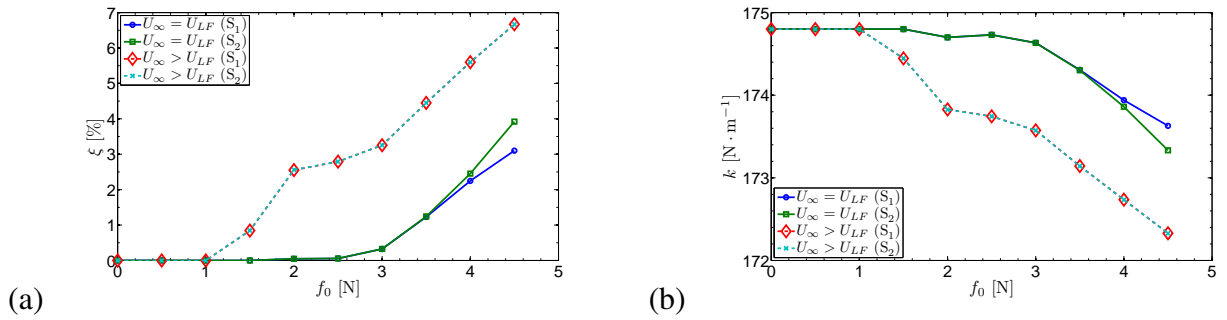


Figure 20 – Steady-state material properties of the two SMA springs – (a) martensitic fractions and (b) stiffness. The imbalance of the material properties between the two springs is evident for $U_\infty = U_{LF}$ when $f_0 > 3$ N and negligible for $U_\infty > U_{LF}$.

4.2.3 A Discussion on the SMA Spring Behavior for the Flutter Boundary and Post-Flutter Cases

Fig. 19 displays the resulting shear stress of the flutter boundary case (of Section 4.2.1) in contrast with that of the post-flutter case (of Section 4.2.2) for increasing preload. Differently from Figs. 13 and 17(b), both tensile and compressive stages of loading are represented in Fig. 19. The airflow speeds considered in the post-flutter case are those of the limiting curve of Fig. 17(a).

The resulting shear stress in loading stages is of concern. From Fig. 7, a positive pitch angle tends to compress the SMA spring S_1 and to extend S_2 . As well, a negative pitch angle tends to extend S_1 and to compress S_2 . Moreover, if the current pitch angle is positive and the angular motion is in the clockwise direction, the pitch angle is increasing. If the pitch angle is negative and the angular motion is in the counter-clockwise direction, the pitch angle is increasing as well, but in opposite sense. Assuming, in the one hand, that the pitch angle increases in the positive (clockwise) sense, S_2 is subject to tensile loading. Assuming, on the other hand, that the pitch angle increases in the negative sense, S_1 is subject to tensile loading. Such stages of tensile loading are valid for both preloaded and non-preloaded springs¹. The upper boundaries of the areas of Fig. 19 represent the shear stress during tensile loadings.

During an angular motion which tends to compress an SMA spring, the level of preload

¹The purpose of preloading the SMAs is to bias the stress state towards the critical stress for the onset of stress-induced phase transformation.

(which imposes tensile loading) will determine if that spring is being actually compressed or unloaded. For small values of preload, the shear stress related to the pitch angle may be larger (in magnitude) than the shear stress due to preload. In such a case, the resulting shear stress is negative and represents a stage of compressive loading. This behavior is verified in Fig. 19 for negative values of τ . If the preload is increased, the compressive shear stress related to the pitch angle may become smaller than the tensile shear stress due to the preload. The resulting shear stress is, therefore, positive and represents that the SMA spring is once again subject to tensile loading. In such a circumstance, the pitch angle is no longer compressing the spring; it is simply unloading the spring (*i.e.*, counter-acting the preload). This behavior is also verified in Fig. 19 for positive values of τ in the lower boundaries of the areas.

In the cases in which the pitch angle counter-acts the preload, the SMA spring is not fully unloaded (due to the considered level of preload). The resulting shear stress remains greater than zero for the complete pitch cycle. As a consequence, the partial $M \rightarrow A$ phase transformation described in Section 4.2.1 is verified. By observing Fig. 19, however, the contrast between the resulting shear stresses of the flutter boundary and post-flutter cases makes evident the reasons for the superior recovery of the austenitic phase of the post-flutter case comparing with that of the flutter boundary case. Since the aeroelastic displacements are larger in the post-flutter regime (than at the linear flutter speed), the unloading related to the pitch angle that counter-acts the preload is also more expressive. The $M \rightarrow A$ phase transformation is almost complete in the post-flutter case. The difference between the martensitic fractions of the two SMA springs is negligible. The corresponding stiffness of the SMA springs is, therefore, practically the same. Fig. 20(a) displays the martensitic fractions of the two SMA springs for the flutter boundary and post-flutter cases. Fig. 20(b) displays the corresponding stiffness. That behavior discussed along with Fig. 16 is also negligible in the post-flutter regime.

4.3 Analysis of Different Assumptions for the Cross-Sectional Representation of the Coiled SMA Wire

So far in this chapter, the aeroelastic behavior of the typical section with SMA springs was investigated by considering that the shear strain, shear stress and martensitic fraction are homogeneously distributed (*i.e.*, constant) along the radius of the coiled SMA wire. However, an improved assumption that represents non-homogeneous cross-sectional distributions was described in Section 2.4.3 and a comparison between both assumptions is presented next. In both cases, the SMA properties of Aguiar et al. (2013) are considered.

The effects of preloaded SMA springs on the aeroelastic behavior of the typical section oscillating at its linear flutter speed reported in Section 4.2.1 are reviewed in Fig. 21(a) (for the homogeneous assumption). Important points are: 1) the aeroelastic behavior is affected by the SMAs only when phase transformations do occur; 2) the aeroelastic displacements decrease (non-monotonically) with increasing preload; 3) the equilibrium position changes with increasing preload (a side effect due to the SMAs). The case for $f_0 = 4$ N is considered in Fig. 21(b) for an increasing number of annular regions. One single region is equivalent to the homogeneous assumption. Two or more regions represent the non-homogeneous assumption. The negative peak amplitudes (dashed curves in red) are mirrored (absolute values) to be compared with the positive peaks (solid curves in blue) so that the changes in the equilibrium position are highlighted. The cross-sectional distributions of shear strain, shear stress and martensitic fraction for the cases of 1, 3, 5, 10, 20 and 30 annular regions of Fig. 21(b) are shown in Fig. 22.

The effects of different cross-sectional scenarios on the post-flutter behavior are also considered. The maximum airflow speeds which satisfy the prescribed limiting aeroelastic displacement ($\alpha < 0.2$ rad) are shown in Fig. 23 for increasing number of annular regions. The aeroelastic displacements are greater at the post-flutter regime than at the flutter boundary. The phase transformations are also more expressive and therefore the effect of the number of annular regions is more significant on the model predictions. The predicted limiting airflow speed decreased from $14.7 \text{ m}\cdot\text{s}^{-1}$ for the homogeneous assumption (or one single annular region) to

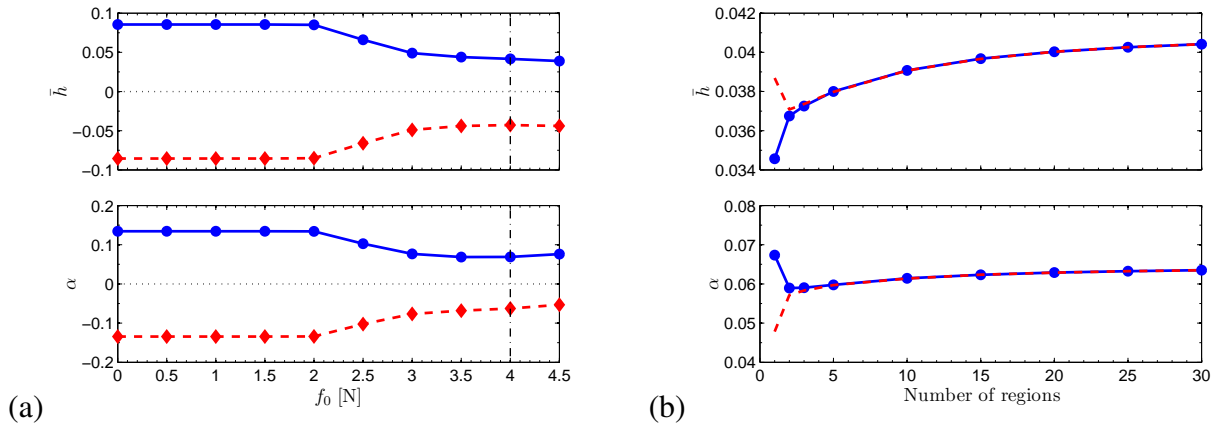


Figure 21 – Aeroelastic behavior of the typical section for the same model parameters and two different assumptions for the cross-sectional representation of the coiled SMA wire – (a) effects of preload and (b) effects of the number of annular regions.

$12.8 \text{ m}\cdot\text{s}^{-1}$ for the non-homogeneous assumption with 30 annular regions.

Overall, the aeroelastic behaviors predicted by both (homogeneous and non-homogeneous) assumptions qualitatively agree. The main differences are related to the amplitudes of oscillation at the flutter boundary and to the limiting airflow speed at the post-flutter regime (for the same preload levels). Since the transformation of austenite into martensite predicted by the former approach is less expressive than that for the latter approach, the effects of the pseudoelastic hysteresis are also less pronounced. The homogeneous assumption underestimates the amplitudes of oscillation at the flutter boundary in less than 5% if compared with the non-homogeneous assumptions. A decrease of 47% of pitch and plunge amplitudes is predicted when the homogeneous assumption is considered while the non-homogeneous assumption predicts an attenuation around 45% in pitch and plunge (both cases for 4 N of preload, *i.e.*, at the imminence of phase transformation for the considered set of model parameters). The limiting airflow speed is overestimated in 12% (from 27% above the linear flutter speed to 13%), also for 4 N of preload. The side effect of changes in the equilibrium position shown in Fig. 16 (Section 4.2.1) also becomes less expressive as the number of annular regions is greater than about five (Fig. 21).

The homogeneous assumption, although less realistic, may provide a good insight on the general model behavior with less computational effort (Fig. 24, for the cases of Fig. 21(b)). The non-homogeneous assumption, on the other hand, provides a better insight on the internal state

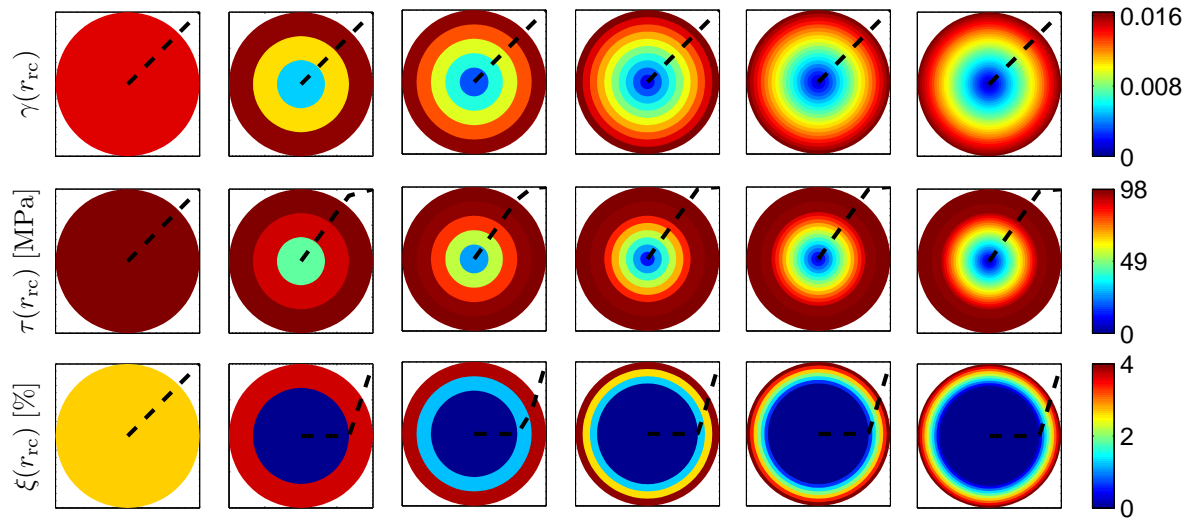


Figure 22 – Cross-sectional distributions of shear strain, shear stress and martensitic fraction for 1, 3, 5, 10, 20 and 30 annular regions.

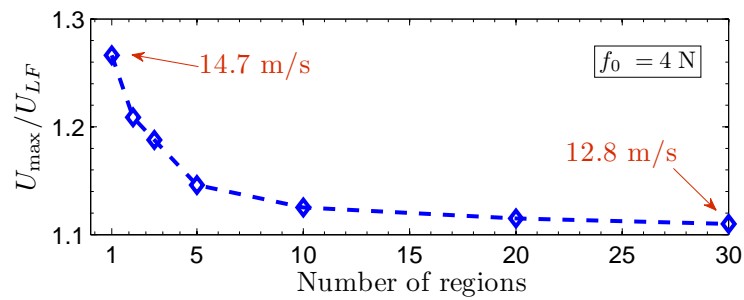


Figure 23 – Maximum airflow speeds with increasing number of annular regions at the post-flutter regime.

of the material and therefore a more realistic prediction of the model behavior. Concerning the computational cost for the non-homogeneous assumption, it is worth mentioning that Fig. 24 was obtained by simulating the system using no parallel computation features (single-threaded process was used). However, since the properties of each of the considered cross-sectional annular regions are independent from each other in the particular modeling approach of this work, multithreaded code can be used to resolve several annular regions simultaneously. This way, the simulation time can be significantly reduced. Depending on the number of available processors, the simulation time for several annular regions can be comparable to the simulation time for one single region.

Concerning the overestimations on the benefits of the SMAs on the aeroelastic behavior

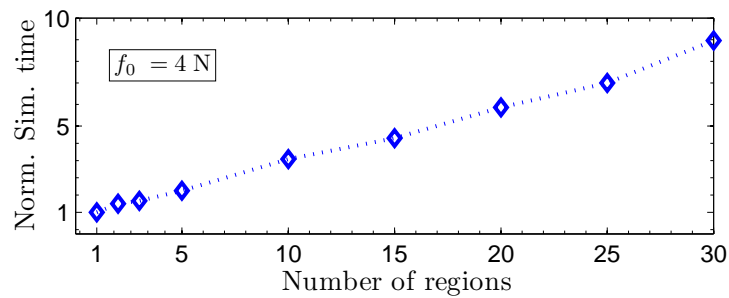


Figure 24 – Normalized simulation time for increasing number of annular regions (normalized by the elapsed time when considering one single annular section).

of the typical section (at and above the flutter speed), two main consequences can be discussed: 1) when the airflow speed is not increased above the linear flutter speed (of the reference case), slightly larger aeroelastic displacements (comparing with the smaller displacements for the homogeneous assumption) do not represent a potentially catastrophic condition since the displacements remain bounded within acceptable levels; 2) when the airflow speed is increased above the flutter speed, upon the initial disturbance the aeroelastic displacements will increase until a LCO is reached (due to the SMAs undergoing phase transformation), whose amplitude can be within a safety limit (from a structural health standpoint) depending on the assumed airflow speed. If the speed is too large, that safety limit will be exceeded, possibly leading to structural failure (in terms of a physical model). For this reason, the non-homogeneous assumption provides a smaller (in terms of maximum speed) post-flutter regime (from 27% to 13% in the maximum airflow speed, avoiding possible structural collapse), while both the homogeneous and non-homogeneous assumptions yield similar behaviors at the flutter boundary.

Effects of Different SMA Constitutive Properties on the Aeroelastic Behavior of the Typical Section

It is important to note that the aeroelastic behavior in the previous chapters was only investigated for an SMA spring with specific constitutive properties and geometry. There is a lack of discussion concerning the effects of different properties of the SMA elements on the aeroelastic behavior of a typical section. Therefore, this chapter extends the investigation and performs a parametric study in order to assess the effects of the constitutive properties of the SMAs (pseudoelastic hysteresis) on the aeroelastic behavior of a typical section. The effects of different characteristics of SMAs such as loop sizes, critical stress levels and tensile-compressive asymmetry are investigated by using six different sets of parameters previously presented in the literature. In practice, an optimum set of properties could be obtained by proper choice of materials, fabrication routes and heat treatment procedures (ELAHINIA et al., 2012).

5.1 Description of the Considered Sets of SMA Constitutive Properties

Six different sets of SMA properties are displayed in Tab. 3. Those properties represent a varied selection of materials from the literature which have been experimentally evaluated.

Thus, scenarios that account for different hysteresis loop sizes, transformation slopes, transformation temperatures and critical stresses can be exploited.

Table 3 – Sets of shape memory alloy properties.

Reference / Parameter	Gillet (G98)	Gall (G99)	Tokuda (T99)	Aguiar (A13)	Sameallah (S14)	Savi (S15)	Units
Alloy	CuAlBe	TiNi	CuAlZnMn	NiTi	CuAlBe	NiTi	
M_s	168	270	238	315	248	298	K
A_s	169	303	243	316	250	290	K
A_f	183	318	258	331	260	303	K
C_A^*	2.9, -2.3	3.5	3, (-2.2)	(6)	(3.5)	(5.6)	MPa·K ⁻¹
C_M^*	2	8, -5	1, (-1)	4	2.2	(5.6)	MPa·K ⁻¹
$\sigma_s^{\min*}$	60	60, -5	70, 0	100	35	(100)	MPa
$\sigma_f^{\min*}$	720, -440	160, -260	188, -220	170	220	(575)	MPa
ε_L^*	3.5, -3	3.4, -2.1	1.6, -1.46	6.7	4.9	7	%
D_M^*	10	11, 80	26, 33	29.9	19.5	22	GPa
D_A	73.2	39	34.9	37.7	60	46	GPa

(-2.2, -1) Changed from -3 and -0.2; (6) changed from 13.8; (3.5) averaged; (5.6, 100, 575) estimated.

The referred works of Tab. 3 are Gillet, Patoor and Berveiller (1998), Gall et al. (1999), Tokuda et al. (1999), Aguiar et al. (2013), Sameallah et al. (2014) and Savi et al. (2015). The acronyms are used in the figures to identify the corresponding set of SMA properties (*e.g.*, G98 stands for Gillet, Patoor and Berveiller (1998)). The properties of Gillet, Patoor and Berveiller (1998), Gall et al. (1999) and Tokuda et al. (1999) have data related to compressive loading (the properties with a second value), so that asymmetry behavior may be investigated. Symmetry is assumed for unavailable compressive properties. Values in brackets are missing in the referred papers and were estimated here, or yield somewhat atypical behavior when considered in the present model and were slightly changed. Those modified values, however, are consistent with the typical ranges for SMA properties reported on the literature (MELTON, 1990; HUANG, 2002).

The critical stress values given in Tab. 3 are the minimum values for stress-induced phase transformation. The actual critical values for the onset and completion of phase transformations depend on the SMA temperature. The temperature is assumed equal to A_f throughout this

study, since this is the minimum temperature at which pseudoelasticity is expected to occur. The resulting critical stresses are given in Tab. 4.

Table 4 – Derived SMA critical stresses for phase transformations.

Reference / Parameter	Gillet 1998	Gall 1999	Tokuda 1999	Aguiar 2013	Sameallah 2014	Savi 2015	Units
$\sigma_s^{M^*}$	90	444, -245	90, -20	164	62	130	MPa
$\sigma_f^{M^*}$	750, -470	544, -500	208, -240	234	247	605	MPa
$\sigma_s^{A^*}$	41, -32	53	45, -33	90	37	76	MPa

One may note that some transition temperatures are below the room temperature. However, as mentioned in Section 2.2.3, alloying combined with adequate heat and mechanical treatments may achieve desired properties with good accuracy for engineering purposes (MELTON, 1990; FRENZEL et al., 2010; HABERLAND et al., 2014). Moreover, the presented model would predict the same behavior for other temperature values as long as the temperature differences (*e.g.*, between M_s and A_f) are kept.

5.1.1 Constitutive Behavior of the Different Sets of SMA Properties

The constitutive behavior (stress-strain) for each set of SMA properties of Table 5 is shown in Fig. 25(a). These figures are obtained by solving the SMA constitutive equation (Eq. (2.16)) for a prescribed input stress value and by assuming the SMA at its stress-free austenite finish temperature (A_f). One should note that the constitutive behavior of an SMA element in Fig. 25 is displayed in terms of normal stress-strain behavior rather than the shear behavior or spring elongation (when referring to the SMA helical springs). The same scale is used in all plots of Fig. 25 to contrast the shape and size of the hysteresis loops of each set of SMA properties. Asymmetry behavior related to compressive loading is shown for the properties of Gillet, Patoor and Berveiller (1998), Gall et al. (1999) and Tokuda et al. (1999) and is presented as dashed lines. Symmetry is assumed when some parameters are not available for compressive loading. The mutual dependence between stress and temperature (or transformation slopes) usually observed in SMAs (BRINSON, 1993) is represented in Fig. 25(b) for each set of SMA properties. The temperature axis ranges from 10% below M_f up to 30% above A_f .

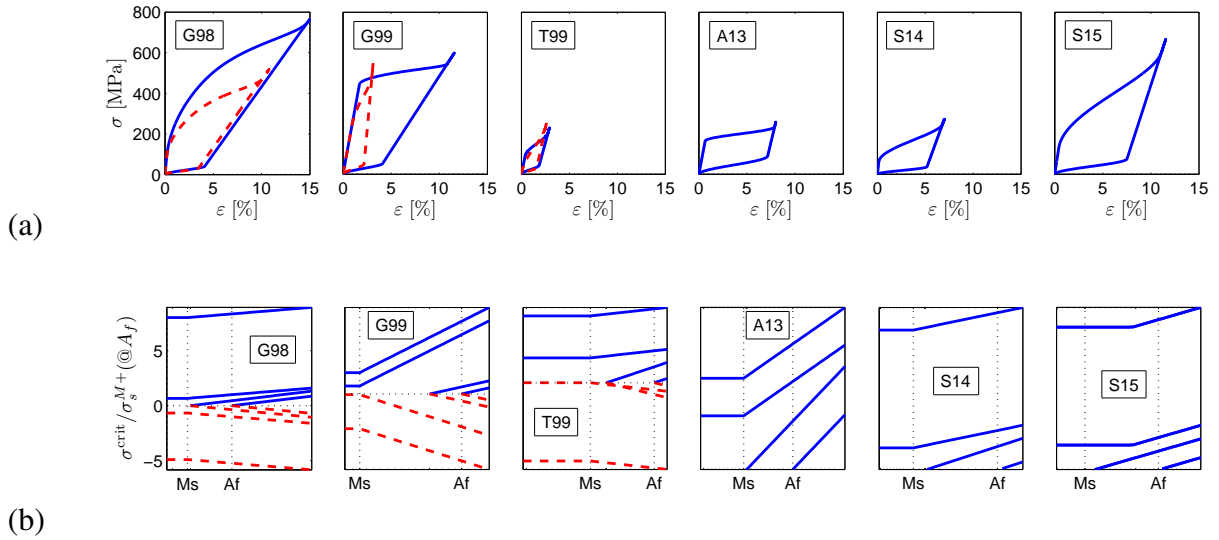


Figure 25 – Constitutive behavior for the sets of SMA parameters – (a) stress-strain behavior and (b) phase transformation slopes.

5.1.2 Description of Derived SMA Spring-Related Properties

To derive all the necessary SMA properties, the spring geometry and also some details of the aeroelastic model are defined. The aeroelastic parameters considered in this chapter are the same of Table 2. In all cases (of Table 3), the same damping properties of the conventional steel springs of Sousa et al. (2011) are assumed in order to analyze only the effects of the pseudo-elastic hysteresis (on the aeroelastic behavior of the typical section), although the damping of SMAs, especially in the martensitic phase, are usually larger than that of conventional materials (LIANG; ROGERS, 1997; VAN HUMBEECK, 2003). In addition, the same Poisson's ratio ($\mu_P = 0.3$) is assumed in all cases of this thesis. Properties related to twinned martensite are not considered since only pseudoelasticity is of concern. The thermal coefficient of expansion is not necessary due to the isothermal assumption of this work and also because its effects are negligible with respect to other effects.

The SMA spring geometry is assumed as $R = 4$ mm, $r = 0.475$ mm, $N = 16.5$ and $L = 38$ mm. Such a geometry yields the spring-related parameters shown in Table 5. The distance w (defined in Fig. 7(b)) is adjusted to keep the same elastic restoring moment in the pitch DOF for all cases, so that the linear aeroelastic behavior (with the SMA springs behaving as linear steel springs) is also the same. This way, the same spring geometry can be considered in all

cases of this chapter. As the distance w changes, the amplitude of the axial deflection (of the SMA springs) induced by the pitch motion also changes. This fact is negligible (comparing with other factors in the model), and the hysteresis may be more expressive for smaller spring elongations depending on the set of SMA properties, as discussed later. For reference purposes, however, the amplitude of axial deflection (named y_α) induced by the greatest peak-to-peak pitch amplitude reported here (0.4 rad) is shown in Table 5 for each case. As well, the preload required for taking the shear stress (at the outer surface of the SMA wire) at its critical value for the onset of forward phase transformation is provided for each spring (f_0^{crit} is the preload f_0 such that $\tau(r) \approx \tau_s^{M+}$). Thus, the SMA springs are initially in fully austenitic phase in all cases since the critical stress is not exceeded.

Table 5 – Derived SMA spring-related parameters.

Reference / Parameter	Gillet 1998	Gall 1999	Tokuda 1999	Aguiar 2013	Sameallah 2014	Savi 2015	Units
k	339	181	162	175	278	213	$\text{N}\cdot\text{m}^{-1}$
w	61.2	83.8	88.6	85.3	67.6	77.2	mm
y_α	24.5	33.5	35.4	34.1	27	30.9	mm
f_0^{crit}	2.2	10.8	2.2	4	1.5	3.2	N

5.2 Analysis of the Aeroelastic Behavior of the Typical Section for the Different Sets of SMA Properties

The aeroelastic behavior of the typical section is investigated in this section for the different SMA properties of Table 3 along with the related properties of Tables 4 and 5, and the aeroelastic parameters of Table 2. The analyses consider both the linear flutter speed and the post-flutter regime. The general aeroelastic behavior is discussed in Section 5.2.1 and a more detailed discussion on the most attractive cases is presented in Section 5.2.2. In certain cases, the aeroelastic behavior is modified by stress-induced phase transformation in compressive loading, allowing a discussion on the effects of tension-compression asymmetry. SMA characteristics that are attractive for the aeroelastic problem are briefly discussed in Section 5.2.3.

5.2.1 Aeroelastic Behavior Considering Different Sets of SMA Properties

The general aeroelastic behavior of the typical section with SMA prings using the different sets of SMA constitutive properties is presented in Fig. 26 (non-preloaded SMA springs cases in Fig. 26(a) and preloaded ones in Fig. 26(b)). The general behavior is discussed and the most attractive cases are discussed in the next section. No phase transformation is achieved during the aeroelastic simulations at the airflow speed of $11.6 \text{ m}\cdot\text{s}^{-1}$ (or $U_\infty/U_{LF} = 1$ in Fig. 26) when the properties of Gall et al. (1999), Aguiar et al. (2013) and Savi et al. (2015) are considered. Therefore, the linear aeroelastic behavior is observed for such conditions and amplitudes of pitch and plunge displacements are constant and similar to the assumed initial condition (in plunge in the case of this study). For such sets of parameters, the system is unstable for airflow speeds above $11.6 \text{ m}\cdot\text{s}^{-1}$ and, therefore, they were not included in Fig. 26. Fig. 26(b) provides the model predictions for the post-flutter regime (the x -axis is the airflow speed normalized by the linear flutter speed of the reference case) when the preloaded SMA springs are considered. In general, the range of airflow speeds with acceptable amplitude is increased (compared to the cases of Fig. 26(a)) since phase transformations are achieved for any pitch displacements due to the preload. For the same set of properties, the peak amplitude of displacements at a certain airflow speed is always smaller in Fig. 26(b) than in Fig. 26(a).

In order to clarify the effects observed in Fig. 26, the time responses of the different cases considered in Fig. 26 at an airflow speed slightly larger than the linear flutter speed (of the linear version of the typical section, $11.6 \text{ m}\cdot\text{s}^{-1}$) are shown in Figs. 27(a) and (b) for no preload and in Figs. 27(c) and (d) for applied preload. In Figs. 27(a) and (b), the responses obtained for the properties of Gall et al. (1999), Aguiar et al. (2013) and Savi et al. (2015) are the same that is obtained for a linear case (assuming steel springs rather than SMA springs), with the steady-state amplitudes depending on the initial conditions (slightly increasing over time due to the unstable nature of the flutter phenomenon). In Figs. 27(c) and (d), similar behavior is observed when the properties of Gall et al. (1999) are considered. The unstable flutter behavior is replaced by stable LCOs when no preload on the SMA springs is considered for the properties of Gillet, Patoor and Berveiller (1998), Sameallah et al. (2014) and Tokuda et al. (1999) (Figs. 27(a) and

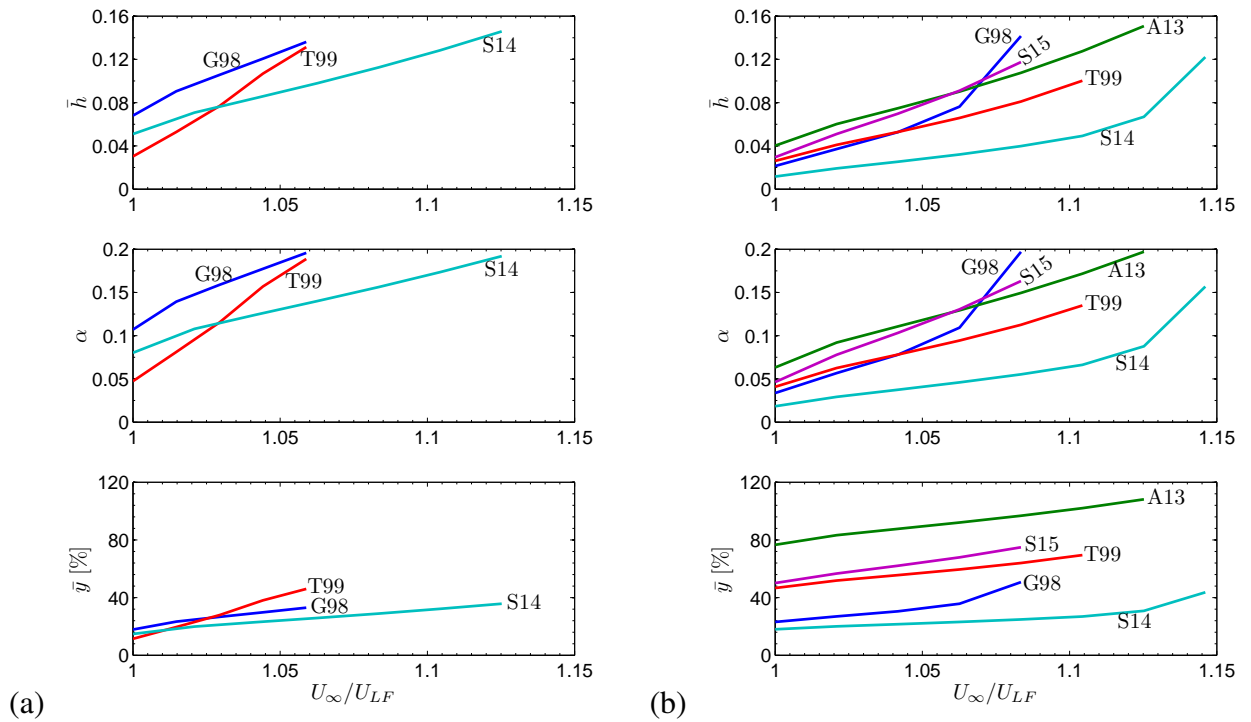


Figure 26 – Dimensionless pitch and plunge peak amplitudes and spring elongation for the SMA properties of Tab. 3 and increasing airflow speed. Non-preloaded SMA springs in (a) and preloaded springs in (b).

(b)). The amplitudes observed in Figs. 27(c) and (d) are smaller than the ones observed in Figs. 27(a) and (b) due to the preloads applied to the springs in each case.

The aeroelastic behavior is sensitive to the SMA properties and the considered preload level at both the linear flutter speed and post-flutter regime. It is worth mentioning that the maximum airflow speed with acceptable amplitudes predicted for the properties of Aguiar et al. (2013) is lower than that reported in Chapter 4 due to the different assumptions for the cross-section of the coiled SMA wire (as discussed earlier in Section 4.3).

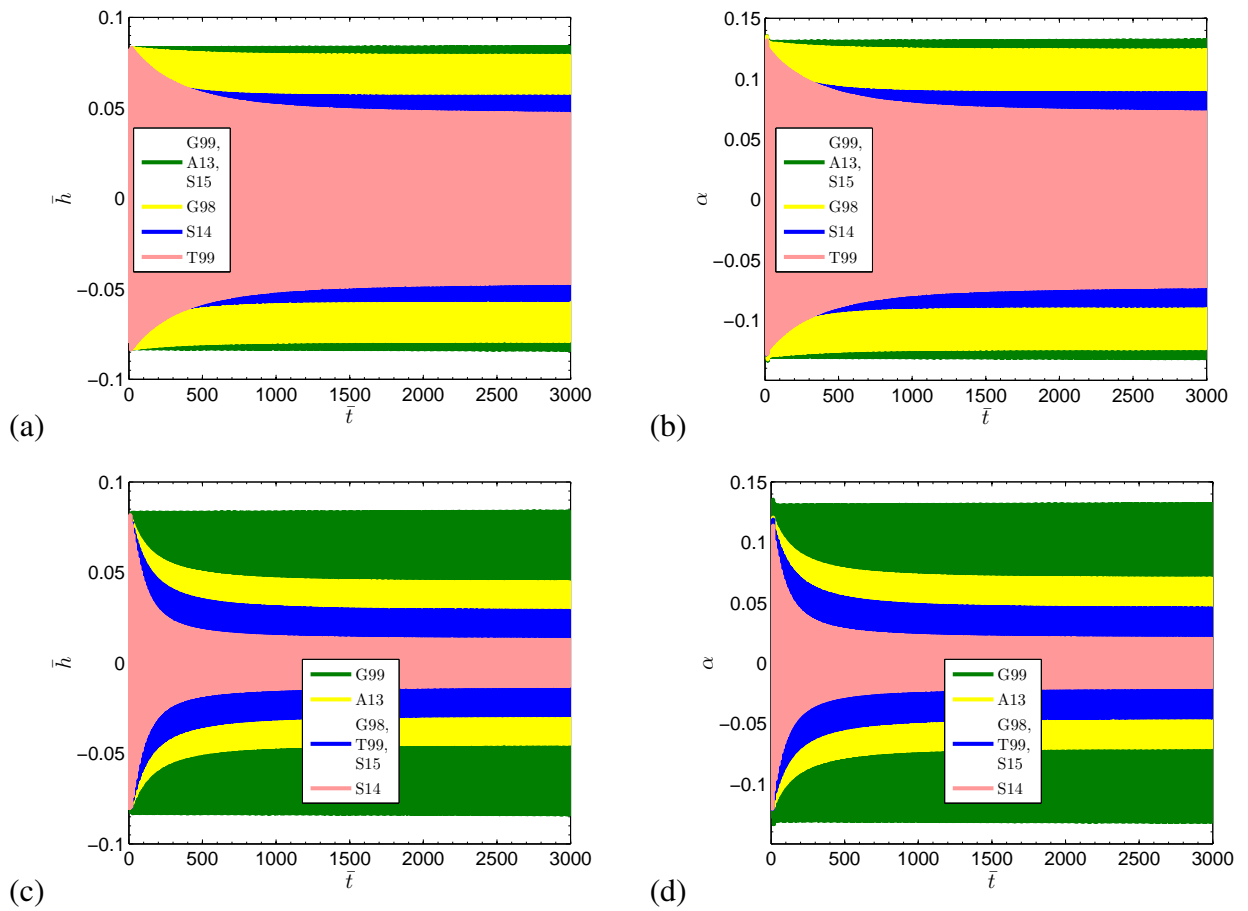


Figure 27 – Aeroelastic behavior of the typical section over time for different sets of SMA properties – (a) plunge and (b) pitch displacements for no preload and for applied preload (c, d). G99, A13 and S15 are represented by the same curve in (a, b), as well as G98, T99 and S15 in (c, d).

5.2.2 A Discussion on the Attractive Cases

The previous section (Figs. 26 and 27) shows that the flutter behavior at the linear flutter speed and the catastrophic unstable oscillations above the linear flutter speed may be replaced by stable LCOs due to the pseudoelastic hysteresis of the SMA springs over a range of airflow speeds. As previously discussed, the amplitude of the LCOs is sensitive to the SMA properties and considered level of applied preload, for example. Therefore, the pseudoelastic hysteresis may be used to attenuate aeroelastic oscillations over a range of airflow speeds. The sets of SMA properties that lead to the largest attenuation are discussed (for either with or without preload applied to the SMA springs). Since the modifications in the aeroelastic behavior are only due to the pseudoelastic hysteresis of the SMAs, the phase transformation kinetics is discussed next to explain the enhanced aeroelastic behavior.

Considering the time response for the properties of Tokuda et al. (1999) presented in Fig. 27(a) (at the flutter boundary and without preload), the behavior of the SMA springs along one cycle of oscillation is addressed next. The typical section motion represented in Fig. 28 (magnified two times) corresponds to one cycle of the transient aeroelastic response, at which phase transformations are more pronounced. As the typical section oscillates, the SMA springs S_1 and S_2 undergo opposite movements with very similar behavior throughout the complete cycle and, therefore, only S_1 is considered in the discussion for brevity. The surfaces of Fig. 28 represent, respectively, the distributions of shear strain (linear), shear stress (nonlinear) and martensitic fraction (mixed) in the cross-section of the coiled SMA wire of spring S_1 during that cycle. The r -axis is the running coordinate along the wire radius (normalized by the wire radius, *i.e.*, $\bar{r} = r_{rc}/r$), t -axis is the dimensionless time corresponding to a complete cycle of the pitch DOF and the z -axis is the shear stress in the upper figures (τ -axis) and the martensitic fraction in the lower figures (ξ -axis). The shear stress is normalized by the critical value for the onset of forward phase transformation in tensile loading (τ/τ_s^{M+}).

The SMA spring is subject to tensile loading in the first half of the cycle and to compressive loading in the second half. The valley encompassed by a dashed curve in the shear stress surface is the stress-induced martensitic plateau related to compressive loading. The dashed

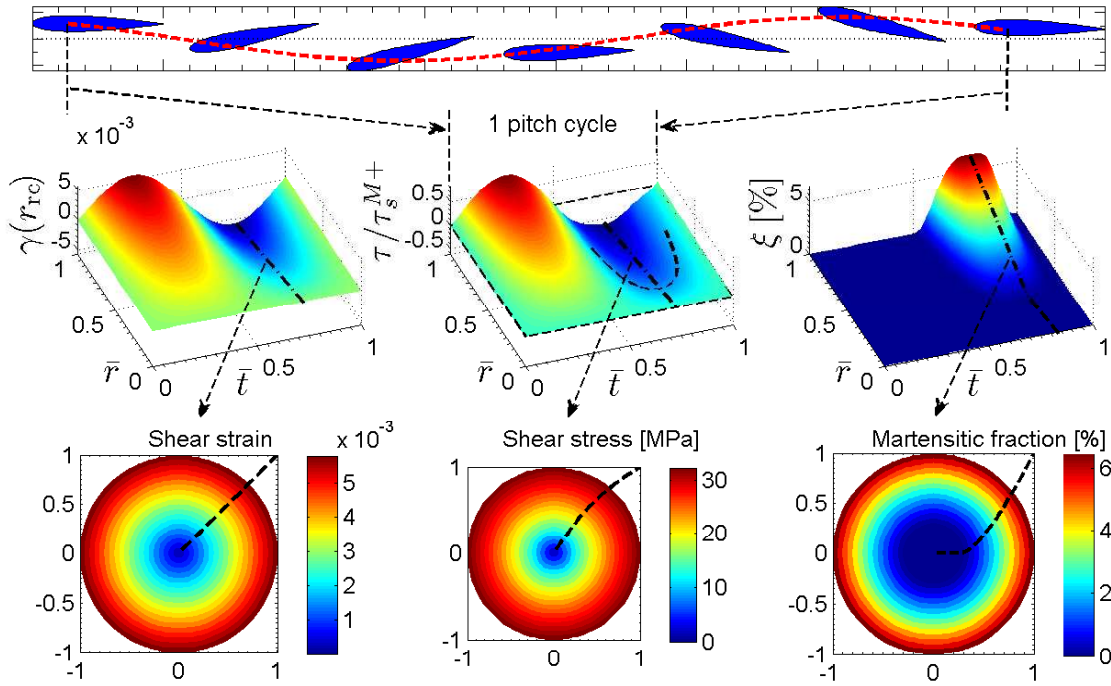


Figure 28 – Typical section motion during one transient cycle of oscillation at the flutter boundary for the SMA properties of Tokuda et al. (1999) without preload. The surfaces represent the cross-section of the coiled SMA wire.

curve indicates the critical radius for phase transformation. Outside the critical radius, the shear stress is a linear function of the radial coordinate. The lower figures show the cross-sectional distributions at the time instant of the most expressive martensitic formation. The dashed lines represent the way the quantities are distributed along the wire radius.

In the particular case of Fig. 28, stress-induced phase transformations occur only for compressive loading because $\tau_s^{M^-} \ll \tau_s^{M^+}$ for the considered set of SMA properties. As the aeroelastic behavior evolves from transient to steady-state and the plunge and pitch displacements decrease (Fig. 27), the phase transformations become less pronounced because the stress-state experienced by the SMA springs (directly related to the pitch motion) also decreases (Fig. 29). For brevity, the case of the flutter boundary and preloaded SMA springs will be discussed later only for the properties of Sameallah et al. (2014), which is more attractive. The post-flutter case for the properties of Tokuda et al. (1999) is discussed next.

The post-flutter time responses at the airflow speeds of $12.3 \text{ m}\cdot\text{s}^{-1}$ and $12.8 \text{ m}\cdot\text{s}^{-1}$ for the

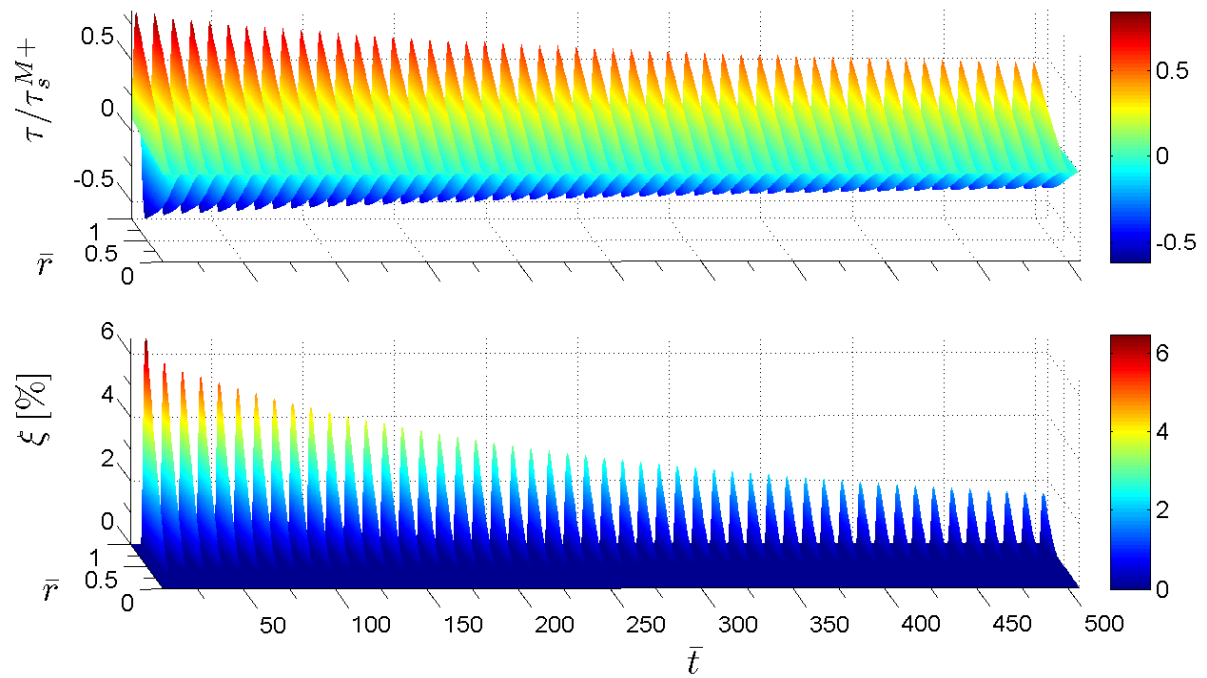


Figure 29 – Phase transformation behavior from transient to steady-state response for the SMA properties of Tokuda et al. (1999). Normalized shear stress (τ/τ_s^{M+}) and martensitic fraction (ξ).

SMA properties of Tokuda et al. (1999) are shown in Fig. 30(a) for both no preload and applied preload, respectively. The airflow speed can be increased about 6% and 10%, respectively, above the linear flutter speed and the oscillations still respect the limiting solution assumed in this work (Fig. 26(d)). A diagram with the normalized maximum shear stress (at the surface of the coiled SMA wire) in terms of the spring elongation is shown in Fig. 30(b). The steady-state cross-sectional distributions of shear stress and martensitic fraction for the case with no preload are shown in Figs. 31(a) and (b), respectively. In addition to the increase in the compressive stress-induced phase transformation due to larger aeroelastic displacements, some phase transformation related to tensile loading is also predicted. The cross-sectional distributions for the case with applied preload are shown in Figs. 31(c) and (d). Dashed lines in the $r - \tau$ plane represent the effect of preload. Due to preload, compressive behavior is no longer achieved in this case.

The cases for the properties of Sameallah et al. (2014) at the flutter boundary (presented earlier in Fig. 27) are of concern. For no preload, stress-induced phase transformations are

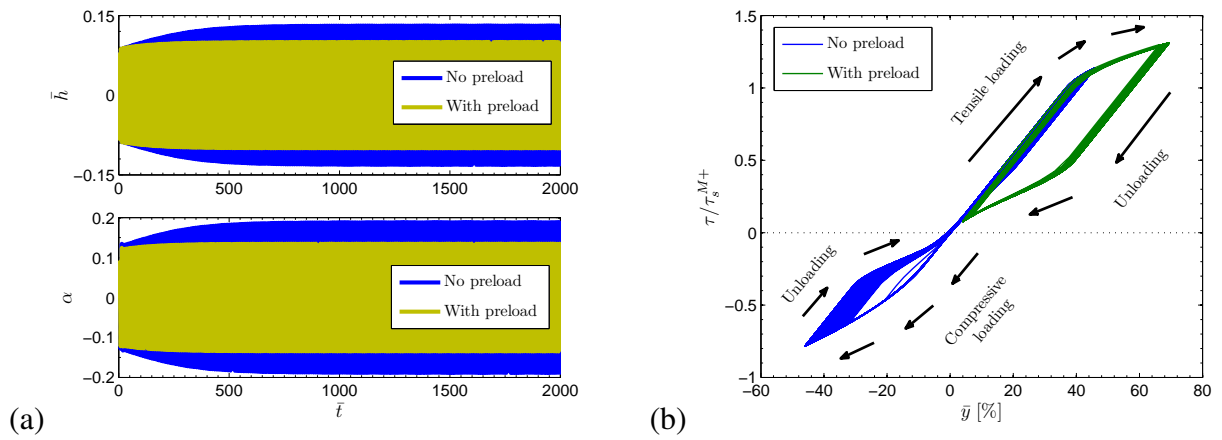


Figure 30 – Post-flutter behavior for the SMA properties of Tokuda et al. (1999), without and with applied preload – (a) time responses of the plunge and pitch DOFs and (b) SMA spring elongation versus the normalized maximum shear stress.

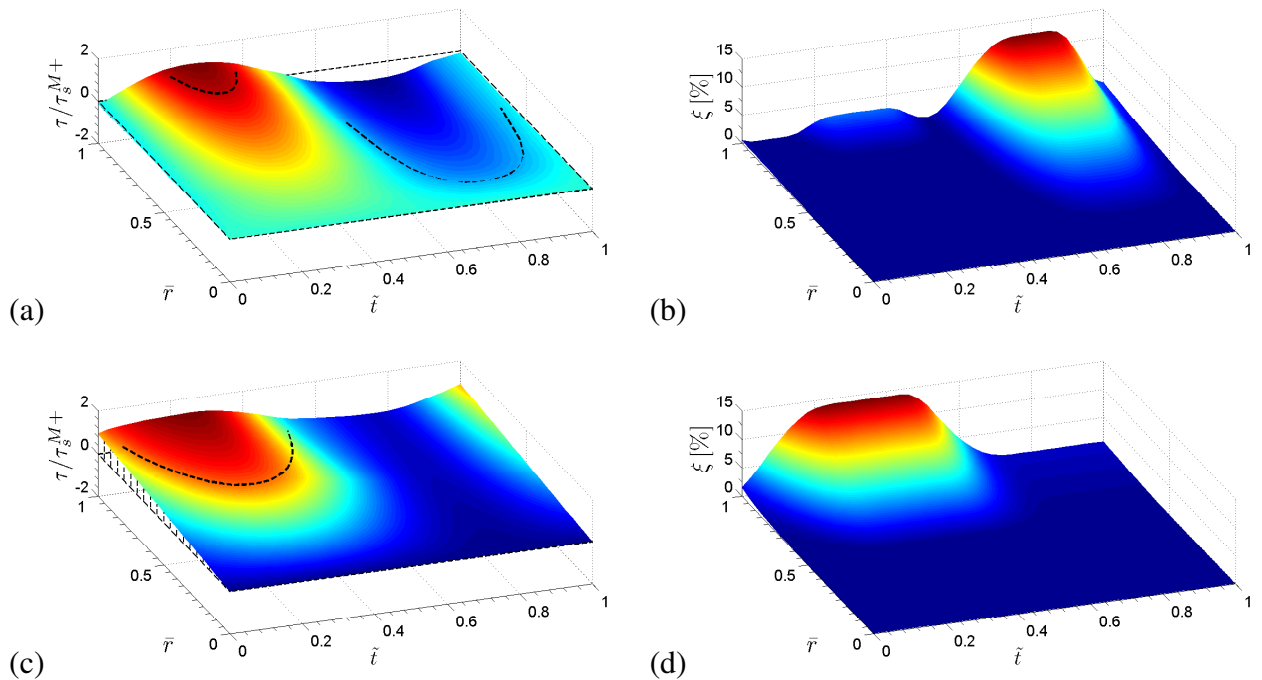


Figure 31 – Post-flutter behavior for the SMA properties of Tokuda et al. (1999). Steady-state cross-sectional distributions of shear stress and martensitic fraction for no preload (a, b) and applied preload (c, d). Dashed lines in the $r - \tau$ plane represent the effect of preload.

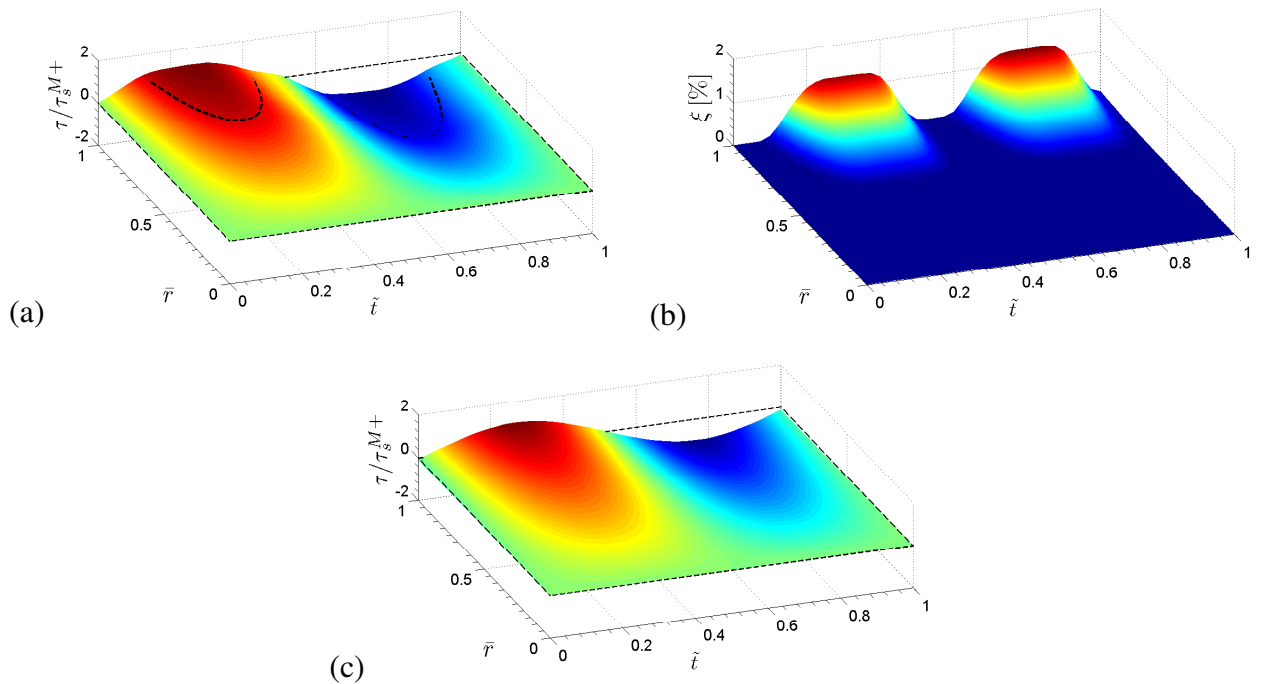


Figure 32 – Cross-sectional distributions of shear stress and martensitic fraction for the SMA properties of Sameallah et al. (2014) during a complete pitch cycle at the flutter boundary and with no preload. Transient (a, b) and steady-state (c) cycles.

predicted in both tensile and compressive stages in a well-balanced way due to the assumed symmetry (since only the properties related to tensile loading are available). The phase transformation behavior during the transient response, which is more evident, is shown in Figs. 32(a) and (b). For the steady-state response, the martensitic fraction is negligible (omitted in Fig. 32) and the shear stress distribution is quite linear (Fig. 32(c)). In spite of exhibiting two phase transformations during one single pitch cycle, the total hysteretic dissipation is less expressive than that for the properties of Tokuda et al. (1999) during one pitch cycle and no preload (because of the lower critical stress in compressive loading). However, when preload is considered, this set of properties yields the largest attenuation among the cases reported here (Fig. 33). In such a case, the SMA springs are under tensile loading during the complete cycle (despite the axial deflection being in opposite sense to preload in the second half of the cycle) and hence there is some unrecovered martensite in the SMAs during the steady-state response (Fig. 33(d)).

The post-flutter behavior for the SMA properties of Sameallah et al. (2014) is of concern. The maximum airflow speed with acceptable amplitudes may increase about 13% for no preload and 15% for applied preload. The corresponding time responses are shown in Fig. 34(a). The

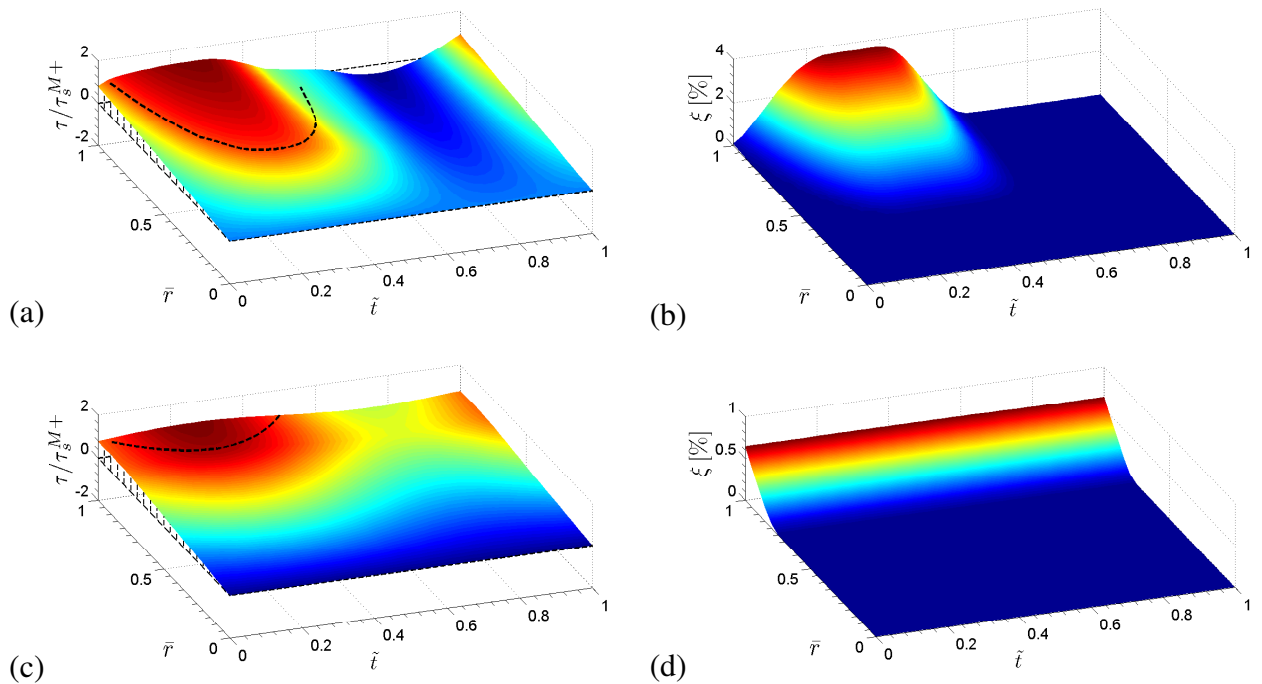


Figure 33 – Cross-sectional distributions of shear stress and martensitic fraction for the SMA properties of Sameallah et al. (2014) during a complete pitch cycle at the flutter boundary and with applied preload. Transient (a, b) and steady-state (c, d) cycles.

hysteretic behaviors are represented in Fig. 34(b). Stress-induced phase transformations are predicted in both the tensile and compressive stages of loading for no preload, being much more pronounced than in the flutter boundary case (without preload). For applied preload, compressive loading is also achieved (in contrast with the same case for the properties of Tokuda et al. (1999), although being unable to exceed τ_s^{M-} and induce phase transformation. The austenitic phase is fully recovered during unloading (in contrast with the flutter boundary case).

The cross-sectional distributions of shear stress and martensitic fraction during a complete steady-state cycle of the pitch DOF are shown in Fig. 35 for no preload and applied preload cases. The martensitic plateau and hence the martensitic fraction are expressive in both cases.

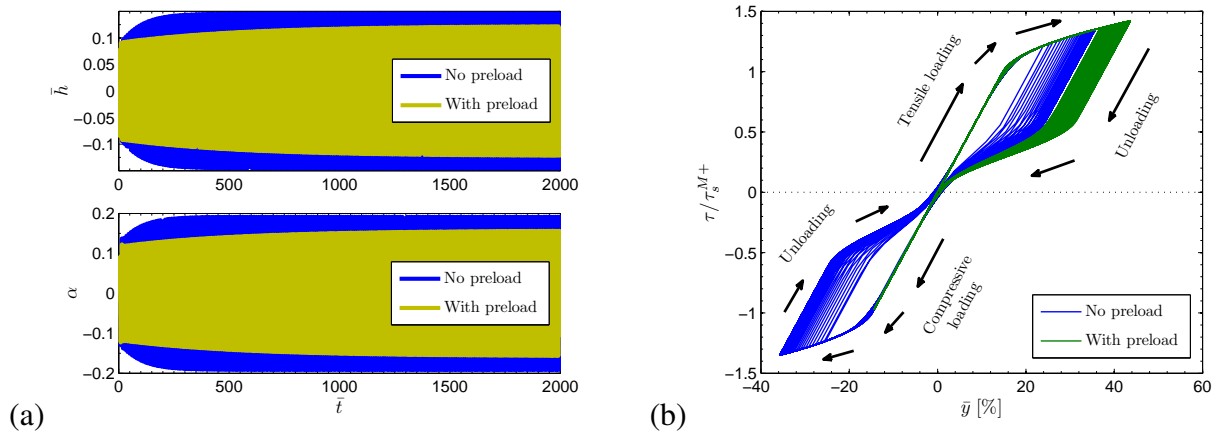


Figure 34 – Post-flutter behavior for the SMA properties of Sameallah et al. (2014). No preload and airflow speed of $13.1 \text{ m}\cdot\text{s}^{-1}$. With applied preload and airflow speed of $13.3 \text{ m}\cdot\text{s}^{-1}$. Plunge and pitch displacements (a). Normalized maximum shear stress versus spring elongation diagram (b).

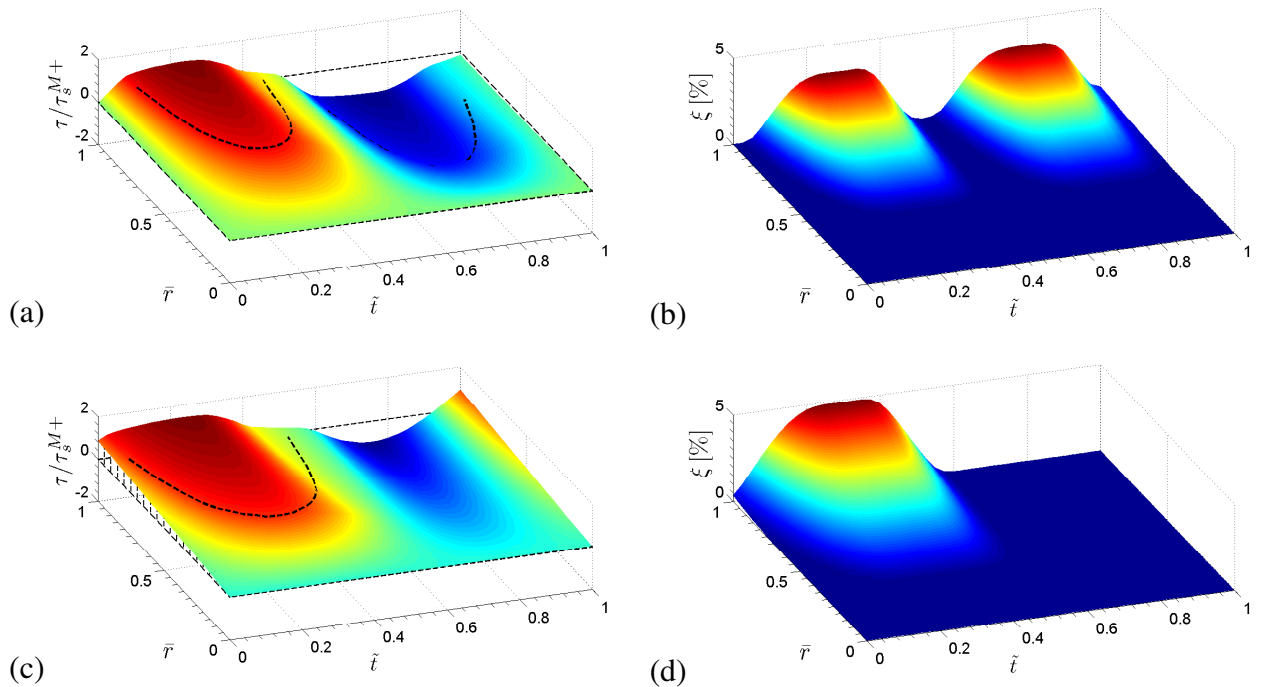


Figure 35 – Cross-sectional distributions of shear stress and martensite fraction for the SMA properties of Sameallah et al. (2014) during a complete steady-state pitch cycle of the post-flutter case. No preload (a, b) and with applied preload (c, d).

5.2.3 General Effects of SMA Parameters on the Aeroelastic Behavior

Having discussed the general aeroelastic behavior for the different sets of SMA properties (Figs. 26 and 27) as well as some details of the transformation kinetics of some specific cases (Figs. 28 to 35), it is important to discuss the effects of some particular parameters (of each set) on the flutter behavior of Figs. 26 and 27. Fig. 26(a) (no preload) shows that for airflows speeds slightly above the linear flutter speed (of the reference linear configuration) the properties of Tokuda et al. (1999) yield the smallest amplitudes (compared to the properties of Gillet, Patoor and Berveiller (1998) and Sameallah et al. (2014)). Table 4 shows that the properties of Tokuda et al. (1999) have a expressively lower compressive critical stress when compared to the critical stress of Gillet, Patoor and Berveiller (1998), resulting in phase transformations at lower pitch angles. However, the properties of Tokuda et al. (1999) lead to a quite small hysteresis loop (Fig. 25), thus limiting its energy dissipating capability, while the properties of Gillet, Patoor and Berveiller (1998) lead to a much larger hysteresis. The latter, on the other hand, has very high stress levels for the completion of phase transformation, what avoids the full exploitation of the hysteretic behavior in the aeroelastic problem (the pitch angle is unable to induce significant phase transformations in such a case). Therefore, larger hysteresis loop is not a sufficient condition for enhanced aeroelastic behavior. The SMA properties of Sameallah et al. (2014) yield intermediate aeroelastic amplitudes at the flutter vicinity (Fig. 26(a)) and wider post-flutter regime (up to 12.5% above the linear flutter speed) with the smallest amplitudes. This enhanced aeroelastic behavior is promoted by an attractive combination of low critical stresses, for both the onset and completion of phase transformation (Table 4), with a considerable recoverable strain (Table 3), thus producing a hysteresis loop with a reasonable area which can be more effectively exploited at smaller aeroelastic displacements than that for the properties of Gillet, Patoor and Berveiller (1998). It is also worth noting that the relatively high elastic modulus obtained from the properties of Sameallah et al. (2014) produces a (also relatively) stiffer spring. At the limiting airflow speed, the spring elongation is no more than 40% of its natural length (Fig. 26(a)), which is usually held by practical SMA springs.

Concerning the preloaded cases of Fig. 26(b), most of the property sets (Gillet, Patoor

and Berveiller (1998), Tokuda et al. (1999), Aguiar et al. (2013) and Savi et al. (2015)) yields an overall similar aeroelastic behavior at airflow speeds slightly above the linear flutter speed (differences in the spring elongation are, however, evident in Fig. 26(b)). The properties of Sameallah et al. (2014) (combination of low critical stresses for both the onset and completion of phase transformation with a considerable recoverable strain results in a hysteresis loop with a reasonable area) yield the more attractive aeroelastic behavior also in this case (lowest LCO amplitudes and wider post-flutter regime). The limiting airflow speed of such a case is almost 15% above the linear flutter speed. Despite the preloaded condition, the spring elongation (for this set) is similar to that for the non-preloaded case. This is related to the spring stiffness as well as to low aeroelastic amplitudes induced by this set of parameters.

In order to illustrate the problem, the properties of Gall et al. (1999) should be discussed. The high critical stresses require large pitch motions for the occurrence of phase transformation (please note the difference between the martensite start and austenite finish temperatures in Table 3). Therefore, for non-preloaded case using the properties of Gall et al. (1999) in Fig. 26(a), the typical section behaves as a linear aeroelastic system since very large pitch angles would be required for any phase transformation (in contrast with the properties of Gillet, Patoor and Berveiller (1998), Tokuda et al. (1999) and Sameallah et al. (2014)). Although some phase transformation is observed for the preloaded condition (Fig. 26(b)), it is unable to yield any mitigation of the aeroelastic oscillations because the pitch contribution to the stress-state of the SMAs is negligible. Thus, no enhanced aeroelastic behavior is verified for this property set. It is fair, however, mentioning that the large hysteresis of the SMA of Gall et al. (1999) could be attractive for a different application other than the proposed aeroelastic configuration of this study.

5.3 Additional Analyses

5.3.1 Effects of the Initial Conditions Applied to the Typical Section

In all cases presented so far in this chapter, the preload is such that the shear stress at the outer surface of the coiled SMA wire almost achieves the critical level for the onset of forward

phase transformation (in tensile loading). In such a case, small pitch motions would be enough to induce some amount of phase transformation. However, it was not discussed so far how the pseudoelastic hysteresis affects the aeroelastic response for different motions from small up to relatively large pitch displacements. Different initial conditions (from up to) applied to the plunge DOF of the typical section at its flutter boundary (when the system is marginally stable) are considered in Fig. 36.

In Fig. 36(a), no preload is considered, while in Fig. 36(c) the same preload of the previous cases is considered. The results show that the aeroelastic response is insensitive to the initial conditions when phase transformations (nonlinearities) are predicted (Fig. 36(c)). If phase transformations do occur (all cases of Fig. 36(c)), the model becomes practically insensitive to the initial conditions, with a quite linear but negligibly small increase in amplitudes for increasing initial condition (details in Fig. 36(d)). In such cases, the steady-state aeroelastic responses approach the same response previously reported in Fig. 27. Dashed lines represent the initial condition-dependent linear behavior that would take place by replacing the SMAs by conventional steel springs. In addition, there is a frequency change related to change in stiffness of SMA springs for the cases in which phase transformation occurs. In contrast, the linear cases are in phase.

Figs. 36(e) and (f) show the normalized maximum shear stress in terms of the spring elongation for transient cycles of the cases of Figs. 36(a) and (c), respectively. The differences in the hysteretic behavior are only due to the magnitude of the pitch displacement. The hysteresis loops become much less pronounced (not shown in Fig. 36) as the steady-state aeroelastic response is achieved (the pitch DOF in particular, also omitted in Fig. 36).

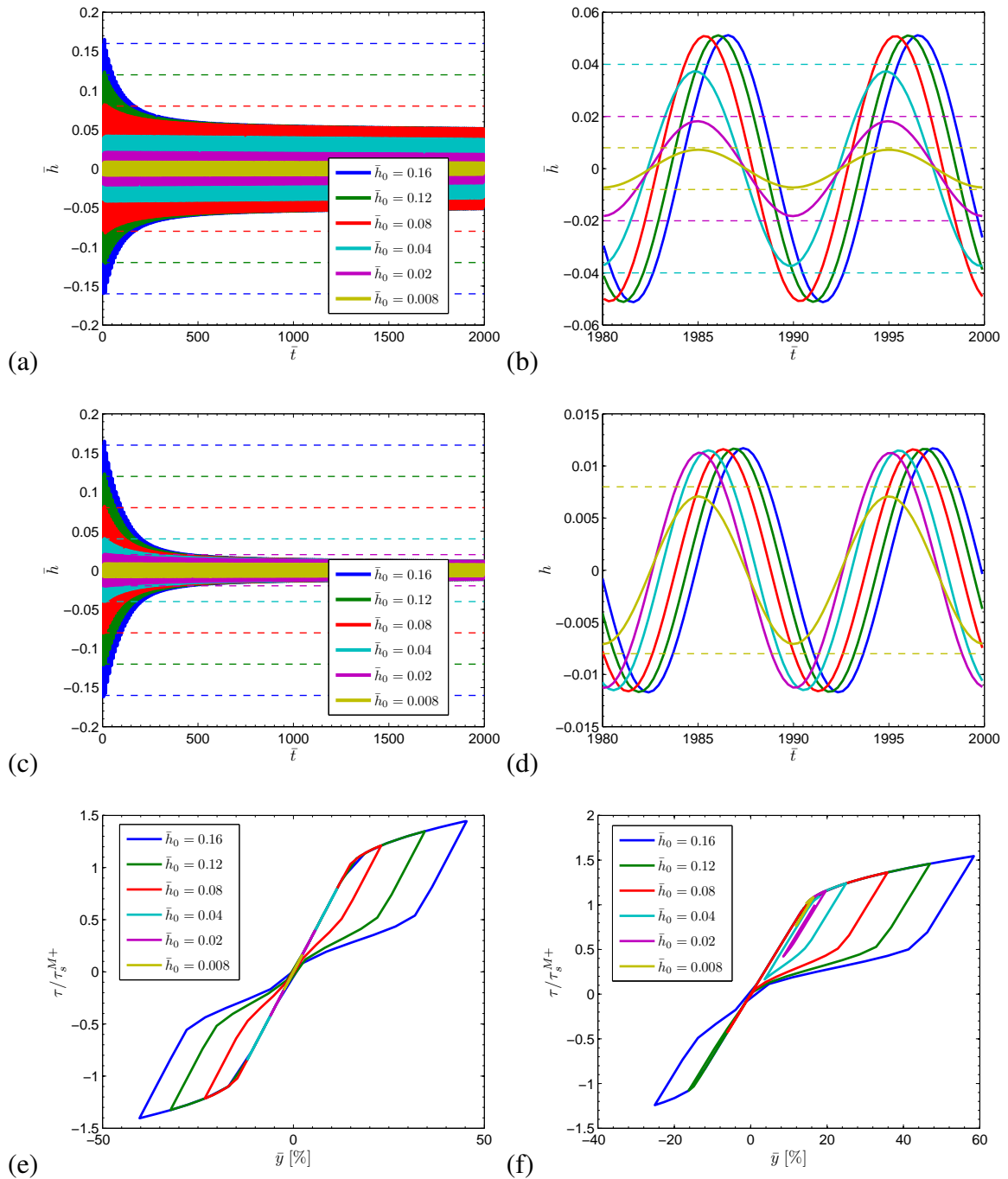


Figure 36 – Time response of the plunge DOF for the SMA parameters of Sameallah et al. (2014) and different initial conditions. No preload (a, b) and with applied preload (c, d). Transient shear stress versus spring elongation for no preload and applied preload (e, f).

5.3.2 A Note on Intermediate Preload Levels

By considering intermediate preload levels (arbitrary values between zero and τ_s^{M+}), no further enhancement to the aeroelastic behavior (with respect to the cases above) was predicted by the proposed model. On the other hand, specific values of preload yield the same aeroelastic behavior than that for a critical preload (at the proximity of τ_s^{M+}). In such cases, one single larger hysteretic loop (induced only by tensile loading) is replaced by two smaller loops (induced by both tensile and compressive stages of loading). This could be beneficial, for example, for improving the fatigue response of the SMAs since the stresses, and hence the transformation strains, are lower.

Effects of the Geometric Properties of the SMA Springs on the Aeroelastic Behavior of the Typical Section

Effects of geometric properties of the SMA springs on the aeroelastic behavior of the typical section are investigated in this chapter. An analysis for the identification of physically achievable spring geometries is conducted first. A typical range of helical spring indices C between 4 and 12 is considered. Both the wire diameter (d) and the spring mean coil diameter (D) are modified (not simultaneously) in such a way the index C is in the range of 4 up to 12 considering small increments. Since $C = D/d$, by assuming d constant (and equal to its nominal value, 0.95 mm) the corresponding coil diameters (D_{var}) range from 3.8 to 11.4 mm. Similarly, for constant D (and equal to 8.0 mm) the range of wire diameters (d_{var}) is between 0.67 and 2.0 mm.

From Eq. (2.26), two ranges of (austenitic) SMA spring stiffness are obtained for D_{var} and d_{var} as $k_D = [60, 1600] \text{ N}\cdot\text{m}^{-1}$ and $k_d = [40, 3400] \text{ N}\cdot\text{m}^{-1}$, respectively and for 16.5 active coils. Please note that k_D and k_d are the spring constants that are combined according to the scheme presented in Fig. 7 to give the pitch stiffness of the typical section. To maintain the same elastic restoring moment in pitch, and therefore the same aeroelastic behavior (assuming all the other parameters constant), the distance w in Fig. 7 has to be adjusted accordingly. However,

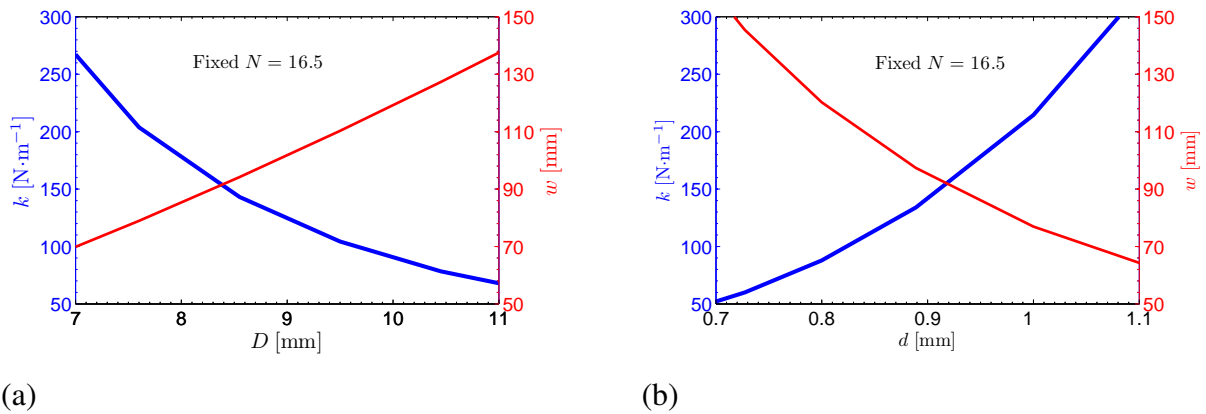


Figure 37 – SMA spring stiffness (k) and the corresponding distance w between the elastic axis and the SMA springs for increasing coil diameter (a) and wire diameter (b).

due to design constraints and also to impractical geometries in an eventual experimental setup, the ranges of stiffness k and distances w have to be limited to a certain range of values.

Fig. 37 displays the spring stiffness (k) and required distance w with the variation of D (Fig. 37(a)) and with the variation of d (Fig. 37(b)). Fig. 37(a) shows that the spring stiffness decreases with increasing spring mean coil diameter (D) and, therefore, w increases with increasing D in order to keep a constant pitch stiffness. On the other hand, the spring stiffness increases with increasing wire diameter (d) and, therefore, w decreases with increasing d in order to keep the resulting pitch stiffness constant.

Another strategy to obtain the same restoring moment in the pitch DOF rather than modifying the distance w is by changing the number of active coils (N) simultaneously to the variation of the spring mean coil diameter or simultaneously to the variation of the wire diameter to keep the nominal SMA spring stiffness. This way, the resulting stiffness, and hence w , are the same despite changes in wire or coil diameters. The number of active coils is calculated by solving Eq. (2.26) for N and by using $k = 175 \text{ N}\cdot\text{m}^{-1}$ along with D_{var} and d_{var} . Once again neglecting impractical values, Fig. 38 displays the number of coils for varying diameters. The number of active coils decreases with increasing spring mean coil diameter (D) while the number of active coils increases with increasing D , in both cases resulting in a constant spring stiffness and, consequently, the same pitch restoring moment for the typical section.

Based on Figs. 37 and 38, the analysis of the effects of geometric nonlinearities of SMA

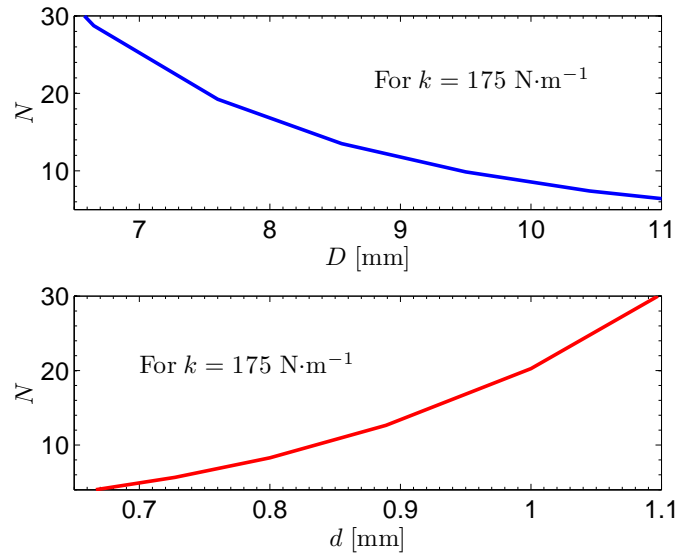


Figure 38 – Number of active coils (N) for varying coil (D) and wire (d) diameters.

springs on the aeroelastic behavior of the typical section is performed for a reduced number of cases, either by assuming D_{var} between 7 mm and 11 mm, or by assuming d_{var} between 0.7 mm and 1.1 mm. In all cases considered in this chapter preloaded SMA springs are considered, so that phase transformations are induced by small pitch displacements. The critical preload (at the imminence of phase transformation) is estimated by solving Eq. (2.20) for the force in terms of the critical stress (*i.e.*, $F = f_0^{\text{crit}}$ and $\tau = \tau_s^{M+}$).

Fig. 39 displays the steady-state peak amplitudes of the plunge and pitch DOFs at the linear flutter speed of the reference case, both normalized by the aeroelastic response of the reference case (that same of the previous chapters, denoted here as \bar{h}_{ref} and α_{ref}). The number of coils of the SMA springs in pitch is fixed ($N = 16.5$) and both the resulting stiffness k (due to the variation of D or d , as displayed in Fig. 37) and distance w are changed (corresponding to the cases of Fig. 37) to keep the pitch restoring elastic moment constant. Fig. 39(a) shows that the pitch and plunge amplitudes increase with increasing D . However, the amplitudes of the preloaded case are always smaller than the amplitudes of the reference case. Moreover, the combination of $D = 7$ mm and the respective w (from Fig. 37(a)) leads to the smallest pitch and plunge amplitudes. A similar behavior is observed for the variation of d and w in Fig. 39(b). However, small wire diameter (d) leads to smaller pitch amplitudes than small values of D .

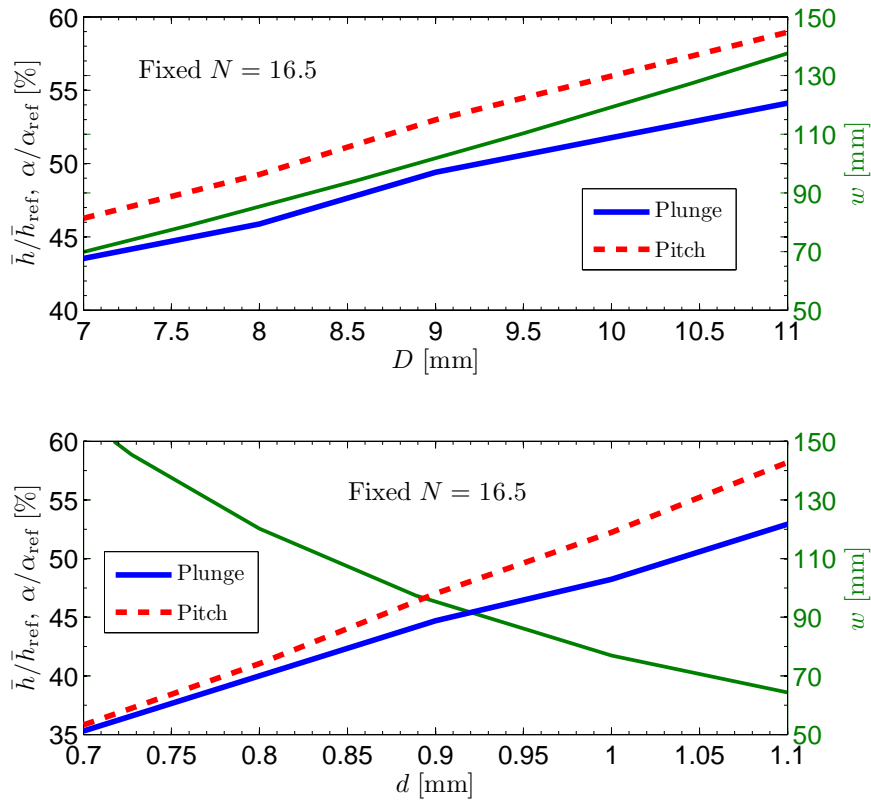


Figure 39 – Steady-state aeroelastic behavior for different SMA spring diameters (with variable stiffness and constant number of coils).

Fig. 40 displays the pitch and plunge peak amplitudes for the case previously discussed in Fig. 38 (spring stiffness kept constant and modifying the number of active coils (and D or d) to keep the pitch stiffness constant. The pitch and plunge amplitudes are always smaller than the amplitudes of the reference case. The amplitudes decrease with increasing D (Fig. 40(a)), and consequently decreasing N (Fig. 38) while the amplitudes increase with increasing d (Fig 40(b)) and decreasing N (Fig. 38).

By comparing the predicted amplitudes of the cases of Figs. 39 and 40, one should note that the smallest pitch and plunge amplitudes are obtained in Fig. 40(b) ($d = 0.7$ mm and $N = 5$). Decreasing the wire diameter is the most favorable condition to achieve phase transformation and improve the pseudoelastic damping for the case of this discussion. Fig. 41 displays the time response of the plunge and pitch DOFs for three different cases at the linear flutter speed: 1) for the reference case (without preload, which exhibits larger amplitudes), 2) for the nominal

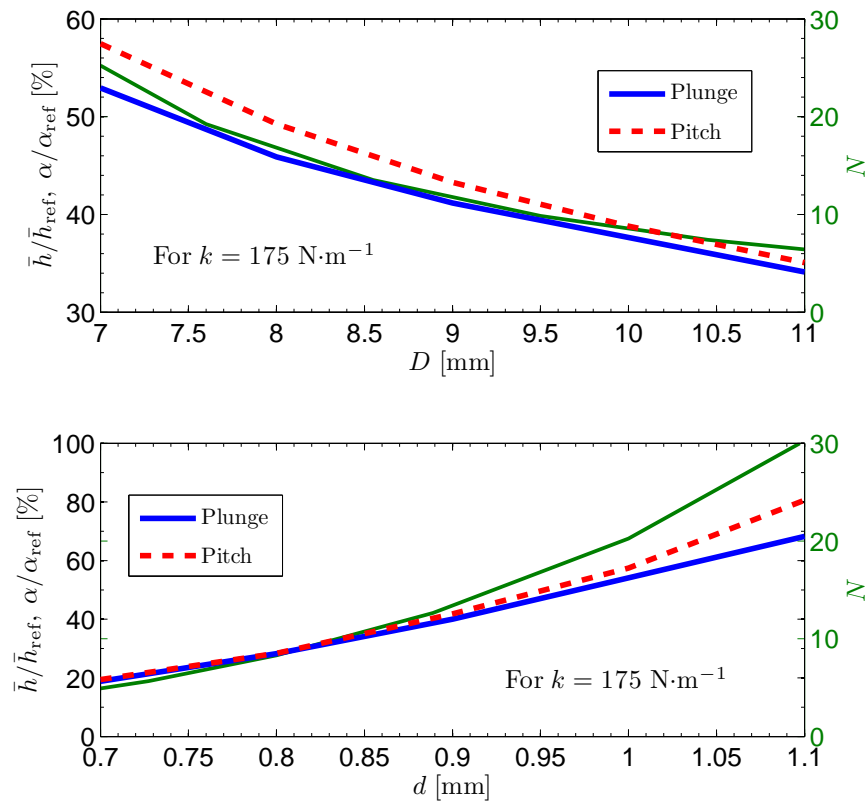


Figure 40 – Steady-state aeroelastic behavior for different SMA spring diameters (with constant stiffness and variable number of coils).

geometry with applied preload (which corresponds to the reference case with added preload, and exhibits intermediate amplitudes), and 3) for the case which yields the smallest aeroelastic amplitudes. Clearly, the effect of pseudoelastic hysteresis of the SMA springs on the aeroelastic behavior of the typical section can be enhanced by adjusting the spring geometric properties.

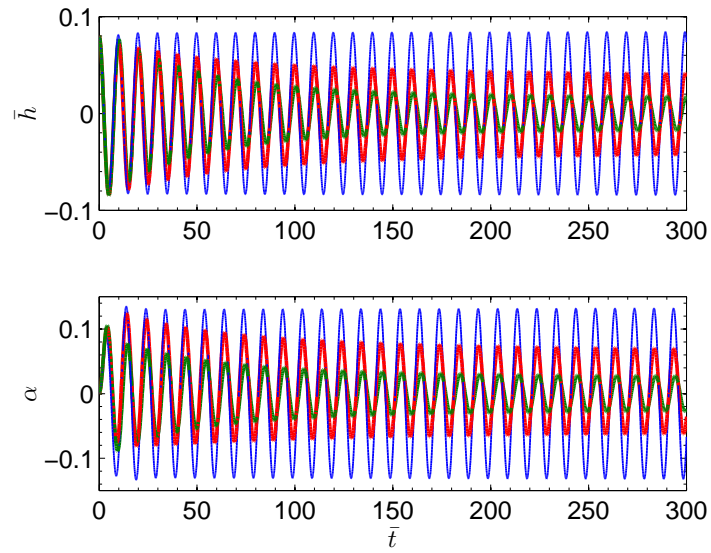


Figure 41 – Time response of the plunge and pitch DOFs for the reference case (without preload, with larger amplitudes), the nominal geometry with applied preload (with intermediate amplitudes) and the case which yields the smallest amplitudes.

Experimental Verification of the Aeroelastic Behavior of the Typical Section with SMA Springs

This chapter presents the experimental verification of the aeroelastic behavior of the typical section with SMA springs. The experiments were conducted at the Laboratory of Aeroelasticity of the Department of Aeronautical Engineering of the São Carlos School of Engineering (University of São Paulo, Brazil). In the next sections, all the apparatus, instrumentation and experimental tests are described.

7.1 General Description of the Experimental Apparatus

The experimental typical section model is slightly different from that proposed in Fig. 7 in such a way the rigid rod is placed along the chordwise direction, as displayed in Fig. 42 (only one SMA spring is shown for clarity). This way, some unnecessary extra mass (due to a larger rod) is avoided.

The blower wind tunnel of Fig. 43 was employed during the experimental tests of the 2-DOF typical section. A Pitot tube associated with a micromanometer (Vectus Importatum) is installed in the tunnel nozzle (of 50 x 50 cm). Fig. 44 shows the measured (and the corrected)

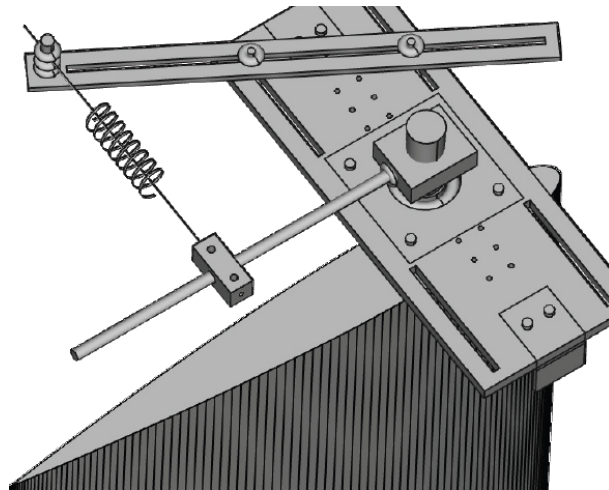


Figure 42 – Sketch of the typical section design employed for the experimental model.

airflow speed for a range of electrical motor rotations. The variation of airflow speed with electrical motor rotation is linear. Since the maximum rotational speed of the electrical motor is 850 rpm, the maximum airflow speed is around $26 \text{ m}\cdot\text{s}^{-1}$. The typical section is placed at the tunnel nozzle as shown in Fig. 45. Fig. 45 shows the experimental setup used for investigating the linear and nonlinear piezoaeroelastic behavior of the typical section. The plunge stiffness is due to the four elastic beams with clamped-clamped end conditions. The free ends of the elastic beams are connected to metal plates at the top and the bottom. Therefore, the experimental setup in this work slightly deviates from the ideal definition of a typical section (where springs are assumed massless), yielding the fixture mass (m_f) defined in Eq. (3.13). A shaft (or pitch axis) is mounted to the upper and the lower plates through a pair of bearings. The pitch stiffness is given by the combined SMA springs (displayed in Fig. 42).



Figure 43 – Blower wind tunnel (picture).

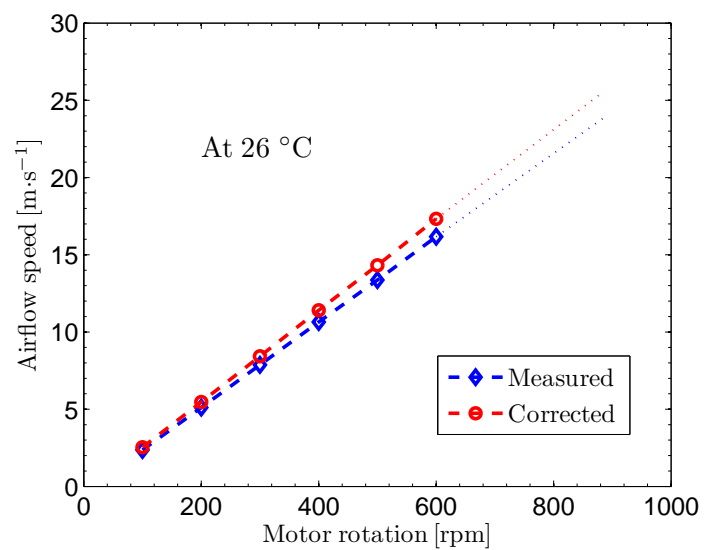


Figure 44 – Verification of the wind tunnel airflow speed capability.



(a)



(b)

Figure 45 – Photography of the typical section model. Views from the leading edge (a) and trailing edge (b).

7.1.1 Instrumentation Used in the Experiments

The pitch angle is measured by a two-channel HEDS-9000 optical incremental encoder (from Avago Technologies) with a two-inch HEDS-9000-T00 codewheel (from US Digital). The codewheel has 2000 counts per revolution, yielding 0.18 mechanical degrees per count. The encoder signal is read by a dSPACE DS1104 R&D controller board with a CP1104 connector panel (from dSPACE GmbH) through a digital input channel. The MATLAB/Simulink and ControlDesk softwares are used for controlling the data acquisition (not for the numerical simulation of the aeroelastic model with SMAs). In Simulink, the “DS1104_MASTER_ENC” and “DS1104_ENCOD_POS” blocks (from RTI dSPACE library) are placed in a model and adjusted according to the encoder type (a single-ended TTL device). The real-time operation of the dSPACE system (through the Simulink model) requires a few specific simulation parameters to be set: the use of a fixed-step solver, discrete time, no block reduction and no code reuse. The step size (of the Simulink model) had to be increased as the complexity of the model increased. In the case of this study, the smallest time step was found (by trial and error) as 8×10^{-4} s (the complete model reads one analogue channel and one digital channel simultaneously). For any smaller time steps, the data acquisition did not start (no apparent error or warning is thrown).

The plunge displacement is measured with a single strain gage¹ bonded on one of the beam springs of the plunge DOF. The strain gage is connected in a quarter-bridge scheme (thus with unity bridge factor²) to a HBM MGCplus AB22A amplifier system (from Hottinger Baldwin Messtechnik). The input characteristics (calibration curve) of the strain gage are adjusted by measuring the electrical signal from the sensor (with the MGCplus Assistant software) for no displacement and for a known displacement. One of the analogue outputs of the HBM system (the BNC connector at the front panel, Vo1) is connected to one of the analogue inputs of the dSPACE system, so that the data acquisition of both the rotary encoder (pitch DOF) and strain gage (plunge DOF) are performed over the same time basis. The HBM system analogue output is adjusted to range from -10 V up to +10 V as the plunge displacement (related to the strain gage

¹A CEA-13-240UZ-120 constantan alloy (Cu-Ni) strain gage from Micro-Measurements (Vishay Precision Group) with resistance of $120.0 \pm 0.3\% \Omega$ and gage factor of $2.120 \pm 0.5\%$ (at 24 °C).

²Hannah and Reed (1992).

deformation) goes from +50 mm up to -50 mm. The dSPACE system scales its analogue input by a factor of 0.1, yielding an input signal between -1 V and +1 V when read by the Simulink model. Thus, the scaling of the (dSPACE) input signal is corrected in the Simulink model for both the 0.1 scaling factor above and also according to the strain gage input characteristics. The total gain is 50.

The ambient temperature is measured with a thermocouple associated with a multimeter (Minipa ET-2082C). The ambient temperature is important for two reasons: 1) to estimate the local air density and therefore to correct the measurement of the airflow speed; 2) to estimate the temperature of the SMA springs, since no other form of thermal activation than the air temperature (*e.g.*, Joule heating) is used to obtain the austenitic phase.

7.2 Identification of the Experimental Parameters

7.2.1 SMA Properties

This section describes the experimental determination of the SMA properties. Before any aeroelastic test, two SMA springs were tested. One of them has a transformation temperature (reported by the manufacturer³) of 45 °C. The other, referred as “air temperature” by the manufacturer, 20 °C. Both springs have the same geometry. The wire diameter is 0.98 mm and the mean coil diameter is 13.78 mm. The number of active coils is 13.5 (arbitrarily chosen).

FORCE-DISPLACEMENT TESTS

A DC power supply (Instrutherm FA-2030) was used to heat the 45 °C spring through Joule heating. A universal testing machine (Instron 5985, dual column floor model for 250 kN) was used to provide displacement-controlled mechanical loadings to the springs. A load cell (Alfa SV-50, with 50 kg of capacity), smaller than that of the testing machine, was placed in a series configuration to provide accurate measurements on the order of about ten Newtons. The HBM amplifier system (described in Section 7.1.1) was used for the acquisition of the load cell data. A Canon EOS 50D 15.1 MP digital camera (with objective lenses 28, EF 135 mm) was used to

³Kellogg's Research Labs.

photograph the spring elongation during the tests. A FLIR ThermoCAM T360 infrared camera was used to verify the SMA temperature. A thermometer (Contemp UT325, along with a K-type⁴ thermocouple) was used to measure the ambient temperature. This apparatus is shown in Fig. 46.

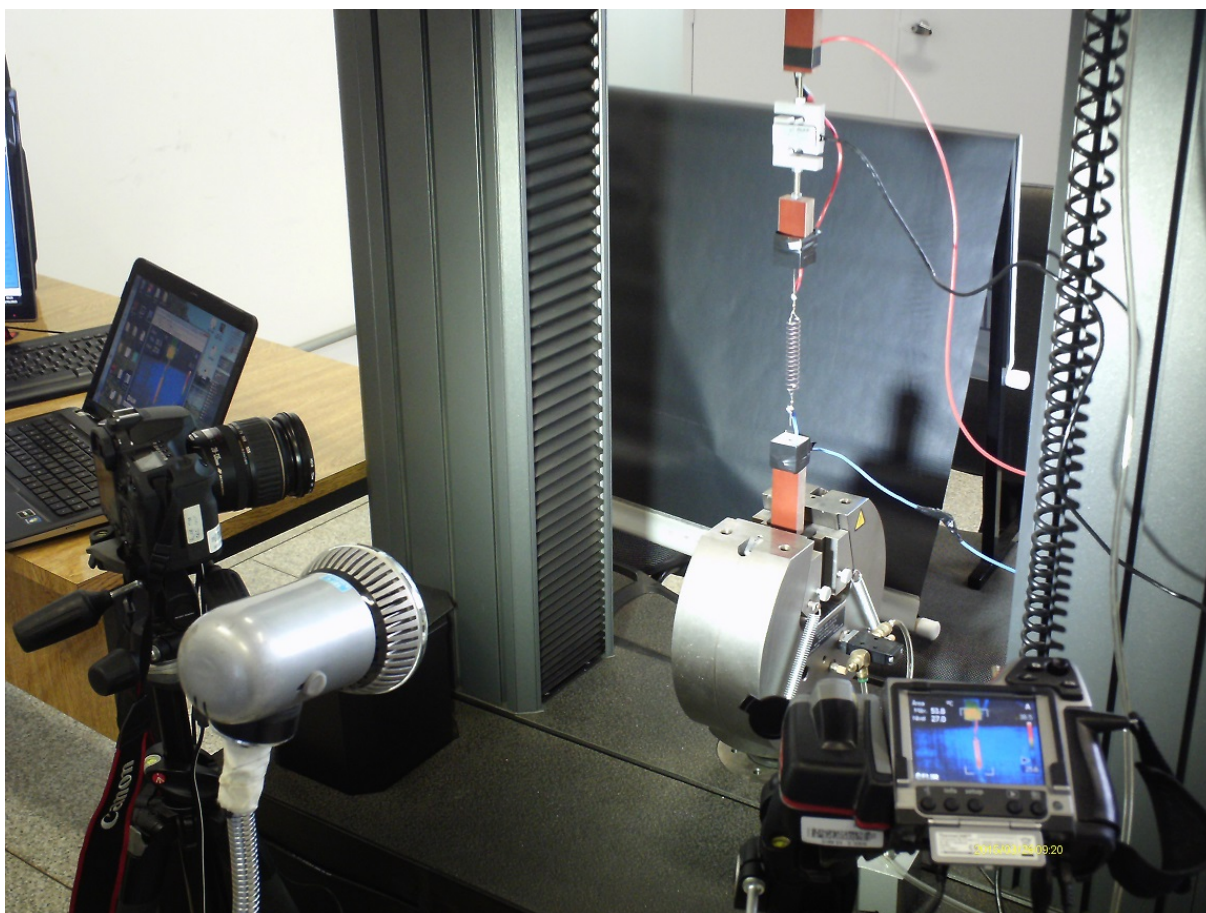
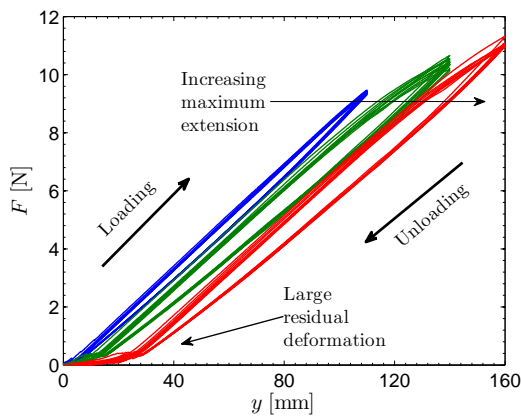


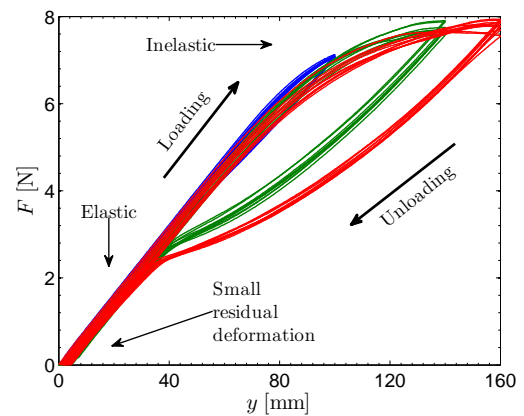
Figure 46 – Photography of the experimental apparatus for testing the SMA springs.

The force-displacement curves for the two tested SMA springs are displayed in Figs. 47(a) (for the 45 °C spring) and 47(b) (for the 20 °C spring). The springs were tested in three cases: with maximum extensions of 100, 140 and 160 mm. An arbitrary loading rate of $100 \text{ mm}\cdot\text{min}^{-1}$ was used in all cases. The tests were conducted at an ambient temperature of 26 °C. The springs were heated and allowed to cool down to the ambient temperature before the tests. Only the 45 °C spring was kept heated during the tests (after the initial heating and cooling procedure). An electrical current of 2 A was applied. As displayed in Fig. 48, the 45 °C spring experienced expressive temperature drops while being elongated due to convective heat transfer.

⁴Chromel (+), Alumel (-).



(a)



(b)

Figure 47 – Experimental force-displacement curves for the two tested SMA springs: the 45 °C spring in (a) and the 20 °C spring in (b).

Such temperature drops resulted in large (permanent) residual deformations because the SMA temperature went below A_f while the spring was being elongated (one should remember that there is a limit for the shape recovery). One may also observe that the area of the hysteretic loops of the 45 °C spring (Fig. 47(a)) are smaller than those for the 20 °C spring. This is an indication of $T \gg A_f$, which significantly increases the critical stresses (thus resembling to linear elastic behavior). Despite this, the SMA temperature went much below A_f with the elongation. Overall, the 20 °C spring exhibited a more attractive behavior and was chosen for the aeroelastic tests.

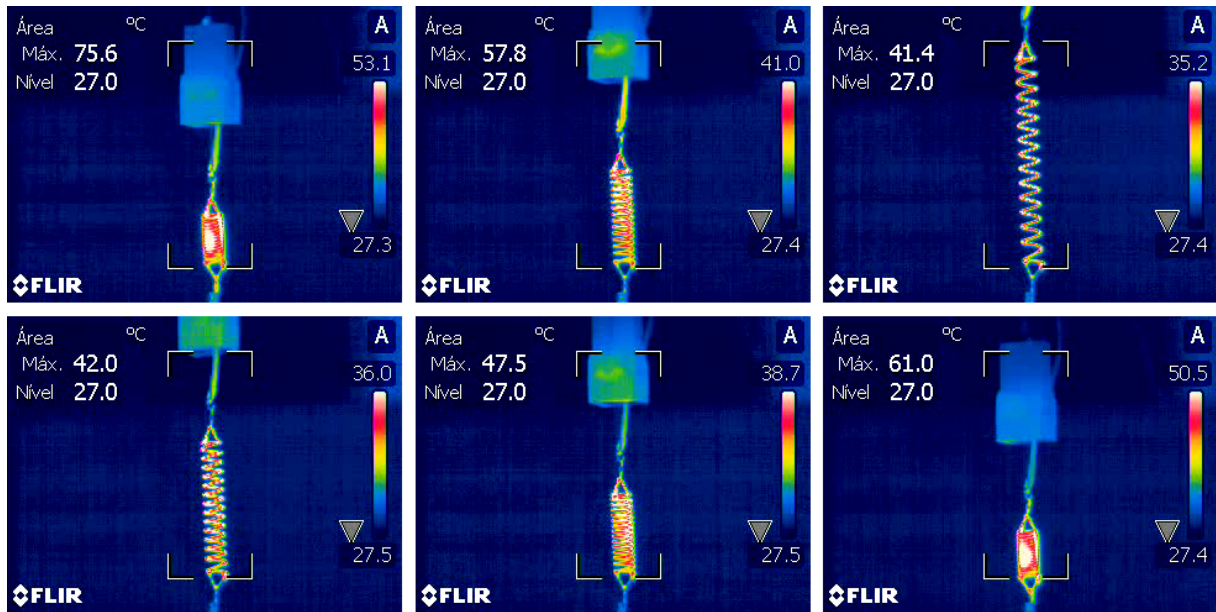


Figure 48 – Infrared pictures of the 45 °C SMA spring during the test.

ESTIMATION OF THERMO-MECHANICAL PROPERTIES

Based on the force-displacement curves of Fig. 47(b) (for the 20 °C spring at 26 °C of ambient temperature), some of the SMA properties can be estimated. The austenitic spring stiffness is estimated from the linear elastic region as $k_A \approx 85 \text{ N}\cdot\text{m}^{-1}$. From Eq. (2.26), the SMA fully-austenitic shear modulus is calculated as $G_A = 29.3 \text{ GPa}$. Hence, from Eq. (2.18), $D_A = 76.1 \text{ GPa}$. The fully-martensitic modulus is of little importance here (even for the simulations), but usually is two to three times lesser than the austenitic modulus. The force at the beginning of the forward phase transformation is about 5.5 N. From Eq. (2.20), τ_s^M is estimated as 209 MPa. The force at the end of the reverse phase transformation is about 2.4 N. Also from Eq. (2.20), τ_f^A is estimated as 91 MPa⁵.

The critical temperatures can also be estimated (for simulation purposes). Assuming $A_f = 20 \text{ °C}$ (reported by the manufacturer) and observing that usually $(A_f - 20 \text{ °C}) \leq M_s \leq (A_f - 10 \text{ °C})$ (*c.f.*, Table 3), one can expect $0 \text{ °C} \leq M_s \leq 10 \text{ °C}$. A mean value of $(A_f - M_s)$ for all of the property sets of Table 3 (excluding that of Gall et al. (1999)) yields about 14 °C. Equally spacing M_s , A_s and A_f (an arbitrary assumption), yields $M_s = 6 \text{ °C}$, $A_s = 13 \text{ °C}$ and $A_f = 20 \text{ °C}$.

⁵Although no DSC tests were conducted to determine the accurate phase transformation temperatures, $\tau_f^A > 0$ is a strong evidence of $T > A_f$ (*i.e.*, pseudoelasticity is ensured at room temperature, as required for the proposed aeroelastic application of this study).

Besides the critical stresses and temperatures, the stress-temperature slopes can also be estimated. Since τ_f^A is expected to be zero when the SMA temperature is the A_f temperature, and by assuming a linear relationship between the critical stresses and temperature (as depicted earlier in Fig. 3), the austenitic stress-temperature slope is estimated as $C_A = \tau_f^A / (T - A_f) \approx 15.1 \text{ MPa} \cdot \text{C}^{-1}$. Similarly, the martensitic slope is estimated as $C_M = (\tau_s^M - \tau_s^{\min}) / (T - M_s) \approx 7.6 \text{ MPa} \cdot \text{C}^{-1}$ by assuming $\tau_s^{\min} \approx 60 \text{ MPa}$ (commonly found in the literature, *c.f.*, Table 3). Moreover, τ_f^{\min} , ε_L and μ_P are assumed to be 100 MPa, 6.7% and 0.3, respectively (also from the literature). These values of stress, temperature and phase transformation slopes are useful for predicting the SMA behavior (when no DSC and/or temperature-controlled stress-strain tests are available), although they are not essential for the experimental tests.

Considering the experimental typical section, in order to keep the distance between the elastic axis and the SMA springs suitable, a stiffer spring (about twice the stiffness above) is desired. Therefore, the number of active coils is reduced to 7 (picture of Fig. 49, with extra coils for the attachment of the springs). The corresponding (austenitic) stiffness is estimated as $181 \text{ N} \cdot \text{m}^{-1}$ (from Eq. (2.26)). The spring deflection at the beginning of the forward phase transformation will be about 31 mm (Eqs. (2.21) and (2.24)). For such a spring deflection, the ratio y/N is about 4.4 mm per coil (the ratio is 11.4 mm for the largest hysteresis loop of Fig. 47(b)). For such level of deflection per coil, the simplified spring model of Section 2.4.2 (which neglects quantities such as the tensile component of stress in the spring) is considered valid for the purposes of this study. This new (stiffer) spring is the one employed in the pitch DOF of the typical section during the experimental tests to be described in Section 7.2.2.

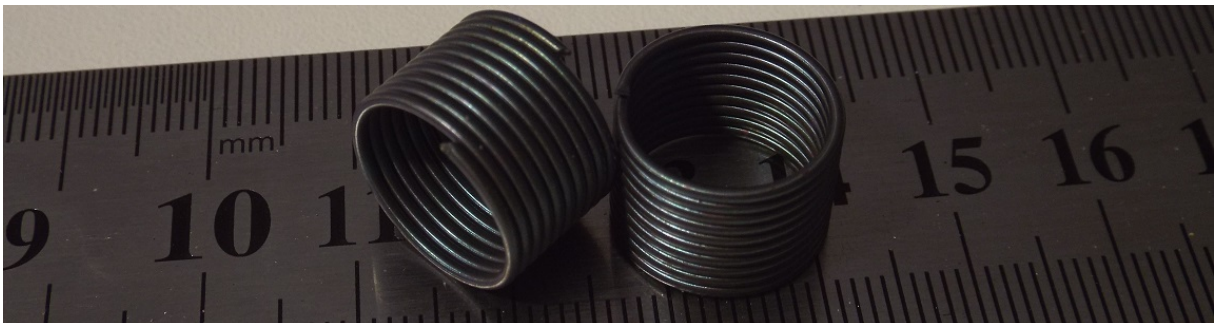


Figure 49 – Photography of the SMA springs used in the aeroelastic tests.

7.2.2 Typical Section Parameters

INERTIAL PROPERTIES

The airfoil mass is 0.789 kg (without the SMA fixture). The SMA fixture (the portion which rotates) adds 54 g to the airfoil mass. The total mass, including fixtures that attach the airfoil to the stationary frame, is 2.084 kg. This total mass is the mass that translates during plunge displacements. The CG was determined by equilibrating the typical section on a 1 mm-thick beam and measuring the distance between the mean thickness of that beam and the center of the elastic axis. Such a distance is 25.8 mm. A steel rod was placed inside the typical section (near the trailing edge, at the three-quarter chord length, and along the span length) to offset the CG in the aft direction, so that increasing the coupling between the plunge and pitch DOFs and therefore decreasing the linear flutter speed.

The moment of inertia (I_α) was determined by placing the typical section horizontally in a free-to-rotate condition (photography of Fig. 50). An arbitrary input angle was applied and the oscillation was measured (with the rotary encoder and the dSPACE system). The period of oscillation, T_α , was determined as 0.7413 s. By using a pendulum equation, $T_\alpha = 2\pi\sqrt{I_\alpha/(mgd)}$, where m is the rotating mass, g is the local gravity acceleration ($9.7876 \text{ m}\cdot\text{s}^{-2}$) and d is the distance between the elastic axis and the CG, the moment of inertia was determined as $3.0 \times 10^{-3} \text{ kg}\cdot\text{m}^2$.

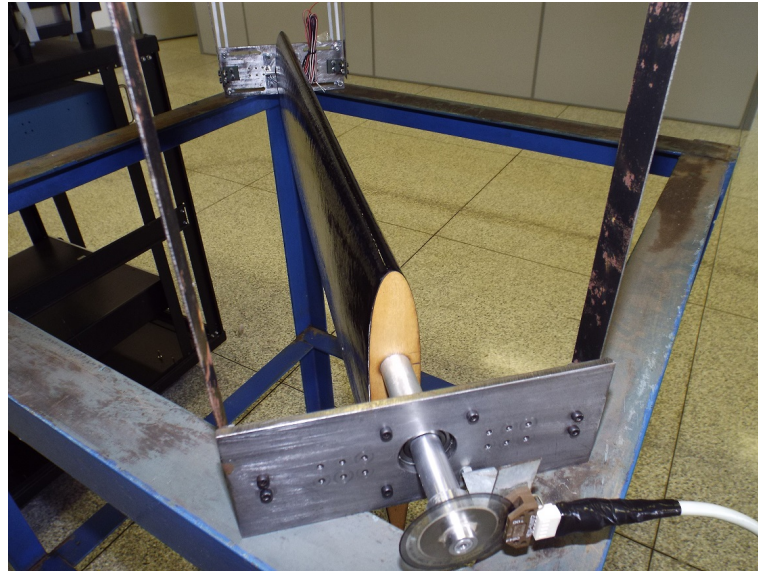


Figure 50 – Photography of the typical section in a pendulum configuration for the measurement of the moment of inertia.

DAMPING AND FREQUENCY PROPERTIES

From the logarithmic decrement method (CRAIG, 1981), the damping ratio may be approximated by,

$$\zeta = \frac{1}{2\pi} \ln \frac{u_P}{u_Q}, \quad (7.1)$$

for small damping ($\zeta < 0.2$) and where u_P and u_Q are two successive peak displacements. From free-vibration tests (Fig. 51) and by using Eq. (7.1), the damping ratio of the plunge DOF was determined as $\zeta_h = 0.0079$. Also from Fig. 51, the damped circular natural frequency of the plunge DOF is $\omega_h^d = 27.32 \text{ rad}\cdot\text{s}^{-1}$ (or 4.35 Hz).

The damping ratio is also defined as,

$$\zeta = \frac{c}{c_{\text{crit}}}, \quad (7.2)$$

where c is the damping coefficient and,

$$c_{\text{crit}} = 2m\omega_n = 2\sqrt{km}, \quad (7.3)$$

is the critical damping, in which ω_n is the undamped natural frequency (ω_h and ω_α for the plunge and pitch DOFs, respectively).

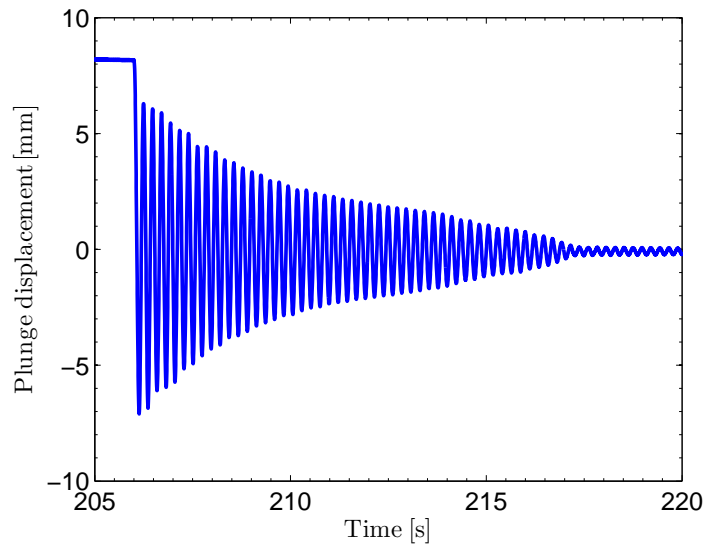


Figure 51 – Free-vibration test for the plunge DOF.

The experimental determination of the undamped natural frequency by using the static-displacement method considers a simple spring-mass system (CRAIG, 1981). A body of weight W (due to the local gravity g) is supported by a spring of stiffness k . The magnitude of the spring force equals to the weight (with opposite direction) for the static displacement u_{st} (at static equilibrium). Thus, $ku_{st} = mg$. Since $\omega_n^2 = k/m$, then $\omega_n^2 = g/u_{st}$. An arbitrary weight of 600 g (5.87 N for the local gravity $g = 9.7876 \text{ m}\cdot\text{s}^{-2}$) was hang on the plunge springs. A scheme with pulleys, one of them movable and attached to one end of the elastic axis, was used. A nylon rope⁶ (supporting the weight) was tied to the other end of the elastic axis. Thus, the actual weight experienced by the plunge springs was three times greater (17.62 N). The static displacement was measured as 8.25 mm. Thus, $\omega_h = 34.44 \text{ rad}\cdot\text{s}^{-1}$ (or 5.48 Hz). From Eq. (7.3), ω_h is calculated as $31.74 \text{ rad}\cdot\text{s}^{-1}$ (or 5.05 Hz).

The same test above was used for the calibration of the strain gage bonded on one of the plunge stiffness beams to measure the plunge displacement. The static displacement for increasing weight is displayed in Fig. 52. One should remember the plunge springs experience three times that loading due to the pulley configuration. This test is also useful for verifying the linearity of the plunge springs. The complete test, from the unloaded (and undeformed) initial state up to the end of the free-vibration test is displayed in Fig. 53.

⁶With diameter of 0.37 mm and load capacity of 8 kg.

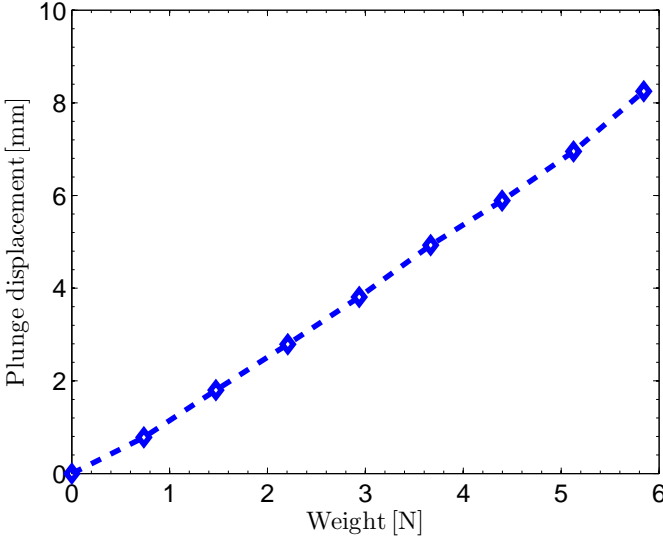


Figure 52 – Static displacement test for the plunge DOF.

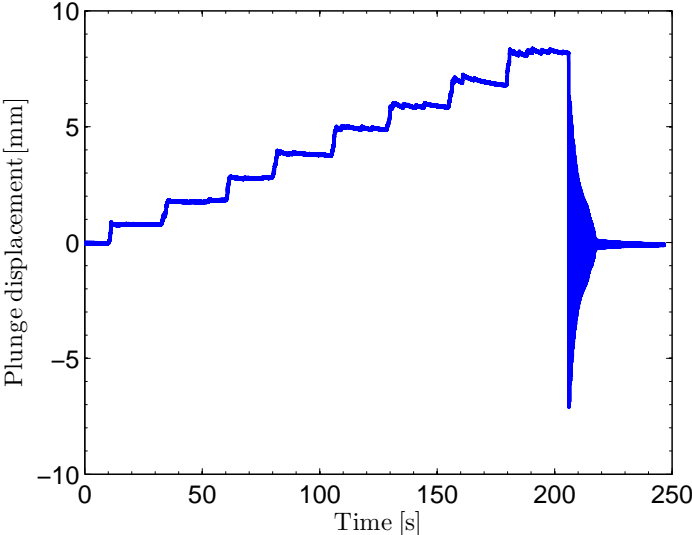


Figure 53 – Static displacement test followed by a free-vibration test.

Similar tests were performed for the pitch DOF. The SMA springs (with seven active coils) were attached to the plunge DOF fixture, so that the SMAs can move along with the plunge displacement (Fig. 54). The other ends of the SMAs were attached at 88 mm from the elastic axis by a rigid shaft (Fig. 55). The SMAs were tested at room temperature (26 °C), initially in the austenitic phase (heated before the tests to ensure the austenitic phase). From Fig. 56 and Eq. (7.1), the damping ratio of the pitch DOF is 0.0927. The damped period of oscillation is 0.3 s. The corresponding (damped) circular natural frequency is $\omega_{\alpha}^d = 20.94 \text{ rad}\cdot\text{s}^{-1}$ (or 3.33 Hz).

Although only the pseudoelastic behavior is of concern in this study, it is known (LIANG; ROGERS, 1997; Van Humbeeck, 2003) that the damping properties of SMAs change with the martensitic fraction⁷. For comparison purposes, however, the free-vibration test (of the pitch DOF with SMA springs) was performed also at low temperature. In such a test, the room temperature was 17 °C and the SMA springs were cooled down with ice for a few minutes before the test (the ice was removed right before the input angle). A more rigorous test with the particular SMAs of this study would require a room temperature below 0 °C to ensure a fully (twinned) martensitic phase. Thus, one may assume the SMAs had a mixed phase with austenite and twinned martensite (probably with more martensite than austenite due to the cooling procedure). The free-vibration test at low temperature is also displayed in Fig. 56. From Eq. (7.1), the damping ratio of the pitch DOF at low temperature (in the martensitic phase) is more than 0.15, which could be even greater if a fully martensitic phase was ensured.

Based on Fig. 57 and Eq. (2.26), the SMA spring (austenitic) stiffness is about $180 \text{ N}\cdot\text{m}^{-1}$, which is close to the expected (theoretical) value of $181 \text{ N}\cdot\text{m}^{-1}$. For an arbitrary load of 3.7 N (375 g), within the linear elastic regime, the static deflection of the SMA spring was measured as 20.1 mm. Thus, from the static displacement method, $\omega_{\alpha} = 22.04 \text{ rad}\cdot\text{s}^{-1}$ (or 3.51 Hz). From Eq. (7.3), the theoretical ω_{α} is $22.12 \text{ rad}\cdot\text{s}^{-1}$ (or 3.52 Hz). Fig. 57(a) includes a curve obtained from the rotary encoder data and another curve obtained from the comparison of pictures. Fig. 57(b) displays a picture of the test.

⁷Many of the SMA properties change with the martensitic fraction, such as the elastic properties, damping properties, electrical properties (*e.g.*, specific resistivity), acoustic properties, etc.

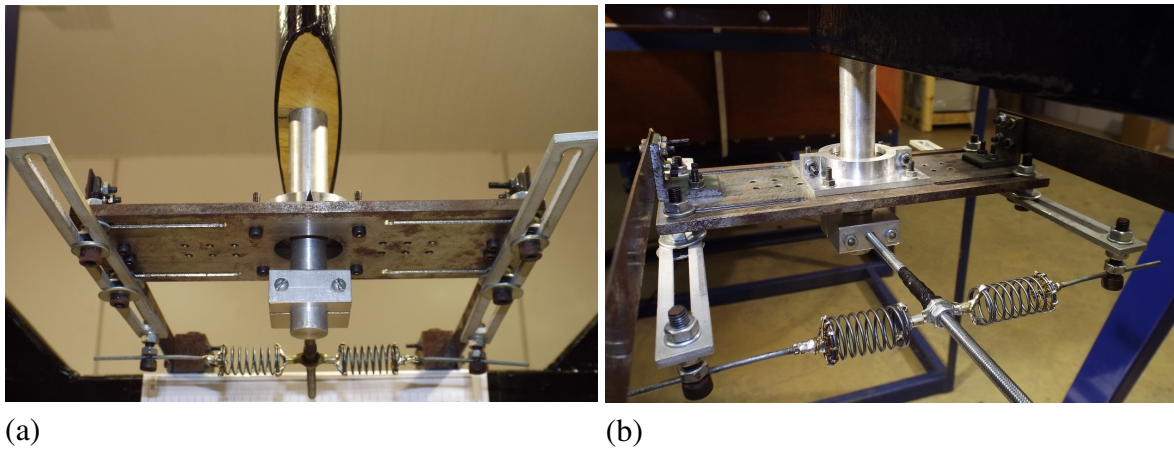


Figure 54 – Pitch DOF with SMA springs (picture). Views from the leading edge (a) and trailing edge (b).

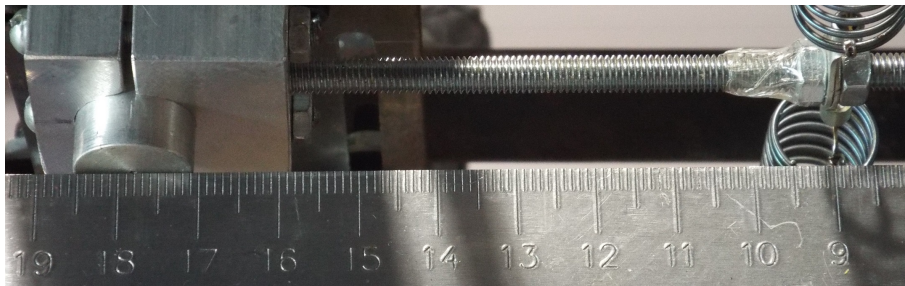


Figure 55 – Distance between the SMA springs and the elastic axis (picture).

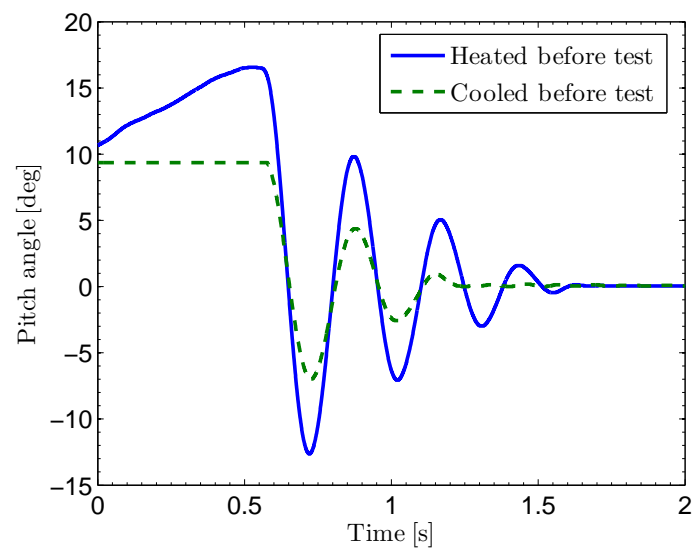
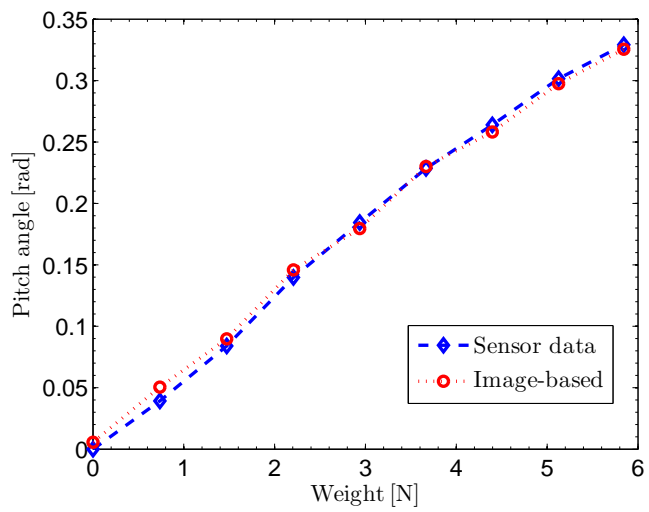
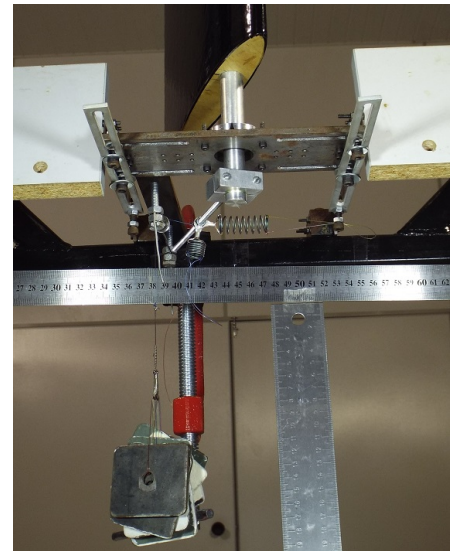


Figure 56 – Free-vibration tests for the pitch DOF.



(a)



(b)

Figure 57 – Static displacement test for the pitch DOF. Experimental data (a) and photography of the test (b).

7.2.3 Summary of the Experimental Model Parameters

The experimental aeroelastic parameters are summarized in Table 6. As well, the experimental SMA constitutive properties are displayed in Table 7.

Table 6 – Experimental aeroelastic parameters.

Symbol	Value	Unit	Description
b	0.125	m	Semichord length
l	0.50	m	Span length
c	-0.5	–	Elastic axis distance from midchord (per b)
x_α	0.2064	–	CG distance from elastic axis (per b)
m	0.843	kg	Rotating mass (pitch DOF)
m_t	2.084	kg	Translating mass (plunge DOF)
I_α	0.0030	kg·m ²	Moment of inertia
k_α	2.858	N·m	Equivalent pitch DOF stiffness
k_h	2100	N·m ⁻¹	Plunge DOF stiffness
ζ_α	0.0927	–	Damping ratio of the pitch DOF
ζ_h	0.0079	–	Damping ratio of the plunge DOF
ω_α	30.87	rad·s ⁻¹	Undamped pitch natural frequency
ω_h	49.91	rad·s ⁻¹	Undamped plunge natural frequency
r_α	0.4772	–	Radius of gyration (per b)

Table 7 – Experimental SMA constitutive properties.

Property	Value	Unit
M_s	279	K
A_s	286	K
A_f	293	K
C_M	$7.6\sqrt{3}$	MPa·K ⁻¹
C_A	$15.1\sqrt{3}$	MPa·K ⁻¹
σ_s^{\min}	100	MPa
σ_f^{\min}	170	MPa
ε_{res}	6.7	%
D_M	38	GPa
D_A	76	GPa
μ_P	0.3	–

7.3 Effect of Pseudoelastic Hysteresis on the Aeroelastic Behavior of a Typical Section

In this section, the aeroelastic behavior of the experimental typical section model with SMA springs is described. Different levels of preload are considered⁸. First, the experimental linear flutter speed is determined by measuring the pitch and plunge displacements for increasing air-flow speeds, arbitrary initial conditions and small preload applied to the SMA springs. After having determined the linear flutter speed, the aeroelastic displacements are measured for increasing airflow speeds at fixed preload values applied to the SMA springs. This way, the effects of pseudoelastic hysteresis of the SMA springs on the aeroelastic behavior are investigated. When the measured aeroelastic displacements become larger than the acceptable limits previously defined (in Section 4.2.2), the procedure is repeated for a slightly larger spring pre-deflection (yielding larger preload).

In all tests, the ambient temperature was between 24 °C and 27 °C (around 26 °C in most of the cases). Although the SMA springs were not directly exposed to the airflow, acrylic covers were employed to avoid forced convection effects. Moreover, a heat gun was employed to keep the temperature inside the acrylic cover constant (although the heat flux was not directed to the

⁸The preload level is always larger than the unloading phase due to the pitch angle (during half of one cycle of oscillation), so that the SMA springs are always in tensile loading.

springs). Before any test, the SMA springs were heated for about 10 s and allowed to cool down to the room temperature.

7.3.1 General Aeroelastic Behavior at the Flutter Boundary

In this section, the general aeroelastic behavior of the typical section is verified for airflow speeds that are around the theoretical linear flutter speed of a typical section defined by the aeroelastic parameters of Table 6. First, a small preload is applied to the SMA springs so that linear aeroelastic behavior (flutter) can be observed (since the SMA springs will be working in the linear elastic region). Later, the preload level is increased so that nonlinear aeroelastic behavior (stable LCOs) can be observed due to the pseudoelastic hysteresis of the SMA springs.

SMALL PRELOAD (LINEAR AEROELASTIC BEHAVIOR)

Although SMA elements exhibit nonlinear behaviors when phase transformations are taking place, it was shown in previous chapters that SMAs can also exhibit linear elastic behaviors for small preloads. This way, the typical section behaves as a linear aeroelastic system (for small preload values) and has a well-defined flutter boundary (or linear flutter speed). From linear theory (*e.g.*, eigenvalue analysis), the theoretical linear flutter speed of the experimental typical section (with the parameters of Table 6) is $13.3 \text{ m}\cdot\text{s}^{-1}$. In this section, the aeroelastic behavior of the typical section is experimentally verified for airflow speeds around the flutter boundary.

A pre-deflection of 17 mm is applied to the SMA springs considered in the experimental typical section model of this work. Since the spring stiffness is $85 \text{ N}\cdot\text{m}^{-1}$ in the linear elastic regime (austenitic), the preload is approximately 3 N. Since the considered SMA springs undergo stress-induced phase transformation for mechanical loads of 5.5 N or larger (Section 7.2.1), the pitch angle during the wind tunnel tests should not exceed 9 degrees to ensure linear elastic behavior (or 14 mm of spring deflection due to the pitch angle). Since the natural length of the SMA springs is 11 mm^9 , the actual limit is slightly smaller to avoid reaching a state of compactation of the springs.

⁹The difference from the natural length of the previous tests (7 mm) is due to the stabilized behavior of the SMA springs after a number of cycles.

The experimental verification is performed for a range of airflow speeds around the theoretical linear flutter speed. At each airflow speed, initial plunge displacements are applied to the typical section (from small displacements up to larger displacements) and the time response measured. If stable aeroelastic behavior is verified (damped oscillations), the airflow speed is slightly increased and the procedure is repeated. As the airflow speed approaches the theoretical critical one, the typical flutter behavior is verified (defining the experimental linear flutter speed). Fig. 58 shows the time history of the plunge displacement at different airflow speeds (slightly below the linear flutter speed). Fig. 59 shows the plunge and pitch displacements at $13.0 \text{ m}\cdot\text{s}^{-1}$ (slightly above the linear flutter speed).

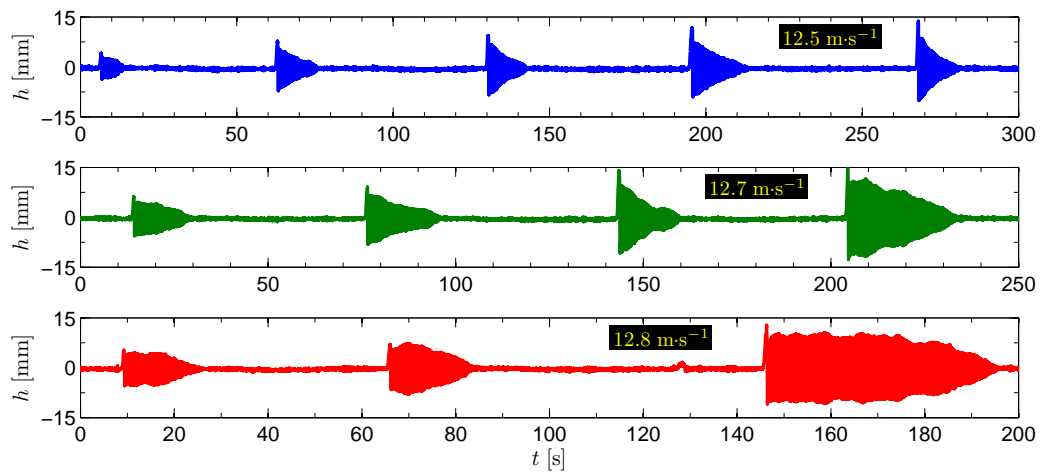


Figure 58 – Experimental plunge displacement in time for different airflow speeds (slightly below the linear flutter speed) and small preload applied to the SMA springs.

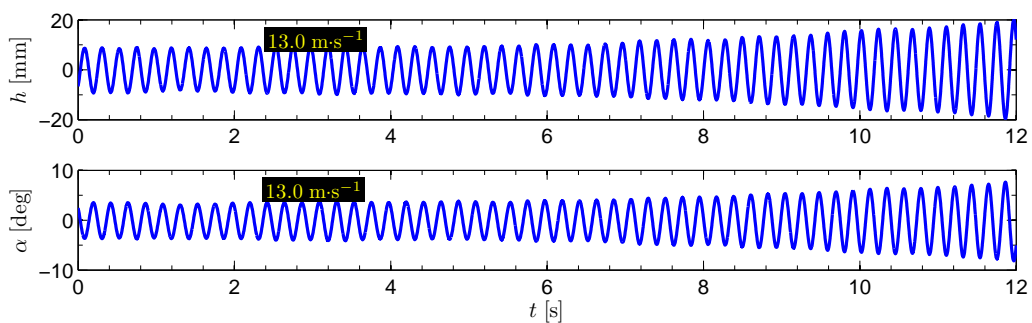


Figure 59 – Experimental plunge and pitch displacements in time at slightly above the linear flutter speed and for small preload applied to the SMA springs.

In Fig. 58, the time history of the plunge displacement for the airflow speed of $12.5 \text{ m}\cdot\text{s}^{-1}$ shows that the system is stable. Although the typical section is stable at $12.7 \text{ m}\cdot\text{s}^{-1}$ and

$12.8 \text{ m}\cdot\text{s}^{-1}$, the decaying behavior is different from the one observed at $12.5 \text{ m}\cdot\text{s}^{-1}$ (since the total damping is larger in this case due to aerodynamic damping). Moreover, at $12.8 \text{ m}\cdot\text{s}^{-1}$ the displacements are around the initial condition for a time period before the oscillations are damped out. It is also possible that the typical section settles onto a flutter-like behavior around that airflow speed for large enough initial condition (DOWELL, 2015). At $13.0 \text{ m}\cdot\text{s}^{-1}$ (Fig. 59), the typical section is unstable. However, it is important to say that in some cases the oscillations are damped out at this airflow speed and in some cases the amplitudes slightly increase along the time. This is expected since the typical section is marginally stable at the flutter boundary. The unstable cases (with increasing amplitudes) are an evidence of linear behavior, although SMA springs are considered in the model (without any phase transformation in the SMA springs for the considered preload level).

LARGER PRELOADS (NONLINEAR AEROELASTIC BEHAVIOR)

The preload applied to the SMA springs is increased for the next tests so that stress-induced phase transformations can take place at small aeroelastic displacements. This way, the nonlinear aeroelastic behavior of the typical section (due to the pseudoelastic hysteresis of the SMA springs) can be verified for airflow speeds around the flutter boundary.

A pre-deflection of 25 mm is imposed to the SMA springs, which corresponds to about 4.5 N of preload (or about 80% of the critical preload). Fig. 60 displays the time history of the plunge displacement measured for a range of airflow speeds. Self-sustained aeroelastic oscillations are observed at the airflow speed of $13 \text{ m}\cdot\text{s}^{-1}$, as in the previous case (with small preload). However, the amplitudes at $13 \text{ m}\cdot\text{s}^{-1}$ in Fig. 59 are growing over time while in Fig. 60 the amplitudes (also at $13 \text{ m}\cdot\text{s}^{-1}$) are constant, evidence of the aeroelastic behavior of the typical section being modified by the pseudoelastic hysteresis of the SMA springs.

The aeroelastic behavior of the typical section with SMA springs is also verified for different initial conditions. In agreement with the numerical predictions of Section 5.3.1, the typical section settles onto LCOs with amplitudes that depend mainly on the level of preload. Such a behavior is displayed in Fig. 61 for the same conditions of Fig. 60 (and $13 \text{ m}\cdot\text{s}^{-1}$).

The post-flutter regime is experimentally verified in the next section.

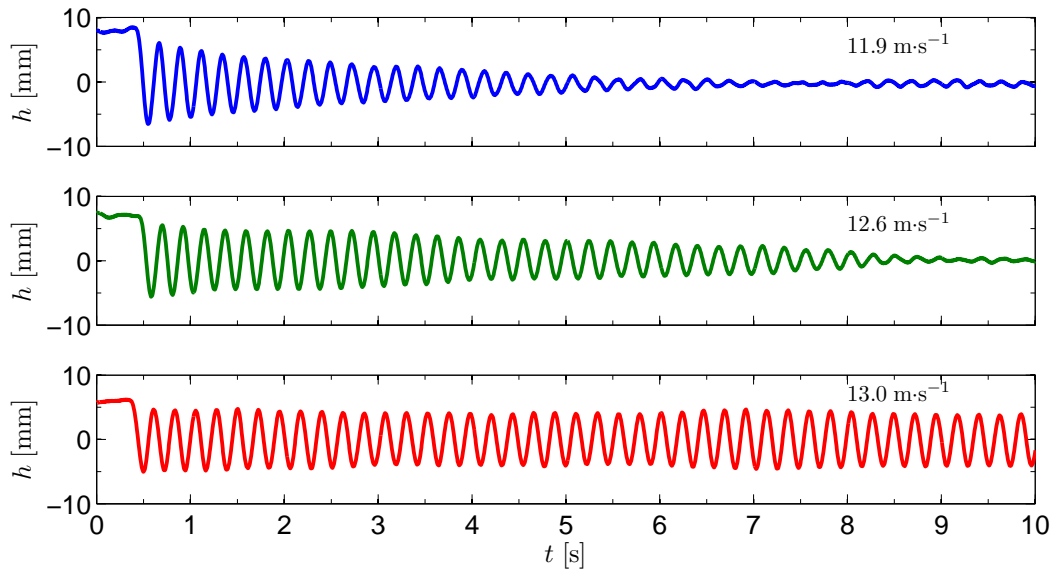


Figure 60 – Experimental plunge displacement in time for different airflow speeds (constant preload level).

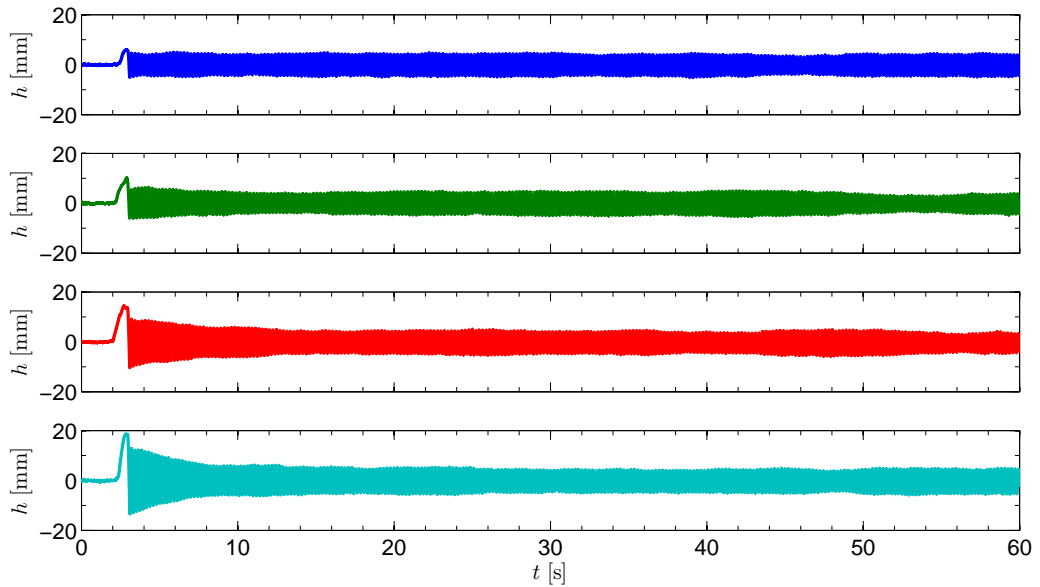


Figure 61 – Aeroelastic behavior of the typical section with preloaded SMA springs at the flutter boundary for different initial conditions.

7.3.2 Post-Flutter Behavior of the Typical Section

Fig. 62 shows the time history of the plunge displacement over a range of airflow speeds. The preload applied to the SMA springs is 4.5 N (the same preload of Figs. 60 and 61) and the plunge displacement is acquired for a few minutes for each airflow speed. Persistent and bounded oscillations (LCOs) are observed due to the pseudoelastic hysteresis of the SMAs. If linear steel springs were employed, the linear aeroelastic system would be unstable for such range of airflow speeds. Therefore, stable LCOs replace unstable oscillations due to the hysteretic behavior of the SMA springs. Fig. 63 displays a detailed view of plunge displacement at different airflow speeds of Fig. 62. The plunge amplitude of the LCO increases with increasing airflow speed. The system is unstable after $13.7 \text{ m}\cdot\text{s}^{-1}$.

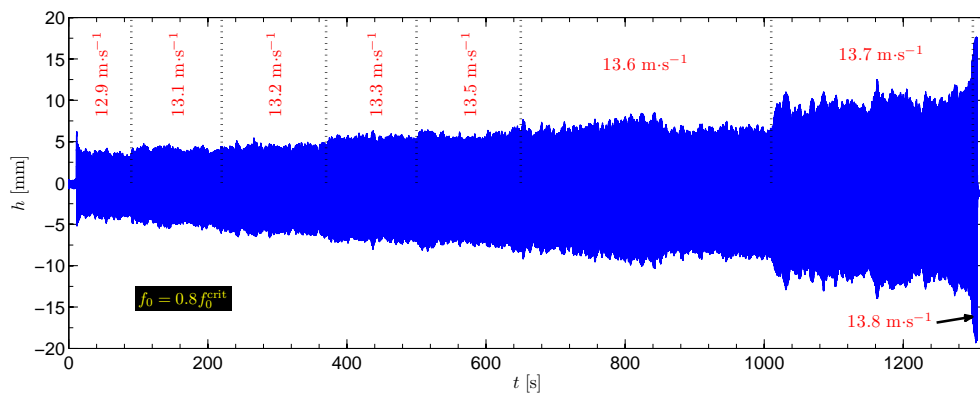


Figure 62 – Experimental plunge displacement for 80% of the critical preload and increasing airflow speed.

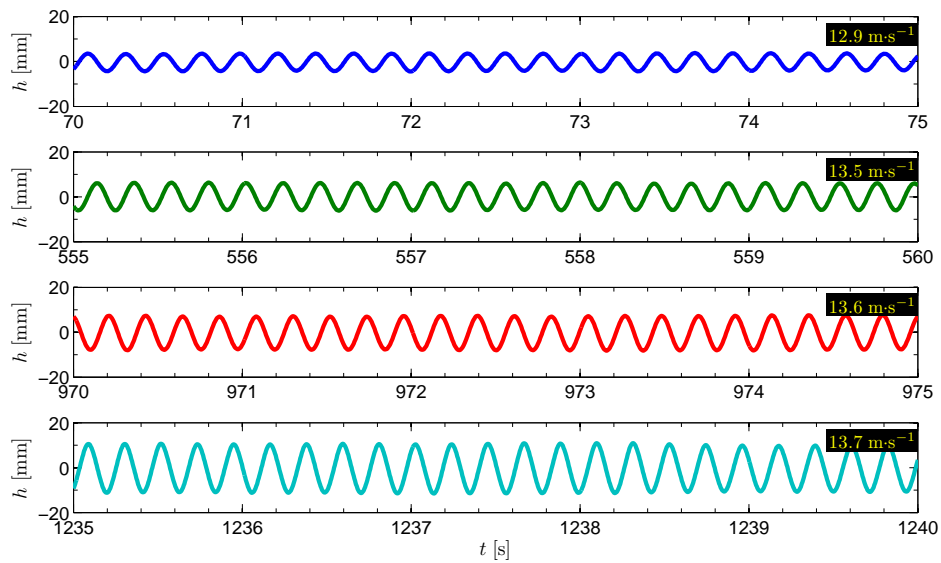


Figure 63 – Experimental plunge displacement for 80% of the critical preload and increasing airflow speed (detail).

Fig. 64 displays the plunge displacement for the SMA springs with a pre-deflection of 28 mm (about 5.0 N of preload, or about 90% of the critical value). Fig. 65 shows detailed views of the bounded oscillations (stable LCOs) for some of the tested airflow speeds. Since the employed preload is 90% of the critical one, smaller pitch displacements (if compared to the previous case, preload of 4.5 N) leads to phase transformation and pseudoelastic hysteresis of SMA springs. Therefore, the range of airflow speeds with LCOs of acceptable amplitude is also increased (the maximum airflow speed is $14 \text{ m}\cdot\text{s}^{-1}$).

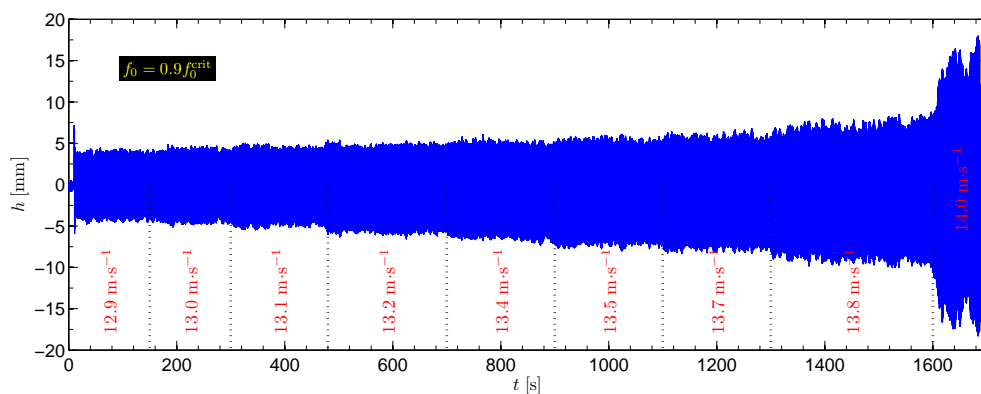


Figure 64 – Experimental plunge displacement for 90% of the critical preload and increasing airflow speed.

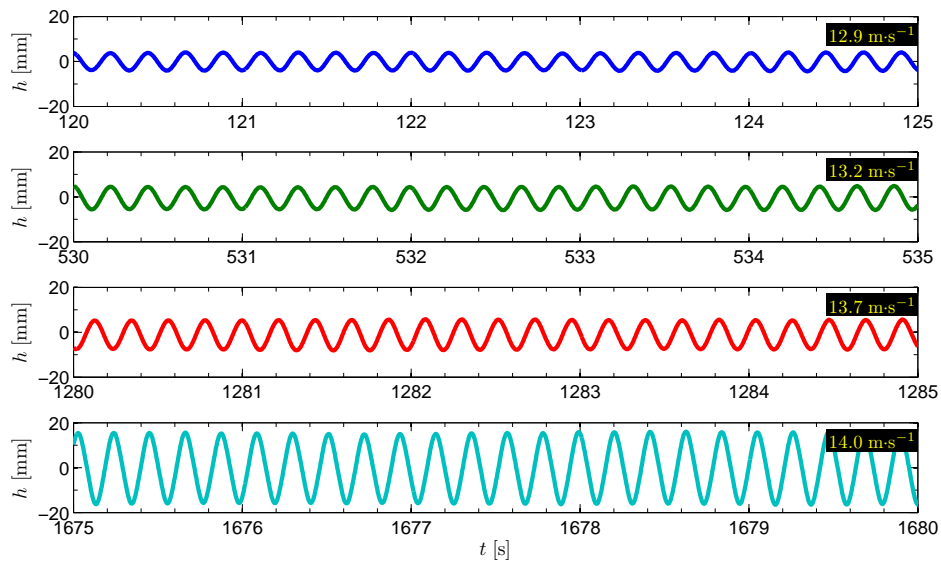


Figure 65 – Experimental plunge displacement for 90% of the critical preload and increasing airflow speed (detail).

The preload is further increased to 5.5 N and the procedure is repeated. Fig. 66 displays the plunge displacement for a pre-deflection of 31 mm (which yields a preload around the critical value of 5.5 N). As in the previous cases, stable LCOs replace the unstable aeroelastic behavior in the post-flutter regime. Fig. 67 shows detailed views of LCOs of some of the airflow speeds. The maximum airflow speed with LCOs of acceptable amplitudes is increased to $14.6 \text{ m}\cdot\text{s}^{-1}$, since any pitch displacement induces phase transformation and pseudoelastic hysteresis.

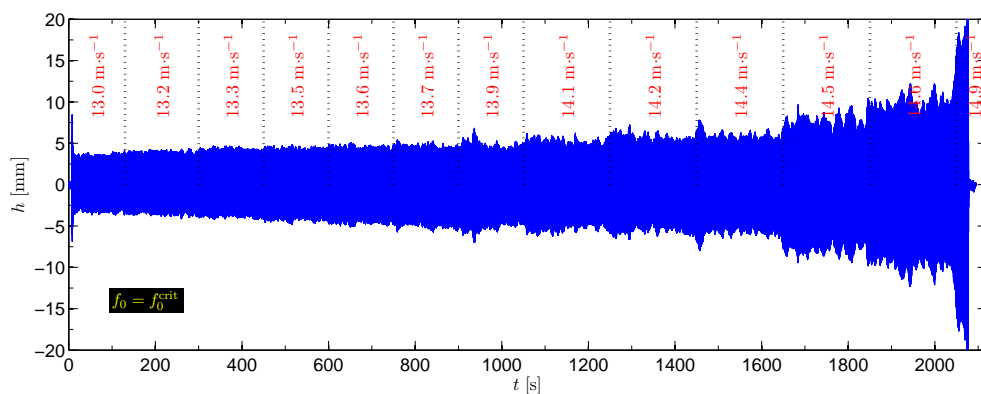


Figure 66 – Experimental plunge displacement for the critical preload and increasing airflow speed.

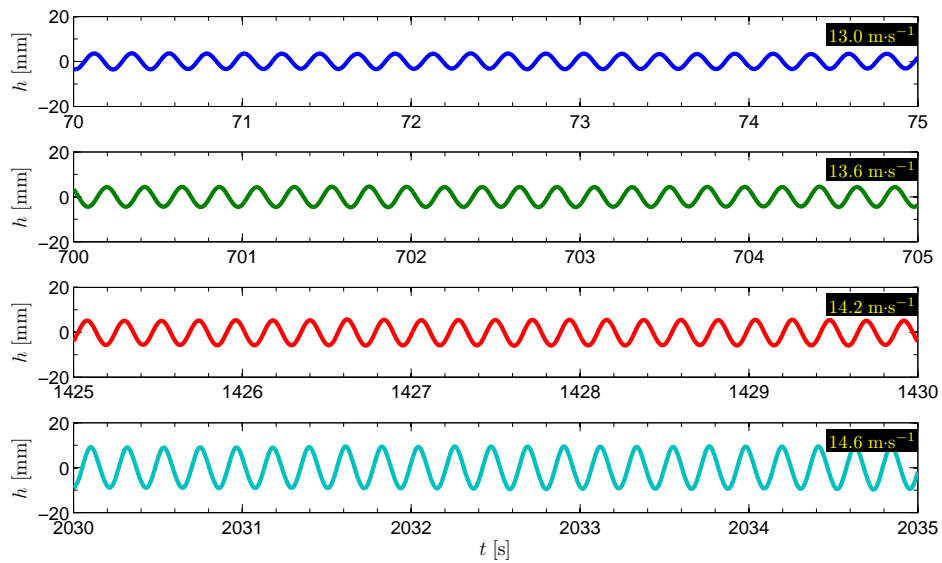


Figure 67 – Experimental plunge displacement for the critical preload and increasing airflow speed (detail).

Fig. 68 displays the plunge displacement for a pre-deflection of 34 mm, which yields a preload slightly above the critical value (since the SMA springs are operating in the martensitic plateau for such a preload condition). As well, details are shown in Fig. 69.

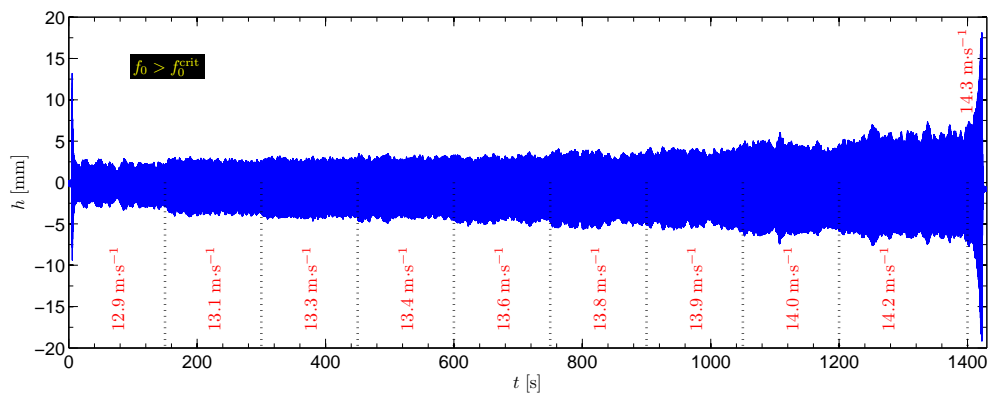


Figure 68 – Experimental plunge displacement for slightly above the critical preload and increasing airflow speed.

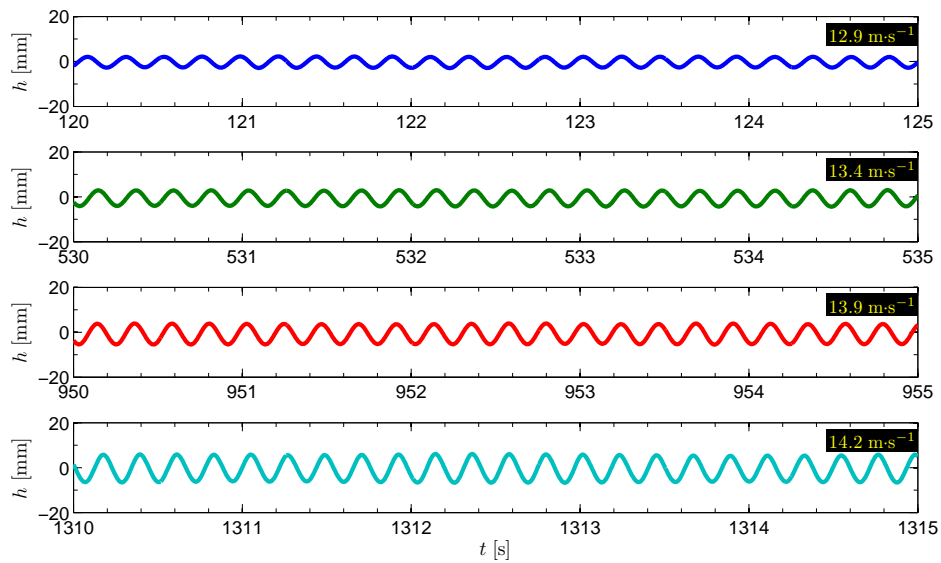


Figure 69 – Experimental plunge displacement for slightly above the critical preload and increasing airflow speed (detail).

The root mean square (RMS) of the plunge displacement with increasing airflow speed is shown in Fig. 70. The bifurcation plots of Fig. 70 include all the previous cases of Figs. 62 to 69. The range of airflow speeds with LCOs of acceptable amplitudes increases with increasing preload values (applied to the SMA springs). Moreover, for each airflow speed, the amplitude of LCOs decrease with increasing preload due to the pseudoelastic behavior of SMAs. Also, it is worth observing that the preload level does not affect the linear flutter speed (since the same preload is applied to both SMA springs). The RMS value of the plunge displacement is considered due to the amplitude variations (related mainly to uncontrolled environmental conditions which affect the temperature of the SMA springs).

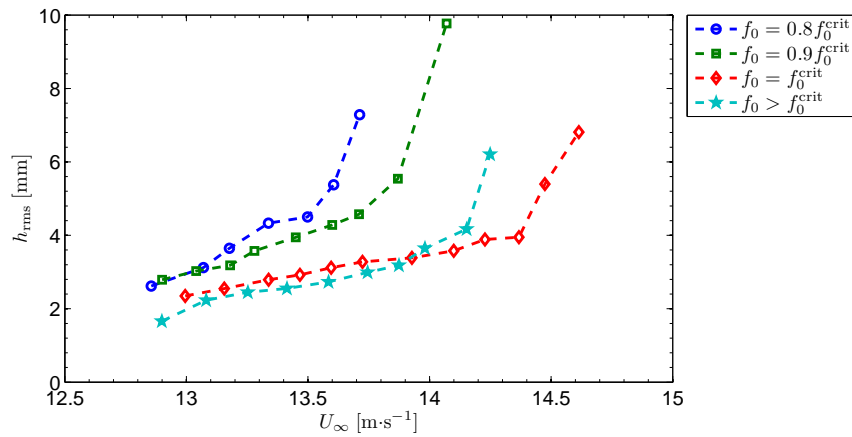


Figure 70 – RMS amplitudes of the plunge displacement for increasing airflow speeds and different preload levels.

Fig. 71 displays a detail of Fig. 70 that includes simulation results for the SMA properties of Table 7. The discrepancies can be assigned mainly to the SMA properties being unknown (the properties were estimated from a simple tensile test, therefore not rigorously determined). It is interesting to note, however, that the experimental behavior is superior to the predicted behavior (in terms of smaller LCO amplitudes) at larger airflow speeds.

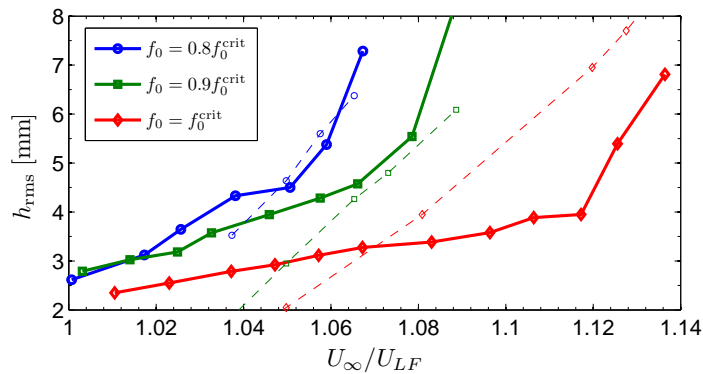


Figure 71 – Detail of the RMS amplitudes of the experimental plunge displacement for increasing airflow speeds and different preload levels along with simulation results.

7.3.3 Further Discussions on the Experimental Behavior of the Typical Section with SMA Springs

Undesired temperature variations are pointed as the main cause of the unexpected behaviors observed during the experimental tests (especially the changes in the amplitudes of the aero-

lastic displacements, shown in the previous section). One may remember from the previous chapters that the critical stresses for phase transformations increase with increasing temperature. This way, as the temperature of the SMA springs increases, an ongoing phase transformation (or in the proximity of taking place) may be ceased (or delayed) as well as stable LCOs replaced by unstable flutter oscillations. As the pitch angle increases or the temperature drops, the phase transformations can restart, transforming the unstable flutter oscillations once again into stable LCOs (the amplitudes may also become excessively large before the phase transformations resume, yielding an unacceptable case). It is also possible that the temperature of the SMAs decreases along a test, allowing that the stress-induced phase transformations take place earlier (and possibly improving the effects of the pseudoelastic hysteresis on the aeroelastic behavior of the typical section). On the other hand, an excessive temperature drop may avoid the complete recovery of the austenitic phase of the SMAs. In such a circumstance, unexpected aeroelastic behavior may also take place (possibly allowing the onset of unstable oscillations). Thus, a thermally isolated chamber for the SMA springs improves the experimental behavior of the typical section.

The overall behavior of the typical section with SMA springs, however, is in good agreement (qualitatively) with the numerical predictions of the previous chapters (in particular, to those of Fig. 26), in spite of the SMAs considered in the experimental tests having different constitutive properties. As observed in Fig. 26, different SMA constitutive properties yield distinct aeroelastic behaviors and the effects of preloaded SMA springs (with distinct sets of parameters) are similar in all cases (*i.e.*, most of the considered property sets are able to reduce the aeroelastic amplitudes at the flutter boundary and also to allow stable post-flutter regimes, as observed for the SMA springs considered in the experimental tests). One should note that the theoretical model (and associated numerical predictions) presented in the previous chapters predicts similar aeroelastic behavior verified during the experimental tests, although different SMA springs (with some unknown constitutive properties) are employed in each case (numerical simulations and experiments).

As final remarks on the experimental behavior of the SMA springs, it is interesting menti-

oning that the same SMA springs were used for all tests (including several tests which are not reported here). Spring replacement was not necessary since no SMA spring failure was observed or exhibited degradation along the tests (a few hundreds of tests were performed, and the total time operating under LCOs is around a few hours). The SMA springs were kept under pre-tensioning for several days (reaching a few weeks). However, no significant permanent deformation in addition to that due to the first dozens of loading cycles (before cyclic stabilization) was observed. One should also remember that no excessively large preload or pitch angles were applied to the SMA springs, thus yielding only partial phase transformations.

*Airfoil-Based Piezoelectric Energy
Harvesting by Exploiting the
Pseudoelastic Hysteresis of Shape
Memory Alloy Springs*

The analysis of an electromechanically coupled typical section with SMA springs for wind energy harvesting is addressed in this chapter. A 2-DOF (namely, pitch and plunge) airfoil is considered and piezoelectric coupling is added to the plunge DOF¹. A load resistance is assumed in the electrical domain of the problem to estimate the electrical power output. As in the previous chapters, SMA coil springs are modeled in the pitch DOF of the typical section. A Ni-Ti alloy that exhibits pseudoelasticity at room temperature is assumed, avoiding the use of external power sources. The effects of preload values of the SMA springs and resistive power generation on the aeroelastic behavior of the wind energy harvester are investigated at the flutter boundary and in a post-flutter regime. Since the nonlinear kinetics of the austenite-to-martensite phase transformation changes the typical linear flutter behavior to stable LCOs over a range of airflow speeds, an innovative and important source of persistent electrical power is presented.

The assumption of constant values of shear strain, shear stress and martensitic fraction in the

¹The same electromechanical properties of Sousa et al. (2011) are assumed in this work.

cross-section of the coiled SMA wire is employed in this chapter, as in Chapter 4. As well, the same aeroelastic parameters and spring geometry of Chapter 4 are assumed here (Table 2). Most of the SMA constitutive properties are also the same (those of Table 1). The only differences are in the critical temperatures for phase transformation, since superelastic springs are assumed in this case. The difference is simply to illustrate that no power consumption mechanisms would be required in a practical application. The same electrical and electromechanical properties of Sousa et al. (2011) are assumed here (*i.e.*, equivalent capacitance of a parallel association of the piezoceramic layers, 120 nF, and the electromechanical coupling term, $1.55 \times 10^{-3} \text{ N}\cdot\text{V}^{-1}$). Such parameters are, however, based on previous works from the literature (ERTURK; INMAN, 2008; ERTURK et al., 2010). The stress-temperature behavior of the considered SMA is displayed in Fig. 72.

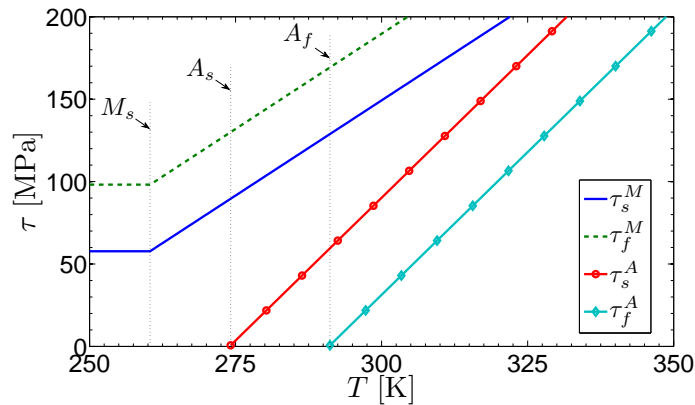


Figure 72 – Stress-temperature relationship of the SMA considered in the energy harvesting problem.

8.1 Electroaeroelastic Behavior of the Typical Section with SMA Springs at the Flutter Boundary

The electroaeroelastic behavior of the airfoil-based wind energy harvester with SMA springs is investigated at the linear flutter speed of the 100 kΩ resistive load (taken arbitrarily²) and for increasing preload applied to the SMA springs. Fig. 73 shows the shear stress behavior of the SMA spring with its elongation. The dashed line is the elongation required for a complete

²The same resistive load is used in Sousa et al. (2011), so that some comparisons can be made.

stress-induced phase transformation (obtained by using the constitutive relationship with a prescribed stress input). The continuous line represents the shear stress due to the pitch angle at the linear flutter speed of the 100 k Ω resistive load (11.85 m·s⁻¹). It is clear that no phase transformation is predicted since the SMA springs are operating in the linear elastic region. The elastic restoring mechanism is due to linear elastic moment (with the fully austenitic shear modulus) and the typical section behaves as a linear aeroelastic system. Preload is then assumed to bias the shear stress towards the critical value for phase transformation, so that the SMA pseudoelastic hysteresis can be effectively exploited.

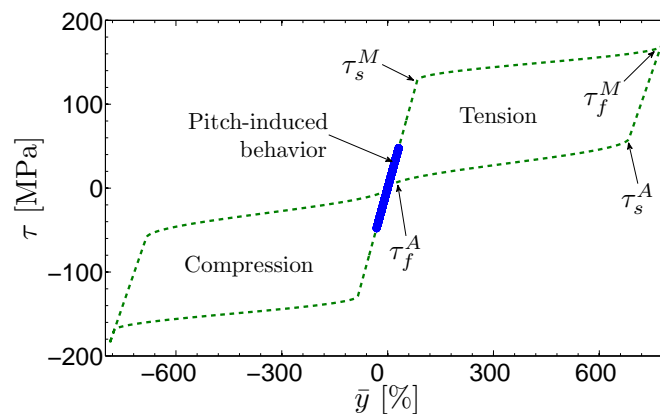


Figure 73 – Shear stress with the elongation of the SMA springs in the energy harvesting problem.

The peak amplitudes of the pitch angle and plunge displacement for the case above and increasing preload is displayed in Fig. 74. For $f_0 \leq 3$ N, no phase transformation is achieved and the linear aeroelastic behavior is verified. For $f_0 > 3$ N, stress-induced phase transformations take place. In such a case, flutter oscillations are converted into stable LCOs, the dependence on the initial conditions disappear and the amplitudes of the LCOs decrease for increasing preload. Figs. 75(a) and (b) display the aeroelastic response over time for three different preload conditions (from Fig. 74). Fig. 75(c) displays the electrical power output for the preload values of 3.5 N and 4.0 N.

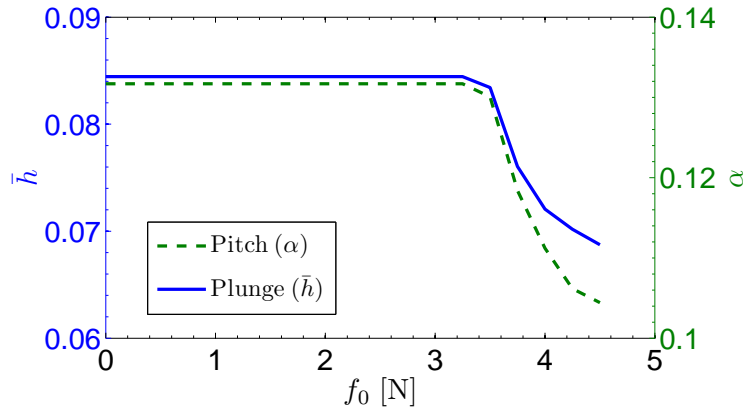


Figure 74 – Steady-state plunge displacement (left axis, continuous line) and pitch angle (right axis, dashed line) in the energy harvesting problem.

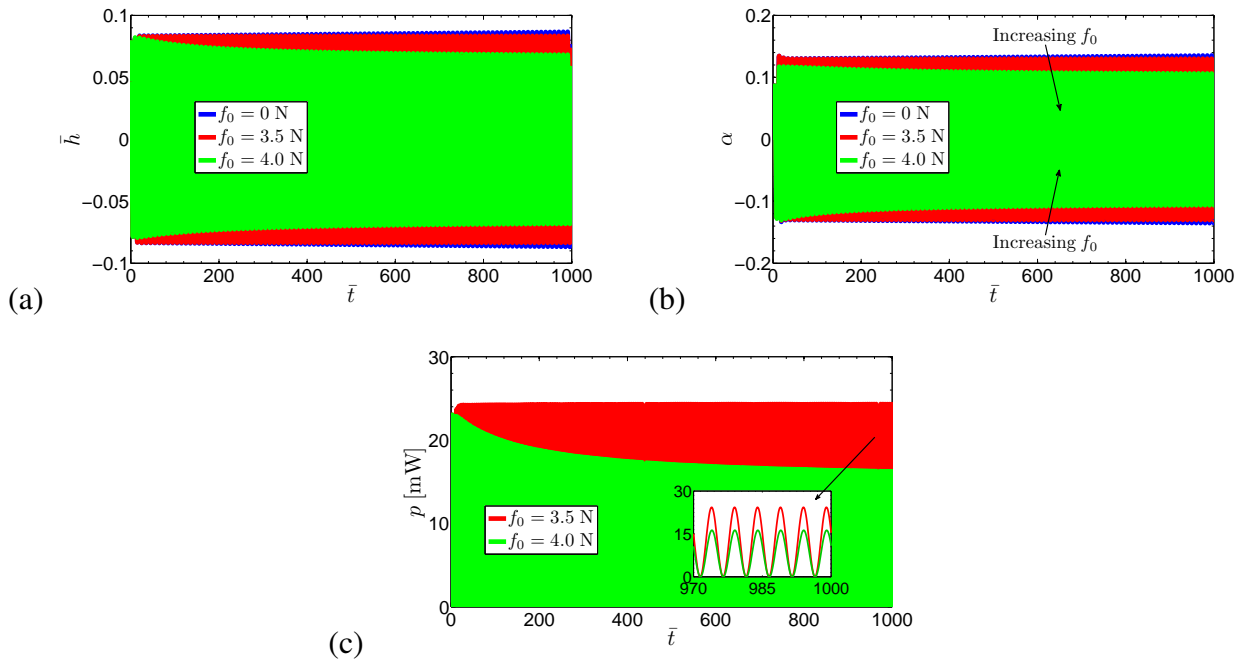


Figure 75 – Time responses for $U_\infty = 11.85 \text{ m}\cdot\text{s}^{-1}$, $R_l = 100 \text{ k}\Omega$ and preloads of 3.5 N and 4.0 N – (a) pitch angle, (b) plunge displacement and (c) electrical power output.

8.2 Electroaeroelastic Behavior of the Typical Section in the Post-Flutter Regime

The presence of nonlinearities in aeroelasticity often results in bifurcations with LCOs above or below the linear flutter speed (DOWELL, 2015). Nonlinearities may be welcome since the catastrophic linear flutter behavior above the linear flutter speed can be replaced by stable LCOs. The previous case study shows that unstable motions around the linear flutter speed can be replaced by LCOs due to phase transformations of the SMA springs. Moreover, it is shown in previous chapters that the presence of preloaded SMA springs in the pitch DOF of the typical section may lead to stable LCOs over a range of airflow speeds above the linear flutter speed. In practice, persistent oscillations over a range of airflow speeds are a favorable condition for wind energy harvesting. In this case study, the modified post-flutter regime (due to pseudoelastic hysteresis of SMAs) is investigated for wind energy harvesting, in contrast with the usual mechanisms reported in the literature of aeroelastic energy harvesting such as concentrated structural nonlinearities (*e.g.*, hardening springs) (SOUSA et al., 2011; ABDELKEFI; NAYFEH; HAJJ, 2012a, 2012b; ABDELKEFI; HAJJ, 2013; BAE; INMAN, 2015).

The same set of preload values and resistive loads of the previous case (at the flutter boundary) are considered. The aeroelastic behavior is investigated for airflow speeds from the linear flutter speed up to $14 \text{ m}\cdot\text{s}^{-1}$. For some conditions in this range of airflow speeds, the predicted aeroelastic amplitudes become unacceptably large for any resistive load or preload level. As in the previous chapters, the limiting pitch angle is assumed as 0.2 rad and for the same reasons. It is important to note, however, that for an airfoil in a power-extraction condition, the peak efficiency is verified for large-amplitude oscillations (KINSEY; DUMAS, 2008). Thus, further performance enhancement might be obtained outside the range of airflow speeds or oscillation amplitudes considered in this study (the goal here is to present and discuss a different nonlinear mechanism from the usually ones employed in the literature for wind energy harvesting, and no optimizations are of concern).

The aeroelastic behavior of the typical section with increasing preload on the SMA springs and $R_l = 100 \text{ k}\Omega$ is displayed in Fig. 76. For any preload value and airflow speed smaller than

$11.85 \text{ m}\cdot\text{s}^{-1}$ the oscillations are damped with time. Linear behavior is predicted for preload values smaller than 2.5 N , showing that stress-induced phase transformations are not achieved for this range of airflow speeds, preload values and the assumed SMA properties. As well, no phase transformations are predicted in the unstable region (while the limiting pitch angle is respected). Since the aeroelastic displacements in post-flutter regime are larger than those at the flutter boundary, the resulting (shear) stress on the SMA springs reaches the martensitic plateau for $f_0 > 2.5 \text{ N}$. For this range of preload, the pseudoelastic hysteresis leads to stable LCOs which are useful for wind energy harvesting. The dashed line in Fig. 76 represents the maximum airflow speed that satisfies the limiting solution for each of the considered preload values. For preload values larger than 4.5 N , the bias stress itself reaches the martensitic plateau and since the discussion is limited to negligible initial martensitic fraction, no further preload is considered. The largest LCO amplitudes which respect the assumed limiting solution are obtained for $13.8 \text{ m}\cdot\text{s}^{-1}$ (for the considered resistive load). In the range of stable LCOs with larger amplitudes (region above the dashed line for $f_0 > 2.5 \text{ N}$), however, the nonlinear electro-elastic dynamics of the piezoelectric material should be considered for an accurate estimation of electrical outputs (LEADENHAM; ERTURK, 2014).

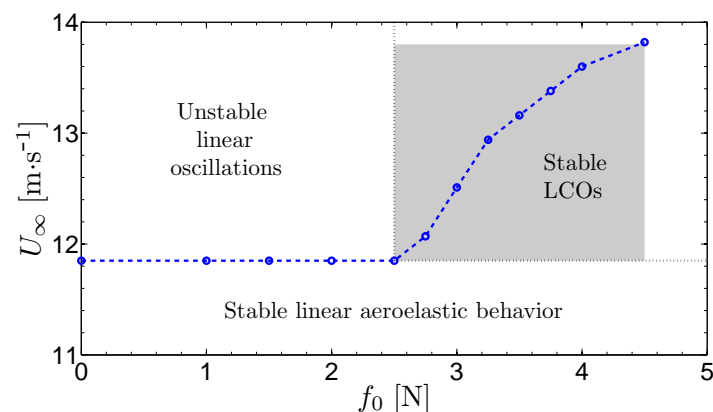


Figure 76 – Limiting airflow speeds for acceptable aeroelastic displacements with increasing preload (in the energy harvesting problem).

The peak amplitudes of the electroaeroelastic variables in the post-flutter regime are displayed in Fig. 77 for different preload values and $R_l = 100 \text{ k}\Omega$ (all points are from the steady-state response). The range of airflow speed of each case (preload) is due to the limiting solution (in terms of pitch and plunge displacements). For any preload value, the aeroelastic displace-

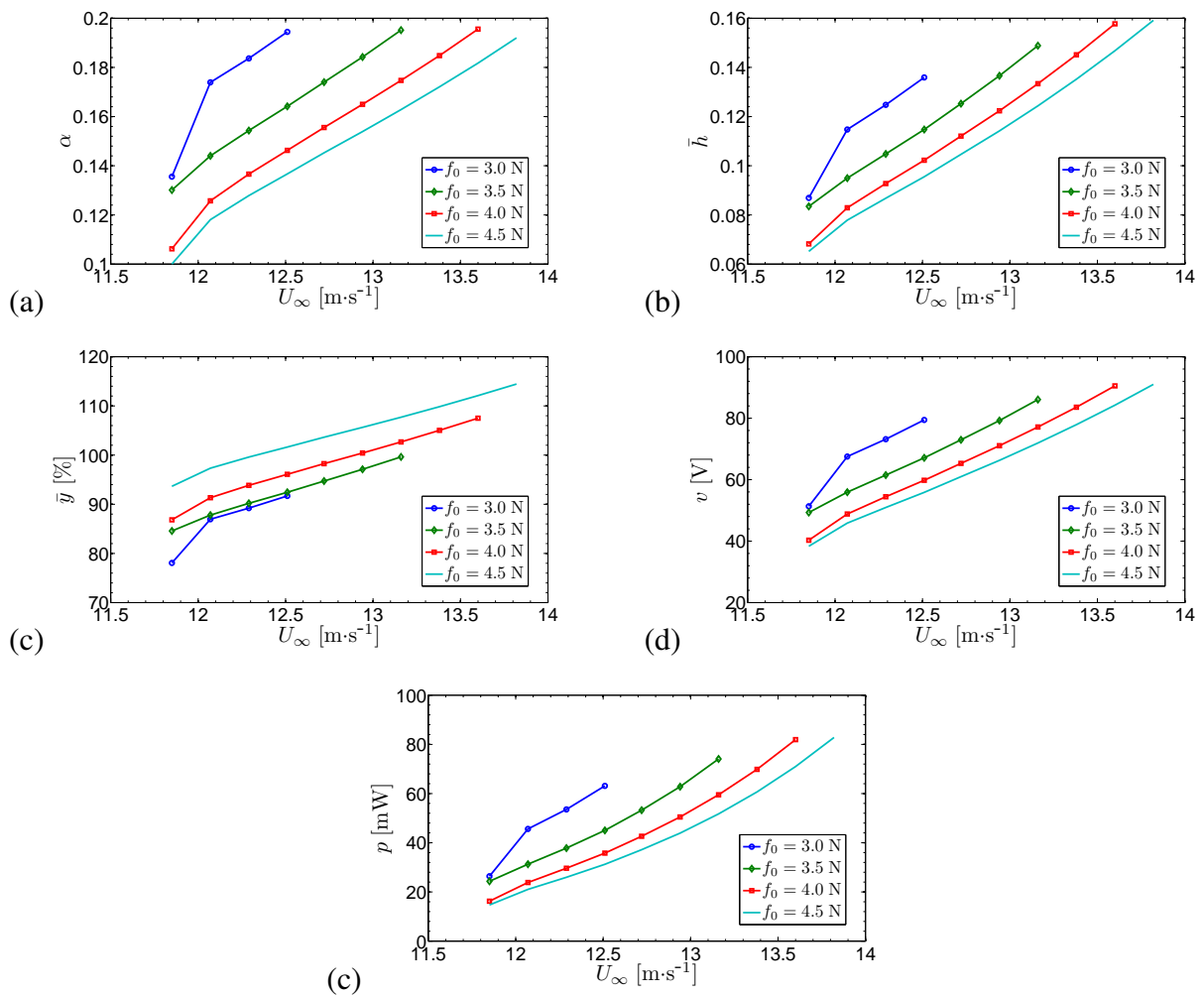


Figure 77 – Electroaeroelastic behavior for increasing airflow speed, different preload conditions and $R_l = 100 \text{ k}\Omega$ – (a) peak amplitude of the pitch angle, (b) peak amplitude of the plunge displacement, (c) SMA spring elongation, (d) peak amplitude of the voltage and (e) the corresponding electrical power output.

ments, as well as the voltage and the electrical power output, increase with increasing airflow speed (due to the increasing aerodynamic loads). It is clear from Fig. 77 that mechanical and electrical outputs are highly sensitive to the preload value on the SMA springs. At a fixed airflow speed, the outputs decrease with increasing preload value (due to the increased hysteretic dissipation promoted by the SMAs, as previously discussed throughout this study). Thus, the power output could be enhanced at a specific airflow speed by adjusting the preload, *i.e.*, the performance of the wind energy harvester could be adjusted to an existing airflow speed (available in the target environment) through the modification of preload since the same power output can be obtained for different preload values and different airflow speeds (Fig. 77(e)).

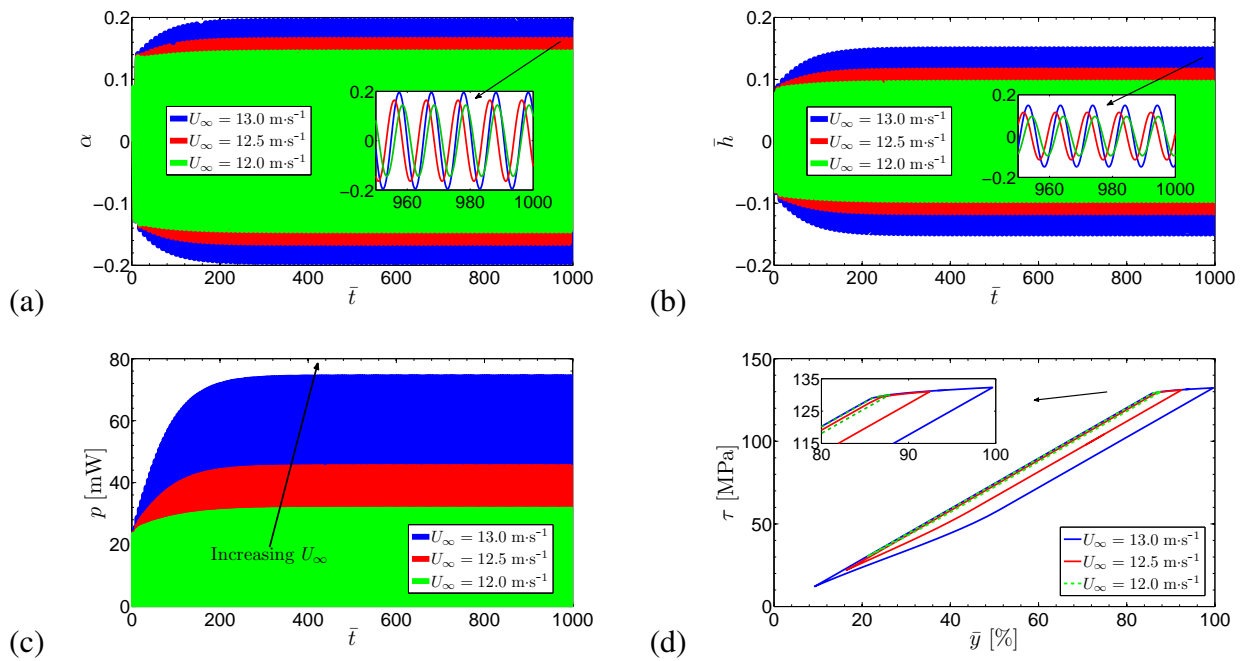


Figure 78 – Aeroelastic responses in time for $f_0 = 3.5 \text{ N}$, $R_l = 100 \text{ k}\Omega$ and different airflow speeds – (a) pitch angle, (b) plunge displacement, (c) electrical power output and (d) hysteretic behavior of the SMA springs.

Fig. 78(a) to (c) displays the pitch angle, plunge displacement and electrical power output in time for $f_0 = 3.5 \text{ N}$, $R_l = 100 \text{ k}\Omega$ and three different airflow speeds ($U_\infty = 12.0 \text{ m}\cdot\text{s}^{-1}$, $U_\infty = 12.5 \text{ m}\cdot\text{s}^{-1}$ and $U_\infty = 13.0 \text{ m}\cdot\text{s}^{-1}$). For any speed, the amplitudes increase until the first stress-induced phase transformation takes place. Upon the first phase transformation, the subsequent ongoing transformations lead to stable LCOs in the post-flutter regime (Figs. 78(a) and (b)) and, therefore, to continuous power generation (Fig. 78(c)). Fig. 78(d) displays the corresponding (steady-state) hysteretic behavior of the SMA spring (shear stress with spring elongation). Although no complete loops are observed, the area of the loop increases with increasing airflow speed, as expected (due to larger displacements), thus contributing to more expressive phase transformations and therefore to stable LCOs over wider post-flutter regimes.

Fig. 79 displays the effects of the resistive load on the electroaeroelastic behavior of the typical section with SMA springs for $U_\infty = 13 \text{ m}\cdot\text{s}^{-1}$ and $f_0 = 3.5 \text{ N}$ (only peak amplitudes are shown for clarity). As previously discussed, LCOs of acceptable amplitudes are observed at this speed and preload due to the nonlinear behavior of the SMA springs. Fig. 79(a) shows that the plunge displacement and the pitch angle decrease with increasing resistive load until $R_l = 250$

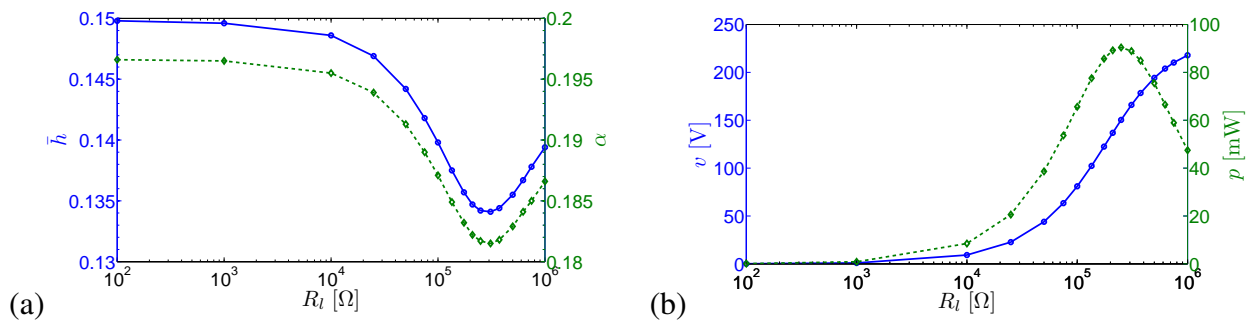


Figure 79 – Effects of the electrical boundary condition on the aeroelastic behavior for $U_\infty = 13 \text{ m}\cdot\text{s}^{-1}$ and $f_0 = 3.5 \text{ N}$ – (a) plunge displacement (left axis, continuous line) and pitch angle (right axis, dashed line); (b) voltage (left axis, continuous line) and electrical power output (right axis, dashed line).

$\text{k}\Omega$. When the resistive load is further increased the aeroelastic displacements also increase. Fig. 79(b) shows that the voltage output increases with increasing resistive load in the entire range. The power output increases for resistive loads from (close to) the short-circuit condition up to $250 \text{ k}\Omega$ (the global optimum resistive load) and decreases as the resistive load is further increased (towards the open-circuit condition). In the vicinity of $R_l = 250 \text{ k}\Omega$, the aeroelastic displacements are approximately 10% smaller than those for the short-circuit condition. In such a case the predicted power output exceeds 90 mW (Fig. 79(b)). For $U_\infty = 14 \text{ m}\cdot\text{s}^{-1}$ and $f_0 = 4.5 \text{ N}$ (the largest values of airflow speed and preload that respect the limiting solution), the optimum resistive load delivers 120 mW of peak electrical power.

For comparison purposes, Sousa et al. (2011) report a power output of about 30 mW for $R_l = 100 \text{ k}\Omega$ (the optimum resistive load in the referred paper) and $U_\infty = 14 \text{ m}\cdot\text{s}^{-1}$ when a polynomial stiffening nonlinearity (one hundred times stiffer than the nominal torsional stiffness) was modeled in the pitch DOF of the same typical section considered in the case of this chapter (however, with steel springs in the referred paper). The nonlinear hardening effect (of the polynomial steel spring) also promotes the conversion of unstable flutter oscillations into stable (persistent) LCOs in the post-flutter regime. In this study (in which SMA springs are considered), a power output of 80 mW is obtained for $R_l = 100 \text{ k}\Omega$ and $U_\infty = 14 \text{ m}\cdot\text{s}^{-1}$ (the same conditions of Sousa et al. (2011)). The enhanced performance shows that the nonlinear aeroelastic behavior of the typical section promoted by the pseudoelastic hysteresis of the SMA springs can be more attractive for airfoil-based wind energy harvesting than the nonlinear beha-

avior associated with hardening steel springs.

One should note that the addition of SMA springs to the typical section produces stable LCOs at the expense of additional energy dissipation. As discussed throughout this study, however, even when incomplete phase transformations take place (yielding small energy dissipation), unstable flutter oscillations are replaced by stable LCOs. Moreover, it was shown that negligible variations in the stiffness of the pitch DOF are predicted for increasing preload because only small, partial, phase transformations are of concern (Fig. 19). Therefore, at the same airflow speed, the combination of small energy dissipation with constant pitch elastic moment (when SMA springs are added) allows larger LCOs than those obtained for a hardening steel spring is employed. This way, at the same airflow speed more energy flows from the fluid to the structure of the typical section with SMA springs than in that case of the typical section with hardening nonlinearity. Since the systems compared in this study have the same amount of piezoelectric material for mechanical-to-electrical energy conversion, the system that enhances the energy flow from the fluid to the structure at the same airflow speed has more mechanical energy available to promote piezoaeroelastic energy harvesting and, consequently, will deliver more electrical power. The use of the pseudoelastic hysteresis of SMA springs as the source of nonlinearity of an airfoil-based wind energy harvester enhances the ability of the system to take energy from the airflow, which will be later converted to electricity by the piezoelectric material.

Summary and Conclusions

9.1 Conclusions

This work presents the modeling, analysis and experimental verification of a 2-DOF typical aeroelastic section with superelastic SMA elements (springs). The focus is on the effects of the pseudoelastic hysteresis of the SMA springs on the aeroelastic behavior of the typical section since the hysteretic behavior (of the SMAs) introduces a nonlinear restoring mechanism related to reversible stress-induced phase transformations, from a parent (austenitic) phase to a product (martensitic) phase. SMA helical springs are considered in the pitch DOF of the typical section (while linear elastic steel springs are considered in the plunge DOF) for (1) the modification of unstable linear behavior to stable nonlinear behavior (*i.e.*, transforming flutter oscillations into LCOs) and (2) the exploitation of the modified behavior (unstable to stable) to promote airfoil-based wind energy harvesting over a range of airflow speeds. Due to the second purpose, electromechanical (piezoelectric) coupling is also modeled (in the plunge DOF of the typical section) along with a resistive load in the electrical domain of the problem (to estimate the electrical power output).

The SMA phase transformation kinetics is described by a modified version of the well-known Brinson's model (BRINSON, 1993). A model for SMA helical springs based on the pure shear assumption is derived following Liang and Rogers (1997) and modified to represent additional SMA behaviors (BUCCHI et al., 2014; POORASADION et al., 2014). Based

on Poorasadion et al. (2014), tensile-compressive asymmetry behavior is included in the SMA modeling. Based on Bucchi et al. (2014), the cross-section of the coiled SMA wire is represented by radial distributions of shear strain, shear stress and martensitic fraction. Isothermal conditions are assumed since the predicted phase transformations are incomplete and a small region in the inelastic plateau is achieved, so that latent heat effects are assumed negligible. The equations of motion of a linear typical section are modified to include the SMA springs (in the pitch DOF). The unsteady aerodynamic loads are obtained based on the model of Edwards (1977), who proposed a state-space representation to Jones (1938)' approximation to Wagner's indicial function (an adaptation of the model of Theodorsen (1935) for arbitrary airfoil motions). The nonlinear governing equations are cast into a state-space representation (including the aerodynamic equations and the SMA springs) and solved with a Runge-Kutta method.

The general aeroelastic behavior of the typical section with SMA springs is discussed in Chapter 4. The effects of preloading the SMA springs are of concern at both the linear flutter speed and at post-flutter regime. At the linear flutter speed, it is shown that for small preload values the typical section behaves like a linear aeroelastic system (with linear elastic steel springs in pitch DOF). The aeroelastic behavior for such a case is assumed as a reference since the aeroelastic behavior is not modified by the pseudoelastic hysteresis of the SMA springs. For larger preload values, stress-induced phase transformations are verified at relatively small aeroelastic displacements. Therefore, the linear aeroelastic behavior is modified due to the nonlinear hysteretic behavior of the SMA springs. The pitch and plunge amplitudes decrease with increasing preload due to the enhanced damping capabilities related to the pseudoelastic hysteresis of the material under preload. When the critical preload values are employed, the pitch and plunge amplitudes are significantly smaller (50% or more, in some cases) than the amplitudes predicted for the linear case (without preload). At the post-flutter regime, the catastrophic linear flutter behavior is replaced by stable LCOs of acceptable amplitudes (for a specific range of preload values) due to the energy dissipating and damping capabilities of the SMA springs. The hysteretic response of the SMA springs increases the upper limit of the post-flutter speed of acceptable response amplitude (according to the criteria of maximum acceptable amplitude assumed in this work) by about 30%.

A parametric study is presented in Chapter 5. The effects of the SMA pseudoelastic hysteresis on the aeroelastic behavior of the typical section are investigated when six different sets of SMA constitutive properties (from the literature) are assumed. The non-homogeneous cross-sectional distributions (described in Section 2.4.3) is considered for improved representation of the SMA behavior. For each of the property sets, the aeroelastic behavior is compared for a range of airflow speeds in the post-flutter regime and for preloaded and non-preloaded SMA springs. Overall, it is shown that the aeroelastic behavior is sensitive to the set of SMA properties and also to the level of preload. Specific sets lead to enhanced aeroelastic behavior at both the flutter boundary (with smaller aeroelastic amplitudes) and post-flutter regime (over a wider range of airflow speeds while the amplitudes remain bounded to acceptable limits). It is shown that the LCO amplitudes in the post-flutter regime are related to a combination of initial conditions, airflow speed and preload applied to the SMA springs, and are strongly affected by the SMA properties. Moreover, the enhanced aeroelastic behavior of the typical section is associated with a combination of low critical stresses (for phase transformation), low stress-temperature transformation slopes and proximity between the martensite start and austenite finish stress-free temperatures. Such a combination yields more expressive phase transformations at small aeroelastic displacements and therefore is attractive to the considered aeroelastic problem. The upper limit of the post-flutter speed is about 15% larger than the linear flutter speed for a specific set of SMA properties. For the same set considered in Chapter 4, the limiting post-flutter speed is about 13% above the linear flutter speed, in contrast with the 30% above the linear flutter speed of Chapter 4 (due to the improved SMA model described in Section 2.4.3).

In Chapter 6, the effects of the pseudoelastic hysteresis of SMA springs with different geometries (wire and coil diameters) on the aeroelastic behavior of the typical section are investigated. Overall, the aeroelastic behavior of the typical section with SMA springs undergoing phase transformation is sensitive to the geometric properties of the SMA springs. Expressive decreases in the aeroelastic amplitudes are predicted for specific spring geometries (usually with small wire diameters or with fewer active coils). It is worth noting that the improvement is only due to the proper choice of the spring geometry, which can be combined with a proper choice also of SMA constitutive properties (as in Chapter 5) as well as of fabrication routes and heat treatment

procedures (ELAHINIA et al., 2012) to further enhance the aeroelastic behavior of the typical section.

The experimental behavior of a 2-DOF typical section model with preloaded SMA springs is discussed (for a range of airflow speeds) in Chapter 7. A particular superelastic Ni-Ti SMA spring (from Kellogg's Research Labs) with a specific geometry is considered for the presented tests. The effects of preloading the springs are of concern. For distinct preload conditions (starting with a small preload), the airflow speed is increased and arbitrary initial plunge displacements are applied to the typical section. Unstable (flutter) oscillations took place at about $13 \text{ m}\cdot\text{s}^{-1}$. For larger preload levels, flutter oscillations are replaced by stable LCOs at both the flutter boundary and post-flutter regime. The aeroelastic behavior of the typical section, therefore, changed from potentially catastrophic (rapidly growing over time) to stable (with persistent amplitudes), as numerically predicted in the previous chapters. Although most of the experimental SMA properties are unknown, the experimental behavior of the typical section (with SMA springs) qualitatively agrees with the numerical predictions. The upper limit of the post-flutter speed is about 13% larger than the (experimental) linear flutter speed, which is in good agreement with Chapter 5 (the highest airflow speed in that chapter is about 15% above the linear flutter speed, while the mean limiting speed among the considered property sets in that same chapter is about 11% above the linear flutter speed).

In Chapter 8, the piezoelectric coupling is considered (in the plunge DOF) along with preloaded superelastic SMA springs (in the pitch DOF) to enable airfoil-based wind energy harvesting over a range of airflow speeds by exploiting the pseudoelastic hysteresis of the SMA springs. As in the previous cases, it is shown that the aeroelastic behavior changes from linear to nonlinear due to the hysteretic behavior of the SMA springs. The aeroelastic amplitudes and the electrical power output decrease with increasing preload level due to the damping capabilities related to the pseudoelastic hysteresis. However, it is important to note that unstable motions around the flutter boundary are replaced by stable LCOs of acceptable amplitudes, allowing persistent power generation. In the post-flutter regime, the catastrophic linear flutter behavior is also replaced by LCOs of acceptable amplitudes. The upper limit of the post-flutter speed

of acceptable response amplitude increases by 20% for the considered SMA properties. The amplitudes of the mechanical and electrical outputs increase with increasing airflow speed for any resistive load. The effect of the resistive load on the electroaeroelastic behavior of the wind energy harvester with SMA springs is also reported. The amplitude of the aeroelastic displacements decreases around 10% in the vicinity of the optimum resistive load (250 k Ω). The maximum theoretical power output of 120 mW is obtained for the optimum resistive load at 14 m·s⁻¹ and 4.5 N of preload. The power output reported for the resistive load of 100 k Ω and preload value of 4.5 N is more than 160% larger than the power output reported in Sousa et al. (2011) (that uses the same typical section with hardening springs in the pitch DOF). Therefore, the numerical predictions reported in Chapter 8 show that the use of the SMA pseudoelastic hysteresis can be more attractive for airfoil-based wind energy harvesting performance enhancement than the use of hardening steel springs. It is also worth observing that the pseudoelastic hysteresis of SMA elements is a novel mechanism to enable wind energy harvesting over a range of airflow speeds.

In short, this work shows that the pseudoelastic hysteresis of SMA elements can be effectively exploited to enhance the aeroelastic behavior of a typical section model by replacing unstable flutter oscillations by stable oscillations of acceptable amplitudes over a range of airflow speeds (starting at the flutter boundary of the typical section). This enhancement is predicted by numerical simulations and verified with experimental tests. It is also shown that the enhanced aeroelastic behavior depends mainly on the constitutive properties of the considered SMA material, geometry of the SMA springs and level of preload applied to the springs. In particular, the post-flutter behavior of the typical section can be significantly enhanced by properly choosing the properties of the SMA element considered in the typical section, geometry of the springs and also the preload level. In practice, an optimum set of properties could be obtained by proper choice of materials, fabrication routes and heat treatment procedures (ELAHINIA et al., 2012) as well as a spring with an optimum geometry can be manufactured. Therefore, the results of this study show that the pseudoelastic effects of SMAs can provide a useful passive method of aeroelastic control.

9.2 Suggestions for Future Work

Concerning the experimental parameter identification, DSC tests can be performed to define the actual transformation temperatures of the SMA springs as well as other thermal properties such as specific heat and latent heat. Temperature-controlled force-displacement tests can be performed at different temperatures to determine the critical stresses for phase transformation and the stress-temperature relationship (the transformation slopes). With well defined SMA constitutive properties, more reliable numerical simulations can be performed. In this regard, different SMA constitutive models as well as more realistic spring models can be employed for better representation of the nonlinear behavior of SMA springs. A heat transfer model can also be included in the proposed modeling to account for release and absorption of latent heat (related to forward and reverse phase transformations, respectively) and convective heat transfer effects. Since isothermal conditions are usually not guaranteed, a strain-rate dependent model can also improve the predictions of the SMA behavior. Moreover, SMAs can exhibit significant material anisotropy (tension-torsion coupling) during stress-induced phase transformations (MEHRABI et al., 2014), while isotropy can be observed during linear elastic regime. This work assumed isotropy throughout the SMA loading-unloading process despite the presence of phase transformation. Therefore, the model of this work can be improved to represent tension-torsion coupling during phase transformation.

With respect to experimental aeroelastic tests, SMA springs with different constitutive properties and different geometries (as discussed in previous chapters) can be employed for the enhancement of the aeroelastic behavior of the typical section. In addition, different SMA elements (other than helical springs) can be considered. SMAs can also be considered in other (or multiple) DOFs of the typical section. The larger damping capabilities of the martensitic phase can also be exploited, as well as the ability of controllable change of elastic properties.

Concerning the electromechanically coupled typical section with SMA springs, several improvements can be made. For accuracy, the optimum resistive load should change with the airflow speed in the numerical predictions presented in Chapter 8, which was not investigated in this work. Nonlinear circuit techniques can be employed either to maximize the electrical

power output or to maximize the damping augmentation of the system. In the energy harvesting configuration, concentrated structural nonlinearities (such as freeplay) can be introduced to induce the appearing of subcritical oscillations, thus enlarging the range of airflow speeds at which persistent oscillations take place (promoting continuous electrical power generation). The combination of piezoceramics with SMAs can also be investigated to further enhance the flutter and post-flutter behavior of the typical section, by decreasing the amplitudes of oscillation and increasing the upper speed limit in the post-flutter regime, respectively.

References

- ABDELKEFI, A.; HAJJ, M. R. Performance enhancement of wing-based piezoaeroelastic energy harvesting through freeplay nonlinearity. *Theoretical and Applied Mechanics Letters*, v. 3, n. 4, p. 041001, 2013. Available from: <<http://link.aip.org/link/TAMLBX/v3/i4/p041001/s1&Agg=doi>>.
- ABDELKEFI, A.; NAYFEH, A. H.; HAJJ, M. R. Design of piezoaeroelastic energy harvesters. *Nonlinear Dynamics*, v. 68, n. 4, p. 519–530, 2012. ISSN 0924-090X. Available from: <<http://link.springer.com/10.1007/s11071-011-0233-x>>.
- ABDELKEFI, A.; NAYFEH, A. H.; HAJJ, M. R. Modeling and analysis of piezoaeroelastic energy harvesters. *Nonlinear Dynamics*, v. 67, n. 2, p. 925–939, 2012. Available from: <<http://link.springer.com/10.1007/s11071-011-0035-1>>.
- ACHENBACH, M.; ATANACKOVIC, T.; MÜLLER, I. A model for memory alloys in plane strain. *International journal of solids and ...*, v. 22, n. 2, p. 171–193, 1986. Available from: <<http://www.sciencedirect.com/science/article/pii/0020768386900065>>.
- AGUIAR, R. A. A. et al. Shape memory alloy helical springs performance: modeling and experimental analysis. *Materials Science Forum*, v. 758, p. 147–156, 2013. Available from: <<http://www.scientific.net/MSF.758.147>>.
- AGUIAR, R. A. A.; SAVI, M. A.; PACHECO, P. M. C. L. Experimental and numerical investigations of shape memory alloy helical springs. *Smart Materials and Structures*, v. 19, n. 2, p. 025008, 2010. Available from: <<http://stacks.iop.org/0964-1726/19/i=2/a=025008?key=crossref.80b6f37dbca1fecdec7c25bde6209d42>>.
- AKAYDIN, H. D.; ELVIN, N. G.; ANDREOPOULOS, Y. Energy Harvesting from Highly Unsteady Fluid Flows using Piezoelectric Materials. *Journal of Intelligent Material Systems and Structures*, v. 21, n. 13, p. 1263–1278, 2010. Available from: <jim.sagepub.com/content/21/13/1263>
<<http://jim.sagepub.com/cgi/doi/10.1177/1045389X10366317>>.
- AKAYDIN, H. D.; ELVIN, N. G.; ANDREOPOULOS, Y. Wake of a cylinder: a paradigm for energy harvesting with piezoelectric materials. *Experiments in Fluids*, v. 49, n. 1, p. 291–304, 2010. Available from: <<http://link.springer.com/10.1007/s00348-010-0871-7>>.
- ALIGHANBARI, H. *Flutter analysis and chaotic response of an airfoil accounting for structural nonlinearities*. Thesis (Doctorate) — Department of Mechanical Engineering, McGill University, Montreal, Canada, 1995.
- ALLEN, J.; SMITS, A. Energy harvesting {EEL}. *Journal of Fluids and Structures*, v. 15, n. 3-4, p. 629–640, 2001. Available from: <<http://www.sciencedirect.com/science/article/pii/S0889974600903554>>.

AN, S.-M. et al. Engineering design framework for a shape memory alloy coil spring actuator using a static two-state model. *Smart Materials and Structures*, v. 21, n. 5, p. 055009, may 2012. ISSN 0964-1726. Available from: <<http://stacks.iop.org/0964-1726/21/i=5/a=055009?key=crossref.22074df2fdb70593582bc6a34e1ad590>>.

ANDANI, M. T. et al. Metals for bone implants. Part 1. Powder metallurgy and implant rendering. *Acta Biomaterialia*, v. 10, n. 10, p. 4058–4070, 2014. Available from: <<http://linkinghub.elsevier.com/retrieve/pii/S1742706114002724>>.

BACHMANN, F. et al. Passive damping of composite blades using embedded piezoelectric modules or shape memory alloy wires: a comparative study. *Smart Materials and Structures*, v. 21, n. 7, p. 075027, 2012. Available from: <<http://stacks.iop.org/0964-1726/21/i=7/a=075027?key=crossref.5896be94f392ebe551449f48a38b811b>>.

BAE, J.-s.; INMAN, D. J. A Preliminary Study on Piezo-aeroelastic Energy Harvesting Using a Nonlinear Trailing-Edge Flap. v. 16, n. 3, p. 407–417, 2015.

BAGHANI, M.; NAGHDABADI, R.; ARGHAVANI, J. A semi-analytical study on helical springs made of shape memory polymer. *Smart Materials and Structures*, v. 21, n. 4, p. 045014, 2012. Available from: <<http://stacks.iop.org/0964-1726/21/i=4/a=045014?key=crossref.74231b63aaca29f57e98d2e2e7f64cc4>>.

BARBARINO, S. et al. A review on shape memory alloys with applications to morphing aircraft. *Smart Materials and Structures*, v. 23, n. 6, p. 063001, 2014. Available from: <<http://iopscience.iop.org/0964-1726/23/6/063001>>.

BARZEGARI, M. M.; DARDEL, M.; FATHI, A. Control of aeroelastic characteristics of cantilever wing with smart materials using state-dependent Riccati equation method. *Journal of Intelligent Material Systems and Structures*, v. 26, n. 8, p. 988–1005, 2015. Available from: <<http://jim.sagepub.com/cgi/doi/10.1177/1045389X14554128>>.

BARZEGARI, M. M. et al. Aeroelastic characteristics of cantilever wing with embedded shape memory alloys. *Acta Astronautica*, v. 79, p. 189–202, 2012. Available from: <<http://www.sciencedirect.com/science/article/pii/S0094576512001385>>.

BHOWMICK, S.; MISHRA, S. K. FNCATB Superelastic damper for seismic vibration mitigation. *Journal of Intelligent Material Systems and Structures*, p. 16, 2015. Available from: <<http://jim.sagepub.com/cgi/doi/10.1177/1045389X15620039>>.

BIL, C.; MASSEY, K.; ABDULLAH, E. J. Wing morphing control with shape memory alloy actuators. *Journal of Intelligent Material Systems and Structures*, v. 24, n. 7, p. 879–898, 2013. Available from: <<http://jim.sagepub.com/cgi/doi/10.1177/1045389X12471866>>.

BISPLINGHOFF, R. L.; ASHLEY, H.; HALFMAN, R. L. *Aeroelasticity*. Cambridge, Massachusetts: Addison-Wesley Publishing Company, Inc., 1955. 860 p.

BRINSON, L. C. One-Dimensional Constitutive Behavior of Shape Memory Alloys: Thermomechanical Derivation with Non-Constant Material Functions and Redefined Martensite Internal Variable. *Journal of Intelligent Material Systems and Structures*, v. 4, n. 2, p. 229–242, 1993. Available from: <<http://jim.sagepub.com/cgi/doi/10.1177/1045389X9300400213>>.

BRYANT, M.; GARCIA, E. Modeling and testing of a novel aeroelastic flutter energy harvester. *Journal of Vibration and Acoustics*, v. 133, p. 011010 (11pp), 2011. Available from: <<http://dx.doi.org/10.1115/1.4002788>>.

BUCCHI, F. et al. A Passive Magneto-Thermo-Mechanical Coupling Actuated by SMA Springs and MR Fluid. *International Journal of Structural Stability and Dynamics*, v. 14, n. 08, p. 1440031, 2014. Available from: <<http://www.worldscientific.com/doi/abs/10.1142/S0219455414400318>>.

BUDYNAS, R. G.; NISBETT, J. K. *Shigley's Mechanical Engineering Design*. 10. ed. [S.l.]: McGraw-Hill Education, 2014. 1104 p. ISBN 0073398209.

BUEHLER, W. J.; WANG, F. E. A summary of recent research on the Nitinol alloys and their potential application in ocean engineering. *Ocean Engineering*, v. 1, p. 105–120, 1968. Available from: <<http://www.sciencedirect.com/science/article/pii/002980186890019X>>.

CONNER, M. D. *Nonlinear aeroelasticity of an airfoil section with control surface freeplay*. Thesis (Doctorate) — Department of Mechanical Engineering and Materials Science, Duke University, 1996.

CRAIG, R. *Structural Dynamics: An Introduction to Computer Methods*. 1. ed. [S.l.]: Wiley, 1981. 544 p. ISBN 0471044997.

D'ASSUNÇÃO, D.; De Marqui Jr, C. Applied self-powered semi-passive control for a 2-degree-of-freedom aeroelastic typical section using shunted piezoelectric materials. *Journal of Intelligent Material Systems and Structures*, v. 26, n. 4, p. 373–385, 2015. Available from: <<http://jim.sagepub.com/cgi/doi/10.1177/1045389X14526797>>.

De Marqui Jr, C.; ERTURK, A.; INMAN, D. J. Piezoaeroelastic modeling and analysis of a generator wing with continuous and segmented electrodes. *Journal of Intelligent Material Systems and Structures*, v. 21, n. 10, p. 983–993, 2010. Available from: <<http://jim.sagepub.com/cgi/doi/10.1177/1045389X10372261>>.

De Marqui Jr, C. et al. Modeling and analysis of piezoelectric energy harvesting from aeroelastic vibrations using the doublet-lattice method. *Journal of Vibration and Acoustics*, v. 133, n. 1, p. 011003, 2011. Available from: <<http://vibrationacoustics.asmedigitalcollection.asme.org/article.aspx?articleid=1471531>>.

DIAS, J. A. C.; De Marqui, C.; ERTURK, A. Three-Degree-of-Freedom Hybrid Piezoelectric-Inductive Aeroelastic Energy Harvester Exploiting a Control Surface. *AIAA Journal*, v. 53, n. 2, p. 394–404, 2015. Available from: <<http://arc.aiaa.org/doi/10.2514/1.J053108>>.

DIAS, J. A. C.; De Marqui Jr, C.; ERTURK, A. Hybrid piezoelectric-inductive flow energy harvesting and dimensionless electroaeroelastic analysis for scaling. *Applied Physics Letters*, v. 102, n. 4, p. 044101, 2013. Available from: <<http://link.aip.org/link/APPLAB/v102/i4/p044101/s1&Agg=doi>>.

DOWELL, E. H. *A Modern Course in Aeroelasticity*. 5. ed. Cham: Springer International Publishing, 2015. 700 p. (Solid Mechanics and Its Applications, v. 217). ISBN 978-3-319-09452-6. Available from: <<http://mechanicaldesign.asmedigitalcollection.asme.org/article.aspx?articleid=1451429>
<<http://link.springer.com/10.1007/978-3-319-09453-3>>.

DUNNMON, J. A. et al. Power extraction from aeroelastic limit cycle oscillations. *Journal of Fluids and Structures*, v. 27, n. 8, p. 1182–1198, 2011. Available from: <www.sciencedirect.com/science/article/pii/S0889974611000211>.

EDWARDS, J. W. *Unsteady aerodynamic modeling and active aeroelastic control*. Thesis (Doctorate) — Department of Aeronautics and Astronautics, Stanford University, Stanford, California, 1977.

EDWARDS, J. W.; ASHLEY, H.; BREAKWELL, J. V. Unsteady aerodynamic modeling for arbitrary motions. *AIAA Journal*, v. 17, n. 4, p. 365–374, 1979. Available from: <<http://arc.aiaa.org/doi/abs/10.2514/3.7348>>.

ELAHINIA, M. H.; AHMADIAN, M. An enhanced SMA phenomenological model: I. The shortcomings of the existing models. *Smart Materials and Structures*, v. 14, n. 6, p. 1297–1308, 2005. Available from: <<http://stacks.iop.org/0964-1726/14/i=6/a=022?key=crossref.356645df188b7494fe51e5de94b4f281>>.

ELAHINIA, M. H.; AHMADIAN, M. An enhanced SMA phenomenological model: II. The experimental study. *Smart Materials and Structures*, v. 14, n. 6, p. 1309–1319, 2005. Available from: <<http://stacks.iop.org/0964-1726/14/i=6/a=023?key=crossref.fc5614a31a7bc0389672fd2bae9d0ac0>>.

ELAHINIA, M. H. et al. Manufacturing and processing of NiTi implants: A review. *Progress in Materials Science*, v. 57, n. 5, p. 911–946, 2012. Available from: <<http://linkinghub.elsevier.com/retrieve/pii/S0079642511001058>>.

ELVIN, N. G.; ERTURK, A. (Ed.). *Advances in Energy Harvesting Methods*. New York, NY: Springer New York, 2013. 455 p. Available from: <<http://link.springer.com/10.1007/978-1-4614-5705-3>>.

ENEMARK, S.; SAVI, M. A.; SANTOS, I. F. Nonlinear dynamics of a pseudo-elastic shape memory alloy system - theory and experiment. *Smart Materials and Structures*, v. 23, n. 8, p. 085018, 2014. Available from: <<http://stacks.iop.org/0964-1726/23/i=8/a=085018?key=crossref.f67d27aef69019401ec6e7adf2a9652d>>.

ERTURK, A.; INMAN, D. J. A distributed parameter electromechanical model for cantilevered piezoelectric energy harvester plates. *ASME Journal of Vibration and Acoustics*, v. 130, n. 4, p. 041002 (15pp), 2008. Available from: <<http://vibrationacoustics.asmedigitalcollection.asme.org/article.aspx?articleid=1471147dx.doi.org/10.1115/1.2890402>>.

ERTURK, A.; INMAN, D. J. *Piezoelectric energy harvesting*. Chichester, UK: John Wiley & Sons, Ltd., 2011. 25009 p. ISBN 9781119991151. Available from: <http://doi.wiley.com/10.1002/9781119991151_stacks.iop.org/0964-1726/18/i=2/a=025009>.

ERTURK, A. et al. On the energy harvesting potential of piezoaeroelastic systems. *Applied Physics Letters*, v. 96, n. 18, p. 184103 (3pp), 2010. Available from: <apl.aip.org/resource/1/applab/v96/i18/p184103_s1>.

FAULKNER, M. G. Experimental determination of thermal and electrical properties of Ni-Ti shape memory wires. *Smart materials and ...*, v. 632, 2000. Available from: <<http://iopscience.iop.org/0964-1726/9/5/307>>.

FRENZEL, J. et al. Influence of Ni on martensitic phase transformations in NiTi shape memory alloys. *Acta Materialia*, Acta Materialia Inc., v. 58, n. 9, p. 3444–3458, 2010. Available from: <<http://linkinghub.elsevier.com/retrieve/pii/S1359645410001059>>.

FROST, M. et al. Modeling of mechanical response of NiTi shape memory alloy subjected to combined thermal and non-proportional mechanical loading: a case study on helical spring actuator. *Journal of Intelligent Material Systems and Structures*, 2015. Available from: <<http://jim.sagepub.com/cgi/doi/10.1177/1045389X15610908>>.

GALL, K. et al. Tension-compression asymmetry of the stress-strain response in aged single crystal and polycrystalline NiTi. *Acta Materialia*, v. 47, n. 4, p. 1203–1217, 1999. Available from: <<http://www.sciencedirect.com/science/article/pii/S1359645498004327> <http://linkinghub.elsevier.com/retrieve/pii/S1359645498004327>>.

GANDHI, F. S.; CHAPUIS, G. Passive damping augmentation of a vibrating beam using pseudoelastic shape memory alloy wires. *Journal of Sound and Vibration*, v. 250, n. 3, p. 519–539, 2002. Available from: <<http://linkinghub.elsevier.com/retrieve/pii/S0022460X01939355>>.

GILLET, Y.; PATOOR, E.; BERVEILLER, M. Calculation of pseudoelastic elements using a non-symmetrical thermomechanical transformation criterion and associated rule. *Journal of Intelligent Material Systems and Structures*, v. 9, n. 5, p. 366–378, 1998. Available from: <<http://jim.sagepub.com/cgi/doi/10.1177/1045389X9800900505>>.

HABERLAND, C. M. H. et al. On the development of high quality NiTi shape memory and pseudoelastic parts by additive manufacturing. *Smart Materials and Structures*, v. 23, n. 10, p. 104002, 2014. Available from: <<http://stacks.iop.org/0964-1726/23/i=10/a=104002?key=crossref.01ca5becf73afa7939fdecb1bf0bbb04>>.

HADI, A. et al. Developing a novel SMA-actuated robotic module. *Sensors and Actuators A: Physical*, Elsevier B.V., v. 162, n. 1, p. 72–81, jul 2010. ISSN 09244247. Available from: <<http://linkinghub.elsevier.com/retrieve/pii/S092442471000275X>>.

HANNAH, R.; REED, S. (Ed.). *Strain Gage Users' Handbook*. 1. ed. [S.l.]: Springer Netherlands, 1992. 476 p.

HARTL, D. J.; LAGOUDAS, D. C. Aerospace applications of shape memory alloys. *Proceedings of the Institution of Mechanical Engineers, Part G: Journal of Aerospace Engineering*, v. 221, n. 4, p. 535–552, 2007. Available from: <<http://pig.sagepub.com/lookup/doi/10.1243/09544100JAERO211>>.

HEMATI, N. Nondimensionalization of the equations of motion for permanent-magnet machines. *Electric Machines & Power Systems*, v. 23, n. 5, p. 541–556, 1995. Available from: <www.tandfonline.com/doi/abs/10.1080/07313569508955642>.

HODGES, D. H.; PIERCE, G. A. *Introduction to structural dynamics and aeroelasticity*. [S.l.]: Cambridge Aerospace Series, 2002. 181 p.

HUANG, W. On the selection of shape memory alloys for actuators. *Materials & design*, n. June 2000, p. 11–19, 2002. Available from: <<http://www.sciencedirect.com/science/article/pii/S0261306901000395>>.

IBRAHIM, R. Recent advances in nonlinear passive vibration isolators. *Journal of Sound and Vibration*, v. 314, n. 3-5, p. 371–452, jul 2008. ISSN 0022460X. Available from: <<http://linkinghub.elsevier.com/retrieve/pii/S0022460X08000436>>.

JANKE, L. Applications of shape memory alloys in civil engineering structures - Overview, limits and new ideas. *Materials and Structures*, v. 38, n. 279, p. 578–592, apr 2005. ISSN 1359-5997. Available from: <<https://www.rilem.net/boutique/fiche.php?cat=journal&reference=1823>>.

JONES, R. T. *Operational treatment of the nonuniform-lift theory in airplane dynamics*. N.A.C.A. Technical Note 667. Washington, 1938. 11 p.

JONES, R. T. *The unsteady lift of a finite wing*. N.A.C.A. Technical Note 682. Washington, 1939. 19 p.

JUNG, H.-J.; LEE, S.-W. The experimental validation of a new energy harvesting system based on the wake galloping phenomenon. *Smart Materials and Structures*, v. 20, n. 5, p. 55022, 2011. Available from: <stacks.iop.org/SMS/20/05502>.

KIEFER, B.; LAGOUDAS, D. C. Magnetic field-induced martensitic variant reorientation in magnetic shape memory alloys. *Philosophical Magazine*, v. 85, n. 33-35, p. 4289–4329, nov 2005. ISSN 1478-6435. Available from: <<http://www.tandfonline.com/doi/abs/10.1080/14786430500363858>>.

KINSEY, T.; DUMAS, G. Parametric study of an oscillating airfoil in a power-extraction regime. *AIAA Journal*, v. 46, n. 6, p. 1318–1330, jun 2008. Available from: <<http://arc.aiaa.org/doi/abs/10.2514/1.26253>>.

KWON, S.-D. A {T-shaped} piezoelectric cantilever for fluid energy harvesting. *Applied Physics Letters*, v. 97, p. 164102 (3pp), 2010. Available from: <apl.aip.org/resource/1/applab/v97/i16/p164102_s1>.

LAGOUDAS, D. C. *Shape Memory Alloys*. Boston, MA: Springer US, 2008. 435 p. Available from: <<http://link.springer.com/10.1007/978-0-387-47685-8>>.

LEADENHAM, S.; ERTURK, A. Unified nonlinear electroelastic dynamics of a bimorph piezoelectric cantilever for energy harvesting, sensing, and actuation. *Nonlinear Dynamics*, v. 79, n. 3, p. 1727–1743, 2014. Available from: <<http://dx.doi.org/10.1007/s11071-014-1770-x>>.

LEO, D. J. *Engineering analysis of smart material systems*. [S.l.]: John Wiley & Sons, Inc., 2007. 556 p.

LIANG, C.; ROGERS, C. One-dimensional thermomechanical constitutive relations for shape memory materials. *Journal of Intelligent Material Systems and Structures*, v. 1, n. 2, p. 207–234, 1990. Available from: <<http://jim.sagepub.com/content/1/2/207.short>>.

LIANG, C.; ROGERS, C. A multi-dimensional constitutive model for shape memory alloys. *Journal of Engineering Mathematics*, v. 26, p. 429–443, 1992. Available from: <<http://link.springer.com/article/10.1007/BF00042744>>.

LIANG, C.; ROGERS, C. A. Design of shape memory alloy springs with applications in vibration control. *Journal of Intelligent Material Systems and Structures*, v. 8, n. 4, p. 314–322, 1997. Available from: <<http://jim.sagepub.com/cgi/doi/10.1177/1045389X9700800404>>.

LIU, X. et al. The effect of ageing treatment on shape-setting and superelasticity of a nitinol stent. *Materials Characterization*, v. 59, n. 4, p. 402–406, apr 2008. ISSN 10445803. Available from: <<http://linkinghub.elsevier.com/retrieve/pii/S1044580307000836>>.

LIU, Y. et al. Shape memory polymers and their composites in aerospace applications: a review. *Smart Materials and Structures*, v. 23, n. 2, p. 023001, feb 2014. ISSN 0964-1726. Available from: <<http://stacks.iop.org/0964-1726/23/i=2/a=023001?key=crossref.df6f3f4044f64f3392af42871c7f6371>>.

MANI, Y.; SENTHILKUMAR, M. Shape memory alloy-based adaptive-passive dynamic vibration absorber for vibration control in piping applications. *Journal of Vibration and Control*, v. 21, n. 9, p. 1838–1847, 2015. Available from: <<http://jvc.sagepub.com/cgi/doi/10.1177/1077546313492183>>.

MEHRABI, R. et al. Anisotropic behavior of superelastic NiTi shape memory alloys; an experimental investigation and constitutive modeling. *Mechanics of Materials*, v. 77, p. 110–124, 2014. Available from: <<http://linkinghub.elsevier.com/retrieve/pii/S0167663614001148>>.

MEHRABI, R.; KADKHODAEI, M.; ELAHINIA, M. H. Constitutive modeling of tension-torsion coupling and tension-compression asymmetry in NiTi shape memory alloys. *Smart Materials and Structures*, v. 23, n. 7, p. 075021, 2014. Available from: <<http://stacks.iop.org/0964-1726/23/i=7/a=075021?key=crossref.11d429f30885c84957050fa7a907347a>>.

MELTON, K. Ni–Ti based shape memory alloys. In: *Engineering Aspects of Shape Memory Alloys*. [S.l.]: Butterworth-Heinemann, 1990. p. 21–35.

MENG, H. et al. Various shape memory effects of stimuli-responsive shape memory polymers. *Smart Materials and Structures*, v. 22, n. 9, p. 093001, sep 2013. ISSN 0964-1726. Available from: <<http://stacks.iop.org/0964-1726/22/i=9/a=093001?key=crossref.d9a1c6afe6e04492c843638ed1b5b205>>.

MIRZAEIFAR, R.; DESROCHES, R.; YAVARI, A. A combined analytical, numerical, and experimental study of shape-memory-alloy helical springs. *International Journal of Solids and Structures*, Elsevier Ltd, v. 48, n. 3-4, p. 611–624, feb 2011. ISSN 00207683. Available from: <<http://linkinghub.elsevier.com/retrieve/pii/S002076831000380X>>.

MISHRA, S. K.; GUR, S.; CHAKRABORTY, S. An improved tuned mass damper (SMA-TMD) assisted by a shape memory alloy spring. *Smart Materials and Structures*, v. 22, n. 9, p. 095016, sep 2013. ISSN 0964-1726. Available from: <<http://stacks.iop.org/0964-1726/22/i=9/a=095016?key=crossref.cd4e27601753511f00e0f3109454c5b8>>.

OZBULUT, O. E.; HURLEBAUS, S.; DESROCHES, R. Seismic response control using shape memory alloys: a review. *Journal of Intelligent Material Systems and Structures*, v. 22, n. 14, p. 1531–1549, 2011. Available from: <<http://jim.sagepub.com/cgi/doi/10.1177/1045389X11411220>>.

- PAIVA, A. et al. A constitutive model for shape memory alloys considering tensile-compressive asymmetry and plasticity. *International Journal of Solids and Structures*, v. 42, n. 11-12, p. 3439–3457, 2005. Available from: <<http://linkinghub.elsevier.com/retrieve/pii/S0020768304006250>>.
- PENG, Z.; ZHU, Q. Energy harvesting through flow-induced oscillations of a foil. *Physics of Fluids*, v. 21, n. 12, p. 123602 (9pp), 2009. Available from: <pof.aip.org/resource/1/phfle6/v21/i12/p123602_s1>.
- PEREZ, M. et al. An electret-based aeroelastic flutter energy harvester. *Smart Materials and Structures*, IOP Publishing, v. 24, n. 3, p. 035004, mar 2015. ISSN 0964-1726. Available from: <<http://stacks.iop.org/0964-1726/24/i=3/a=035004?key=crossref.eb1243854f6334e55beea64072644081>>.
- PETERS, D. A.; KARUNAMOORTHY, S.; CAO, W.-M. Finite state induced flow models. Part I: Two-dimensional thin airfoil. *Journal of Aircraft*, v. 32, n. 2, p. 313–322, mar 1995. ISSN 0021-8669. Available from: <<http://arc.aiaa.org/doi/abs/10.2514/3.46718>>.
- POBERING, S.; EBERMEYER, S.; SCHWESINGER, N. Generation of electrical energy using short piezoelectric cantilevers in flowing media. In: AHMADIAN, M.; GHASEMI-NEJHAD, M. N. (Ed.). *Proc. SPIE 7288, Active and Passive Smart Structures and Integrated Systems 2009*. [s.n.], 2009. p. 728807. Available from: <<http://proceedings.spiedigitallibrary.org/proceeding.aspx?doi=10.1117/12.815189>>.
- POORASADION, S. et al. An improvement on the Brinson model for shape memory alloys with application to two-dimensional beam element. *Journal of Intelligent Material Systems and Structures*, v. 25, n. 15, p. 1905–1920, 2014. Available from: <<http://jim.sagepub.com/cgi/doi/10.1177/1045389X13512187>>.
- RAO, A.; SRINIVASA, A. R. A three-species model for simulating torsional response of shape memory alloy components using thermodynamic principles and discrete Preisach models. *Mathematics and Mechanics of Solids*, v. 20, n. 3, p. 345–372, 2015. Available from: <<http://mms.sagepub.com/cgi/doi/10.1177/1081286514545917>>.
- Rezaei Da, H.; KADKHODAEI, M.; NAHVI, H. Analysis of nonlinear free vibration and damping of a clamped-clamped beam with embedded prestrained shape memory alloy wires. *Journal of Intelligent Material Systems and Structures*, v. 23, n. 10, p. 1107–1117, jul 2012. ISSN 1045-389X. Available from: <<http://jim.sagepub.com/cgi/doi/10.1177/1045389X12441509>>.
- SALEEB, A. F. et al. Large scale simulation of NiTi helical spring actuators under repeated thermomechanical cycles. *Smart Materials and Structures*, v. 22, n. 9, p. 094006, 2013. Available from: <<http://stacks.iop.org/0964-1726/22/i=9/a=094006?key=crossref.c81fc07447e123a365456e67f71b5917>>.
- SAMEALLAH, S. et al. Direct numerical determination of stabilized dissipated energy of shape memory alloys under cyclic tensile loadings. *Journal of Intelligent Material Systems and Structures*, v. 26, n. 16, p. 2137–2150, 2014. Available from: <<http://jim.sagepub.com/cgi/doi/10.1177/1045389X14549869>>.
- SAVI, M. A. et al. Nonlinear geometric influence on the mechanical behavior of shape memory alloy helical springs. *Smart Materials and Structures*,

v. 24, n. 3, p. 035012, 2015. Available from: <<http://stacks.iop.org/0964-1726/24/i=3/a=035012?key=crossref.21b8084531c8bed13724fc95c7a830b9>>.

SAVI, M. A. et al. Tensile-compressive asymmetry influence on shape memory alloy system dynamics. *Chaos, Solitons & Fractals*, v. 36, n. 4, p. 828–842, 2008. Available from: <<http://linkinghub.elsevier.com/retrieve/pii/S0960077906008848>>.

SCALET, G. et al. An experimental, theoretical and numerical investigation of shape memory polymers. *International Journal of Plasticity*, v. 67, p. 127–147, apr 2015. ISSN 07496419. Available from: <<http://linkinghub.elsevier.com/retrieve/pii/S0749641914002010>>.

SCZERZENIE, F.; GUPTA, S. The Effect of Alloy Formulation on the Transformation Temperature Range of Ni-Ti Shape Memory Alloys. In: PELTON, A. R.; DUERIG, T. W. (Ed.). *SMST 2003: Proceedings of the International Conference on Shape Memory and Superelastic Technologies*. [S.l.: s.n.], 2004. p. 15–22.

SOUSA, V. C. et al. Enhanced aeroelastic energy harvesting by exploiting combined nonlinearities: theory and experiment. *Smart Materials and Structures*, v. 20, p. 094007 (8pp), 2011. Available from: <stacks.iop.org/SMS/20/094007>.

St. Clair, D. et al. A scalable concept for micropower generation using flow-induced self-excited oscillations. *Applied Physics Letters*, v. 96, n. 14, p. 144103, 2010. Available from: <<http://scitation.aip.org/content/aip/journal/apl/96/14/10.1063/1.3385780>>.

TANAKA, K.; KOBAYASHI, S.; SATO, Y. Thermomechanics of transformation pseudoelasticity and shape memory effect in alloys. *International Journal of Plasticity*, v. 2, p. 59–72, 1986. Available from: <<http://www.sciencedirect.com/science/article/pii/0749641986900161>>.

TANG, L. et al. Cantilevered flexible plates in axial flow: energy transfer and the concept of flutter-mill. *Journal of Sound and Vibration*, v. 326, n. 1-2, p. 263–276, 2009. Available from: <[sciencedirect.com/science/article/pii/S0022460X09004076](http://www.sciencedirect.com/science/article/pii/S0022460X09004076)
<<http://linkinghub.elsevier.com/retrieve/pii/S0022460X08010067>
<<http://linkinghub.elsevier.com/retrieve/pii/S0022460X09004076>>.

TAWFIK, M.; RO, J.-J.; MEI, C. Thermal post-buckling and aeroelastic behaviour of shape memory alloy reinforced plates. *Smart Materials and Structures*, v. 11, n. 2, p. 297–307, apr 2002. ISSN 0964-1726. Available from: <<http://iopscience.iop.org/0964-1726/11/2/313> <<http://stacks.iop.org/0964-1726/11/i=2/a=313?key=crossref.fec6280ece45c7bc860310565906b5ab>>.

THEODORSEN, T. *General theory of aerodynamic instability and the mechanism of flutter*. [S.l.], 1935. 23 p.

TOKUDA, M. et al. Thermomechanical behavior of shape memory alloy under complex loading conditions. *International Journal of Plasticity*, v. 15, n. 2, p. 223–239, 1999. Available from: <<http://linkinghub.elsevier.com/retrieve/pii/S0749641998000667>>.

TRICKEY, S. *Global and local dynamics of an aeroelastic system with a control surface freplay nonlinearity*. 148 p. Thesis (Doctorate) — Duke University, 2000. Available from: <<http://adsabs.harvard.edu/abs/2000PhDT.....133T>>.

Van Humbeeck, J. Damping capacity of thermoelastic martensite in shape memory alloys. *Journal of Alloys and Compounds*, v. 355, p. 58–64, 2003. Available from: <<http://www.sciencedirect.com/science/article/pii/S0925838803002688>>.

WAGNER, H. Über die Entstehung des dynamischen Auftriebes von Tragflügeln. *ZAMM-Journal of Applied Mathematics and Mechanics/Zeitschrift für Angewandte Mathematik und Mechanik*, v. 5, n. 1, p. 17–35, 1925.

YUN, C. Y.; KIM, D. S.; KIM, S. J. Stability augmentation of helicopter rotor blades using passive damping of shape memory alloys. *International Journal of Aeronautical and Space Sciences*, v. 7, n. 1, p. 137–147, 2006. Available from: <http://ijass.org/On_line/admin/files/7-1-14.pdf>.

ZHAO, L.; TANG, L.; YANG, Y. Synchronized charge extraction in galloping piezoelectric energy harvesting. *Journal of Intelligent Material Systems and Structures*, v. 27, n. 4, p. 453–468, mar 2016. Available from: <<http://jim.sagepub.com/cgi/doi/10.1177/1045389X15571384>>.

ZHU, D. et al. A novel miniature wind generator for wireless sensing applications. In: *IEEE Sensors 2010*. [s.n.], 2010. Available from: <eprints.ecs.soton.ac.uk/21682/>.

APPENDIX A - Lagrange Equations for the Piezoaeroelastic System

Hamilton's Principle for an electromechanical system (in the absence of dissipative effects) is given (ERTURK; INMAN, 2011),

$$\int_{t_1}^{t_2} (\delta T - \delta U + \delta W_{ie} + \delta W_{nc}) dt = 0, \quad (\text{A.1})$$

where δT is the variation in the total kinetic energy, δU is the variation in the total potential energy, δW_{ie} is the variation in the total electrical energy and W_{nc} is the virtual work due to the non-conservative components of mechanical force and electrical charge.

The kinetic energy may be expressed in terms of generalized coordinates and their time-derivatives as,

$$T = T(q_1, q_2, \dots, q_n, \dot{q}_1, \dot{q}_2, \dots, \dot{q}_n), \quad (\text{A.2})$$

while the potential and electrical energies are expressed in terms of the generalized coordinates only,

$$U = U(q_1, q_2, \dots, q_n), \quad (\text{A.3})$$

$$W_{ie} = W_{ie}(q_1, q_2, \dots, q_n), \quad (\text{A.4})$$

where q_k represents each of the n coordinates of the considered system.

The variations of T , U and W_{ie} are, respectively,

$$\delta T = \sum_{k=1}^n \left(\frac{\partial T}{\partial q_k} \delta q_k + \frac{\partial T}{\partial \dot{q}_k} \delta \dot{q}_k \right), \quad (\text{A.5})$$

$$\delta U = \sum_{k=1}^n \frac{\partial U}{\partial q_k} \delta q_k, \quad (\text{A.6})$$

$$\delta W_{ie} = \sum_{k=1}^n \frac{\partial W_{ie}}{\partial q_k} \delta q_k, \quad (\text{A.7})$$

and the virtual work W_{nc} is,

$$\delta W_{nc} = \sum_{k=1}^n Q_k \delta q_k, \quad (\text{A.8})$$

where Q_k are non-conservative forces.

Hamilton's Principle (Eq. (A.1)) becomes, therefore,

$$\int_{t_1}^{t_2} \sum_{k=1}^n \left[\left(\frac{\partial T}{\partial q_k} - \frac{\partial U}{\partial q_k} + \frac{\partial W_{ie}}{\partial q_k} + Q_k \right) \delta q_k + \frac{\partial T}{\partial \dot{q}_k} \right] dt = 0, \quad (\text{A.9})$$

by assuming $\delta q_k = 0$ when $t = t_1$ and $t = t_2$.

By integrating (by parts) the last term of the equation above, Hamilton's Principle may be expressed as,

$$\int_{t_1}^{t_2} \sum_{k=1}^n \left[\frac{\partial T}{\partial q_k} - \frac{\partial U}{\partial q_k} + \frac{\partial W_{ie}}{\partial q_k} + Q_k - \frac{d}{dt} \left(\frac{\partial T}{\partial \dot{q}_k} \right) \right] \delta q_k dt = 0. \quad (\text{A.10})$$

For arbitrary virtual displacements, Eq. (A.10) reduces to the Lagrange electromechanical equation,

$$\frac{d}{dt} \left(\frac{\partial T}{\partial \dot{q}_k} \right) - \frac{\partial T}{\partial q_k} + \frac{\partial U}{\partial q_k} - \frac{\partial W_{ie}}{\partial q_k} = Q_k, \quad (\text{A.11})$$

and the dissipative effects can be introduced into the model as non-conservative forces.

APPENDIX B - Matrices of the Aerodynamic Model

The matrices which correspond to the non-circulatory aerodynamics are given (EDWARDS, 1977),

$$\mathbf{M}_{nc} = \begin{bmatrix} -\pi \left(\frac{1}{8} + a^2 \right) & -2T_{13} & \pi a \\ -2T_{13} & \frac{T_3}{\pi} & T_1 \\ \pi a & T_1 & -\pi \end{bmatrix}, \quad (\text{B.1})$$

$$\mathbf{K}_{nc} = \begin{bmatrix} 0 & -(T_{10} + T_4) & 0 \\ 0 & \frac{1}{\pi} (T_4 T_{10} - T_5) & 0 \\ 0 & 0 & 0 \end{bmatrix}, \quad (\text{B.2})$$

$$\mathbf{B}_{nc} = \begin{bmatrix} \pi \left(a - \frac{1}{2} \right) & 2p + \left(\frac{1}{2} - a \right) T_4 & 0 \\ -p + T_1 + \frac{T_4}{2} & \frac{T_{11} T_4}{2\pi} & 0 \\ -\pi & T_4 & 0 \end{bmatrix}. \quad (\text{B.3})$$

The matrices which correspond to the circulatory portion are given,

$$\mathbf{R} = \begin{bmatrix} 2\pi \left(a + \frac{1}{2} \right) \\ -T_{12} \\ -2\pi \end{bmatrix}, \quad (\text{B.4})$$

$$\mathbf{S}_1 = \begin{bmatrix} 1 & \frac{T_{10}}{\pi} & 0 \end{bmatrix}, \quad (\text{B.5})$$

$$\mathbf{S}_2 = \begin{bmatrix} \left(\frac{1}{2} - a \right) & \frac{T_{11}}{2\pi} & 1 \end{bmatrix}, \quad (\text{B.6})$$

$$\mathbf{S}_3 = \begin{bmatrix} 0.006825 \left(\frac{U}{b}\right)^2 & 0.10805 \left(\frac{U}{b}\right) \end{bmatrix}. \quad (\text{B.7})$$

The matrices corresponding to the two augmented (aerodynamic) equations of the state-space model (in dimensionless form) are given,

$$\tilde{\mathbf{D}} = \frac{1}{\omega_h^2} \mathbf{D}, \quad (\text{B.8})$$

$$\tilde{\mathbf{E}}_1 = \frac{1}{\omega_h^2} \left(\frac{U}{b}\right) \begin{bmatrix} \mathbf{0} \\ \mathbf{S}_1 \end{bmatrix}, \quad (\text{B.9})$$

$$\tilde{\mathbf{E}}_2 = \frac{1}{\omega_h} \begin{bmatrix} \mathbf{0} \\ \mathbf{S}_2 \end{bmatrix}, \quad (\text{B.10})$$

$$\tilde{\mathbf{F}}_p = \frac{1}{\omega_h^2} \begin{bmatrix} 0 & 1 \\ -0.01365 \left(\frac{U}{b}\right)^2 & -0.3455 \left(\frac{U}{b}\right) \end{bmatrix}. \quad (\text{B.11})$$

APPENDIX C - Theodorsen Constants

The geometric constants required for the matrices of Appendix B (known as Theodorsen constants) are given Theodorsen (1935),

$$T_1 = -\frac{1}{3}\sqrt{1-c^2}(2+c^2) + c\cos^{-1}c, \quad (\text{C.1})$$

$$T_2 = c(1-c^2) - \sqrt{1-c^2}(1+c^2)\cos^{-1}c + c(\cos^{-1}c)^2, \quad (\text{C.2})$$

$$T_3 = -\left(\frac{1}{8} + c^2\right)(\cos^{-1}c)^2 + \frac{1}{4}\sqrt{1-c^2}\cos^{-1}c(7+2c^2) - \frac{1}{8}c(1-c^2)(5c^2+4), \quad (\text{C.3})$$

$$T_4 = -\cos^{-1}c + c\sqrt{1-c^2}, \quad (\text{C.4})$$

$$T_5 = -(1-c^2) - (\cos^{-1}c)^2 + 2c\sqrt{1-c^2}\cos^{-1}c, \quad (\text{C.5})$$

$$T_6 = T_2, \quad (\text{C.6})$$

$$T_7 = -\left(\frac{1}{8} + c^2\right)\cos^{-1}c + \frac{1}{8}c\sqrt{1-c^2}(7+2c^2), \quad (\text{C.7})$$

$$T_8 = -\frac{1}{3}\sqrt{1-c^2}(2c^2+1) + c\cos^{-1}c, \quad (\text{C.8})$$

$$T_9 = \frac{1}{2}\left[\frac{1}{3}\left(\sqrt{1-c^2}\right)^3 + aT_4\right], \quad (\text{C.9})$$

$$T_{10} = \sqrt{1-c^2} + \cos^{-1}c, \quad (\text{C.10})$$

$$T_{11} = \cos^{-1}c(1-2c) + \sqrt{1-c^2}(2-c), \quad (\text{C.11})$$

$$T_{12} = \sqrt{1-c^2}(2+c) - \cos^{-1}c(2c+1), \quad (\text{C.12})$$

$$T_{13} = \frac{1}{2}[-T_7 - (c-a)T_1], \quad (\text{C.13})$$

$$T_{14} = \frac{1}{16} + \frac{1}{2}ac, \quad (\text{C.14})$$

where a is defined for a typical section with a control surface (a is the dimensionless position

of the control surface hinge line from the midchord). This is not the case of this study (since a 2-DOF typical section is considered) and hence the constants which depend on a are not used by the matrices of Appendix B. All of the Theodorsen constants are presented, however, for a sense of completeness. Furthermore, c is the dimensionless position of the elastic axis from the midchord.

APPENDIX D - Isothermal and Non-Isothermal Assumptions for the SMA Behavior

For comparison purposes, a heat transfer model based on the works of Hadi et al. (2010) and Faulkner (2000) was also included in the aeroelastic model of this work. The referred thermal model includes heat storage, convective heat transfer, Joule heating and latent heat (release and absorption of heat related to forward and reverse phase transformations, respectively). Based on the referred works, the following heat transfer equation was considered,

$$m_s c_p \dot{T} = \frac{V^2}{R(\xi)} + m_s L_h \dot{\xi} - h_c A_c (T - T_\infty) \quad (\text{D.1})$$

where m_s is the mass of the SMA spring, c_p is specific heat, V is voltage, R is electrical resistance of the SMA spring, h_c is the convective heat transfer coefficient, A_c is the circumferential area of the SMA spring, T is the SMA temperature, T_∞ is the ambient temperature and L_h is the latent heat. One may note the latent heat term is related to the rate of change in the martensitic fraction, which also introduces loading rate dependency to the model.

The electrical resistance of the SMA can be expressed as function of the martensitic fraction,

$$R(\xi) = R_A + \xi (R_M - R_A) \quad (\text{D.2})$$

where R_A and R_M are the electrical resistances of the fully austenitic and fully martensitic phases, respectively.

Moreover, the SMA spring considered in Hadi et al. (2010) is from the same manufacturer

of the SMA spring employed in Aguiar et al. (2013). The SMA springs employed in both works are very similar to each other and since this work assumed the SMA constitutive properties of Aguiar et al. (2013) (and similar spring geometry), it is reasonable to assume that both SMA springs have also similar thermal and electrical properties. Therefore, by employing the SMA constitutive properties of Aguiar et al. (2013) (the same properties employed in Chapter 4) and the SMA thermal and electrical properties of Hadi et al. (2010) (displayed in Table 8), the aeroelastic behavior of the typical section is presented next for both the isothermal and non-isothermal assumptions. The aeroelastic parameters are also the same of Chapter 4.

Table 8 – SMA thermal and electrical properties.

Property	Value	Unit
m_s	1.18×10^{-3}	kg
c_p	350	$\text{J} \cdot \text{kg}^{-1} \cdot ^\circ\text{C}^{-1}$
L_h	6025	$\text{J} \cdot \text{kg}^{-1} \cdot ^\circ\text{C}^{-1}$
R_A	0.7246	Ω
R_M	0.8197	Ω
h_c	150	$\text{J} \cdot \text{m}^{-2} \cdot ^\circ\text{C}^{-1} \cdot \text{s}^{-1}$
A_c	9.77×10^{-4}	m^2

For the simulations, the ambient temperature is assumed as 23°C . For the considered parameters (Tables 1 and 8), an input voltage of 1.93 V yields to the steady-state SMA temperature of 58°C (which is the same value of A_f in Table 1). The corresponding critical stresses are, therefore, the same ones of Chapter 4. The initial plunge displacement and preload levels are also the same.

Figs. 80 to 83 display the aeroelastic and SMA spring behaviors for the simulation parameters described above and isothermal and non-isothermal conditions. Non-preloaded and preloaded SMA springs ($f_0 = 0 \text{ N}$ and $f_0 = 3 \text{ N}$, respectively) are considered for the typical section at the flutter boundary. For the preloaded case, post-flutter regime is also considered. The same conditions (preload levels and airflow speeds) were assumed in Chapter 4. One should note that the results obtained for the isothermal and non-isothermal conditions are similar (with negligible differences). Therefore, the isothermal assumption was employed throughout this work (in all of the previous chapters).

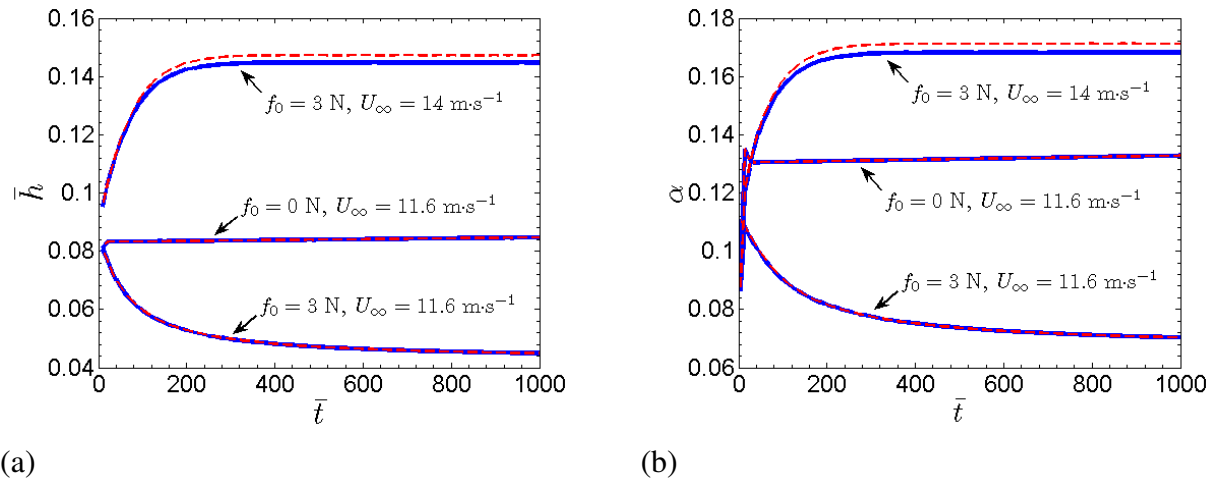


Figure 80 – (a) Plunge and (b) pitch peak amplitudes (continuous lines: isothermal; dashed lines: non-isothermal).

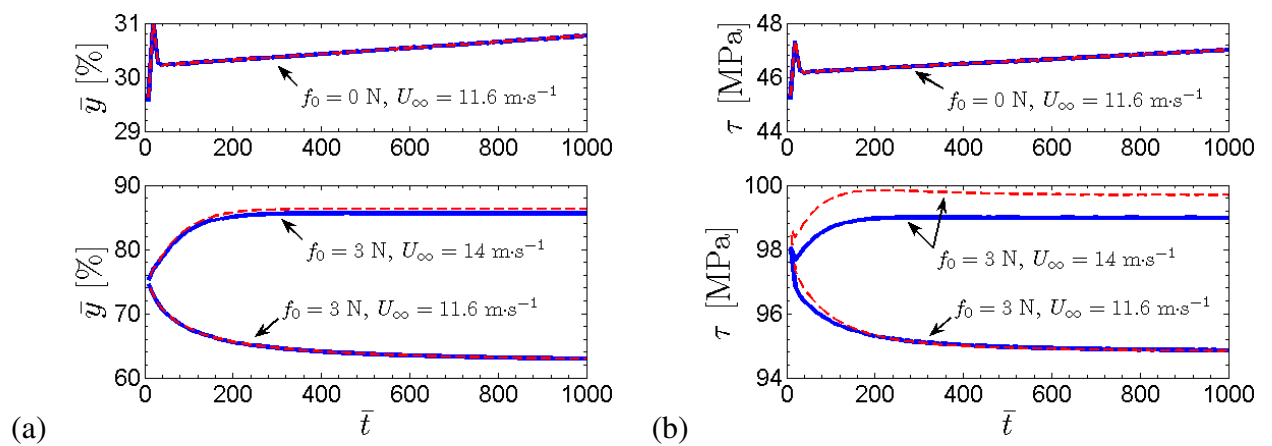


Figure 81 – Behavior of the SMA springs – (a) elongation and (b) shear stress in time (continuous lines: isothermal; dashed lines: non-isothermal).

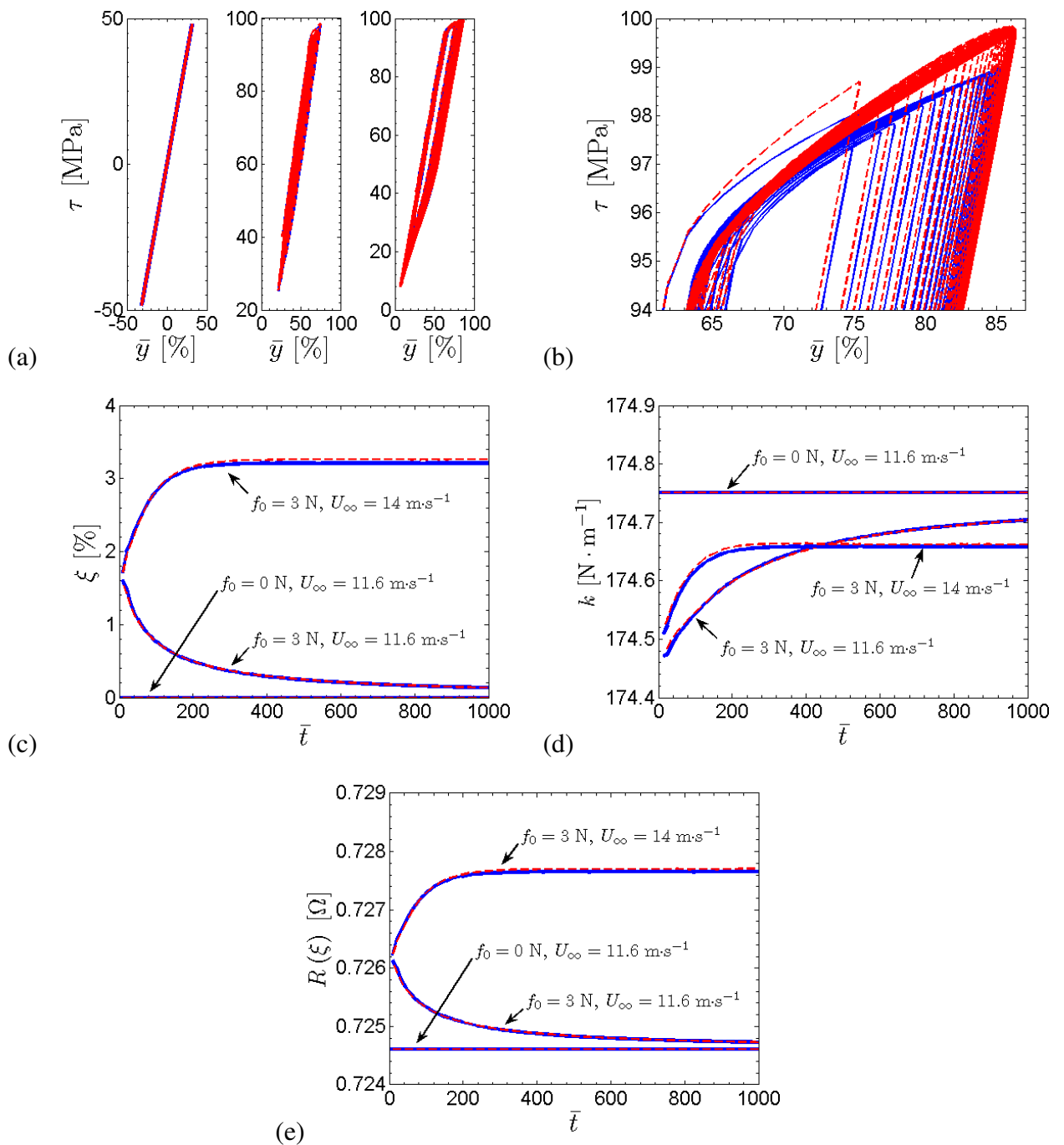


Figure 82 – Behavior of the SMA springs – (a) shear stress-elongation diagrams (for $f_0 = 0$ N and 11.6 m·s⁻¹, $f_0 = 3$ N and 11.6 m·s⁻¹ and also $f_0 = 3$ N and 14 m·s⁻¹), (b) detail of the diagram for 14 m·s⁻¹, (c) martensitic fraction, (d) stiffness and (e) electrical resistance (continuous lines: isothermal; dashed lines: non-isothermal).

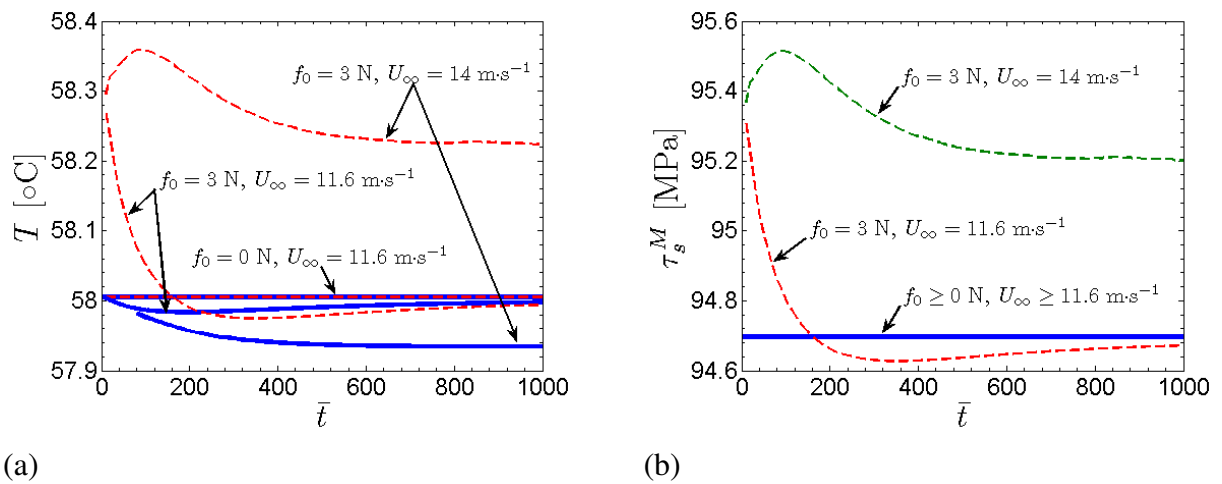


Figure 83 – Temperature variations (a) and the corresponding critical stress τ_s^M (b) (continuous lines: isothermal; dashed lines: non-isothermal).

The effects of thermal expansion on the overall aeroelastic response are small and are not considered in this work.

Publications

- SOUSA, V. C.; DE MARQUI JR., C. Effect of pseudoelastic hysteresis of shape memory alloy springs on the aeroelastic behavior of a typical airfoil section. **Journal of Intelligent Material Systems and Structures**, v. 27, n. 1, p. 117–133, 2016. Published online before print December 19, 2014.
DOI: 10.1177/1045389X14563862.
Available from: <jim.sagepub.com/content/early/2014/12/18/1045389X14563862>
- SOUSA, V. C.; DE MARQUI JR., C. Airfoil-based piezoelectric energy harvesting by exploiting the pseudoelastic hysteresis of shape memory alloy springs. **Smart Materials and Structures**, v. 24, n. 12, p. 125014 (13pp), 2015.
DOI: 10.1088/0964-1726/24/12/125014.
Available from: <iopscience.iop.org/article/10.1088/0964-1726/24/12/125014>
- SOUSA, V. C.; DE MARQUI JR., C.; ELAHINIA, M. H. Effect of constitutive model parameters on the aeroelastic behavior of an airfoil with shape memory alloy springs. **Journal of Vibration and Control**. Published online before print July 25, 2016. DOI: 10.1177/1077546316657501.
Available from:
<jvc.sagepub.com/content/early/2016/07/21/1077546316657501>